University of Sheffield

Quantum scalar field theory on anti-de Sitter space-time with Robin boundary conditions

Sivakumar Namasivayam

Submitted in partial fulfilment for the degree of
Doctor of Philosophy

School of Mathematics and Statistics

July 2024

Supervisor: Professor Elizabeth Winstanley

To my wife, Susan...

for your unwavering support, understanding,
and encouragement throughout my mathematical journey
...thank you

Acknowledgements

Firstly, I would like to express my sincere gratitude and thanks to my supervisor Elizabeth Winstanley for giving me the opportunity to study the wonderful subject of quantum field theory in curved space-time. Her enthusiasm and patience is exemplary and my research would not have been possible without her help and guidance.

I would also like to thank the School of Mathematics and Statistics for the travel allowance which gave me the chance to attend and present at some amazing conferences both at home and abroad. Also, I would like to thank the staff at the University of Sheffield High Power Computing service on which most of the numerical computations in this thesis were performed.

Finally, I would like to thank the many staff and students, past and present, of the Sheffield CRAG group who have made my time in Sheffield so enjoyable. I will miss you all.

Abstract

In this thesis we study a real quantum scalar field propagating on three (adS3) and four (adS4) dimensional anti-de Sitter space-time with Dirichlet, Neumann and Robin boundary conditions imposed at the space-time boundary. Using Hadamard renormalisation, we numerically compute the vacuum polarisation (VP) on adS3 for a scalar field with general mass and coupling and compare our results with those obtained for the massless, conformally coupled field on adS4. We find that both the vacuum (v.e.v.) and thermal (t.e.v.) expectation values of the VP with Robin boundary conditions converge to the Neumann result at the space-time boundary, except Dirichlet, which has its own limit.

We also numerically compute the v.e.v.s and t.e.v.s of the renormalised stress energy tensor (RSET) for a massless, conformally coupled scalar field on adS4 as well as for the scalar field with general mass and coupling on adS3. Dirichlet, Neumann and Robin boundary conditions are applied at the space-time boundary in both cases. On adS3, we find that with particular values of the coupling constant, we obtain RSETs with negative energy density profiles throughout some or all of the space-time.

Using a selection of the RSETs, obtained for the scalar field with general mass and coupling on adS3, we examine the backreaction of the numerically computed RSETs on the underlying space-time metric. We focus on some of the key features of the quantum-corrected metrics so obtained and make suggestions for future research in this area.

Declaration of Authorship

I hereby confirm that, except where clear reference is made to the work of others, this thesis is my own work. I am aware of the University's Guidance on the Use of Unfair Means (www.sheffield.ac.uk/ssid/unfair-means). This work has not been previously been presented for an award at this, or any other, university. The following publications have arisen from work in this thesis

- S. Namasivayam and E. Winstanley. Vacuum polarization on three-dimensional anti-de Sitter space-time with Robin boundary conditions. Gen. Rel. Grav., 55:13, 2023.
- T. Morley, S. Namasivayam, and E. Winstanley. Renormalized stress-energy tensor on global anti-de Sitter space-time with Robin boundary conditions. Gen. Rel. Grav., 56:38, 2024.
- S. Namasivayam and E. Winstanley. Renormalised stress energy tensor on three dimensional anti-de Sitter space-time with Robin boundary conditions for a scalar field with generalised mass and coupling. In preparation, 2024.
- S. Namasivayam and E. Winstanley. Quantum-corrected metric on three dimensional anti-de Sitter space-time. In preparation, 2024.

Sivakumar Namasivayam

Contents

List of Tables

List of Figures

Preface

Chapters 1 and 2 contain review material and no original research. The work in Chapter 3 on the RSET on adS4 for the massless, conformally coupled scalar field with Robin boundary conditions used some preliminary MATHEMATICA codes provided by Tom Morley. This was developed further by the author and used for the numerical computations of the RSET. The Green's functions in Section 3.2 as well as the expressions used to compute the RSET with Robin boundary conditions (3.37) were obtained from [71]. All the numerical computations and plots in Chapter 3 were produced by the author and are the subject of a recent publication [70].

Chapter 4 contains work by the author although the mode sum solutions to the Klein-Gordon equation have appeared in [29]. The calculation of an upper bound for the Robin parameter ζ_{crit} on adS3, for the scalar field with general mass and coupling, is new. The work in Chapter 5 on the VP of a scalar field with general mass and coupling with Robin boundary conditions is new work and has been published [73]. All numerical calculations and plots in this chapter were produced by the author.

Chapter 6 contains original research on the computation of the RSET for a scalar field with general mass and coupling. All the numerical computations and plots have been produced by the author and plans are in place for a future publication [75]. Chapter 7 on the quantum-corrected metric also contains original research by the author and it is hoped will provide the basis for a future publication [74].

Notation

In this thesis the following notation is adopted

- The metric signature used in this thesis is $(-,+,+,+)$.
- We set the constants $\hbar = c = 1$. Newton's constant G is given explicitly in Einstein's field equations but in all the numerical computations in this thesis we have set $G = 1$.
- The set of natural numbers $\mathbb{N}$ and strictly negative integers $\mathbb{Z}^-$ are

$$\mathbb{N} = \{0, 1, 2, \dots\},$$
$$\mathbb{Z}^- = \{0, -1, -2, \dots\}.$$

- The Einstein summation convention is used when the same index appears in a superscript and subscript in a product. For example

$$a_\mu b^\mu = \sum_{\mu=0}^{n} a_\mu b^\mu = a_0 b^0 + a_1 b^1 + \cdots + a_n b^n. \tag{1}$$

- The partial derivative is denoted by

$$F_{,\mu} = \partial_\mu F = \frac{\partial F}{\partial x^\mu}. \tag{2}$$

- The covariant derivative is denoted by

$$G^\rho{}_{;\mu} = \nabla_\mu G^\rho = G^\rho{}_{,\mu} + \Gamma^\rho{}_{\mu\nu} G^\nu,$$
$$G_{\rho\,;\mu} = \nabla_\mu G_\rho = G_{\rho\,,\mu} - \Gamma^\nu{}_{\rho\,\mu} G_\nu,$$

where $\Gamma^\lambda_{\mu\nu}$ is the Christoffel symbol defined as

$$\Gamma^\lambda_{\mu\nu} = \frac{1}{2} g^{\lambda\sigma} \Big\{ \partial_\mu g_{\sigma\nu} + \partial_\nu g_{\mu\sigma} - \partial_\sigma g_{\mu\nu} \Big\}. \tag{3}$$

Chapter 1

Introduction

The two greatest physical theories of the twentieth century are general relativity (GR) and quantum mechanics (QM). Einstein's theory of general relativity [41] is a theory of gravity. This superseded the previous Newtonian version which had held sway for almost three hundred years. GR is encapsulated in Einstein's field equations

$$R_{\mu\nu} - \frac{1}{2}R\, g_{\mu\nu} + g_{\mu\nu}\Lambda = 8\pi G\, T_{\mu\nu}, \tag{1.1}$$

where $R_{\mu\nu}$ is the Ricci tensor, R is the Ricci scalar, $g_{\mu\nu}$ is the metric tensor, Λ is the cosmological constant, G is Newton's constant and $T_{\mu\nu}$ is the stress energy tensor (SET). The metric tensor $g_{\mu\nu}$ encodes the geometry of the underlying space-time whilst the SET contains the information about the matter/energy content. GR can be usefully encapsulated by Wheeler's famous saying that '..matter tells space how to curve, and space tells matter how to move..' [68].

GR is a highly successful theory of gravity which has been successfully tested by observations and experiments. For instance, GR has successfully predicted the perihelion of Mercury [41], which was not fully accounted for using Newtonian physics. GR has also predicted the bending of light rays by the Sun, which was first confirmed by Eddington during the 1919 solar eclipse [40]. Furthermore, in the first terrestrial test of its kind, Pound and Rebka were able to measure the gravitational redshift of photons in a tower at Harvard University [85].

Quantum mechanics and its relativistic counterpart, quantum field theory (QFT), describe the Universe at the scale of fundamental particles. QFT proposes that particles are excitations of quantum fields that pervade throughout space and time. It is a probabilistic theory where observables are Hermitian operators acting on the Fock space of states. QFT is integral to the Standard Model (SM) of particle physics which describes the electromagnetic, strong and weak nuclear forces.

Whilst both QFT and GR are extremely successful in describing the Universe in their own scales, they are fundamentally incompatible with each other. GR is a classical theory of gravity formulated before the emergence of QM, where the motion of massive bodies is a result of the curvature of the underlying space-time rather that the exchange of virtual particles as in the SM. In everyday life it is hard to see how two theories describing the Universe at such different scales would ever need to be compatible, apart form an aesthetic desire to have all the fundamental laws of physics unified into a single theory of everything. However, there are two areas of physics where GR and QFT meet face to face, namely in the early Universe and in the study of black holes. Stephen Hawking's seminal work in the mid 1970s [53] demonstrated the interface between QFT and GR and and played an

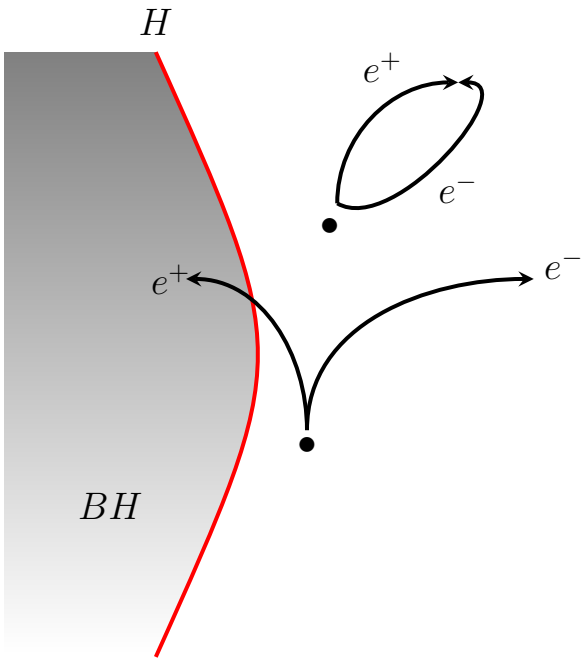

Figure 1.1: Heuristic picture of Hawking radiation. Vacuum fluctuations outside an event horizon (H) of a black hole (BH) create particle/anti-particle pairs (e^-/e^+) which usually annihilate each other. Occasionally an anti-particle will fall into the BH whilst its positive energy partner will escape to infinity as Hawking radiation (adapted from [23]).

important role in the evolution of quantum field theory in curved space-time (QFTCS). Hawking showed that near the event horizon of a collapsing black hole , virtual particle/ anti-particle pairs can form out of the vacuum of space, see Figure 1.1. Usually such particle/anti-particle pairs reunite and annihilate each other but occasionally an anti-particle falls into the black hole, reducing its mass and entropy. Meanwhile the positive energy partner is emitted with a thermal spectrum as Hawking radiation.

Over the last few decades, there have been many attempts to unify GR and QM. String theory postulates that the fundamental building blocks of matter are tiny vibrating strings (open or closed) and that different particles are represented by different excitations of these fundamental strings (see [103] for an introductory account). The massless, spin-2 graviton naturally comes out of all consistent versions of string theory. The graviton is a hypothetical particle that mediates the gravitational interaction in much the same way as the photon mediates the electromagnetic force. Another candidate for a unified theory is loop quantum gravity (see [7] for a short review). This aims to quantise the geometry of space-time into discrete elements rather than the smooth continuous manifold of GR.

In this thesis we use QFTCS as an approximation to quantum gravity (see [17, 48, 78, 102] for reviews). In QFTCS we study quantum fields propagating on a background classical curved space-time which is described by a smooth manifold $\mathfrak{M}$ possessing a classical metric $g_{\mu\nu}$. We promote the SET $T_{\mu\nu}$ to an operator valued distribution such that (1.1) becomes

$$R_{\mu\nu} - \frac{1}{2} R\, g_{\mu\nu} + g_{\mu\nu}\Lambda = 8\pi G \,\langle \hat{T}_{\mu\nu} \rangle, \tag{1.2}$$

where $\langle\hat{T}_{\mu\nu}\rangle$ is the expectation value of the stress energy tensor. We take a metric which is a solution to the vacuum Einstein's equation (where the right hand side of (1.2) is zero) and use this to compute the expectation values of operators involving a quantum field Φ. Such expectation values include the vacuum polarisation $\langle\hat{\Phi}^2\rangle$ and, importantly, the expectation value of the stress energy tensor $\langle\hat{T}_{\mu\nu}\rangle$. Once determined, we can then use $\langle\hat{T}_{\mu\nu}\rangle$ as the source term in (1.2) to compute the quantum corrections (backreaction) to the original metric, directly interfacing GR with QFT. However, it is likely that QFTCS has a limited range of validity and will break down if the curvature of the space-time approaches the Planck scale [102].

This chapter contains some of the key principles and concepts used later in this thesis and is laid out as follows. In Section 1.1, we set out some of the basic principles of QFT in flat space-time, including the derivation of the Klein-Gordon equation and the establishment of canonical commutation relations. Much of this will be found in standard textbooks of QFT (see for example [64, 82]). In Section 1.2 we progress to an arbitrary curved space-time background and highlight the key differences between QFT in flat and curved space-time. In Section 1.3 we give an overview of Green's functions, in particular the Feynman propagator, which is fundamental in determining expectation values of operators such as the stress energy tensor. In Section 1.4 we give a brief outline of the advantages of QFT in Euclidean space. As the Feynman propagator is divergent in the coincidence limit we need to employ a renormalisation procedure to extract physically meaningful expectation values. This is the subject of Section 1.5 in which we refer extensively to [35, 61] and focus specifically on the results in three and four dimensions. In Section 1.6 we discuss the SET, including its classical derivation from the action and the construction of a renormalised SET (RSET). This is followed in Section 1.7 by a description of Wald's axioms and uniqueness theorem which gives validity to the RSETs obtained from our renormalisation procedure. In Section 1.8 we describe the classical and quantum energy conditions which seek to place bounds on the energy densities of the RSET to avoid exotic (possibly unrealistic) space-times such as wormholes. Finally in Section 1.9 we set this thesis in context with current work in the literature and provide motivation for the research contained within.

§ 1.1 Quantum field theory in flat space-time

In order to formulate a QFT on a curved background we first consider a QFT in flat space-time. The following applies to a real scalar field. We start with a classical field, $\Phi(\mathbf{x}, t)$, in an $n-$dimensional space-time with Lagrangian density $\mathcal{L}(\Phi, \partial^\mu\Phi)$ given by

$$\mathcal{L}(\Phi, \partial^\mu\Phi) = -\frac{1}{2}\partial_\mu\Phi\partial^\mu\Phi - \frac{1}{2}m^2\Phi^2, \tag{1.3}$$

where m is the mass of the field, $\mathbf{x}$ refers to the spatial coordinates, t the time coordinate and we have used the Minkowski metric to raise and lower indices. The corresponding action $\mathcal{S}$ is

$$\mathcal{S}[\Phi, g_{\mu\nu}] = \int \mathcal{L}(\Phi, \partial^\mu\Phi)\, d^n\mathbf{x}. \tag{1.4}$$

We can obtain the equation of motion for the scalar field by equating to zero the variation in the action $\mathcal{S}$ corresponding to variations in Φ, giving

$$\begin{aligned}\delta\mathcal{S} &= \int \left\{ \frac{\partial\mathcal{L}}{\partial\Phi}\delta\Phi + \frac{\partial\mathcal{L}}{\partial(\partial^\mu\Phi)}\delta(\partial^\mu\Phi) \right\} d^n\mathbf{x} \\ &= \int \delta\Phi \left\{ \frac{\partial\mathcal{L}}{\partial\Phi} - \partial^\mu \left[\frac{\partial\mathcal{L}}{\partial(\partial^\mu\Phi)} \right] \right\} d^n\mathbf{x}, \end{aligned} \tag{1.5}$$

where we have assumed that the boundary terms vanish. As we require $\delta\mathcal{S} = 0$ we must have

$$\partial^\mu \left[\frac{\partial\mathcal{L}}{\partial(\partial^\mu\Phi)} \right] - \frac{\partial\mathcal{L}}{\partial\Phi} = 0. \tag{1.6}$$

This is the Euler-Lagrange equation for the scalar field. Computing the terms in (1.6) and using (1.3) gives the Klein-Gordon equation

$$\partial_\mu\partial^\mu\Phi - m^2\Phi = 0. \tag{1.7}$$

A basic set of solutions to (1.7) is formed by the plane waves

$$\Phi_{\mathbf{p}}(\mathbf{x}, t) = \mathcal{A}\, e^{-i\omega t + i\mathbf{p}.\mathbf{x}}, \tag{1.8}$$

where ω is the frequency, $\mathbf{p}$ the momentum which satisfies the relation $m^2 = \omega^2 - |\mathbf{p}|^2$ and $\mathcal{A}$ is a normalisation constant. We only consider $\omega > 0$ when $\Phi_{\mathbf{p}}$ represents positive frequency modes. The complex conjugate $\Phi^*_{\mathbf{p}}$ gives the negative frequency modes. We can calculate the constant $\mathcal{A}$ in (1.8) by defining an inner product for two solutions Φ_1, Φ_2 of (1.7) as

$$\langle\Phi_1, \Phi_2\rangle = -i \int_\Sigma (\Phi_1\partial_t\Phi_2^* - \Phi_2^*\partial_t\Phi_1) d^{n-1}\mathbf{x}, \tag{1.9}$$

where Σ is an equal time hypersurface. Defining our two solutions as

$$\Phi_1(\mathbf{x}, t) = \mathcal{A}_1 e^{-i\omega_1 t} e^{i\mathbf{p}_1.\mathbf{x}}, \qquad \Phi_2(\mathbf{x}, t) = \mathcal{A}_2 e^{-i\omega_2 t} e^{i\mathbf{p}_2.\mathbf{x}} \tag{1.10}$$

we have

$$\langle\Phi_1, \Phi_2\rangle = \int_\Sigma \mathcal{A}_1\mathcal{A}_2^*(\omega_1 + \omega_2) e^{i(\omega_2 - \omega_1)t} e^{i(\mathbf{p}_1 - \mathbf{p}_2).\mathbf{x}}\, d^{n-1}\mathbf{x}. \tag{1.11}$$

Using the Fourier transform of the n-dimensional Dirac delta function

$$(2\pi)^{n-1}\delta^{n-1}(\mathbf{p}_1 - \mathbf{p}_2) = \int e^{i(\mathbf{p}_1 - \mathbf{p}_2).\mathbf{x}}\, d^{n-1}\mathbf{x}, \tag{1.12}$$

we have

$$\langle\Phi_1, \Phi_2\rangle = \mathcal{A}_1\mathcal{A}_2^*(\omega_1 + \omega_2) e^{i(\omega_2 - \omega_1)t} (2\pi)^{n-1}\delta^{n-1}(\mathbf{p}_1 - \mathbf{p}_2). \tag{1.13}$$

We require that the modes are orthonormal, so $\langle\Phi_1, \Phi_2\rangle = \delta^{n-1}(\mathbf{p}_1 - \mathbf{p}_2)$, and therefore the constant $\mathcal{A}$ is given by

$$\mathcal{A} = \frac{1}{\sqrt{2\omega(2\pi)^{n-1}}}. \tag{1.14}$$

To quantise the classical field we promote the field to an operator-valued distribution, i.e. $\Phi(t,\mathbf{x}) \to \hat{\Phi}(t,\mathbf{x})$ and establish equal time commutation relations

$$\begin{aligned}
&[\hat{\Phi}(t,\mathbf{x}),\hat{\Phi}(t,\mathbf{x}')] = \hat{\Phi}(t,\mathbf{x})\hat{\Phi}(t,\mathbf{x}') - \hat{\Phi}(t,\mathbf{x}')\hat{\Phi}(t,\mathbf{x}) = 0,\\
&[\hat{\pi}(t,\mathbf{x}),\hat{\pi}(t,\mathbf{x}')] = 0,\\
&[\hat{\Phi}(t,\mathbf{x}),\hat{\pi}(t,\mathbf{x}')] = i\delta^{(n-1)}(\mathbf{x}-\mathbf{x}'),
\end{aligned} \tag{1.15}$$

where $\hat{\pi}(t,\mathbf{x})$ is the conjugate momentum given by

$$\hat{\pi}(t,\mathbf{x}) = \partial_t\hat{\Phi}(t,\mathbf{x}) = \dot{\hat{\Phi}}(t,\mathbf{x}). \tag{1.16}$$

We can expand the quantised field in terms of the orthonormal modes (1.8) as

$$\hat{\Phi}(t,\mathbf{x}) = \int \Big(\hat{a}_{\mathbf{p}}\hat{\Phi}_{\mathbf{p}}(t,\mathbf{x}) + \hat{a}^{\dagger}_{\mathbf{p}}\hat{\Phi}^{*}_{\mathbf{p}}(t,\mathbf{x})\Big)d^{n-1}\mathbf{p}, \tag{1.17}$$

where $\hat{a}_{\mathbf{p}}$ and $\hat{a}^{\dagger}_{\mathbf{p}}$ are annihilation and creation operators respectively and obey the canonical commutation relations (CCR)

$$\begin{aligned}
&[\hat{a}_{\mathbf{p}},\hat{a}_{\mathbf{p}'}] = 0,\\
&[\hat{a}^{\dagger}_{\mathbf{p}},\hat{a}^{\dagger}_{\mathbf{p}'}] = 0,\\
&[\hat{a}_{\mathbf{p}},\hat{a}^{\dagger}_{\mathbf{p}'}] = \delta^{(n-1)}(\mathbf{p}-\mathbf{p}').
\end{aligned} \tag{1.18}$$

In global Minkowski space-time there is a preferred vacuum state $|0\rangle$ on which all inertial observers agree, and which we define as

$$\hat{a}_{\mathbf{p}}|0\rangle = 0. \tag{1.19}$$

This is the state with the lowest possible energy, relative to an inertial observer, with no particles present and which is invariant under the Poincaré group of transformations. The Minkowski vacuum respects the symmetries of the underlying space-time. In curved space-times, however, there is no unique definition of a vacuum state as discussed in the next section.

§ 1.2 Quantum field theory in curved space-time

To generalise the flat space-time action $\mathcal{S}$ (1.4) to the case of a curved space-time, we introduce the metric $g_{\mu\nu}$, change the ordinary partial derivatives to covariant ones ($\partial_\mu \to \nabla_\mu$) and use the covariant volume element, i.e. $d^n\mathbf{x} \to \sqrt{-g}\,d^n\mathbf{x}$, where g is the determinant of the metric. The action in curved space-time now becomes

$$\mathcal{S}[\Phi, g_{\mu\nu}] = \int -\frac{1}{2}\Big\{g^{\mu\nu}\nabla_\mu\Phi\nabla_\nu\Phi + (m^2+\xi R)\Phi^2\Big\}\sqrt{-g}\,d^n\mathbf{x}, \tag{1.20}$$

where we introduce a new term ξ, the coupling constant which couples the field to the background curvature. For minimal coupling we have $\xi = 0$ and for conformal coupling we have

$$\xi_c = \frac{(n-2)}{4(n-1)}. \tag{1.21}$$

The Klein-Gordon equation (1.7) in curved space-time now becomes

$$\Big[\Box - (m^2 + \xi R)\Big]\Phi = 0, \tag{1.22}$$

where $\Box$ is the D'Alembertian operator in curved space-time given by

$$\begin{aligned}\Box\Phi &= g^{\mu\nu}\nabla_\mu\nabla_\nu\,\Phi \\ &= g^{\mu\nu}\left(\partial_\mu\partial_\nu - \Gamma^\lambda_{\mu\nu}\partial_\lambda\right)\Phi.\end{aligned} \tag{1.23}$$

The Christoffel symbol, or connection coefficient $\Gamma^\lambda_{\mu\nu}$, is formed from the derivatives of the metric tensor $g_{\mu\nu}$ and is given by

$$\Gamma^\lambda_{\mu\nu} = \frac{1}{2}g^{\lambda\sigma}\Big\{\partial_\mu g_{\sigma\nu} + \partial_\nu g_{\mu\sigma} - \partial_\sigma g_{\mu\nu}\Big\}. \tag{1.24}$$

In a curved space-time, the scalar product (1.9) generalises to [17]

$$\langle\Phi_1, \Phi_2\rangle = -i\int_\Sigma (\Phi_1\partial_\mu\Phi_2^* - \Phi_2^*\partial_\mu\Phi_1)\sqrt{-g}\,n^\mu d\Sigma, \tag{1.25}$$

where, assuming global hyperbolicity, Σ is a non-compact, space-like hypersurface with unit normal n^μ, $d\Sigma$ is the volume element in Σ and g is the determinant of $g_{\mu\nu}$. It can be shown that $\langle\Phi_1, \Phi_2\rangle$ is independent of the chosen hypersurface Σ [55]. As in the flat space-time case, we perform a mode expansion of the scalar field in terms of an orthonormal basis of modes as

$$\hat{\Phi}(t, \mathbf{x}) = \sum_i \Big[\hat{a}_i f_i(t, \mathbf{x}) + \hat{a}_i^\dagger f_i^*(t, \mathbf{x})\Big], \tag{1.26}$$

where we have used the index i to label the modes and the annihilation and creation operators $\hat{a}_i, \hat{a}_i^\dagger$ obey the CCR

$$\begin{aligned}[\hat{a}_i, \hat{a}_{i'}] &= 0, \\ [\hat{a}_i^\dagger, \hat{a}_{i'}^\dagger] &= 0, \\ [\hat{a}_i, \hat{a}_{i'}^\dagger] &= \delta^{(n-1)}(i - i').\end{aligned} \tag{1.27}$$

In (1.26) i is a continuum index in $n-1$ spatial dimensions but we adapt the schema in [17] and represent the mode expansion as a sum over i rather than an integral. As in the flat space case we can define a vacuum state $|0_f\rangle$ that is annihilated by all the annihilation operators

$$\hat{a}_i|0_f\rangle = 0. \tag{1.28}$$

However, suppose we have a different set of orthonormal basis modes g_j with expansion

$$\hat{\Phi}(t, \mathbf{x}) = \sum_j \Big[\hat{b}_j g_j(t, \mathbf{x}) + \hat{b}_j^\dagger g_j^*(t, \mathbf{x})\Big], \tag{1.29}$$

where $\hat{b}_j, \hat{b}_j^\dagger$ are a new set of annihilation and creation operators that also obey the CCR (1.27). We can, therefore, also define another vacuum state $|0_g\rangle$

$$\hat{b}_j|0_g\rangle = 0. \tag{1.30}$$

As the f_i modes form an orthonormal basis, we can expand the g_j modes terms of the f_i modes as

$$\begin{aligned} g_j &= \sum_i \Big[\alpha_{ji} f_i + \beta_{ji} f_i^*\Big], \\ f_i &= \sum_j \Big[\alpha_{ji}^* g_j - \beta_{ji} g_j^*\Big]. \end{aligned} \tag{1.31}$$

The relations in (1.31) are known as Bogoliubov transformations and the matrices α_{ij}, β_{ij} are known as Bogoliubov coefficients, which can be expressed as [17]

$$\alpha_{ij} = \langle g_i, f_j\rangle, \qquad \beta_{ij} = -\langle g_i, f_j^*\rangle. \tag{1.32}$$

Using the orthonormality of the modes we can relate the operators as

$$\begin{aligned} \hat{a}_i &= \sum_j (\alpha_{ji}\hat{b}_j + \beta_{ji}^*\hat{b}_j^\dagger), \\ \hat{b}_j &= \sum_i (\alpha_{ji}^*\hat{a}_i - \beta_{ji}^*\hat{a}_i^\dagger). \end{aligned} \tag{1.33}$$

The Bogoliubov coefficients also satisfy the normalisation conditions

$$\begin{aligned} \sum_k (\alpha_{ik}\alpha_{jk}^* - \beta_{ik}\beta_{jk}^*) &= \delta_{ij}, \\ \sum_k (\alpha_{ik}\beta_{jk} - \beta_{ik}\alpha_{jk}) &= 0. \end{aligned} \tag{1.34}$$

Now consider a system in the $f-$vacuum state $|0_f\rangle$ where no particles are found by an observer using the f_i basis modes. Then the number of particles seen by an observer using the g_j basis of modes is determined by the expectation value of its number operator $\hat{N}_j = \hat{b}_j^\dagger \hat{b}_j$ given by [17]

$$\langle 0_f|N_j|0_f\rangle = \sum_i |\beta_{ij}|^2. \tag{1.35}$$

If any of $\beta_{ij} \neq 0$ then an observer using one set of modes will see particles in a vacuum defined by another set of basis modes. This may be appreciated by observing in (1.33) that the β_{ij} coefficient mixes creation operators from one basis into the annihilation operators of another.

Thus, the notion of particles in curved space-time is observer dependent. Whilst there is no unique definition of a vacuum state on a general curved background, in this thesis we choose the global adS vacuum state as our preferred vacuum state. This is defined using global coordinates on the whole of the adS space-time and retains all the symmetries of adS. However, unlike the Minkowski vacuum, the global adS vacuum is not unique but depends on the boundary conditions.

As we shall see in later chapters, observables calculated using either Dirichlet or Neumann boundary conditions respect the underlying adS symmetry but, in the case of the vacuum polarisation, application of Dirichlet or Neumann boundary conditions produce different vacuum expectation values.

Having formulated a QFT in a curved space-time and developed mode-sum expressions for the quantum scalar field $\hat{\Phi}$ we now turn our attention to computing expectation values. Two expectation values calculated in this thesis are the vacuum polarisation $\langle\hat{\Phi}^2\rangle$ and the stress energy tensor $\langle\hat{T}_{\mu\nu}\rangle$. These expectation values are derived using Green's functions [17] and this is the subject of the next Section.

§ 1.3 Green's functions

In this section we make the assumption that we are in a space-time where the there exists a vacuum state $|0\rangle$, which may or may not be unique and that we have a choice of time coordinate t where time-ordering is possible. By this we mean that we have a space-time with a global time coordinate which we can use to unambiguously define the order of events in time. These assumptions are valid in the covering space of anti de-Sitter space-time where there are no closed time-like curves. In a general curved space-time, the Green's functions satisfy the inhomogeneous equation

$$\Big[\Box - (m^2 + \xi R)\Big]\mathcal{G}(x,x') = -\frac{1}{\sqrt{-g}}\delta^n(x-x'), \tag{1.36}$$

where δ^n is the $n-$dimensional Dirac delta function, $\mathcal{G}$ refers to any one of a number of Green's functions and x, x' represents two space-time points. We start with the formulation of Green's functions for a vacuum state $|0\rangle$ and then use these zero temperature or vacuum Green's functions to derive nonzero temperature or thermal Green's functions. Of particular importance amongst the family of Green's functions are the Pauli-Jordan or Schwinger Green's function G, the anticommutator (Hadamard's elementary) function $G^{(1)}$ and the Feynman propagator G_F. The vacuum Pauli-Jordan and anticommutator Green's functions are given by [17]

$$\begin{aligned} iG(x,x') &= \langle 0|[\hat{\Phi}(x), \hat{\Phi}(x')]|0\rangle, \\ G^{(1)}(x,x') &= \langle 0|\{\hat{\Phi}(x), \hat{\Phi}(x')\}|0\rangle. \end{aligned} \tag{1.37}$$

They can be split into their respective positive and negative frequency parts as

$$\begin{aligned} iG(x,x') &= G^{+}(x,x') - G^{-}(x,x'), \\ G^{(1)}(x,x') &= G^{+}(x,x') + G^{-}(x,x'), \end{aligned} \tag{1.38}$$

where $G^{\pm}(x,x')$ are called Wightman functions given by

$$\begin{aligned} G^{+}(x,x') &= \langle 0|\hat{\Phi}(x)\hat{\Phi}(x')|0\rangle, \\ G^{-}(x,x') &= \langle 0|\hat{\Phi}(x')\hat{\Phi}(x)|0\rangle. \end{aligned} \tag{1.39}$$

The Wightman functions are not Green's functions and satisfy the homogeneous version of (1.36). Also it should be noted that although we refer to G and $G^{(1)}$ as Green's functions (adopting the terminology in [17]), they also satisfy the homogeneous version of (1.36).

Of the Green's functions mentioned above only the Feynman propagator $G_F(x,x')$ satisfies (1.36) and is defined as

$$iG_F(x,x') = \langle 0|\mathcal{T}(\hat{\Phi}(x)\hat{\Phi}(x'))|0\rangle, \tag{1.40}$$

where $\mathcal{T}$ denotes that the fields are time-ordered. For two space-time points with time coordinates t, t', time-ordering requires that

$$\mathcal{T}(\Phi(x)\Phi(x')) = \begin{cases} \hat{\Phi}(x)\hat{\Phi}(x') & \text{if} \quad t > t' \\ \hat{\Phi}(x')\hat{\Phi}(x) & \text{if} \quad t' > t. \end{cases} \tag{1.41}$$

The Feynman propagator can also be expressed as

$$iG_F(x,x') = \Theta(t-t')G^+(x,x') + \Theta(t'-t)G^-(x,x'), \tag{1.42}$$

where Θ is the Heaviside function given by

$$\Theta(t-t') = \begin{cases} 1 & \text{if} \quad t > t' \\ 0 & \text{if} \quad t < t'. \end{cases} \tag{1.43}$$

If $t = t'$ then time ordering is not applicable and we have $iG_F(x,x')|_{t=t'} = \langle 0|\hat{\Phi}(x)\hat{\Phi}(x')|0\rangle$.

Two other Green's functions of note are the retarded G_R and advanced G_A Green's functions defined as [17]

$$\begin{aligned} G_R(x,x') &= -\Theta(t-t')G(x,x'), \\ G_A(x,x') &= \Theta(t'-t)G(x,x'). \end{aligned} \tag{1.44}$$

We can also define the Feynman propagator in terms of G_R and G_A by

$$G_F(x,x') = -\widetilde{G}(x,x') - \frac{1}{2}iG^{(1)}(x,x'), \tag{1.45}$$

where $\widetilde{G}$ is the average of G_R and G_A

$$\widetilde{G}(x,x') = \frac{1}{2}\left[G_R(x,x') + G_A(x,x')\right]. \tag{1.46}$$

Having derived expressions for the Green's functions for a vacuum state $|0\rangle$, we now consider Green's functions in a nonzero temperature or thermal state with inverse temperature $\beta = 1/T$, where T is the temperature of the thermal state. Unlike the vacuum Green's functions which have been calculated in a pure (vacuum) state, an equilibrium system at an inverse temperature β is described by a grand canonical ensemble of states [17]. Thus we can define thermal Green's functions by replacing the vacuum expectation values by the ensemble average $\langle \quad \rangle_\beta$ of mixed thermal states. For the Wightman functions for example we have

$$\begin{aligned} G^+_\beta(x,x') &= \langle\hat{\Phi}(x)\hat{\Phi}(x')\rangle_\beta, \\ G^-_\beta(x,x') &= \langle\hat{\Phi}(x')\hat{\Phi}(x)\rangle_\beta, \end{aligned} \tag{1.47}$$

which satisfy the periodicity property [17]

$$G^{\pm}_{\beta}(t,\mathbf{x};t',\mathbf{x}') = G^{\mp}_{\beta}(t+i\beta,\mathbf{x};t',\mathbf{x}'). \tag{1.48}$$

Thermal Green's functions can be expressed as an infinite sum of the corresponding vacuum Green's functions. For instance, for the anticommutator, we have

$$G^{(1)}_{\beta}(t,\mathbf{x};t',\mathbf{x}') = \sum_{j=-\infty}^{\infty} G^{(1)}(t+ij\beta,\mathbf{x};t',\mathbf{x}'), \tag{1.49}$$

where the vacuum Green's function is recovered for $j=0$.

As we will see later in this thesis, Green's functions are used in the determination of expectation values such as $\langle\hat{\Phi}^2\rangle$ and $\langle\hat{T}_{\mu\nu}\rangle$. However, as we will discuss in the next Section, formulating Green's functions in Euclidean space has proven to be a powerful technique for the calculation of expectation values and their subsequent numerical computations.

§ 1.4 Quantum field theory in Euclidean space

The Green's functions discussed in the previous section have integral representations. For example, in flat space-time the Feynman propagator can be expressed as [17]

$$iG_F(x,x') = \frac{1}{(2\pi)^n}\int \frac{e^{i\mathbf{k}.(\mathbf{x}-\mathbf{x}')}e^{-ik^0(t-t')}}{(k^0)^2-|\mathbf{k}|^2-m^2}\,d^n\mathbf{k}, \tag{1.50}$$

where $|\mathbf{k}|^2 = (k^1)^2+\cdots+(k^{n-1})^2$. The integral (1.50) can be evaluated as a contour with the k^0 integral having poles at $(k^0)^2 = |\mathbf{k}|^2+m^2$. The integral is therefore performed by deforming the contour integral around the poles, with the different Green's functions having different contour deformations. Figure 1.2 shows examples of integration contours for the Feynman propagator, the advanced and retarded Green's functions.

Alternatively, we can use an $i\epsilon$-prescription [17] and write the Feynman propagator in flat space-time as

$$iG_F = \lim_{\epsilon\to 0}\frac{1}{(2\pi)^n}\int \frac{e^{i\mathbf{k}.(\mathbf{x}-\mathbf{x}')}e^{-ik^0(t-t')}}{(k^0)^2-|\mathbf{k}|^2-m^2+i\epsilon}\,d^n\mathbf{k}, \tag{1.51}$$

where the $i\epsilon$ term shifts the poles of the integration away from the real line (Figure 1.2).

However, it can be seen that the relationship between the poles and the integration contour for the Feynman propagator is unchanged if the contour of integration is rotated in the complex plane by $\pi/2$, to lie on the imaginary k^0 axis (Figure 1.2). This is achieved by making the transformation

$$t = -i\tau, \tag{1.52}$$

and is called a Wick rotation, giving the Wick rotated metric a Euclidean signature $(+,+,+,+)$. The k_0 exponential term in (1.50) can now be expressed as $e^{-i\kappa(\tau-\tau')}$, where $\kappa = -ik_0$. The integration variable is now κ and the integration (1.51) can now be performed without going through the poles, allowing the Feynman propagator to be determined without the need for an $i\epsilon$ prescription.

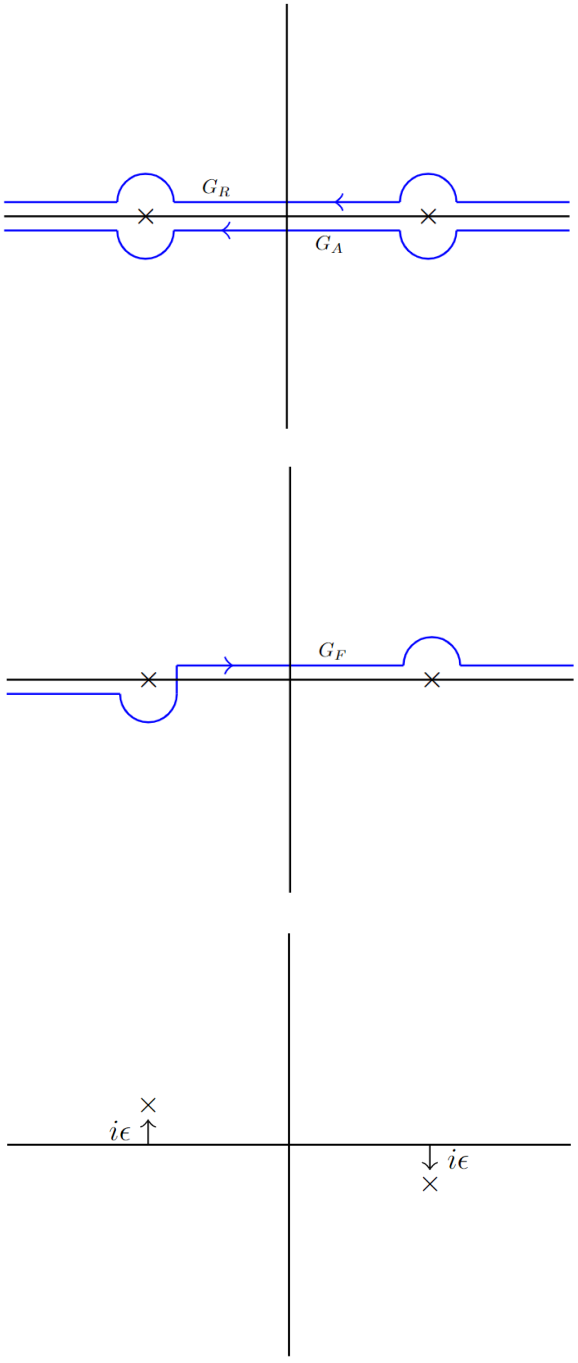

Figure 1.2: Example of contour integrals in the complex k^0 plane for the advanced G_A and retarded G_R Green's functions (top) and the Feynman propagator G_F (middle). The poles on the real axis, represented by $\times$, are at $k^0 = \pm\sqrt{|\mathbf{k}|^2 + m^2}$. Using the $i\epsilon$ prescription we can shift the poles away from the real axis (adapted from [17]).

Note that Wick rotation is not possible for the other Green's functions mentioned in Section 1.3 as rotation of the contour integrals will cross one of the poles (see Figure 1.2 (top) for the advanced and retarded Green's functions).

For the scalar field, the Feynman propagator with Lorentzian signature is related to the Euclidean Green's function G_E by [17]

$$iG_F(t,\mathbf{x};t'\mathbf{x}') = G_E(i\tau,\mathbf{x};i\tau',\mathbf{x}'). \tag{1.53}$$

In a curved space-time, the Euclidean Green's function satisfies

$$\Big[\Box_E - (m^2+\xi R)\Big]G_E(x,x') = -\frac{1}{\sqrt{g_E}}\delta^n(x-x'), \tag{1.54}$$

where g_E is the determinant of the Euclidean metric and the D'Alembertian in Euclidean space $\Box_E$ is an elliptical operator. The Euclidean Green's function obtained from (1.54), if one exists, is unique for a given state [17, 100] and thus it is often easier to work in Euclidean space (see Chapters 3, 5, 6) and then transform back to Lorentzian space afterwards. Indeed, it has been shown that in static space-times, the Euclidean Green's function obtained on a Riemannian manifold, by a Wick rotation, agrees with the Feynman propagator on Lorentzian space-time [100]. Also it has been shown that the thermal Euclidean Green's function for a massless, conformally coupled scalar field on adS4 with Dirichlet and Neumann boundary conditions, is equivalent to the Green's function on a Lorentzian background [71].

Of the many Green's functions discussed in Section 1.3, the Feynman propagator is of particular significance as we will use this to derive expectation values of the quantum scalar field. However, in the coincidence limit where $x \to x'$, the Feynman Green's function is divergent and we therefore need to find a way of extracting a meaningful quantity from it in order to compute expectation values. To this end we employ a renormalisation procedure and this is the subject of the next section.

§ 1.5 Hadamard renormalisation

In Minkowski space-time, the global vacuum state $|0\rangle$ achieves special significance. It is the state with lowest energy and the absence of particles (for an inertial observer). In classical field theory the vacuum state corresponds to the absence of the field i.e. $\Phi(t,\mathbf{x}) = 0$, which solves the classical Klein-Gordon equation (1.7). However for the quantum vacuum state, in order to satisfy the commutation relations (1.15), the field maintains a nonzero value even in a state with the lowest possible energy. Heuristically, this can be considered as the field fluctuating [72].

Considering the quantum field as a set of harmonic oscillators, a simple calculation of the vacuum energy for a non-interacting quantum scalar field, E_0 gives [17]

$$E_0 = \langle 0|H|0\rangle = \sum_{\mathbf{p}} \frac{1}{2}\omega, \tag{1.55}$$

where $\mathbf{p}$ refers to the momenta, ω the frequency of the modes (1.8) and H is the Hamiltonian given by

$$H = \frac{1}{2}\sum_{\mathbf{p}} (\hat{a}^\dagger_{\mathbf{p}}\hat{a}_{\mathbf{p}} + \hat{a}_{\mathbf{p}}\hat{a}^\dagger_{\mathbf{p}})\,\omega. \tag{1.56}$$

It can be seen from (1.55) that the vacuum energy is not only nonzero, it is also divergent for large $\mathbf{p}$. The problem of an infinite vacuum energy density in QFT is circumvented in flat space-time by a process called *normal ordering*, denoted by ::. This entails that whenever we have a product of creation and annihilation operators, the annihilation operator is situated to the right of the creation operator giving $: \hat{a}_{\mathbf{p}}\hat{a}^{\dagger}_{\mathbf{p}} :\rightarrow \hat{a}^{\dagger}_{\mathbf{p}}\hat{a}_{\mathbf{p}}$. Thus the Hamiltonian (1.56) becomes $: H := \sum_{\mathbf{p}} \hat{a}^{\dagger}_{\mathbf{p}}\hat{a}_{\mathbf{p}}\,\omega$ and the problematic $\frac{1}{2}\,\omega$ term in (1.55) vanishes.

The process of renormalisation in curved space-time is more complex. Energy in the form of the stress energy tensor $\langle\hat{T}_{\mu\nu}\rangle$ is a source of gravity and influences the space-time curvature that we are studying. Therefore, we cannot simply discard it by re-scaling the zero point energy, and consider energy differences, as in flat space-time. Instead, a different approach is required for curved space-times. A number of renormalisation schemes are described in the literature. These include the adiabatic approach [77], the deWitt-Schwinger method [37, 38, 86], zeta-function regularisation [42, 54], dimensional renormalisation [18, 92] and the Pauli-Villars approach [79]. In this thesis we use a technique called Hadamard renormalisation [35], named after Jacques Hadamard [51] who worked on the singularity structure of second order elliptic and hyperbolic equations. Hadamard renormalisation depends on the representation of the Feynman propagator in Hadamard form as a Hadamard parametrix $G_S(x,x')$ for points x, x' that are in a normal neighbourhood. This means that the points x and x' are connected by a unique geodesic. It has been shown [49] that if the Feynman propagator has a Hadamard structure in an open neighbourhood of a Cauchy surface on a C^{∞} globally hyperbolic manifold, then it has this form everywhere.

Before giving formal expressions for the Hadamard parametrix, we introduce two important quantities, Synge's world function $\sigma(x,x')$ and the van Vleck-Morette determinant $\Delta(x,x')$ [96]. Synge's world function $\sigma(x,x')$ is defined as [91]

$$\sigma(x,x') = \frac{1}{2}[s(x,x')]^2, \tag{1.57}$$

where $s(x,x')$ is the geodesic interval separating two space-time points x and x'.

Assuming x and x' are in a normal neighbourhood, we can also write the world function as [84]

$$\sigma(x,x') = \frac{1}{2}(\lambda_1 - \lambda_0)\int_z g_{\mu\nu}t^{\mu}t^{\nu}d\lambda, \tag{1.58}$$

where $t^{\mu} = \frac{dz}{d\lambda}$ is the tangent vector to the unique geodesic $z(\lambda)$ connecting x and x' and λ is an affine parameter. In (1.58), we suppose $x = z(\lambda_0)$ and $x' = z(\lambda_1)$. The world function satisfies [35]

$$2\sigma = \sigma^{;\mu}\sigma_{;\mu}, \tag{1.59}$$

and in addition we note that

$$\begin{aligned}
&\sigma(x,x') < 0 \qquad (x,x') \quad \text{time-like separated,}\\
&\sigma(x,x') = 0 \qquad (x,x') \quad \text{null separated,}\\
&\sigma(x,x') > 0 \qquad (x,x') \quad \text{space-like separated.}
\end{aligned} \tag{1.60}$$

It can be seen from (1.57) and (1.60) that the geodesic interval s is imaginary for time-like separated points.

The van Vleck-Morette determinant $\Delta(x,x')$ [96] provides information as to how geodesics that start at the point x converge or spread out at the point x'. It is defined as [35, 97]

$$\Delta(x,x') = [-g(x)]^{-\frac{1}{2}} \det\left\{\sigma_{;\mu\nu'}(x,x')\right\} \left[-g(x')\right]^{-\frac{1}{2}}, \tag{1.61}$$

where $g(x)$, $g(x')$ is the determinant of the metric at the space-time points x and x' respectively. In $n-$dimensions, $\Delta(x,x')$ satisfies the differential equation

$$\Box\sigma = n - 2\Delta^{-\frac{1}{2}}\Delta^{\frac{1}{2}}_{;\mu}\sigma^{;\mu}, \tag{1.62}$$

as well as the boundary condition

$$\lim_{x\to x'} \Delta(x,x') = 1. \tag{1.63}$$

The exact form of the Hadamard parametrix depends on the number of space-time dimensions. Décanini and Folacci [35] developed the Hadamard renormalisation of the stress energy tensor for a general space-time in $D \geq 2$ dimensions. In this thesis we are concerned with space-times in three and four dimensions. In four dimensions the Hadamard form of the Feynman propagator is given by

$$G^{(4)}_F(x,x') = \frac{i}{8\pi^2}\left(\frac{U^{(4)}(x,x')}{\Big[\sigma(x,x')+i\epsilon\Big]} + V(x,x')\,\ln\{\sigma(x,x')+i\epsilon\} + W^{(4)}(x,x')\right), \tag{1.64}$$

where the superscript (4) denotes we are in four dimensions (three-dimensional versions are given below) and $U^{(4)}(x,x')$, $V(x,x')$ and $W^{(4)}(x,x')$ are biscalars regular in the coincidence limit ($x \to x'$). For time-like and space-like separated points, these are given by

$$\begin{aligned} U^{(4)}(x,x') &= \Delta^{\frac{1}{2}}(x,x'), \\ V(x,x') &= \sum_{n=0}^{\infty} V_n(x,x')\sigma^n(x,x'), \\ W^{(4)}(x,x') &= \sum_{n=0}^{\infty} W_n(x,x')\sigma^n(x,x'), \end{aligned} \tag{1.65}$$

where $n \in \mathbb{N}$. The $i\epsilon$ term in (1.64) is introduced to give impart a singularity structure to $G^{(4)}_F(x,x')$ consistent with the notion of it being a time-ordered product (Section 1.4). The coefficients $V_n(x,x')$ satisfy the recursion relations [35]

$$\begin{aligned} &2(n+1)(n+2)V_{(n+1)} + 2(n+1)V_{(n+1);\mu}\,\sigma^{;\mu} \\ &\quad - 2(n+1)V_{(n+1)}\Delta^{-1/2}\Delta^{1/2}_{;\mu}\,\sigma^{;\mu} + \Big[\Box - (m^2+\xi R)\Big]V_n = 0, \qquad \text{for} \qquad n \in \mathbb{N}, \end{aligned} \tag{1.66}$$

with V_0 given by

$$2V_0 + 2V_{0;\mu}\sigma^{;\mu} - 2V_0\Delta^{-1/2}\Delta^{1/2}_{;\mu}\sigma^{;\mu} + \Big[\Box - (m^2+\xi R)\Big]\Delta^{1/2} = 0. \tag{1.67}$$

The coefficients $W_n^{(4)}(x,x')$ have the recursion relations [35]

$$\begin{aligned}
&2(n+1)(n+2)W^{(4)}_{(n+1)} + 2(n+1)W^{(4)}_{(n+1);\mu}\,\sigma^{;\mu} \\
&\qquad - 2(n+1)W^{(4)}_{(n+1)}\Delta^{-1/2}\Delta^{1/2}_{\;;\mu}\,\sigma^{;\mu} + 2(2n+3)V_{(n+1)} + 2V_{(n+1)\,;\mu}\sigma^{;\mu} \\
&\qquad\qquad - 2V_{(n+1)}\Delta^{-1/2}\Delta^{1/2}_{\;;\mu}\sigma^{;\mu} + \Big[\Box - (m^2+\xi R)\Big]W_n^{(4)} = 0 \qquad \text{for} \qquad n\in\mathbb{N}, \quad (1.68)
\end{aligned}$$

with $W_0^{(4)}$ unconstrained.

In three space-time dimensions the Hadamard parametrix has a simpler form as there is no coefficient $V_n(x,x')$ and no logarithmic term. The Hadamard expansion of the Feynman propagator, in three dimensions, thus becomes

$$G_F^{(3)}(x,x') = \frac{i}{4\sqrt{2}\pi}\left(\frac{U^{(3)}(x,x')}{\Big[\sigma(x,x')+i\epsilon\Big]} + W^{(3)}(x,x')\right), \tag{1.69}$$

where the superscript (3) signifies that we are in three dimensions. The coefficient $W^{(3)}(x,x')$ has an expansion analogous to (1.65) with recursion relations

$$\begin{aligned}
&(n+1)(2n+3)W^{(3)}_{(n+1)} + 2(n+1)W^{(3)}_{(n+1)\,;\mu}\sigma^{;\mu} \\
&\quad - 2(n+1)W^{(3)}_{(n+1)}\Delta^{-1/2}\Delta^{1/2}_{\;;\mu}\sigma^{;\mu} + \Big[\Box - (m^2+\xi R)\Big]W_n^{(3)} = 0 \qquad \text{for} \qquad n\in\mathbb{N}, \quad (1.70)
\end{aligned}$$

where again the $W_0^{(3)}$ term is unconstrained (see below). The coefficient $U^{(3)}(x,x')$ has an expansion of the form

$$U^{(3)}(x,x') = \sum_{n=0}^{\infty} U_n^{(3)}(x,x')\sigma^n(x,x'), \tag{1.71}$$

with $U_n^{(3)}(x,x')$ satisfying the recursion relations

$$\begin{aligned}
&(n+1)(2n+1)U^{(3)}_{(n+1)} + (2n+1)U^{(3)}_{(n+1)\,;\mu}\sigma^{;\mu} \\
&\quad - (2n+1)U^{(3)}_{(n+1)}\Delta^{-1/2}\Delta^{1/2}_{\;;\mu}\,\sigma^{;\mu} + \Big[\Box - (m^2+\xi R)\Big]U_n^{(3)} = 0 \qquad \text{for} \qquad n\in\mathbb{N}, \quad (1.72)
\end{aligned}$$

with $U_0^{(3)}$ given by

$$U_0^{(3)}(x,x') = \Delta^{\frac{1}{2}}. \tag{1.73}$$

The Hadamard coefficients $U_n(x,x')$ and $V_n(x,x')$ can be determined by integrating the recursion relations (1.66, 1.72) along the unique geodesic connecting the two space-time points x and x' and, from [35], are unique, purely geometric objects. In contrast, the coefficients $W_n(x,x')$ in both three and four dimensions are unconstrained by the recursion relations (1.68, 1.70) and are not purely geometric objects as we have freedom to choose the W_0 term. Once chosen, however, the subsequent terms in the recurrence relations (1.68, 1.70) with $n \geq 1$, are uniquely determined. We thus decompose the Hadamard parametrix into a purely geometric, state-independent part that

diverges in the coincidence limit and a regular state-dependent part. In four dimensions the singular part of the Hadamard parametrix is given by

$$G^{(4)}_{F,\,\mathrm{sing}}(x,x') = \frac{i}{8\pi^2}\left(\frac{U^{(4)}(x,x')}{\Big[\sigma(x,x')+i\epsilon\Big]} + V(x,x')\,\ln\{\sigma(x,x')+i\epsilon\}\right), \tag{1.74}$$

whilst in three dimensions it is

$$G^{(3)}_{F,\,\mathrm{sing}}(x,x') = \frac{i}{4\sqrt{2}\pi}\left(\frac{U^{(3)}(x,x')}{\Big[\sigma(x,x')+i\epsilon\Big]}\right). \tag{1.75}$$

The divergent part of the Hadamard parametrix contains all the singularities of the Green's function in the coincidence limit. Likewise the regular state-dependent part of the Hadamard function is given by

$$G^{(4)}_{F,\,\mathrm{reg}}(x,x') = \frac{i}{8\pi^2}W^{(4)}(x,x'), \tag{1.76}$$

in four dimensions and

$$G^{(3)}_{F,\,\mathrm{reg}}(x,x') = \frac{i}{4\sqrt{2}\pi}W^{(3)}(x,x'), \tag{1.77}$$

in three dimensions.

Renormalised expectation values of the product of field operators such as $\langle\hat{\Phi}^2\rangle$ and $\langle\hat{T}_{\mu\nu}\rangle$ are obtained by subtracting the singular part of the Hadamard parametrix (1.74, 1.75) from the Feynman Green's function before taking the coincidence limit [17]. For example the vacuum polarisation is derived from

$$\langle\hat{\Phi}^2\rangle_{\mathrm{ren}} = \lim_{x'\to x}[-iG_F(x,x') - (-iG_{F,\,\mathrm{sing}}(x,x'))]. \tag{1.78}$$

Determination of the renormalised expectation value of the stress energy tensor is more elaborate and this is the subject of the next Section.

§ 1.6 Stress-energy tensor

Determination of the expectation value of the renormalised stress energy tensor $\langle\hat{T}_{\mu\nu}\rangle$ is a fundamental aspect of QFTCS as it acts as the source term in Einstein's field equations (1.2). We can obtain an expression for the classical stress energy tensor by varying the action $\mathcal{S}$ (1.20) with respect to the metric tensor $g_{\mu\nu}$ to give

$$T_{\mu\nu} = \frac{2}{\sqrt{-g}}\frac{\delta\mathcal{S}[\Phi,g_{\mu\nu}]}{\delta g^{\mu\nu}}. \tag{1.79}$$

It can be shown that in the classical case [35], $T_{\mu\nu}$ is given by

$$\begin{aligned} T_{\mu\nu} = (1-2\xi)\nabla_\mu\Phi\nabla_\nu\Phi + \left(2\xi-\frac{1}{2}\right)g_{\mu\nu}g^{\rho\sigma}\nabla_\rho\Phi\nabla_\sigma\Phi - \frac{1}{2}g_{\mu\nu}m^2\Phi^2 \\ - 2\xi\Phi\nabla_\mu\nabla_\nu\Phi + 2\xi g_{\mu\nu}\Phi\Box\Phi + \xi\left(R_{\mu\nu}-\frac{1}{2}g_{\mu\nu}R\right)\Phi^2, \end{aligned} \tag{1.80}$$

and satisfies the conservation equation

$$\nabla_\nu T^{\mu\nu} = 0. \tag{1.81}$$

For the massless, conformally coupled scalar field, with $m = 0$ and $\xi = \xi_c$ (1.21), the stress energy tensor is traceless in the classical scenerio

$$T^\mu_\mu = 0. \tag{1.82}$$

If we were to model the classical scalar field as a perfect fluid, that is a fluid consisting of non-interacting particles distributed isotropically, we can write the stress energy tensor $T_{\mu\nu}$ in tensorial form as

$$T^{\mu\nu} = (\rho + P)\, U^\mu U^\nu + P g^{\mu\nu}, \tag{1.83}$$

where ρ is the energy density of the fluid, P is its pressure and U^σ is the four-velocity of the fluid.

We now consider the case of a quantum scalar field and the discussion in the remainder of this section is based largely on [35] except where otherwise referenced. The expectation value of the stress energy tensor in a quantum state $|\psi\rangle$ given by

$$\langle\psi|T_{\mu\nu}(x)|\psi\rangle = \lim_{x'\to x} \left\{ \mathcal{T}_{\mu\nu}(x,x')[-iG_F(x,x')] \right\}. \tag{1.84}$$

The second order differential operator, $\mathcal{T}_{\mu\nu}(x,x')$ is given by

$$\begin{aligned}\mathcal{T}_{\mu\nu}(x,x') = (1-2\xi) g_\nu^{\ \nu'} \nabla_\mu \nabla_{\nu'} + \left(2\xi - \frac{1}{2}\right) g_{\mu\nu} g^{\rho\sigma'} \nabla_\rho \nabla_{\sigma'} - 2\xi g_\mu^{\ \mu'} g_\nu^{\ \nu'} \nabla_{\mu'} \nabla_{\nu'} \\ + 2\xi g_{\mu\nu} \nabla_\rho \nabla^\rho + \xi \Big(R_{\mu\nu} - \frac{1}{2} g_{\mu\nu} R \Big) - \frac{1}{2} g_{\mu\nu}\, m^2,\end{aligned} \tag{1.85}$$

where $g_{\mu\nu'}$ denotes the bivector (not a tensor) of parallel transport between the points x and x' and which satisfies [37]

$$g_{\mu\nu'}{}_{;\rho}\, \sigma^{;\rho} = 0, \tag{1.86}$$

with

$$\lim_{x'\to x} g_{\mu\nu'} = g_{\mu\nu}. \tag{1.87}$$

However, as the Feynman propagator is divergent in the coincidence limit, the term in the right hand side of (1.84) is essentially meaningless. This problem can be fixed [98] by removing from the right hand side of (1.84) the purely geometric, state-independent part of the Hadamard form of the Feynman propagator given in (1.74, 1.75), whilst keeping the regular state dependent part $W(x,x')$. Putting this together, the renormalised expectation value of the stress energy tensor (RSET) can be expressed as

$$\begin{aligned}\langle\psi|\hat{T}_{\mu\nu}(x)|\psi\rangle = \frac{1}{8\pi^2}\Bigg[- w_{\mu\nu} + \frac{1}{2}(1-2\xi) w_{;\mu\nu} - \frac{1}{2}\left(2\xi - \frac{1}{2}\right) g_{\mu\nu} \Box w \\ + \xi R_{\mu\nu}\, w - g_{\mu\nu} v_1 \Bigg] + \Theta_{\mu\nu},\end{aligned} \tag{1.88}$$

where

$$w(x) = \lim_{x'\to x} W(x,x'), \qquad w_{\mu\nu}(x) = \lim_{x'\to x} W_{;\mu\nu}(x,x'), \tag{1.89}$$

and $\Theta_{\mu\nu}$ is a state-independent geometric tensor depending on the mass and coupling constant of the field and satisfies

$$\Theta^{\mu\nu}_{\ ;\nu} = 0. \tag{1.90}$$

The $g_{\mu\nu}v_1$ term in (1.88) is a biscalar which is state-independent and regular in the coincidence limit and ensures that the RSET is conserved, with v_1 given by

$$v_1 = \lim_{x\to x'} V_1(x,x'). \tag{1.91}$$

$V_1(x,x')$ is determined by using the recurrence relations (1.66, 1.67). In three dimensions $v_1 = 0$, whereas in four dimensions v_1 is explicitly given by

$$v_1 = \frac{1}{8}m^4 + \frac{1}{4}\left(\xi - \frac{1}{6}\right)m^2 R - \frac{1}{24}\left(\xi - \frac{1}{5}\right)\Box R + \frac{1}{8}\left(\xi - \frac{1}{6}\right)^2 R^2 \\ - \frac{1}{720}R_{\mu\nu}R^{\mu\nu} + \frac{1}{720}R_{\mu\nu\rho\sigma}R^{\mu\nu\rho\sigma}. \tag{1.92}$$

There are two sources of ambiguity in the geometric tensor $\Theta_{\mu\nu}$. The first $\Theta^{\mathcal{M}^2}_{\mu\nu}$ is related to the renormalised mass scale $\mathcal{M}$ introduced into (1.64) to make the argument of the logarithmic term dimensionless. The second comes from the ability to add any conserved geometric tensor $\widetilde{\Theta}_{\mu\nu}$ to the RSET. Thus we can write

$$\Theta_{\mu\nu} = \Theta^{\mathcal{M}^2}_{\mu\nu} + \widetilde{\Theta}_{\mu\nu}. \tag{1.93}$$

The ambiguity in $\Theta^{\mathcal{M}^2}_{\mu\nu}$ only exists in even space-time dimensions and is therefore not present when we consider the RSET in adS3 in Chapter 6. We can express $\Theta^{\mathcal{M}^2}_{\mu\nu}$ in terms of the mass scale $\mathcal{M}$ in four dimensions as

$$\Theta^{\mathcal{M}^2}_{\mu\nu} = -\frac{1}{8\pi^2}\lim_{x\to x'}\mathcal{T}(x,x')V(x,x')\ln\mathcal{M}^2. \tag{1.94}$$

Explicitly the conserved geometric tensor in three dimensions $\widetilde{\Theta}^{(3)}_{\mu\nu}$ is given by

$$\widetilde{\Theta}^{(3)}_{\mu\nu} = A\,m^3\,g_{\mu\nu} + B\,m^2\left[R_{\mu\nu} - \frac{1}{2}R\,g_{\mu\nu}\right], \tag{1.95}$$

where A and B are dimensionless constants. It can be seen that $\widetilde{\Theta}^{(3)}_{\mu\nu} = 0$ in the massless case. The conserved geometric tensor in four dimensions $\widetilde{\Theta}^{(4)}_{\mu\nu}$ is given by

$$\widetilde{\Theta}^{(4)}_{\mu\nu} = A\,m^4\,g_{\mu\nu} + B\,m^2\left[R_{\mu\nu} - \frac{1}{2}R\,g_{\mu\nu}\right] + C_1\,\mathcal{H}^{(1)}_{\mu\nu} + C_2\,\mathcal{H}^{(2)}_{\mu\nu} + C_3\,\mathcal{H}^{(3)}_{\mu\nu}, \tag{1.96}$$

where C_1, C_2 and C_3 are dimensionless constants and the conserved, rank two tensors $\mathcal{H}^{(i)}_{\mu\nu}$ are given

by

$$\mathcal{H}^{(1)}_{\mu\nu} = 2R_{;\mu\nu} - 2RR_{\mu\nu} + g_{\mu\nu}\left[-2\Box R + \frac{1}{2}R^2\right],$$

$$\mathcal{H}^{(2)}_{\mu\nu} = R_{;\mu\nu} - \Box R_{\mu\nu} - 2R^{pq}R_{p\mu q\nu} + g_{\mu\nu}\left[-\frac{1}{2}\Box R + \frac{1}{2}R_{pq}R^{pq}\right],$$

$$\mathcal{H}^{(3)}_{\mu\nu} = 2R_{;\mu\nu} - 4\Box R_{\mu\nu} + 4R^{p}{}_{\mu}R_{p\nu} - 4R^{pq}R_{p\mu q\nu} - 2R^{pqr}{}_{\mu}R_{pqr\nu} + g_{\mu\nu}\left[\frac{1}{2}R_{pqrs}R^{pqrs}\right]. \tag{1.97}$$

The tensors $\mathcal{H}^{(i)}_{\mu\nu}$ are related to each other by

$$\mathcal{H}^{(1)}_{\mu\nu} - 4\mathcal{H}^{(2)}_{\mu\nu} + \mathcal{H}^{(3)}_{\mu\nu} = 0. \tag{1.98}$$

Thus, we can eliminate one of the three conserved rank two tensors in (1.96) by setting, without loss of generality, $C_1 = 0$ or $C_2 = 0$ or $C_3 = 0$.

The geometric tensor $\Theta^{\mathcal{M}^2}_{\mu\nu}$ is related to the trace of the RSET which, for the massless, conformally coupled scalar field on adS4, can be expressed as

$$\langle\psi|\hat{T}^{\mu}_{\mu}|\psi\rangle = \frac{v_1}{4\pi^2} + g^{\mu\nu}\Theta^{\mathcal{M}^2}_{\mu\nu}. \tag{1.99}$$

However, for the massless, conformally coupled field $g^{\mu\nu}\Theta^{\mathcal{M}^2}_{\mu\nu} = 0$ and hence the trace of the RSET in four dimensions reduces to

$$\langle\psi|\hat{T}^{\mu}_{\mu}|\psi\rangle = \frac{v_1}{4\pi^2}. \tag{1.100}$$

Thus, after renormalisation the RSET has a nonzero trace, unlike its classical counterpart (1.82). This nonzero trace is often referred to as the 'trace anomaly' [17, 48, 102]. As $\Theta^{\mathcal{M}^2}_{\mu\nu}$ and the term v_1 in (1.99) are zero in odd dimensions, the trace anomaly does not exist in adS3 in the massless, conformally coupled case (see Chapter 6).

§ 1.7 Wald's axioms for the stress energy tensor

In order to achieve a degree of consistency and validity for the many renormalisation schemes used to find a finite, physically reasonable RSET, Wald [98, 99] set out a number of axioms which any RSET should satisfy. These are summarised as follows

(i) **Conservation:** The expectation values of the RSET are conserved, i.e. $\nabla_\nu\langle\hat{T}^{\mu\nu}\rangle_{\rm ren} = 0$

(ii) **Causality:** For a state in the asymptotic past at a point q ("in" state), we must have that $\langle\hat{T}^{\mu\nu}\rangle_{\rm ren}$ depends only on events in the causal past of q and that for states in the asymptotic future of q ("out" states), $\langle\hat{T}^{\mu\nu}\rangle_{\rm ren}$ depends only on the causal future of q.

(iii) **Consistency:** For a pair of orthogonal states such that $\langle\Phi|\Psi\rangle = 0$, the matrix element of $\langle\Phi|\hat{T}_{\mu\nu}|\Psi\rangle$ should agree with the formal expression which produces finite results.

(iv) **Normal ordering:** This requires that the RSET reduces to the normal ordered expectation value in Minkowski space-time, i.e. that $\langle \hat{T}^{\mu\nu} \rangle_{\text{ren}} = \langle : \hat{T}^{\mu\nu} : \rangle$.

As a consequence of the above axioms, Wald proved a uniqueness theorem [98] which states that any RSET that satisfies the above axioms will be unique up to the addition of a locally conserved purely geometric tensor $\Theta_{\mu\nu}$ (see Section 1.6). Thus if we have two RSETs, $\langle \hat{T}_{\mu\nu} \rangle^A$ and $\langle \hat{T}_{\mu\nu} \rangle^B$ that satisfy Wald's axioms we have

$$\langle \hat{T}_{\mu\nu} \rangle^A - \langle \hat{T}_{\mu\nu} \rangle^B = \Theta_{\mu\nu}. \tag{1.101}$$

Wald also showed that $\Theta_{\mu\nu}$ is a multiple of the identity operator and depends only of the space-time geometry. The uniqueness theorem acts as a criterion to establish the validity of a RSET obtained from a renormalisation method. Indeed, it was shown in [98, 99] that Hadamard renormalisation does satisfy Wald's axioms.

§ 1.8 Classical energy conditions

Einstein's field equations of GR (1.1) formulate a relationship between the metric tensor and the stress energy tensor without stipulating what physical form either should take. Thus it is possible to use an arbitrary metric in (1.1) and obtain a stress energy tensor that is conserved. However, it has long been known that this can lead to unphysical phenomena such as closed time-like loops, superluminal travel and wormholes [55, 62]. One strategy to overcome this problem is to require that physically reasonable matter fields obey certain energy conditions which limit the arbitrariness of the stress energy tensor. There are four commonly used energy conditions. Using the stress energy tensor of a perfect fluid (1.83) as an example, these are [28, 62]

(i) **Weak Energy Condition (WEC):** this stipulates that for any future-directed time-like vector V^μ, we have $T_{\mu\nu}V^\mu V^\nu \geq 0$, or equivalently that $\rho \geq 0$ and $\rho + P \geq 0$. Put simply this requires that for all observers, the energy density component of $T_{\mu\nu}$ is never negative.

(ii) **Null Energy Condition (NEC):** this stipulates that for a null vector K^μ, we have $T_{\mu\nu}K^\mu K^\nu \geq 0$, or that $\rho + P \geq 0$. This allows for negative energy density so long as it is compensated for by a positive pressure.

(iii) **Dominant Energy Condition (DEC):** This incorporates the WEC for time-like vectors ($T_{\mu\nu}V^\mu V^\nu \geq 0$), as well as requiring that $-T^\mu_\nu V^\nu$ is a future-directed causal vector field (nonspace-like). This requires that $\rho \geq |P|$ and is often interpreted as the requirement that the flux of energy is not superluminal.

(iv) **Strong Energy Condition (SEC):** This requires that

$$\left(T_{\mu\nu} - \frac{1}{(n-2)} T^\lambda_\lambda \, g_{\mu\nu} \right) V^\mu V^\nu \geq 0, \tag{1.102}$$

where n is the number of space-time dimensions. In other words we have $\rho + P \geq 0$ *and* $\rho + 3P \geq 0$. The SEC was used in the singularity theorems of Hawking [52] and Penrose [80] and implies the NEC rather than the WEC. Simply put, the SEC implies that gravity is attractive. The individual energy conditions imply the existence of another as shown in Figure 1.3.

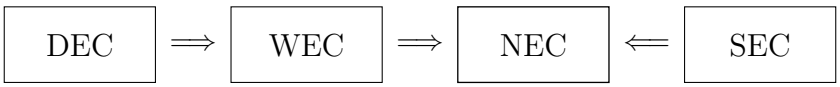

Figure 1.3: Interrelationships between the different energy conditions.

Whilst most classical forms of matter such as nonrelativistic ideal gases or pressureless dust obey the DEC, it was realised in the 1960s that quantum field theory implies that the energy density of quantum fields can be negative at least for a short time period [43]. It was shown in [47] that the existence of negative energy and, in particular, negative energy fluxes could lead to the violation of the second law of thermodynamics. This violation could be overcome if the magnitude and duration of the energy flux satisfied

$$|F| \lesssim \tau^{-2}, \tag{1.103}$$

where F is the flux and τ the duration that it lasts. This suggested that whilst it is possible for quantum fields to break the pointwise classical energy conditions, they could only do this for a short time. Indeed, (1.103) is the first example of what has become to be known as a quantum energy inequality (QEI). QEIs consider the average of the stress energy tensor over causal curves and place lower (nonzero) bounds on local averages of energy densities of quantum fields. QEIs can limit the ability of quantum fields to support exotic space-times such as wormholes [44, 45].

Whilst most classical, minimally coupled fields obey the classical energy conditions, this is not the case for nonminimally coupled ($\xi \neq 0$) scalar fields which can violate all the energy conditions [11, 62]. However, no complete formulation of a QEI for a non-minimally coupled scalar field has been provided to date [62] and in Minkowski space-time, non-minimally coupled fields can enjoy large negative energy densities for prolonged periods of time [44]. We will also see in Chapter 6 that non-minimally coupled fields in adS3 can have negative energy densities for most or all of the space-time.

§ 1.9 Overview of the thesis and motivation

In this thesis we study a real, free quantum scalar field propagating on a background anti-de Sitter space-time (adS). We numerically determine the vacuum (v.e.v.) and thermal (t.e.v.) expectation values of the square of the field $\langle\hat{\Phi}^2\rangle$ (vacuum polarisation) and the RSET $\langle\hat{T}_{\mu\nu}\rangle$. AdS is a maximally symmetric solution to Einstein's field equations (1.1), with a constant negative curvature. However, the possession of a time-like boundary at spatial infinity means that adS is not a globally hyperbolic space-time. This necessitates the use of boundary conditions at spatial infinity in order to have a well-posed quantum field theory [8, 58, 59]. In this thesis we apply Dirichlet, Neumann and Robin boundary boundary conditions to the scalar field at the space-time boundary. Robin boundary conditions may be considered as as a linear combination of Dirichlet and Neumann. The study of different boundary conditions is expected to result in a rich variety of expectation values.

The vacuum polarisation (VP) of a massless, conformally coupled scalar field on four-dimensional anti de-Sitter space-time (adS4) has previously been determined [71], subject to Dirichlet, Neumann and Robin boundary conditions. In [71], it was found that at the space-time boundary, both the v.e.v.s and t.e.v.s of the VP converged towards the Neumann result for all Robin boundary

conditions except Dirichlet, which had its own limit. In this thesis we study the VP for a scalar field with general mass and coupling on a three dimensional adS background (adS3). Our motivation is to determine whether the results in [71] are reproduced when we allow the mass and coupling constant of the field to vary.

In the computation of $\langle \hat{T}_{\mu\nu} \rangle$, we start with a massless, conformally coupled scalar field on adS4. We seek to determine whether the finding in [71] for the VP also applies to the v.e.v.s and t.e.v.s of the RSET. We analyse the behaviour of the RSET as it approaches the space-time boundary and thus provide some analytical evidence to support our numerical results. We then compute $\langle \hat{T}_{\mu\nu} \rangle$ for a scalar field with general mass and coupling on an adS3 background. Allowing the mass and coupling constant to vary results in a wide variety of $\langle \hat{T}_{\mu\nu} \rangle$, some of which have negative energy densities for a majority (or all) of space-time, thus violating the classical energy conditions (see Section 1.8).

Finally we use a selection of $\langle \hat{T}_{\mu\nu} \rangle$ as the source term in (1.2) to determine the backreaction or quantum corrections to the underlying adS3 metric. This is a fundamental aspect of QFTCS as it directly shows the interplay between quantum fields and the geometry of space-time.

This thesis is set out as follows.

- **Chapter 1:** Here we lay out some of the key concepts used in this thesis as well as the motivation for and brief outline of the research that follows.
- **Chapter 2:** We describe the geometry and other important features of adS space-time. We discuss the need for boundary conditions due to the non-global hyperbolicity of adS and demonstrate a mapping of adS to the globally hyperbolic Einstein Static Universe (ESU).
- **Chapter 3:** The v.e.v.s and t.e.v.s of the RSET for a massless, conformally coupled scalar field on adS4 are derived, using Dirichlet, Neumann and Robin boundary conditions. We study the behaviour of the RSET at the space-time boundary and give analytic support to the numerical results found. Much of the work in this chapter has appeared in a recent publication [70].
- **Chapter 4:** Here we lay out some of the background mathematical results for quantum scalar field theory on an adS3 background. We find mode solutions to the Klein-Gordon equation in terms of hypergeometric functions. We derive an upper limit to the parameter ζ used in the Robin boundary condition in order to obtain mode solutions that are classically stable.
- **Chapter 5:** We compute the renormalised VP for a scalar field with general mass and coupling on adS3. We determine the Green's function on an adS3 background and use Hadamard renormalisation to obtain the v.e.v.s and t.e.v.s of the VP subject to Dirichlet, Neumann and Robin boundary conditions. We also examine the behaviour of the VP at the space-time boundary. Much of the work in this chapter has also appeared in a recent publication [73].
- **Chapter 6:** We determine the v.e.v.s and t.e.v.s of the RSET for a quantum scalar field with general mass and coupling on adS3, subject to Dirichlet, Neumann and Robin boundary conditions. Varying the mass and coupling constant has resulted in a rich spectrum of RSETs, some with negative energy densities. It is anticipated that this will form the subject of a future publication [75].

- **Chapter 7:** We conclude our research by using a selection of the RSETs obtained in Chapter 6 as the source term in the semi-classical Einstein's equations (1.2) and compute the corrections to the underlying space-time metric. It is anticipated that this will also form the subject of a future publication [74].
- **Chapter 8:** We provide a summary of the research covered in this thesis as well as plans for future research.

Chapter 2

Anti-de Sitter space-time

Anti-de Sitter space-time (adS) is a maximally symmetric solution to Einstein's field equations (1.1) with a constant negative cosmological constant ($\Lambda < 0$). A negative cosmological constant implies that the expansion of the Universe should be decelerating, contrary to recent observations [81]. Nonetheless, adS has many rich properties, making it a very interesting space-time to explore. Undoubtedly one of the reasons why adS has been studied so extensively in recent years is its role in the adS/CFT (conformal field theory) correspondence first postulated by Maldecena in 1997 (see [1] for a review). In the adS/CFT correspondence it is proposed that a type IIB supersymmetric string theory in an $n-$dimensional adS bulk is dual to a QFT on its $(n-1)-$dimensional Minkowski boundary (Figure 2.1). The adS/CFT correspondence means we can formulate QFTs on a boundary that are dual to a higher dimensional, more complicated, theory of quantum gravity in the bulk.

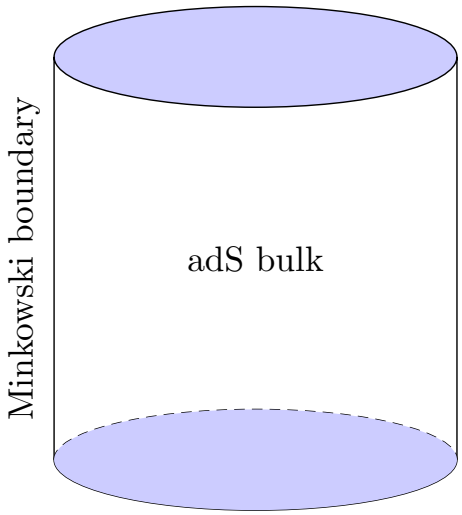

Figure 2.1: Schematic of the adS/CFT correspondence. Theories of quantum gravity in the 'bulk' are postulated to be dual to QFTs on a lower dimensional Minkowski boundary.

In this chapter we describe aspects of adS space-time. In Section 2.1 we discuss the key geometric features of adS and how it is conformal to the Einstein Static Universe (ESU). In Section 2.2 we describe the Poincaré patch which plays a key role in the ads/CFT correspondence. In Section 2.3, we discuss some of the properties associated with a maximally symmetric space-time. As adS is not

a globally hyperbolic space-time, we need to apply boundary conditions at the time-like boundary in order to have a meaningful QFT. This is discussed further in Section 2.4. Finally, in Section 2.5, we conclude this chapter with a summary of the key features of adS space-time.

§ 2.1 Geometry of anti de-Sitter space-time

We can consider $n-$dimensional anti-de Sitter space-time (adS_n) as an $n-$dimensional single-sheeted hyperboloid embedded in an $(n+1)-$ dimensional flat space, $\mathbb{R}^{(n-1,2)}$ [14, 55, 88], with metric $\eta_{\alpha\beta} = \mathrm{diag}(-1, 1, 1, \ldots, 1, -1)$. Using the coordinates, χ^α ($\alpha = 0, 1, 2, ...n$), the equation for the hyperboloid in the embedding space is,

$$-(\chi^0)^2 + (\chi^1)^2 + (\chi^2)^2 + ... + (\chi^{n-1})^2 - (\chi^n)^2 = -L^2, \tag{2.1}$$

where $L > 0$ is the radius of the waist of the hyperboloid, Figure 2.2 and is related to the cosmological constant by

$$\Lambda = -\frac{(n-2)(n-1)}{2L^2}. \tag{2.2}$$

For all the numerical calculations in the later chapters in this thesis, we set $L = 1$. This is a common technique used in this field of study and simply means that we rescale the units so that the curvature radius of adS is dimensionless and other quantities (such as the cosmological constant and Ricci scalar) are expressed in terms of units of L.

In (2.1), there are two time-like coordinates, χ^0, χ^n, whilst χ^i, $i = 1, ..., (n-1)$ are space-like. The metric on the embedding space is given by

$$ds^2 = -(d\chi^0)^2 + (d\chi^1)^2 + (d\chi^2)^2 + ... + (d\chi^{n-1})^2 - (d\chi^n)^2. \tag{2.3}$$

We now choose a suitable set of dimensionless coordinates for adS space-time [60]

$$\begin{aligned} &t, && -\pi \leq t \leq \pi, \\ &\rho, && 0 \leq \rho < \frac{\pi}{2}, \\ &\theta_j, && 0 \leq \theta_j \leq \pi, \quad j = 1, 2, ..., n-3, \\ &\phi, && 0 \leq \phi < 2\pi, \end{aligned} \tag{2.4}$$

where ρ is the radial coordinate, θ_j are polar coordinates and ϕ is the azimuthal coordinate. The time coordinate t is periodic with period 2π, meaning we have somewhat unphysical, closed time-like curves, see Figure 2.2. We can circumvent this by considering the covering space, CadS, where the time coordinate is 'unwrapped' to give $t \in (-\infty, \infty)$. We use the following coordinate

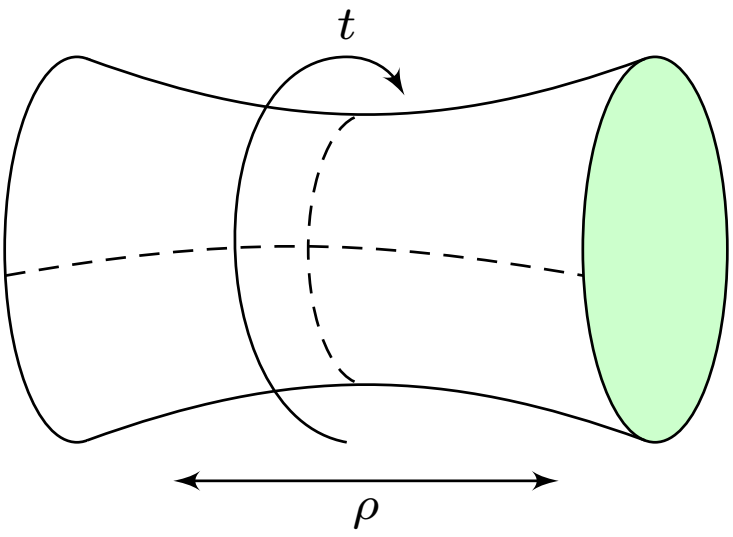

Figure 2.2: Schematic of adS space-time, with the $(n-2)$ angular coordinates omitted. Pure adS admits closed time-like curves (adapted from [4]).

transformations for the embedding space [4, 69]

$$\begin{aligned}
\chi^0 &= L\cos t\sec\rho,\\
\chi^1 &= L\tan\rho\cos\theta_1,\\
\chi^2 &= L\tan\rho\sin\theta_1\cos\theta_2,\\
&\vdots\\
\chi^{n-2} &= L\tan\rho\sin\theta_1\sin\theta_2\ldots\sin\theta_{n-3}\cos\phi,\\
\chi^{n-1} &= L\tan\rho\sin\theta_1\sin\theta_2\ldots\sin\theta_{n-3}\sin\phi,\\
\chi^n &= L\sin t\sec\rho.
\end{aligned} \tag{2.5}$$

Taking the derivatives in (2.5) we have

$$\begin{aligned}
d\chi^0 &= L(-\sin t\sec\rho\,dt+\cos t\sec\rho\tan\rho\,d\rho),\\
d\chi^1 &= L(\sec^2\rho\cos\theta_1\,d\rho-\tan\rho\sin\theta_1\,d\theta_1),\\
&\vdots\\
d\chi^n &= L(\cos t\sec\rho\,dt+\sin t\sec\rho\tan\rho\,d\rho).
\end{aligned} \tag{2.6}$$

Substituting the derivatives in (2.6) into the metric (2.3) gives the adS$_n$ metric

$$ds^2 = L^2\sec^2\rho\left(-dt^2+d\rho^2+\sin^2\rho\left[d\theta_1^2+\sum_{i=2}^{n-3}d\theta_i^2\prod_{j=1}^{i-1}\sin^2\theta_j+d\phi^2\prod_{j=1}^{n-3}\sin^2\theta_j\right]\right). \tag{2.7}$$

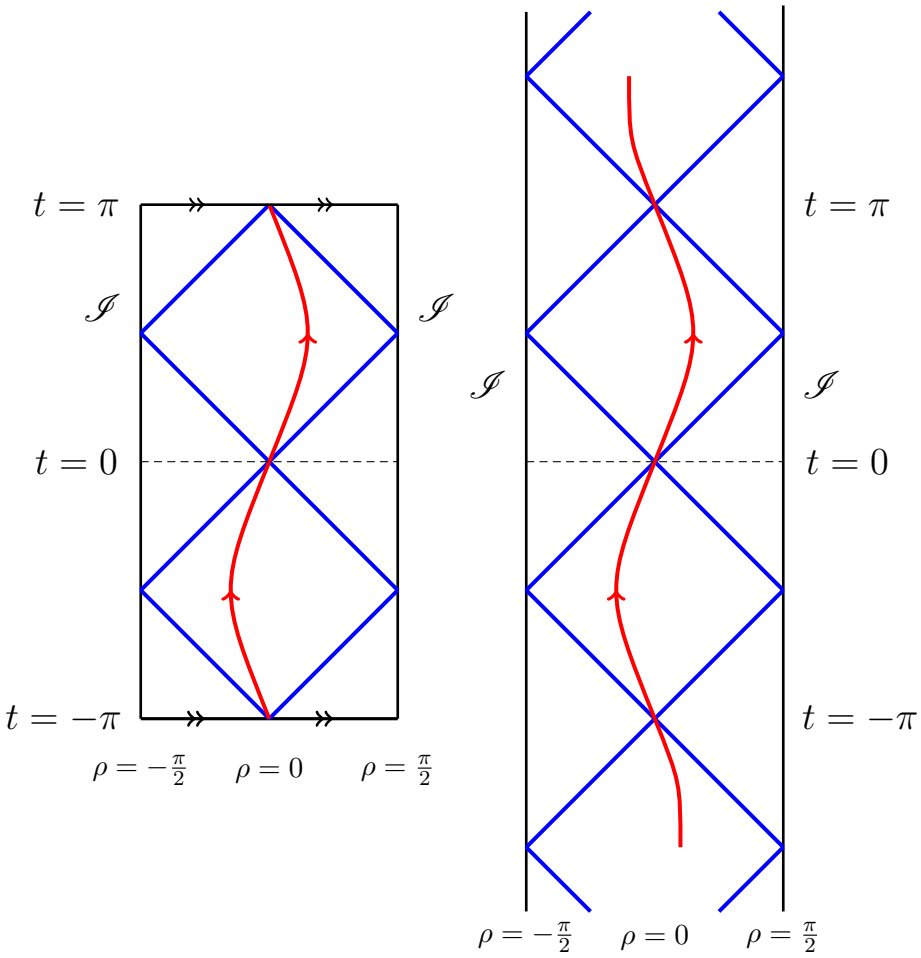

Figure 2.3: Penrose diagram of pure adS space-time (left) in two dimensions. The horizontal lines with arrows are identified, showing that in adS the time coordinate is periodic with period 2π. In the covering space CadS (right) $t \in (-\infty, \infty)$. The red curves show a possible time-like worldlines and the blue lines represent null rays (adapted from [8]).

In four dimensions, (2.7) becomes

$$ds^2 = L^2 \sec^2 \rho \left(-dt^2 + d\rho^2 + \sin^2 \rho \left[d\theta^2 + \sin^2 \theta \, d\phi^2\right]\right), \tag{2.8}$$

whilst the adS3 metric is

$$ds^2 = L^2 \sec^2 \rho \left(-dt^2 + d\rho^2 + \sin^2 \rho \, d\phi^2\right). \tag{2.9}$$

The Carter-Penrose diagrams for adS and CadS are shown in Figure 2.3 in two dimensions for clarity. The presence of a time-like boundary in both adS and CadS means that null rays can reach the space-time boundary in finite coordinate time. Therefore, neither adS nor CadS is a globally hyperbolic space-time, as a result of which we need to impose boundary conditions at the space-time boundary $\mathscr{I}$ in order to have a meaningful QFT [8, 12, 15, 29, 31, 32, 34, 50, 58, 59, 101]. More will be said about this later, in Section 2.4.

The boundary of adS (at $\rho = \pi/2$) is not part of the adS space-time which can hinder the imposition of boundary conditions at the space-time boundary [58, 59]. We can bypass this issue

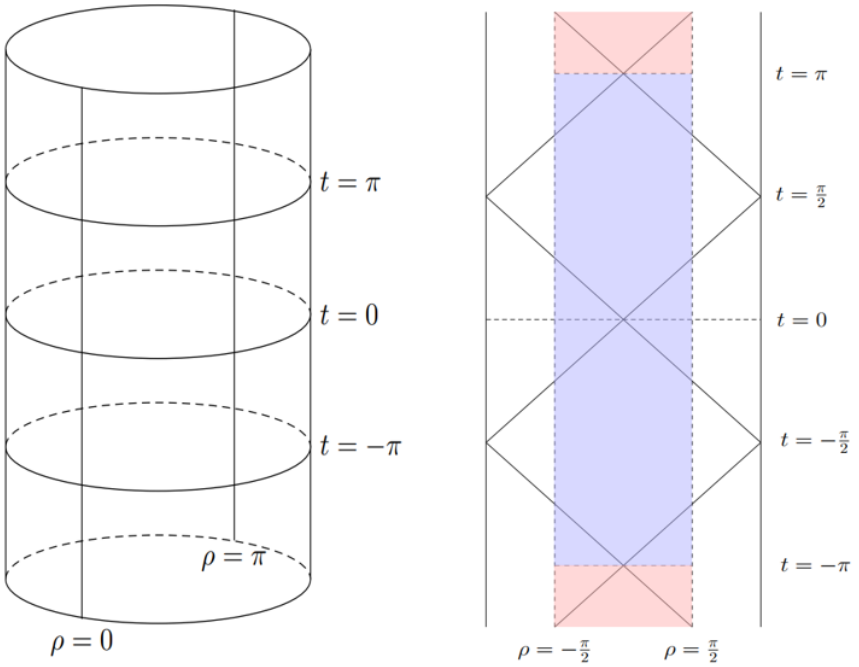

Figure 2.4: ESU cylinder in two dimensions (left). AdS space-time (right) is conformal to half of the ESU. Pure adS is shown in blue whilst the covering space is in red (adapted from [4]).

by mapping the adS space-time to the Einstein Static Universe (ESU) [8] (see Figure 2.4). In four dimensions, the ESU can be considered as a four-dimensional cylinder, with no boundary, embedded in a five-dimensional Minkowski space, giving the ESU metric as [55]

$$ds^2 = L^2 \left(-dt^2 + d\rho^2 + \sin^2\rho \left[d\theta^2 + \sin^2\theta \, d\phi^2\right]\right). \tag{2.10}$$

ESU is globally hyperbolic and its metric is conformal to that of the adS metric (2.8). We can make a conformal transformation of the adS metric to that of the ESU

$$g^{\text{adS}}_{\mu\lambda} = \Omega^2 \, g^{\text{ESU}}_{\mu\lambda}, \qquad \Omega = \sec\rho. \tag{2.11}$$

The resultant mapping of the adS space-time onto the ESU is shown in Figure 2.4. As we shall see in Chapters 3, 4 and 5 this facilitates the imposition of boundary conditions at the adS boundary which is now part of the space-time.

§ 2.2 The Poincaré patch

The Poincaré fundamental domain or Poincaré patch (PadS) represents half of the adS space-time and plays a fundamental role in the adS/CFT correspondence [1, 13]. Transformation to the

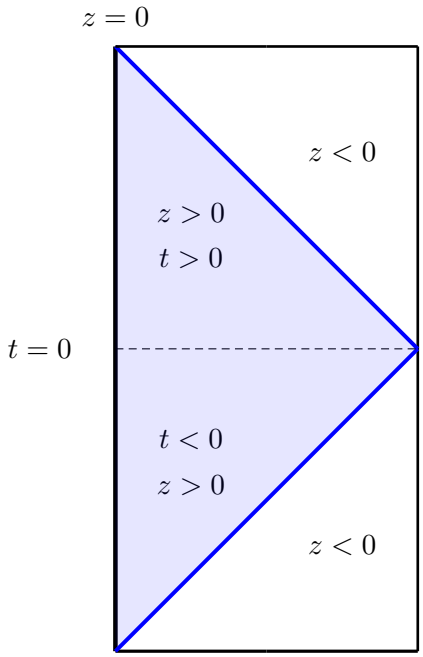

Figure 2.5: Penrose diagram for the Poincaré patch shown in blue.

Poincaré patch requires a change of the embedding space coordinates (2.5) to give [13]

$$\begin{aligned}
\chi^0 &= \frac{1}{2z}(z^2 + L^2 + \bar{x}^2 - t^2), \\
\chi^i &= \frac{Lx^i}{z}, \qquad i = 1, 2 \ldots (n-2), \\
\chi^{n-1} &= \frac{1}{2z}(z^2 - L^2 + \bar{x}^2 - t^2), \\
\chi^n &= \frac{Lt}{z},
\end{aligned} \tag{2.12}$$

where

$$\bar{x}^2 = \sum_{i=1}^{n-2} (x^i)^2, \tag{2.13}$$

and z acts as the radial coordinate, given by

$$\frac{1}{z} = \frac{\chi^0 - \chi^{n-1}}{L^2}. \tag{2.14}$$

The Poincaré patch metric now takes the form

$$ds^2 = \frac{L^2}{z^2}\left(-dt^2 + d\bar{x}^2 + dz^2\right). \tag{2.15}$$

The radial coordinate z effectively splits the adS space-time into two regions corresponding to $z > 0$ and $z < 0$ (Figure 2.5). Each of these regions represents half of the adS space-time, with the

Poincaré patch usually given by $z > 0$. The plane $z = 0$ is a time-like boundary which is not part of the PadS space-time as can be seen from (2.14).

Formulating a quantum field theory on PadS has some advantages. PadS is conformal to Minkowski space-time (see (2.15)) and its boundary is asymptotically flat. QFTs formulated on PadS [30, 83], still require that boundary conditions are stipulated at the time-like boundary $z = 0$. However, one disadvantage of working on PadS is the possible existence of bound states particularly for Robin boundary conditions [30]. In this thesis we work exclusively in global adS coordinates where we have the global adS vacuum state, which respects the underlying symmetries of the space-time, and apply boundary conditions at the time-like boundary at $\rho = \pi/2$.

§ 2.3 Properties of maximally symmetric space-times

If the metric of a space-time is unchanged in the direction of a given coordinate x^μ then the metric is said to possess a symmetry in the direction of x^μ. Consider for example four-dimensional Minkowski space-time with metric

$$ds^2 = \eta_{\mu\nu} dx^\mu dx^\nu = -dt^2 + dx^2 + dy^2 + dz^2. \tag{2.16}$$

This space-time has a total of ten isometries; these are the four translations, $x^\mu \to x^\mu + \alpha^\mu$, three boosts and three rotational isometries, $x^\mu \to \Lambda^\mu_\nu x^\nu$, where Λ^μ_ν is the rotation matrix. For a general metric $g_{\mu\nu}$ which is independent of the coordinate x^σ, the vector $K = \partial_\sigma$ is known as a Killing vector and is a generator of an isometry. This means that a test particle moving in the direction of K^μ experiences an invariant geometry. Killing vectors obey Killing's equation

$$\nabla_\mu K_\nu + \nabla_\nu K_\mu = 0, \tag{2.17}$$

where ∇_λ are covariant derivatives. It can be shown [90] that the maximum number of Killing vectors on an $n-$dimensional manifold is $\frac{1}{2}\, n(n+1)$ and a space-time possessing the maximum number of Killing vectors is said to be *maximally symmetric*. AdS4 has a total of ten isometries. These are four translations, in three spatial and one time direction, three rotations and three boosts. Ads3 has a total of six isometries. The isometries of adS can be understood as residing in the underlying embedding space (see Section 2.1).

An interesting property of the Riemann tensor, $R_{\lambda\sigma\mu\nu}$, is that in any maximally space-time it can be expressed as

$$R_{\lambda\sigma\mu\nu} = \frac{R}{n(n-1)} \left(g_{\lambda\mu} g_{\sigma\nu} - g_{\lambda\nu} g_{\sigma\mu} \right), \tag{2.18}$$

where R the Ricci scalar. The Ricci tensor $R_{\mu\nu}$ can be expressed in terms of the metric tensor as

$$R_{\mu\nu} = \frac{2\Lambda}{n-2} g_{\mu\nu}, \tag{2.19}$$

where Λ is the cosmological constant related to the Ricci scalar by

$$R = \frac{n\Lambda}{\frac{n}{2} - 1}. \tag{2.20}$$

The cosmological constant Λ may be negative, positive or zero, corresponding respectively to n-dimensional anti-de Sitter, de Sitter or Minkowski space-times.

There is another useful benefit of a space-time possessing maximum symmetry when it comes to the geodesic interval (Section 1.5). Consider a biscalar quantity $a(x, x')$ dependent on two space-time points (x, x') connected by a unique geodesic. If $a(x, x')$ respects the underlying maximal space-time symmetry, we can express this as

$$a(x, x') \to a(s), \tag{2.21}$$

where $s(x, x')$ is the geodesic interval separating the two space-time points (x, x'). In adS, the geodesic interval, for space-like separated points, is given by

$$s(x, x') = L \cos^{-1}\left(\frac{\cos\Delta t - \sin\rho \sin\rho' \cos\gamma}{\cos\rho\cos\rho'}\right), \tag{2.22}$$

where $\Delta t = t' - t$ and γ represents the angular separation of the space-time points given by

$$\cos\gamma_{\text{adS4}} = \cos\theta\cos\theta' + \sin\theta\sin\theta'\cos(\phi - \phi'), \tag{2.23}$$

in adS4 and

$$\cos\gamma_{\text{adS3}} = \cos(\phi - \phi'), \tag{2.24}$$

in adS3. For time-like separated points, where $s(x, x')$ is purely imaginary (see Section 1.5), we change the cos term in (2.22) to cosh.

We can also give explicit expressions for Synge's world function. In adS4 it is given by [2]

$$\sigma(x, x') = \frac{L^2}{2}\left[\cos^{-1}\left(\frac{\cos\Delta t - \sin\rho\sin\rho'\cos\gamma}{\cos\rho\cos\rho'}\right)\right]^2, \tag{2.25}$$

whilst in adS3, the world function becomes

$$\sigma(x, x') = \frac{L^2}{2}\left[\cos^{-1}\left(\frac{\cos\Delta t - \sin\rho\sin\rho'\cos\gamma}{\cos\rho\cos\rho'}\right)\right]^2. \tag{2.26}$$

In adS$_n$ the van Vleck-Morette determinant is given by [60]

$$\Delta(x, x') = \left[\frac{\sqrt{2\sigma}}{L}\csc\left(\frac{\sqrt{2\sigma}}{L}\right)\right]^{n-1}, \tag{2.27}$$

which corresponds to the result in [2] for $n = 4$.

As we will see in Chapter 5, the expression (2.21) will prove useful when calculating expectation values such as the vacuum polarisation in states which respect the underlying symmetry of adS space-time. This includes the vacuum state when Dirichlet or Neumann boundary conditions are applied.

§ 2.4 Boundary conditions

The lack of global hyperbolicity of adS space-time necessitates the imposition of boundary conditions at the space-time boundary in order to have a well-posed quantum field theory [8, 58, 59]. Quantisation on adS space-times was first initiated in [8], where the authors discussed transparent and reflective boundary conditions applied to a massless scalar field conformally coupled to the ESU (see Figure 2.6). Boundary conditions are applied to the conformal field at the adS space-time boundary which is now part of the ESU (see Section 2.1). Following this, the conformal field is mapped back onto adS.

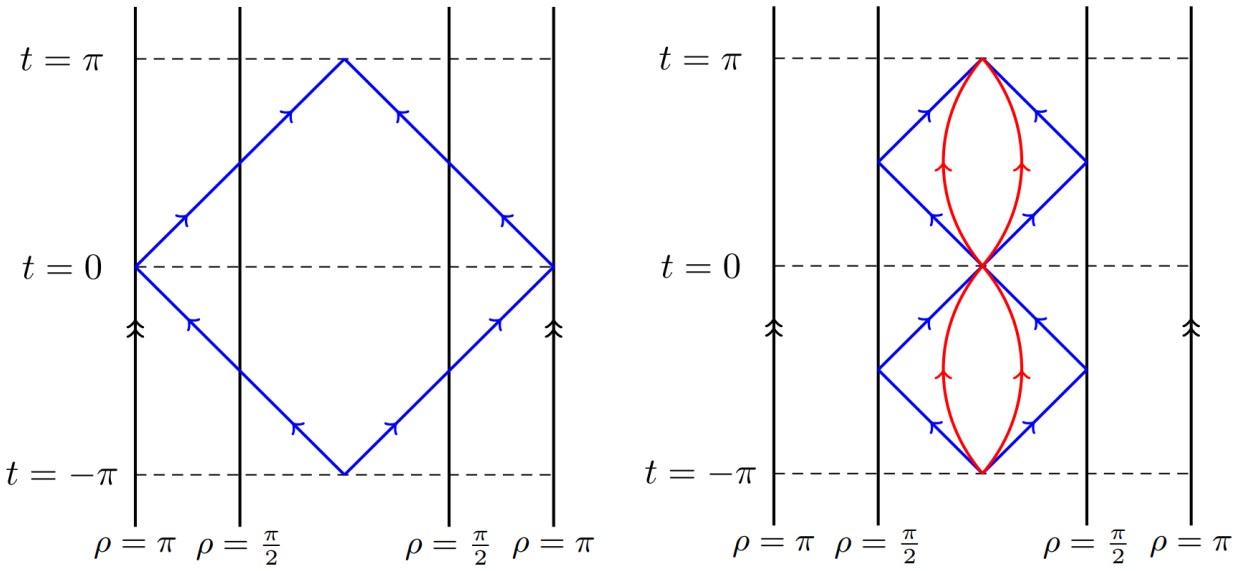

Figure 2.6: Transparent (left) and reflective (right) boundary conditions for adS mapped onto the ESU. Vertical lines with arrows are identified. See text for further details (adapted from [4]).

With transparent boundary conditions, the scalar field modes are free to pass beyond the adS boundary at $\rho = \pi/2$ and continue around the ESU cylinder to reappear at the other side. In reflective boundary conditions, the modes are 'reflected' back at the adS boundary ($\rho = \pi/2$). In this thesis we will focus on reflective boundary conditions of which there are two simple types; Dirichlet and Neumann. For the Dirichlet boundary condition we require that the field modes are zero at the space-time boundary, whilst for the Neumann boundary condition we require that the normal derivative of the field is zero at the space-time boundary on ESU.

Boundary conditions on adS for a massive scalar field were analysed further by Ishibashi and Wald [58, 59, 101], who showed that the possible choices of dynamics of the scalar field correspond to the choices of self-adjoint extensions of the spatial component of the wave operator. They showed that any dynamical evolution for a scalar field in a static space-time must respect causality, time translation and reflection invariance, as well as having a conserved energy functional and be in agreement with the globally hyperbolic case. They also showed that the freedom to choose the self-adjoint extensions corresponds to all the possible boundary conditions that can be applied at the space-time boundary and the choice of boundary conditions is dependent on the mass and coupling constant of the field. More will be said about this in Chapter 4.

Dirichlet and Neumann are the simplest boundary conditions and the most commonly studied in the literature. However we can also consider (reflective) Robin boundary conditions which, in the case of a massless, conformally coupled field, can be considered as a linear combination of Dirichlet and Neumann boundary conditions [59] parameterised by a Robin parameter, ζ

$$\Phi \ \cos\zeta + \frac{\partial\Phi}{\partial\rho} \ \sin\zeta = 0 \quad \text{as} \quad \rho \to \frac{\pi}{2}, \quad \zeta \in [0, \pi]. \tag{2.28}$$

It can be seen from (2.28) that for $\zeta = 0$, we recover the Dirichlet boundary condition and for $\zeta = \pi/2$ we recover the Neumann boundary condition. It will be shown in Chapter 4 that there is an upper bound for the Robin parameter, ζ_{crit}, beyond which our scalar field is classically unstable. We will also see that the value of ζ_{crit} depends on the mass and coupling constant of the field. Therefore, when applying Robin boundary conditions we will restrict ourselves to $0 \leq \zeta < \zeta_{\text{crit}}$.

Applying different valid boundary conditions gives rise to an extensive set of possible quantum states that can be studied on an adS background. In the context of the adS/CFT correspondence this will amount to new theories in the 'bulk'. However, the boundary conditions mentioned above are not the only ones that can be applied at the space-time boundary (see [22, 31, 32, 33, 34, 50] for more general boundary conditions that can be applied). For example in [32, 33], the authors discuss the use of generalised boundary conditions of Wentzell type in the Poincaré patch of a n-dimensional adS space-time. This involved the use of the second time derivative of the field at the asymptotic boundary.

§ 2.5 Conclusions

In this chapter we have highlighted some of the key features of anti-de Sitter space-time. It is a maximally symmetric solution to Einstein's field equations of general relativity with a constant negative curvature and plays a key role in the adS/CFT correspondence. We have shown how the space-time can be pictured geometrically and how the metric is formulated in $n-$dimensions. Being a non-globally hyperbolic space-time means we need to impose boundary conditions at the space-time boundary in order to have a well-posed quantum field theory. We have discussed some of the main boundary conditions used in the literature and made reference to studies where other boundary conditions are applied. Our focus in this thesis is in the reflective boundary conditions of Dirichlet, Neumann and in particular Robin type.

Chapter 3

Renormalised stress energy tensor in adS4

A fundamental aspect of QFTCS is the determination of the expectation values of the RSET. This acts as the source term in Einstein's field equations (1.2) when we adopt the semi-classical approach to quantum gravity. In this chapter we determine the v.e.v.s and t.e.v.s of the RSET of a massless, conformally coupled quantum scalar field on the covering space of global adS4. We apply Dirichlet, Neumann and Robin boundary conditions to the scalar field at the space-time boundary and compute the expectation values numerically using MATHEMATICA. Much of the contents of this chapter has appeared in a recent publication [70].

In [71], the renormalised VP was computed for a massless, conformally coupled scalar field on adS4 with Robin boundary conditions applied to all field modes at the space-time boundary. The VP is the expectation value of the square of the field, $\langle\hat{\Phi}^2\rangle$, and is the simplest nonzero expectation value we can calculate. For both v.e.v.s and t.e.v.s it was found that, on the space-time boundary, the VP converged to the Neumann value for all Robin boundary conditions except for Dirichlet, which had a different value (see Figure 3.1). As we will see later in Chapter 5, the same conclusion

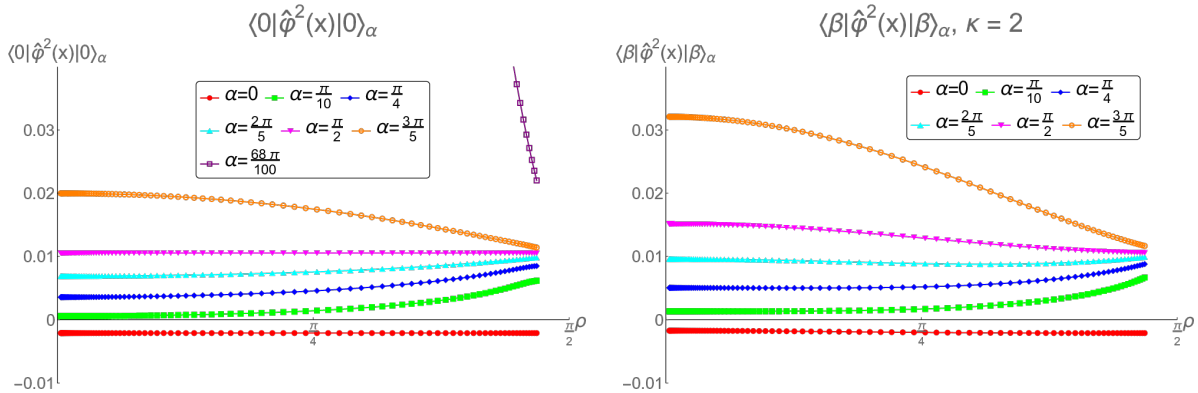

Figure 3.1: V.e.v.s (left) and t.e.v.s (right) of the VP for a massless, conformally coupled scalar field, Φ, in adS4, from [71]. The Robin parameter is represented by α. For the t.e.v.s (right), κ is related to the temperature, T, by $\kappa = 2\pi T$. The magenta line on both plots represents the VP with Neumann boundary conditions, $\alpha = \pi/2$, whilst the red line represents the Dirichlet boundary condition, $\alpha = 0$. See text for further details.

is reached for the VP on three-dimensional adS for a scalar field with nonzero mass and values of the coupling to the space-time curvature for which Robin boundary conditions can be applied. It would therefore seem that the Neumann boundary condition reflects the generic behaviour of the VP, as we approach the space-time boundary, rather than the Dirichlet boundary conditions, even though it is the latter that is most widely studied in the literature. However, in [12], when Robin boundary conditions were applied to only to a subset of the scalar field modes corresponding to s-wave perturbations, it was found that the VP for a massless, conformally coupled scalar field on adS4 converged to the Dirichlet value on the space-time boundary [12].

It is natural to ask whether the result in [71] also extends to the v.e.v.s and t.e.v.s of the RSET for a massless, conformally coupled scalar field on adS4 and this is the focus of this chapter. In [12], the authors applied Robin boundary conditions to just a subset of modes and it was found that the RSET again took the same value as for Dirichlet boundary conditions at the space-time boundary. In this chapter, we follow [71] and employ Euclidean methods to determine the v.e.v.s and t.e.v.s of the RSET, whilst applying Robin boundary conditions to *all* field modes. We pay particular attention to how the expectation values depend on the Robin parameter and temperature in the case of the t.e.v.s.

This chapter is structured as follows. In Section 3.1, we describe the construction of the v.e.v.s and t.e.v.s of a massless, conformally coupled quantum scalar field with Dirichlet and Neumann boundary conditions, as set out in [2]. In Section 3.2 we outline the construction of the vacuum and thermal Green's functions for a massless, conformally coupled, scalar field on four-dimensional adS, as set out in [71], highlighting the extra contribution provided by applying Robin boundary conditions. In Section 3.3, we calculate the expectation values of the RSET in both vacuum and thermal states. A discussion of the numerical methods used in the computation of the expectation values is given in Section 3.4 together with an estimate of the errors involved. The results for the v.e.v.s of the RSET with Robin boundary conditions are given in Section 3.5, followed in Section 3.6 by a discussion of how we were able to reproduce the results in [12] using Euclidean methods. The t.e.v.s of the RSET with Robin boundary conditions are presented in Section 3.7. The behaviour of the nonzero components of the RSET as we approach the space-time boundary is explored in Section 3.8 and finally we present our conclusions in Section 3.9.

§ 3.1 Vacuum and thermal expectation values of a quantum scalar field with Dirichlet and Neumann boundary conditions

Anti-de Sitter space-time at finite temperature was discussed in [2], where the v.e.v.s and t.e.v.s of a massless, conformally coupled scalar field were determined for Dirichlet and Neumann boundary conditions. In global coordinates the metric of adS4 is given in (2.8). The zero temperature anticommutator $G_0^{(1)}(x,x')$ (1.37), for massless, conformally coupled scalar field obeying (1.36), is given by [2]

$$G_0^{(1)}(x,x') = -\frac{1}{4\pi^2 L^2}\Big\{(1-Z)^{-1} \pm (1+Z)^{-1}\Big\}, \tag{3.1}$$

and is related to the Feynman Green's function by (1.45). The invariant biscalar function $Z(x,x')$ in (3.1) is related to the geodesic interval (2.22) and is given by

$$Z(x,x') = \frac{\cos(t-t') - \sin\rho\sin\rho'\cos\gamma}{\cos\rho\cos\rho'}, \tag{3.2}$$

where the angular separation of the space-time points γ is given by (2.23). In (3.1), the + sign refers to Dirichlet boundary conditions whilst the − sign refers to Neumann.

If the field is held at an inverse temperature β, the finite temperature propagator $G^{(1)}_\beta$ becomes [2]

$$G^{(1)}_\beta(x,x') = -\frac{1}{4\pi^2L^2}\Big\{J_\beta(t,\rho;t'\rho') \pm J_\beta(t+\pi,-\rho;t',\rho')\Big\}, \tag{3.3}$$

where

$$J_\beta(t,\rho;t',\rho') = \sum_{n=-\infty}^{+\infty}\left\{1 - Z(t+in\beta,\rho;t'\rho';\gamma)\right\}^{-1}, \tag{3.4}$$

and we have expressed $Z(x,x')$ as $Z(t,\rho;t',\rho';\gamma)$ (see (1.49)). As we are in pure adS, the time coordinate is periodic with period 2π (see Section 2.1). Furthermore, for a scalar field in equilibrium at inverse temperature β, the two-point function (3.3) is periodic in time with period $i\beta$ [2, 17]. Thus, the function J_β (3.4) is a doubly periodic function of imaginary time t, with periodicity properties

$$\begin{aligned} J_\beta(t,\rho;t',\rho') &= J_\beta(t+2\pi,\rho;t',\rho'), \\ J_\beta(t,\rho;t',\rho') &= J_\beta(t+i\beta,\rho;t',\rho'). \end{aligned} \tag{3.5}$$

It was shown in [2] that the function J_β is a meromorphic function in the complex $t-$plane and also an elliptic function and thus it is possible to find the following expression for the propagator

$$\begin{aligned} G^{(1)}_\beta(t,\rho;t',\rho';\gamma) = -\frac{1}{4\pi^2L^2}\Bigg[&(1-Z)^{-1} \pm (1+Z)^{-1} \\ &- 4\cos\rho\cos\rho'\sum_{k=1}^{\infty}\left(\frac{\sin k\eta(\rho,\rho';\gamma)}{\sin\eta(\rho,\rho';\gamma)} \pm (-1)^k\frac{\sin k\eta(-\rho,\rho';\gamma)}{\sin\eta(-\rho,\rho';\gamma)}\right)\frac{\cos k(t-t')}{e^{k\beta}-1}\Bigg], \end{aligned} \tag{3.6}$$

where

$$\eta(\rho,\rho';\gamma) = \cos^{-1}\left[\cos\rho\cos\rho' + \sin\rho\sin\rho'\cos\gamma\right]. \tag{3.7}$$

It can be seen that in the zero temperature limit, $\beta\to\infty$, (3.6) reduces to the zero temperature form (3.1). Using the exact form of the symmetric function, $G^{(1)}_\beta$ (3.6), the authors in [2] were able calculate the expectation values of the VP and the RSET. They used the Hadamard parametrix of $G^{(1)}_\beta$ given in (1.64). As we are considering a massless, conformally coupled field, we have $V(x,x')=0$ to second order [61] and the log term in (1.64) is now absent giving

$$G^{(1)}_\beta(x,x') = \frac{1}{4\pi^2}\left(\frac{\Delta^{1/2}(x,x')}{\sigma(x,x')} + W(x,x')\right), \tag{3.8}$$

where Δ is the van Vleck-Morette determinant (2.27) and $\sigma(x,x')$ is Synge's world function (2.25). The difference in the prefactors in (1.64) and (3.8) can be gleaned from the relationship between the Feynman propagator and the anticommutator function (1.45).

The biscalar $W(x,x')$ has a short distance expansion of the form [2, 35]

$$W(x,x') = w(x) - \frac{1}{2}w_{,\mu}(x)\sigma^{,\mu} + \frac{1}{2}w_{\mu\nu}(x)\sigma^{,\mu}\sigma^{,\nu} + \dots, \tag{3.9}$$

where

$$w(x) = \lim_{x'\to x} W(x,x'), \qquad w_{\mu\nu}(x) = \lim_{x'\to x} W_{;\mu\nu}(x,x'). \tag{3.10}$$

It was shown in [2] that for Dirichlet and Neumann boundary conditions

$$w(x) = \frac{1}{L^2}\left\{\left[\frac{1}{3} + 4\cos^2\rho\, f_1\left(\frac{\beta}{L}\right)\right] \pm \left[-\frac{1}{2} + 2\cot\rho\, S_0\left(\frac{\beta}{L},\rho\right)\right]\right\}, \tag{3.11}$$

where

$$\begin{aligned} f_m(x) &= \sum_{n=1}^{\infty} n^m (e^{nx}-1)^{-1}, \\ S_m(x,\rho) &= \sum_{n=1}^{\infty} n^m (-1)^n (e^{nx}-1)^{-1}\sin(2n\rho). \end{aligned} \tag{3.12}$$

The expectation value of the VP in adS4 is given by [2, 16, 20]

$$\langle\hat{\Phi}^2\rangle = \frac{w}{8\pi^2}. \tag{3.13}$$

In the zero temperature limit ($\beta\to\infty$), (3.11) becomes

$$\lim_{\beta\to\infty} w = \frac{1}{L^2}\left(\frac{1}{3} \mp \frac{1}{2}\right) \tag{3.14}$$

where now the $-$ sign refers to the Dirichlet boundary condition and the $+$ sign to the Neumann. Putting together (3.13) and (3.14) we arrive at the expressions for the v.e.v of the VP with Dirichlet, $\langle\hat{\Phi}^2\rangle_0^D$, and Neumann, $\langle\hat{\Phi}^2\rangle_0^N$, boundary conditions in adS4 as

$$\langle\hat{\Phi}^2\rangle_0^D = -\frac{1}{48\pi^2L^2} \qquad \text{and} \qquad \langle\hat{\Phi}^2\rangle_0^N = \frac{5}{48\pi^2L^2}. \tag{3.15}$$

These results match those in [61, 71] for the Dirichlet case. The expressions for the renormalised t.e.v.s of the SET with Dirichlet and Neumann boundary conditions are also given in [2], but there is a typographical error with a missing $\cot\rho$ term in line 2 (personal communication from E. Winstanley), so the equation should read:

$$\langle\hat{T}_{\mu\nu}\rangle_{\beta}^{D/N} = \frac{1}{8\pi^2 L^4}\left\{\left[-\frac{1}{120}+\frac{4}{3}\cos^4\rho\ f_3\left(\frac{\beta}{L}\right)\right]g_{\mu\nu}+\left[\frac{16}{3}\cos^4\rho\, f_3\left(\frac{\beta}{L}\right)\right]t_\mu t_\nu\right\}$$
$$\pm\frac{\cot\rho}{8\pi^2 L^4}\left\{\left[-\frac{1}{6}\csc^2\rho\ \cos 2\rho\ S_0\left(\frac{\beta}{L},\rho\right)+\frac{1}{3}\cot\rho\ C_1\left(\frac{\beta}{L},\rho\right)+\frac{2}{3}\cos^2\rho\ S_2\left(\frac{\beta}{L},\rho\right)\right]g_{\mu\nu}\right.$$
$$+\left[\frac{1}{6}(3-\cot^2\rho)S_0\left(\frac{\beta}{L},\rho\right)+\cot\rho\left(1-\frac{2}{3}\cos^2\rho\right)C_1\left(\frac{\beta}{L},\rho\right)+2\cos^2\rho\ S_2\left(\frac{\beta}{L},\rho\right)\right]t_\mu t_\nu$$
$$\left.+\left[\frac{1}{6}(3\csc^2\rho-4)S_0\left(\frac{\beta}{L},\rho\right)+\cot\rho\left(\frac{2}{3}\sin^2\rho-1\right)C_1\left(\frac{\beta}{L},\rho\right)-\frac{2}{3}\cos^2\rho\ S_2\left(\frac{\beta}{L},\rho\right)\right]\rho_\mu\rho_\nu\right\}, \tag{3.16}$$

where $g_{\mu\nu}$ is the space-time metric and t_μ, ρ_μ are unit vectors in the t and ρ directions respectively given by

$$t_\mu = L\sec\rho\,(1,0,0,0), \qquad \rho_\mu = L\sec\rho\,(0,1,0,0), \tag{3.17}$$

and obey the normalisation conditions $t_\mu t^\mu = -1$ and $\rho_\mu\rho^\mu = 1$. In (3.16), the Dirichlet boundary condition is denoted by the + sign whilst the Neumann boundary condition has the − sign. The functions f_m, S_m are given in (3.12) and C_m is given by

$$C_m(x,\rho) = \sum_{n=1}^{\infty} n^m(-1)^n(e^{nx}-1)^{-1}\cos(2n\rho). \tag{3.18}$$

In the zero temperature limit (i.e. when $\beta\to\infty$), the v.e.v. of the RSET $\langle\hat{T}_{\mu\nu}\rangle_0^{D/N}$ derived from (3.16), reduces to

$$\langle\hat{T}_{\mu\nu}\rangle_0^{D/N} = -\frac{1}{960\pi^2 L^4}\,g_{\mu\nu}. \tag{3.19}$$

This is in agreement with the calculation in [61] for a scalar field with Dirichlet boundary conditions. Notably, the v.e.v. of the RSET (3.19) is the same for both Dirichlet and Neumann boundary conditions. This is not seen with the vacuum polarisation in adS4 [71] or adS3 (see Chapter 5). For both Dirichlet and Neumann boundary conditions, the vacuum state respects the maximal symmetry of the underlying adS space-time, and therefore the RSET will be a constant multiple of the metric, $\langle\hat{T}_{\mu\nu}\rangle_0^{D/N} = \alpha g_{\mu\nu}$, for some constant α. Taking the trace, $\alpha = \langle\hat{T}^\mu_\mu\rangle_0^{D/N}/4$. For a massless, conformally coupled scalar field, the trace $\langle\hat{T}^\mu_\mu\rangle_0^{D/N}$ is fixed to be the trace anomaly, which, on four-dimensional adS is [61]

$$\langle\hat{T}^\mu_\mu\rangle = -\frac{1}{240\pi^2 L^4}. \tag{3.20}$$

Therefore, for a massless, conformally coupled scalar field, the v.e.v. of the RSET for a maximally symmetric state is entirely determined by the trace anomaly and is independent of any boundary conditions applied.

§ 3.2 Euclidean Green's functions

In the previous section we described the derivation of the v.e.v.s and t.e.v.s of the RSET of a massless, conformally coupled scalar field with Dirichlet and Neumann boundary conditions in Lorentzian adS4 space-time. In order to compute the corresponding expectation values with Robin boundary conditions we work in Euclidean space, where the Green's functions are unique and have a well-defined distribution (Section 1.4).

The Euclidean metric is obtained from the adS metric (2.8) by performing a Wick rotation, $t \to -i\tau$, which gives

$$ds^2 = L^2 \sec^2\rho\,[d\tau^2 + d\rho^2 + \sin^2\rho\,(d\theta^2 + \sin^2\theta\,d\phi^2)]. \tag{3.21}$$

For a thermal state at temperature, T, the thermal Euclidean Green's function is periodic in time, with period $1/T$ and has the mode-sum form [71]

$$G^E_{\zeta,\beta}(x,x') = \frac{\kappa}{8\pi^2 L^2}\cos\rho\,\cos\rho' \sum_{n=-\infty}^{\infty} e^{in\kappa\Delta\tau} \sum_{\ell=0}^{\infty}(2\ell+1)P_\ell(\cos\gamma)g_{\omega\ell}(\rho,\rho') \tag{3.22}$$

where $\omega = n\kappa$ is the quantised frequency, $\Delta\tau = \tau - \tau'$ represents the temporal separation of the space-time points, $g_{\omega\ell}(\rho,\rho')$ is the radial Green's function, $P_\ell(x)$ is a Legendre polynomial and κ is given by

$$\kappa = 2\pi T. \tag{3.23}$$

The angular separation of the space-time points γ is given by (2.23). For vacuum states, the Euclidean Green's function is no longer periodic in time and takes the form [71]

$$G^E_{\zeta}(x,x') = \frac{1}{8\pi^2 L^2}\cos\rho\cos\rho' \int_{\omega=-\infty}^{\infty} d\omega\, e^{i\omega\Delta\tau} \sum_{\ell=0}^{\infty}(2\ell+1)P_\ell(\cos\gamma)g_{\omega\ell}(\rho,\rho'). \tag{3.24}$$

The radial Green's function $g_{\omega\ell}$ satisfies the inhomogeneous equation

$$\left\{\frac{d}{d\rho}\left(\sin^2\rho\frac{d}{d\rho}\right) - \omega^2\sin^2\rho - \ell(\ell+1)\right\} g_{\omega\ell}(\rho,\rho') = \delta(\rho-\rho'). \tag{3.25}$$

Consider now the solutions to the homogeneous version of (3.25). Let $p_{\omega\ell}$ be the solution regular at the space-time origin ($\rho = 0$) and $q_{\omega\ell}$ the solution regular at the space-time boundary ($\rho = \pi/2$) which satisfies the relevant boundary conditions. The general solution to the homogeneous version of (3.25) can be given in terms of the conical (Mehler) functions as

$$p_{\omega\ell}, q_{\omega\ell} = \frac{1}{\sqrt{\sin\rho}}\left[C_1 P^{-\ell-1/2}_{i\omega-1/2}(\cos\rho) + C_2 P^{-\ell-1/2}_{i\omega-1/2}(-\cos\rho)\right], \tag{3.26}$$

where C_1 and C_2 are constants (determined below) and $P^\nu_\mu(z)$ are associated Legendre functions. The radial Green's function $g_{\omega\ell}$ is built from $p_{\omega\ell}$, $q_{\omega\ell}$ as

$$g_{\omega\ell}(\rho,\rho') = \frac{p_{\omega\ell}(\rho_<)q_{\omega\ell}(\rho_>)}{N^E_{\omega\ell}}, \tag{3.27}$$

where $N^E_{\omega\ell}$ is a normalisation constant and we have used the definitions $\rho_< = \min\{\rho, \rho'\}$ and $\rho_> = \max\{\rho, \rho'\}$. The normalisation constant $N^E_{\omega\ell}$ in (3.27) can be determined by integrating both sides of (3.25) to give [69]

$$N^E_{\omega\ell} = \sin^2\rho\, \mathcal{W}\{p_{\omega\ell}, q_{\omega\ell}\}, \tag{3.28}$$

where $\mathcal{W}\{p_{\omega\ell}, q_{\omega\ell}\}$ is the Wronskian of the two solutions to (3.25) defined by

$$\mathcal{W}\{p_{\omega\ell}, q_{\omega\ell}\} = p_{\omega\ell}\frac{dq_{\omega\ell}}{d\rho} - q_{\omega\ell}\frac{dp_{\omega\ell}}{d\rho}. \tag{3.29}$$

Calculation of the Wronskian gives [69, 71]

$$N^E_{\omega\ell} = \frac{2}{|\Gamma(\ell+1+i\omega)|^2}. \tag{3.30}$$

Requiring regularity at the space-time origin ($\rho = 0$) gives

$$p_{\omega\ell}(\rho) = \frac{1}{\sqrt{\sin\rho}} P^{-\ell-1/2}_{i\omega-1/2}(\cos\rho), \tag{3.31}$$

where the constant in (3.26) has been absorbed into the normalisation constant. We now impose Robin boundary conditions on $q_{\omega\ell}$ at the space-time boundary ($\rho \to \pi/2$), of the form [71]

$$q_{\omega\ell}(\rho)\cos\zeta + \frac{dq_{\omega\ell}(\rho)}{d\rho}\sin\zeta = 0, \tag{3.32}$$

where $\zeta \in [0, \pi)$ is the Robin parameter (2.28), with $\zeta = 0$ and $\zeta = \pi/2$ denoting Dirichlet and Neumann boundary conditions respectively. This gives

$$q^\zeta_{\omega\ell}(\rho) = \frac{1}{\sqrt{\sin\rho}}\left[C^\zeta_{\omega\ell} P^{-\ell-1/2}_{i\omega-1/2}(\cos\rho) + P^{-\ell-1/2}_{i\omega-1/2}(-\cos\rho)\right], \tag{3.33}$$

where the constant $C^\zeta_{\omega\ell}$ is given by [71]

$$C^\zeta_{\omega\ell} = \frac{2|\Gamma(\frac{i\omega+\ell+2}{2})|^2\tan\zeta - |\Gamma(\frac{i\omega+\ell+1}{2})|^2}{2|\Gamma(\frac{i\omega+\ell+2}{2})|^2\tan\zeta + |\Gamma(\frac{i\omega+\ell+1}{2})|^2}. \tag{3.34}$$

It is clear from (3.34) that $C^\zeta_{\omega\ell}$ will diverge if there are values of the Robin parameter ζ which satisfy

$$2\tan\zeta = -\frac{|\Gamma(\frac{i\omega+\ell+1}{2})|^2}{|\Gamma(\frac{i\omega+\ell+2}{2})|^2}. \tag{3.35}$$

We can define an upper limit for the Robin parameter ζ_{crit}. For values of the Robin parameter, ζ, in the interval $\zeta_{\text{crit}} < \zeta < \pi$, we will obtain purely imaginary values of ω that satisfy (3.35). This will lead to mode solutions of the scalar field equation that are exponentially growing and therefore classically unstable [71]. We therefore restrict our consideration of Robin boundary conditions to $\zeta < \zeta_{\text{crit}}$ (see Section 4.5 for the definition of ζ_{crit} for the scalar field with general mass and

coupling on adS3). We will see in Chapters 4–6 that the value of $\zeta_{\rm crit}$ is dependent on the mass and coupling constant of the scalar field as well as the number of space-time dimensions. For a massless, conformally coupled scalar field on adS4, we find that $\zeta_{\rm crit} \sim 0.68\pi$ [71].

From (3.34) it can be seen that for the Dirichlet boundary condition ($\zeta = 0$), $C^0_{\omega\ell} = -1$ and for the Neumann boundary condition ($\zeta = \pi/2$), $C^{\pi/2}_{\omega\ell} = 1$. These give

$$\begin{aligned} q^D_{\omega\ell}(\rho) &= \frac{1}{\sqrt{\sin\rho}}\left[P^{-\ell-1/2}_{i\omega-1/2}(-\cos\rho) - P^{-\ell-1/2}_{i\omega-1/2}(\cos\rho)\right], \\ q^N_{\omega\ell}(\rho) &= \frac{1}{\sqrt{\sin\rho}}\left[P^{-\ell-1/2}_{i\omega-1/2}(-\cos\rho) + P^{-\ell-1/2}_{i\omega-1/2}(\cos\rho)\right]. \end{aligned} \tag{3.36}$$

Following [71], we now write the vacuum and thermal Euclidean Green's function with Robin boundary conditions as

$$\begin{aligned} G^E_{\zeta,0}(x,x') &= G^E_{D,0}(x,x')\cos^2\zeta + G^E_{N,0}(x,x')\sin^2\zeta + G^E_{R,0}(x,x')\sin 2\zeta, \\ G^E_{\zeta,\beta}(x,x') &= G^E_{D,\beta}(x,x')\cos^2\zeta + G^E_{N,\beta}(x,x')\sin^2\zeta + G^E_{R,\beta}(x,x')\sin 2\zeta, \end{aligned} \tag{3.37}$$

where $G^E_{D,0}(x,x')$ and $G^E_{D,\beta}(x,x')$ are the vacuum and thermal Euclidean Green's functions, with Dirichlet boundary conditions, given by

$$\begin{aligned} G^E_{D,0}(x,x') = \frac{1}{16\pi^2L^2}\frac{\cos\rho\cos\rho'}{\sqrt{\sin\rho\sin\rho'}}\int_{\omega=-\infty}^{\infty} d\omega\, e^{i\omega\Delta\tau}\sum_{\ell=0}^{\infty}(2\ell+1)P_\ell(\cos\gamma)|\Gamma(\ell+1+i\omega)|^2 \\ \times P^{-\ell-1/2}_{i\omega-1/2}(\cos\rho_<)\left[P^{-\ell-1/2}_{i\omega-1/2}(-\cos\rho_>) - P^{-\ell-1/2}_{i\omega-1/2}(\cos\rho_>)\right], \\ G^E_{D,\beta}(x,x') = \frac{\kappa}{16\pi^2L^2}\frac{\cos\rho\cos\rho'}{\sqrt{\sin\rho\sin\rho'}}\sum_{n=-\infty}^{\infty} e^{in\kappa\Delta\tau}\sum_{\ell=0}^{\infty}(2\ell+1)P_\ell(\cos\gamma)|\Gamma(\ell+1+in\kappa)|^2 \\ \times P^{-\ell-1/2}_{in\kappa-1/2}(\cos\rho_<)\left[P^{-\ell-1/2}_{in\kappa-1/2}(-\cos\rho_>) - P^{-\ell-1/2}_{in\kappa-1/2}(\cos\rho_>)\right]. \end{aligned} \tag{3.38}$$

$G^E_{N,0}(x,x')$ and $G^E_{N,\beta}(x,x')$ are the vacuum and thermal Euclidean Green's functions, with Neumann boundary conditions, given by

$$\begin{aligned} G^E_{N,0}(x,x') = \frac{1}{16\pi^2L^2}\frac{\cos\rho\cos\rho'}{\sqrt{\sin\rho\sin\rho'}}\int_{\omega=-\infty}^{\infty} d\omega\, e^{i\omega\Delta\tau}\sum_{\ell=0}^{\infty}(2\ell+1)P_\ell(\cos\gamma)|\Gamma(\ell+1+i\omega)|^2 \\ \times P^{-\ell-1/2}_{i\omega-1/2}(\cos\rho_<)\left[P^{-\ell-1/2}_{i\omega-1/2}(-\cos\rho_>) + P^{-\ell-1/2}_{i\omega-1/2}(\cos\rho_>)\right], \\ G^E_{N,\beta}(x,x') = \frac{\kappa}{16\pi^2L^2}\frac{\cos\rho\cos\rho'}{\sqrt{\sin\rho\sin\rho'}}\sum_{n=-\infty}^{\infty} e^{in\kappa\Delta\tau}\sum_{\ell=0}^{\infty}(2\ell+1)P_\ell(\cos\gamma)|\Gamma(\ell+1+in\kappa)|^2 \\ \times P^{-\ell-1/2}_{in\kappa-1/2}(\cos\rho_<)\left[P^{-\ell-1/2}_{in\kappa-1/2}(-\cos\rho_>) + P^{-\ell-1/2}_{in\kappa-1/2}(\cos\rho_>)\right]. \end{aligned} \tag{3.39}$$

$G^E_{R,0}(x,x')$ and $G^E_{R,\beta}(x,x')$ are the vacuum and thermal regular contributions, with mode sums

given by

$$G^E_{R,0}(x,x') = \frac{1}{16\pi^2 L^2}\frac{\cos\rho\,\cos\rho'}{\sqrt{\sin\rho\,\sin\rho'}}\int_{\omega=-\infty}^{\infty} d\omega\, e^{i\omega\Delta\tau} \times \sum_{\ell=0}^{\infty} D^{\zeta}_{\omega\ell} P_\ell(\cos\gamma) P^{-\ell-1/2}_{i\omega-1/2}(\cos\rho)\, P^{-\ell-1/2}_{i\omega-1/2}(\cos\rho'), \tag{3.40}$$

and

$$G^E_{R,\beta}(x,x') = \frac{\kappa}{16\pi^2 L^2}\frac{\cos\rho\,\cos\rho'}{\sqrt{\sin\rho\,\sin\rho'}}\sum_{n=-\infty}^{\infty} e^{in\kappa\Delta\tau} \times \sum_{\ell=0}^{\infty} D^{\zeta}_{\omega\ell} P_\ell(\cos\gamma) P^{-\ell-1/2}_{in\kappa-1/2}(\cos\rho)\, P^{-\ell-1/2}_{in\kappa-1/2}(\cos\rho'), \tag{3.41}$$

where the constant $D^{\zeta}_{\omega\ell}$ is given by

$$D^{\zeta}_{\omega\ell} = (1+2\ell)|\Gamma(1+\ell+i\omega)|^2 \left[\frac{2|\Gamma(\frac{i\omega+\ell+2}{2})|^2\cos\zeta - |\Gamma(\frac{i\omega+\ell+1}{2})|^2\sin\zeta}{2|\Gamma(\frac{i\omega+\ell+2}{2})|^2\sin\zeta + |\Gamma(\frac{i\omega+\ell+1}{2})|^2\cos\zeta}\right], \tag{3.42}$$

with $\omega = n\kappa$ in the thermal sum (3.41). The terms $G^E_{R,0}(x,x')$ and $G^E_{R,\beta}(x,x')$ are not Green's functions as they do not satisfy (1.54) and are regular in the coincidence limit.

§ 3.3 Expectation values of the RSET

Having given expressions for the vacuum and thermal Green's functions for the massless, conformally coupled scalar field in adS4, we now determine the expectation values of the RSET. For a quantum state $|\Psi\rangle$, the expectation value of the RSET, in Euclidean space, can be expressed as

$$\langle\Psi|\hat{T}_{\mu\nu}(x)|\Psi\rangle = \lim_{x'\to x}\left\{\mathcal{T}_{\mu\nu}(x,x')\left[G^E(x,x') - G_{F,\mathrm{sing}}(x,x')\right] - g_{\mu\nu}v_1(x,x')\right\}, \tag{3.43}$$

where $G_{F,\mathrm{sing}}(x,x')$ is the singular part of the Hadamard parametrix (1.74), which is independent of the quantum state. For the massless, conformally coupled field, the second order differential operator $\mathcal{T}_{\mu\nu}(x,x')$ (1.85) takes the form

$$\mathcal{T}_{\mu\nu} = \frac{2}{3}g_\nu{}^{\nu'}\nabla_\mu\nabla_{\nu'} - \frac{1}{6}g_{\mu\nu}g^{\rho\sigma'}\nabla_\rho\nabla_{\sigma'} - \frac{1}{3}g_\mu{}^{\mu'}g_\nu{}^{\nu'}\nabla_{\mu'}\nabla_{\nu'} + \frac{1}{3}g_{\mu\nu}\nabla_\rho\nabla^\rho + \frac{1}{6}\Big(R_{\mu\nu} - \frac{1}{2}g_{\mu\nu}R\Big), \tag{3.44}$$

where $g_{\mu\nu'}$ represents the bivector of parallel transport between the points x and x' (1.86).

For the numerical calculations of the RSET in this chapter, we use the alternative expression for the RSET given in equation (19) in [35] for a massless, conformally coupled scalar field in four dimensions, namely

$$\langle\Psi|\hat{T}_{\mu\nu}(x)|\Psi\rangle = \frac{1}{8\pi^2}\left[-w_{\mu\nu} + \frac{1}{3}w_{;\mu\nu} - \frac{1}{12}g_{\mu\nu}\Box w + \frac{1}{6}R_{\mu\nu}\,w\right], \tag{3.45}$$

where w and $w_{\mu\nu}$ are given in (3.10).

Using (3.37, 3.43) we can write the expressions for the vacuum/thermal expectation values of the stress energy tensor with Robin boundary conditions, $\langle\hat{T}_{\mu\nu}\rangle^{\zeta}$, as

$$\begin{aligned}\langle\hat{T}_{\mu\nu}\rangle^{\zeta} = &\lim_{x'\to x}\{\mathcal{T}_{\mu\nu}(x,x')\left[G_D^E(x,x') - G_{F,\mathrm{sing}}(x,x')\right] - g_{\mu\nu}v_1(x,x')\}\cos^2\zeta \\ &+ \lim_{x'\to x}\left\{\mathcal{T}_{\mu\nu}(x,x')\left[G_N^E(x,x') - G_{F,\mathrm{sing}}(x,x')\right] - g_{\mu\nu}v_1(x,x')\right\}\sin^2\zeta \\ &+ \lim_{x'\to x}\{\mathcal{T}_{\mu\nu}(x,x')G_R^E(x,x')\}\sin 2\zeta. \quad (3.46)\end{aligned}$$

The final term in (3.46) is regular in the coincidence limit. As the singular terms $\mathcal{T}_{\mu\nu}(x,x')G_{F,\mathrm{sing}}(x,x')$ and the final subtraction term $g_{\mu\nu}v_1(x,x')$ are both state-independent, we can express the expectation values of the RSET when Robin boundary conditions are applied in terms of those when Dirichlet or Neumann boundary conditions are applied:

$$\langle\hat{T}_{\mu\nu}\rangle^{\zeta}_{\mathrm{ren}} = \langle\hat{T}_{\mu\nu}\rangle^{D}_{\mathrm{ren}}\cos^2\zeta + \langle\hat{T}_{\mu\nu}\rangle^{N}_{\mathrm{ren}}\sin^2\zeta + \lim_{x'\to x}\{\mathcal{T}_{\mu\nu}(x,x')G_R^E(x,x')\}\sin 2\zeta. \quad (3.47)$$

From henceforth, the 'ren' subscript will be omitted and it may be assumed that all $\langle\hat{T}_{\mu\nu}\rangle$ terms are renormalised. The t.e.v.s of the RSET with Dirichlet and Neumann boundary conditions have been given in (3.16).

The expression $\lim_{x'\to x}\{\mathcal{T}_{\mu\nu}(x,x')G^E_{R,\beta}(x,x')\}$ in the final term in (3.47) has been evaluated with MATHEMATICA. Using the recurrence relations for the conical functions [39, §14.10.1], the nonzero components of this contribution to the v.e.v.s of the RSET are given by

$$\begin{aligned}\langle\hat{T}^{\tau}_{\tau}\rangle^{\zeta}_{R,0} = \frac{\cos\rho\cot^3\rho}{192L^4\pi^2}\sum_{\ell=0}^{\infty}\int_{\omega=-\infty}^{\infty}d\omega\, D^{\zeta}_{\omega\ell}\Bigg\{ &-2\,\chi^2_{\omega\ell}\,[P^{-3/2-\ell}_{i\omega-1/2}(\cos\rho)]^2\,\sin^2\rho \\ &-2\ell\,\chi_{\omega\ell}\,P^{-3/2-\ell}_{i\omega-1/2}(\cos\rho)P^{-1/2-\ell}_{i\omega-1/2}(\cos\rho)\sin 2\rho \\ &-\left[2\ell(2\ell+1)+2(1-\ell^2-5\omega^2)\sin^2\rho\right][P^{-1/2-\ell}_{i\omega-1/2}(\cos\rho)]^2\Bigg\}, \quad (3.48)\end{aligned}$$

$$\begin{aligned}\langle\hat{T}^{\rho}_{\rho}\rangle^{\zeta}_{R,0} = \frac{\cos\rho\cot^3\rho}{192L^4\pi^2}\sum_{\ell=0}^{\infty}\int_{\omega=-\infty}^{\infty}d\omega\, D^{\zeta}_{\omega\ell}\Bigg\{ &6\,\chi^2_{\omega\ell}\,[P^{-3/2-\ell}_{i\omega-1/2}(\cos\rho)]^2\,\sin^2\rho \\ &+2(3\ell+2)\,\chi_{\omega\ell}\,P^{-3/2-\ell}_{i\omega-1/2}(\cos\rho)P^{-1/2-\ell}_{i\omega-1/2}(\cos\rho)\sin 2\rho \\ &+\left[2\ell-2(1+4\ell+3\ell^2+3\omega^2)\sin^2\rho\right][P^{-1/2-\ell}_{i\omega-1/2}(\cos\rho)]^2\Bigg\}, \quad (3.49)\end{aligned}$$

$$\begin{aligned}\langle\hat{T}^{\theta}_{\theta}\rangle^{\zeta}_{R,0} = \frac{\cos\rho\cot^3\rho}{192L^4\pi^2}\sum_{\ell=0}^{\infty}\int_{\omega=-\infty}^{\infty}d\omega\, D^{\zeta}_{\omega\ell}\Bigg\{ &-2\,\chi^2_{\omega\ell}\,[P^{-3/2-\ell}_{i\omega-1/2}(\cos\rho)]^2\sin^2\rho \\ &-2(\ell+1)\,\chi_{\omega\ell}\,P^{-3/2-\ell}_{i\omega-1/2}(\cos\rho)P^{-1/2-\ell}_{i\omega-1/2}(\cos\rho)\sin 2\rho \\ &+2\left[\ell^2+(1+2\ell+\ell^2-\omega^2)\sin^2\rho\right][P^{-1/2-\ell}_{i\omega-1/2}(\cos\rho)]^2\Bigg\}, \quad (3.50)\end{aligned}$$

with $\langle\hat{T}^{\phi}_{\phi}\rangle^{\zeta}_{R,0} = \langle\hat{T}^{\theta}_{\theta}\rangle^{\zeta}_{R,0}$. In (3.48–3.50) the subscripts $R, 0$ refer to the vacuum regular contribution in (3.37). The constant $D^{\zeta}_{\omega\ell}$ is given by (3.42) and

$$\chi_{\omega\ell} = 1 + 2\ell + \ell^2 + \omega^2. \tag{3.51}$$

For the corresponding expressions for the thermal expectation values we replace ω with $n\kappa$ and change the integral to a sum to obtain

$$\begin{aligned}\langle\hat{T}^{\tau}_{\tau}\rangle^{\zeta}_{R,\beta} = \frac{\kappa\cos\rho\cot^3\rho}{192L^4\pi^2}\sum_{\ell=0}^{\infty}\sum_{n=-\infty}^{\infty} D^{\zeta}_{n\ell}\Big\{ &-2\,\chi^2_{n\ell}\,[P^{-3/2-\ell}_{in\kappa-1/2}(\cos\rho)]^2\,\sin^2\rho \\ &-2\ell\,\chi_{n\ell}\,P^{-3/2-\ell}_{in\kappa-1/2}(\cos\rho)P^{-1/2-\ell}_{in\kappa-1/2}(\cos\rho)\sin 2\rho \\ &-\left[2\ell(2\ell+1)+2(1-\ell^2-5n^2\kappa^2)\sin^2\rho\right][P^{-1/2-\ell}_{in\kappa-1/2}(\cos\rho)]^2\Big\},\end{aligned} \tag{3.52}$$

$$\begin{aligned}\langle\hat{T}^{\rho}_{\rho}\rangle^{\zeta}_{R,\beta} = \frac{\kappa\cos\rho\cot^3\rho}{192L^4\pi^2}\sum_{\ell=0}^{\infty}\sum_{n=-\infty}^{\infty} D^{\zeta}_{n\ell}\Big\{ &6\,\chi^2_{n\ell}\,[P^{-3/2-\ell}_{in\kappa-1/2}(\cos\rho)]^2\,\sin^2\rho \\ &+2(3\ell+2)\,\chi_{n\ell}\,P^{-3/2-\ell}_{in\kappa-1/2}(\cos\rho)P^{-1/2-\ell}_{in\kappa-1/2}(\cos\rho)\sin 2\rho \\ &+\left[2\ell-2(1+4\ell+3\ell^2+3n^2\kappa^2)\sin^2\rho\right][P^{-1/2-\ell}_{in\kappa-1/2}(\cos\rho)]^2\Big\},\end{aligned} \tag{3.53}$$

$$\begin{aligned}\langle\hat{T}^{\theta}_{\theta}\rangle^{\zeta}_{R,\beta} = \frac{\kappa\cos\rho\cot^3\rho}{192L^4\pi^2}\sum_{\ell=0}^{\infty}\sum_{n=-\infty}^{\infty} D^{\zeta}_{n\ell}\Big\{ &-2\,\chi^2_{n\ell}\,[P^{-3/2-\ell}_{in\kappa-1/2}(\cos\rho)]^2\sin^2\rho \\ &-2(\ell+1)\,\chi_{n\ell}\,P^{-3/2-\ell}_{in\kappa-1/2}(\cos\rho)P^{-1/2-\ell}_{in\kappa-1/2}(\cos\rho)\sin 2\rho \\ &+2\left[\ell^2+(1+2\ell+\ell^2-n^2\kappa^2)\sin^2\rho\right][P^{-1/2-\ell}_{in\kappa-1/2}(\cos\rho)]^2\Big\},\end{aligned} \tag{3.54}$$

and $\langle\hat{T}^{\phi}_{\phi}\rangle^{\zeta}_{R,\beta} = \langle\hat{T}^{\theta}_{\theta}\rangle^{\zeta}_{R,\beta}$. In (3.52–3.54) the subscripts R, β refer to the thermal regular contribution in (3.37). The $D^{\zeta}_{n\ell}$ and $\chi_{n\ell}$ terms are obtained from the corresponding terms in (3.42, 3.51) by replacing ω with $n\kappa$. It is straightforward to verify that the last term in (3.46) has vanishing trace as expected since the trace anomaly (see Section 1.6) is contained in the other two terms in (3.46).

§ 3.4 Numerical computations

The v.e.v.s and t.e.v.s of the RSET have been calculated numerically using MATHEMATICA. The sums in (3.16) converge very rapidly and were computed up to $n = 100$. The relative error in curtailing the $n-$sum to 100 was only $\sim 10^{-40}$ compared to if the $n-$sum was performed to 500. For the regular contribution to the expectation values (3.48–3.54), when Robin boundary conditions are applied, a cutoff for the $\ell-$sum and $\omega-$integration (or sum over n) had to be chosen to make the computations tractable. For the v.e.v.s, the integral over ω is performed first before summing over ℓ. It is found that the ω-integral converges very quickly for fixed ℓ. This is shown in Figure 3.2

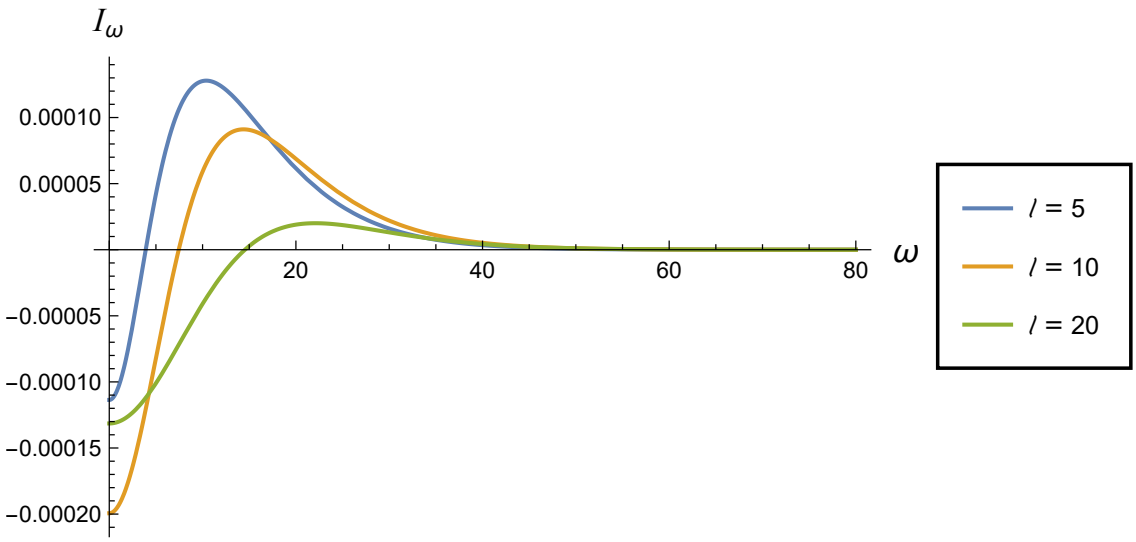

Figure 3.2: The integrand I_ω in (3.48) as a function of ω for fixed $\zeta = \pi/10$ and $\rho = 94\pi/200$ with a selection of values of ℓ.

where we plot (as an example) the integrand I_ω in (3.48) for three fixed values of ℓ. The ω-integral was performed over the interval $|\omega| \leq 100$ and the relative error entailed in curtailing the $\omega-$integral to 100 compared to 170 was $\sim 2.4 \times 10^{-6}$ for $\ell = 20$, $\rho = 94\pi/200$, $\zeta = \pi/10$. For the t.e.v.s the $n-$sum also converges rapidly and the sum over n was performed to $|n| \leq 50$. The relative error in curtailing the $|n|-$sum to 50 compared with 100 is $\sim 10^{-10}$ for $\ell = 20$, $\rho = 94\pi/200$, $\zeta = \pi/10$.

Determining the appropriate limit for the $\ell-$ sum was complicated by the fact that the $\ell-$sum exhibits nonuniform convergence with respect to the radial coordinate ρ as was found with the computation of the VP in adS4 [71]. The ℓ-sum converges more quickly nearer the origin and more slowly as the space-time boundary is approached (Figure 3.3). This nonuniform convergence of the $\ell-$ sum was observed for both the vacuum and thermal regular contributions with similar plots seen also for the different values of κ studied.

Clearly, the more modes used in the computations for the expectation values, the more accurate the final result, but owing to the time taken in the numerical computations with MATHEMATICA (even using the University Sharc HPC), a pragmatic approach had to be taken. For the v.e.v.s, the ℓ-sum was performed over the interval $0 \leq \ell \leq 100$. This was then compared to the value obtained if the $\ell-$sum and $\omega-$integration were each performed to 170 for particular values of ρ and ζ. For example, the relative error in (3.48) was calculated for $\zeta = 3\pi/10$ and $\rho = 94\pi/200$ and was order 10^{-2}. This error was much smaller away from the space-time boundary, for example being of order 10^{-18} at $\rho = 3\pi/10$ and $\rho = \pi/20$. However, it should be remembered that the regular contributions to the RSET in (3.48–3.54) represent only a small proportion of the overall value. For example, the regular contribution (3.48) to the v.e.v. of the RSET at $\rho = 94\pi/200$ and $\zeta = 3\pi/10$ as a fraction of the total v.e.v. was order 10^{-6}, meaning that the errors in the numerical calculations of the regular contributions to the SET were much less significant in the overall results and plots.

For the t.e.v.s, attempts to perform the $\ell-$sum to the same levels as in the vacuum case proved computationally challenging. Therefore, the $\ell-$sum was performed over the interval $0 \leq \ell \leq 50$.

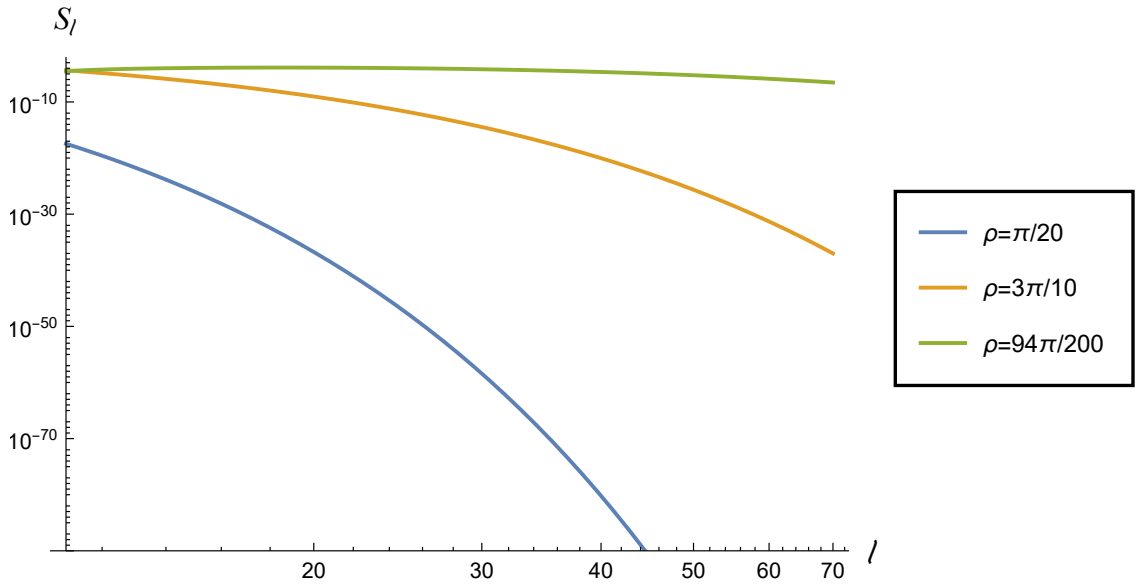

Figure 3.3: Log-log plot of the summand S_ℓ in (3.52) as a function of ℓ. Plots are for three different values of the radial coordinate ρ, demonstrating nonuniform convergence of the $\ell-$sum. There is slower convergence of the $\ell-$sum nearer the space-time boundary. In each case $\zeta = 3\pi/5$, $\kappa = 1/2$ and the n-sum has been performed to 50.

This was compared to performing the $\ell-$ and $\omega-$ sums to 170 for fixed ζ and three different values of ρ. The relative errors in the numerical computation of (3.52) were very much dependent on the space-time location and the value of κ and hence temperature. Away from the boundary, the relative errors were extremely small but increased as we approached the space-time boundary. For $\kappa = 1/2$ ($\zeta = \pi/10$), the relative error in the numerical computation of (3.52) at $\rho = 80\pi/200$, for example, was $\sim 3.5 \times 10^{-5}$. Indeed, as a result of increasing errors encountered close to the boundary, the numerical calculation of (3.52), for $\kappa = 1/2$ was performed up to $\rho = 85\pi/200$ only. Despite this we will find in Section 3.7 (Figures 3.8–3.10) that we can still draw reasonable conclusions as to the behaviour of the RSET as the space-time boundary is approached in the thermal state with $\kappa = 1/2$. The relative errors near the space-time boundary improved somewhat with increasing κ. For $\rho = 90\pi/200$, $\zeta = \pi/10$ for instance, the relative errors were $\sim 2 \times 10^{-10}$ and $\sim 5 \times 10^{-11}$ for $\kappa = 2$ and $\kappa = 2\pi$ respectively.

§ 3.5 Vacuum expectation values of the RSET with Robin boundary conditions

Whilst the v.e.v.s of the RSET with either Dirichlet or Neumann boundary conditions respect the maximum symmetry of the underlying space-time, this is not the case when Robin boundary conditions are applied, as shown in Figure 3.4. For all values of $\zeta \neq 0, \pi/2$ each component of the RSET varies with the radial coordinate ρ. The energy density $-\langle \hat{T}^\tau_\tau \rangle^\zeta_0$ is positive throughout the space-time, reaching the common vacuum Dirichlet/Neumann value at the space-time boundary. This is in contrast to the findings in [12] where the energy density is negative on most of the space-time and only becomes positive as the boundary is reached. This is likely due to the application of

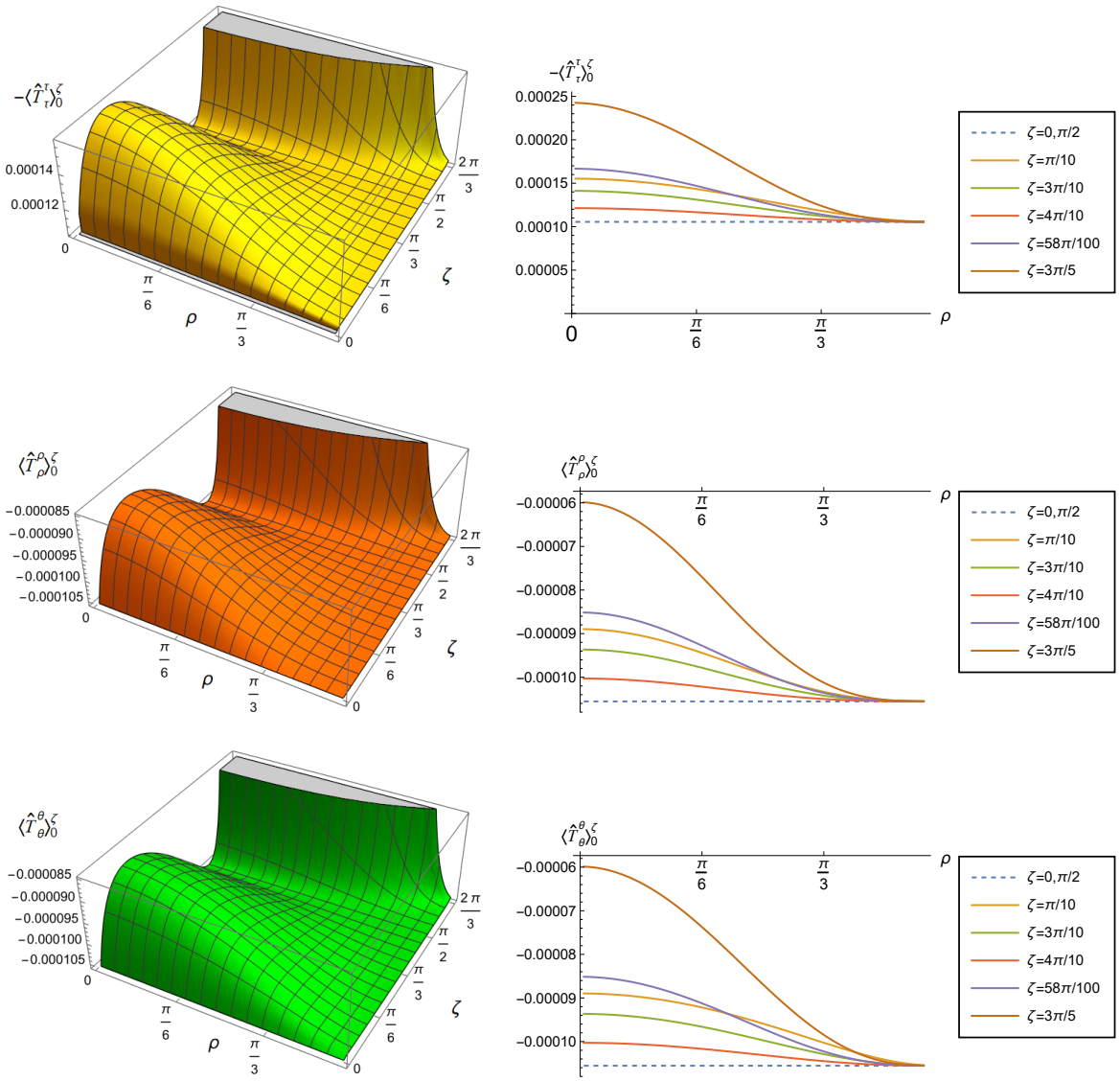

Figure 3.4: Renormalised v.e.v.s of the different components of the RSET with Robin boundary conditions. The top row shows the energy density component of the RSET, $-\langle\hat{T}^{\tau}_{\tau}\rangle^{\zeta}_{0}$, the middle row shows the $\langle\hat{T}^{\rho}_{\rho}\rangle^{\zeta}_{0}$ component and the bottom row shows the $\langle\hat{T}^{\theta}_{\theta}\rangle^{\zeta}_{0}$ component ($\langle\hat{T}^{\phi}_{\phi}\rangle^{\zeta}_{0} = \langle\hat{T}^{\theta}_{\theta}\rangle^{\zeta}_{0}$) . On the left is the 3D surface plot showing the variation of the nonzero RSET components with ρ and ζ. On the right is shown $\langle T^{\nu}_{\mu}\rangle^{\zeta}_{0}$ as a function of ρ for a selection of values of the Robin parameter ζ. The results for Dirichlet and Neumann boundary conditions are shown with dashed lines.

Robin boundary conditions to only a subset of the modes in [12], see Section 3.6. The $\langle\hat{T}^{\rho}_{\rho}\rangle^{\zeta}_{0}$ and $\langle\hat{T}^{\theta}_{\theta}\rangle^{\zeta}_{0}$ components, plotted in Figure 3.4, attain their greatest value at the space-time origin (for $\zeta \neq 0, \pi/2$) and converge to the common Dirichlet/Neumann value as the space-time boundary is reached ($\rho \to \pi/2$). The values of all components of the RSET, at the space-time origin, increase as ζ increases from zero, attain a maximum at some value of $\zeta \in (0, \pi/2)$ and then decrease as ζ approaches $\pi/2$. As ζ increases above $\pi/2$, these quantities increase rapidly as ζ approaches $\zeta_{\text{crit}} \approx 0.68\pi$. Whilst the v.e.v.s of the $\langle\hat{T}^{\rho}_{\rho}\rangle^{\zeta}_{0}$ and $\langle\hat{T}^{\theta}_{\theta}\rangle^{\zeta}_{0}$ components of the RSET are negative, they are greater (less negative) for Robin boundary conditions than when Dirichlet/Neumann boundary conditions are applied. However, the variation in the v.e.v.s of the RSET components due to varying the boundary conditions is rather small, at roughly the percent level.

Whilst it may seem at first glance that the v.e.v.s of the $\langle\hat{T}^{\rho}_{\rho}\rangle^{\zeta}_{0}$ and $\langle\hat{T}^{\theta}_{\theta}\rangle^{\zeta}_{0}$ components are the same (see Figure 3.4), there is in fact a subtle difference. Writing the components of the SET in the Landau decomposition, analogous to that used in the thermal state [4] gives

$$\langle\hat{T}^{\nu}_{\mu}\rangle^{\zeta}_{0} = \text{Diag}\Big\{ -E^{\zeta}_{0},\, P^{\zeta}_{0} + \Pi^{\zeta}_{0}, P^{\zeta}_{0} - \frac{1}{2}\Pi^{\zeta}_{0}, P^{\zeta}_{0} - \frac{1}{2}\Pi^{\zeta}_{0}\Big\} \tag{3.55}$$

where E^{ζ}_{0} is the energy density, P^{ζ}_{0} the pressure and Π^{ζ}_{0} the shear stress or pressure deviator [4]. The pressure deviator is a measure of the difference between the RSET of the quantum scalar field compared with that seen if the field were modelled as a classical gas of photons (as it vanishes in the latter case (1.83)). As the $\langle\hat{T}^{\theta}_{\theta}\rangle^{\zeta}_{0}$ component of the RSET is greater than the $\langle\hat{T}^{\rho}_{\rho}\rangle^{\zeta}_{0}$ component, Figure 3.5 shows $-\Pi^{\zeta}_{0}$ as a function of the radial parameter ρ for the vacuum state. For both Dirichlet and Neumann boundary conditions, the vacuum pressure deviator is zero (not shown in Figure 3.5). For the other Robin boundary conditions, Π^{ζ}_{0} vanishes at both the origin and boundary of the space-time and attains its maximum absolute value between the two.

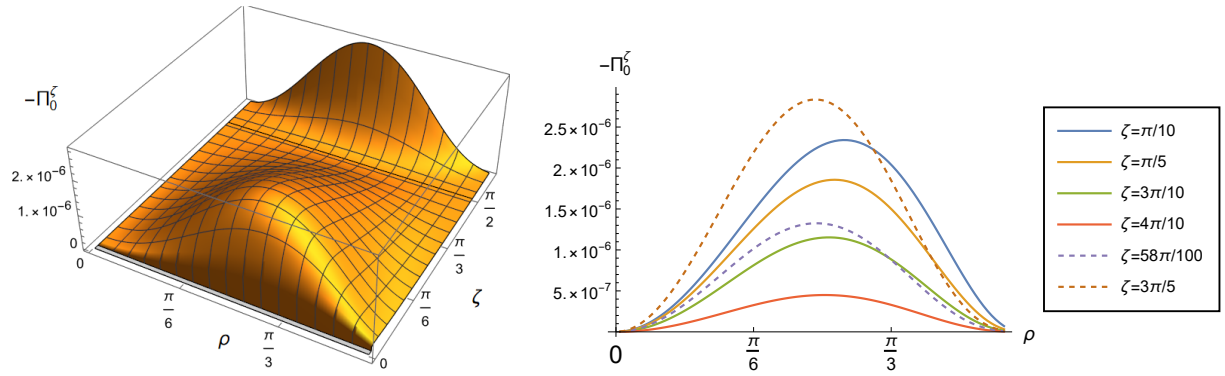

Figure 3.5: 3D surface plot of the vacuum pressure deviator $-\Pi^{\zeta}_{0}$ as a function of the radial coordinate ρ and the Robin parameter ζ (left). The (negative) pressure deviator is shown with a selection of Robin parameters (right) with $\zeta > \pi/2$ shown dotted.

§ 3.6 Comparison with Barroso and Pitelli paper [12]

As mentioned in Section 3.5, we find that the energy density component of the massless, conformally coupled scalar field, $-\langle\hat{T}^{\tau}_{\tau}\rangle^{\zeta}_{0}$, is positive throughout the space-time (see Figure 3.4). This is in contrast to the findings in [12], where the energy density is negative on most of the space-time and only becomes positive as the boundary is reached. In [12], the authors applied Robin boundary conditions to only the $\ell = 0$ modes whilst the remaining modes obeyed Dirichlet boundary conditions. In this section, as a check of our methodology, we will reproduce the results in [12] for the VP, $\langle\hat{\Phi}^2\rangle$, and the RSET using Euclidean methods. As in [12] we apply Robin boundary conditions only to the $\ell = 0$ modes whilst subjecting the remaining $\ell-$modes to Dirichlet boundary conditions. As the v.e.v.s and t.e.v.s are known for Dirichlet boundary conditions we simply consider the differences in the expectation values when we apply Robin boundary conditions to the $\ell = 0$ modes.

We start with the vacuum Euclidean Green's function (3.24), and apply boundary conditions to $q^{\zeta}_{\omega\ell}(\rho)$ given in (3.33). In [71], the $q^{\zeta}_{\omega\ell}(\rho)$ solution with Robin boundary conditions applied is expressed as a combination of the Dirichlet and Neumann boundary solutions as follows

$$q^{\zeta}_{\omega\ell}(\rho) = q^{D}_{\omega\ell}(\rho)\cos^2\zeta + q^{N}_{\omega\ell}(\rho)\sin^2\zeta + \frac{1}{\sqrt{\sin\rho}}\left(C^{\zeta}_{\omega\ell} + \cos 2\zeta\right) P^{-\ell-1/2}_{i\omega-1/2}(\cos\rho), \tag{3.56}$$

where $C^{\zeta}_{\omega\ell}$ is given by (3.34). The extra contribution $\delta q^{\zeta}_{\omega 0}$, obtained by applying the Robin boundary condition to the $\ell = 0$ mode only, is given by

$$\delta q^{\zeta}_{\omega 0} = q^{\zeta}_{\omega 0} - q^{D}_{\omega 0} = \sin^2\zeta\,(q^{N}_{\omega 0} - q^{D}_{\omega 0}) + \frac{1}{\sqrt{\sin\rho}}\left(C^{\zeta}_{\omega 0} + \cos 2\zeta\right) P^{-1/2}_{i\omega-1/2}(\cos\rho). \tag{3.57}$$

From (3.36) we have

$$q^{N}_{\omega 0} - q^{D}_{\omega 0} = \frac{2}{\sqrt{\sin\rho}} P^{-1/2}_{i\omega-1/2}(\cos\rho), \tag{3.58}$$

giving

$$\begin{aligned}\delta q^{\zeta}_{\omega 0} &= \frac{2\sin^2\zeta}{\sqrt{\sin\rho}}\, P^{-1/2}_{i\omega-1/2}(\cos\rho) + \frac{1}{\sqrt{\sin\rho}}\left[C^{\zeta}_{\omega 0} + \cos 2\zeta\right] P^{-1/2}_{i\omega-1/2}(\cos\rho) \\ &= \frac{1}{\sqrt{\sin\rho}}\left[C^{\zeta}_{\omega 0} + 1\right] P^{-1/2}_{i\omega-1/2}(\cos\rho).\end{aligned} \tag{3.59}$$

From (3.27) we can write

$$\delta g_{\omega 0}(\rho,\rho') = \frac{p_{\omega 0}(\rho_<)\,\delta q_{\omega 0}(\rho_>)}{N^{E}_{\omega 0}} = \frac{|\Gamma(1+i\omega)|^2 p_{\omega 0}\,\delta q_{\omega 0}}{2}, \tag{3.60}$$

where $\delta g_{\omega 0}(\rho,\rho')$ is the extra contribution to the radial component of the Green's function obtained by applying Robin boundary conditions to only the $\ell = 0$ modes. The normalisation constant $N^{E}_{\omega 0}$ is given in (3.30) with $\ell = 0$. The Robin contribution to the vacuum Green's function, $\delta G^{\zeta}_{0}(x,x')$, is

$$\delta G_0^{\zeta}(x,x') = \frac{\cos\rho\cos\rho'}{16\pi^2 L^2}\int_{-\infty}^{\infty} d\omega\, e^{i\omega\Delta\tau} P_0(\cos\gamma)|\Gamma(1+i\omega)|^2 \frac{1}{\sqrt{\sin\rho\,\sin\rho'}}\left[C_{\omega 0}^{\zeta}+1\right] \times P_{i\omega-1/2}^{-1/2}(\cos\rho)P_{i\omega-1/2}^{-1/2}(\cos\rho'). \quad (3.61)$$

Taking the coincidence limit we have

$$\delta\langle\hat{\Phi}^2\rangle_0^{\zeta} = \frac{\cos^2\rho}{16\pi^2 L^2\sin\rho}\int_{-\infty}^{\infty} d\omega\,|\Gamma(1+i\omega)|^2\left[C_{\omega 0}^{\zeta}+1\right]\left[P_{i\omega-1/2}^{-1/2}(\cos\rho)\right]^2, \quad (3.62)$$

where $\delta\langle\hat{\Phi}^2\rangle_0^{\zeta}$ is the extra contribution to the vacuum polarisation, $\langle\hat{\Phi}^2\rangle_0^{\zeta}$, arising from applying Robin boundary conditions to only the $\ell = 0$ modes, as in [12]. The corresponding term for the v.e.v. of the energy density component of the RSET is

$$\delta\langle\hat{T}_{\tau}^{\tau}\rangle_0^{\zeta} = \frac{\cos\rho\cot^3\rho}{192L^4\pi^2}\int_{\omega=-\infty}^{\infty} d\omega\, D_{\omega 0}^{\zeta}\Big\{ -2\,(1+\omega^2)^2\,[P_{i\omega-1/2}^{-3/2}(\cos\rho)]^2\,\sin^2\rho - \left[2(1-5\omega^2)\sin^2\rho\right][P_{i\omega-1/2}^{-1/2}(\cos\rho)]^2\Big\}, \quad (3.63)$$

where $D_{\omega 0}$ is given by (3.42) with $\ell = 0$.

The quantity $\delta\langle\hat{\Phi}^2\rangle_0^{\zeta}$ has been computed numerically using MATHEMATICA with the integral over ω performed in the interval $|\omega| \leq 100$. Figure 3.6 shows $\delta\langle\hat{\Phi}^2\rangle_0^{\zeta}$ plotted as a function of ρ for a range of Robin parameters, ζ. Using only the $\ell = 0$ modes means we avoid the issue of nonuniform convergence of the $\ell-$sum (Section 3.4), allowing the computations to be readily performed. It is difficult to make direct comparisons between Figure 3.6 and the corresponding figure in [12] as there is a different definition of the Robin parameter in [12] to that used in this thesis (3.32) with no one-to-one correspondence between the two definitions. Qualitatively the two plots are similar. Both profiles are positive throughout the space-time, have very similar shapes and are monotonically decreasing as the space-time boundary is approached. In particular, the profile for the Neumann boundary condition in Figure 3.6 is qualitatively similar to the equivalent one in [12] with the value at the space-time origin seemingly a match in the two plots as far as can be ascertained.

Using (3.63), the extra contribution to the RSET, $\delta\langle\hat{T}_{\tau}^{\tau}\rangle_0^{\zeta}$, when Robin boundary conditions are applied to only the $\ell = 0$ modes, has been computed numerically using MATHEMATICA. The $\omega-$integration in (3.63) was performed to $|\omega| \leq 100$. The results are shown in Figure 3.7 for a range of the Robin parameters ζ. Comparing the Neumann results between Figure 3.7 and the corresponding plot in [12] shows comparable profiles, whilst the remaining plots are qualitatively similar, as in the case of $\delta\langle\hat{\Phi}^2\rangle_0^{\zeta}$. We conclude, therefore, that using Euclidean methods to compute the VP and RSET gives the same result as remaining in Lorentzian space-time.

§ 3.7 Thermal expectation value of the SET with Robin boundary conditions

The t.e.v.s of the nonzero components of the RSET with various values of κ (3.23) are shown in Figures 3.8–3.10 (as in the vacuum state, the $\langle\hat{T}_{\phi}^{\phi}\rangle_{\beta}^{\zeta}$ component has the same values as the $\langle\hat{T}_{\theta}^{\theta}\rangle_{\beta}^{\zeta}$

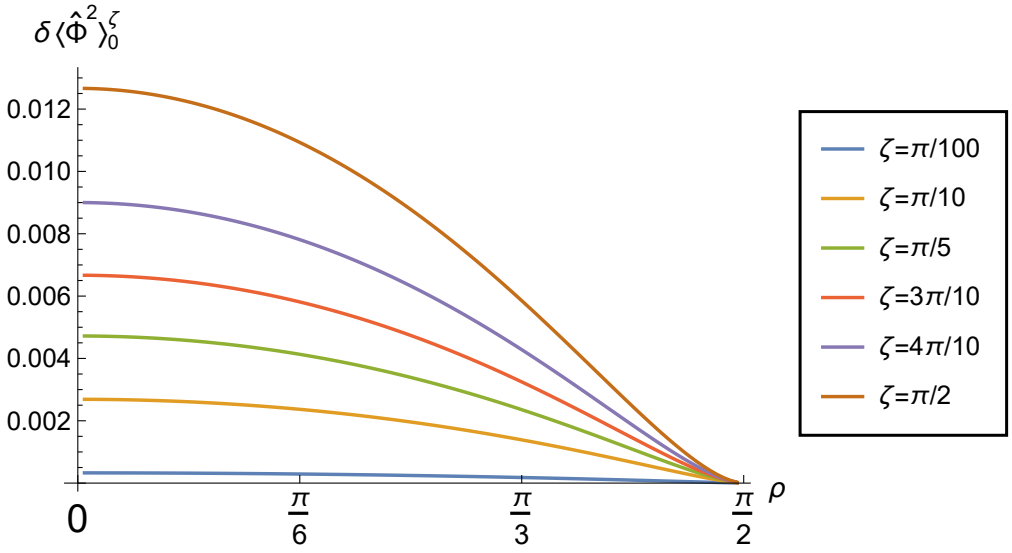

Figure 3.6: The extra contribution to the v.e.v of the VP, $\delta\langle\hat{\Phi}^2\rangle_0^\zeta$, with a range of Robin boundary conditions applied to only the $\ell = 0$ modes. This plot is comparable to the corresponding plot in [12].

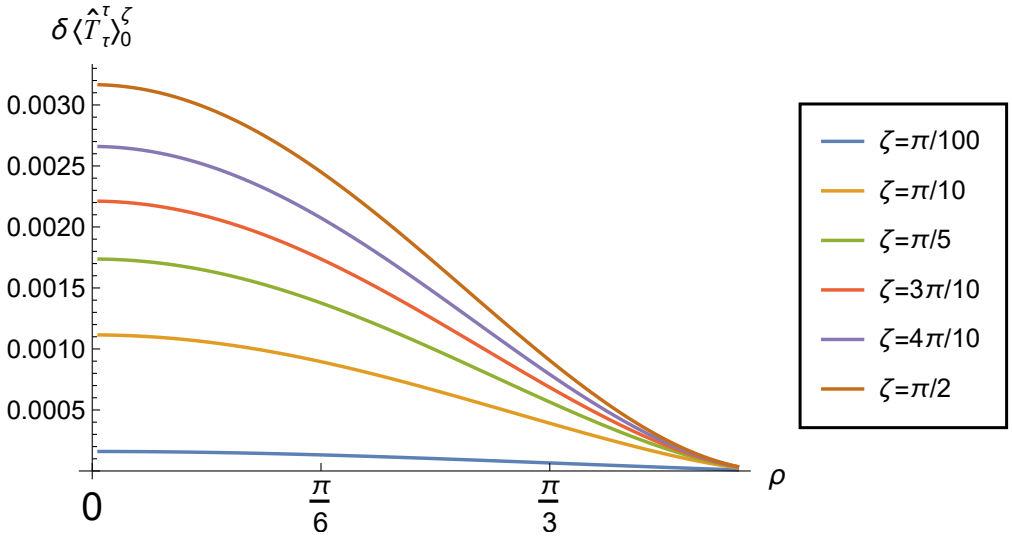

Figure 3.7: The extra contribution, $\delta\langle\hat{T}^\tau_\tau\rangle_0^\zeta$, to the v.e.v of the energy density component of the RSET, arising from applying Robin boundary conditions to only the $\ell = 0$ modes. The plot shows a range of Robin parameters ζ, with the Neumann plot ($\zeta = \pi/2$) comparable to the corresponding plot in [12].

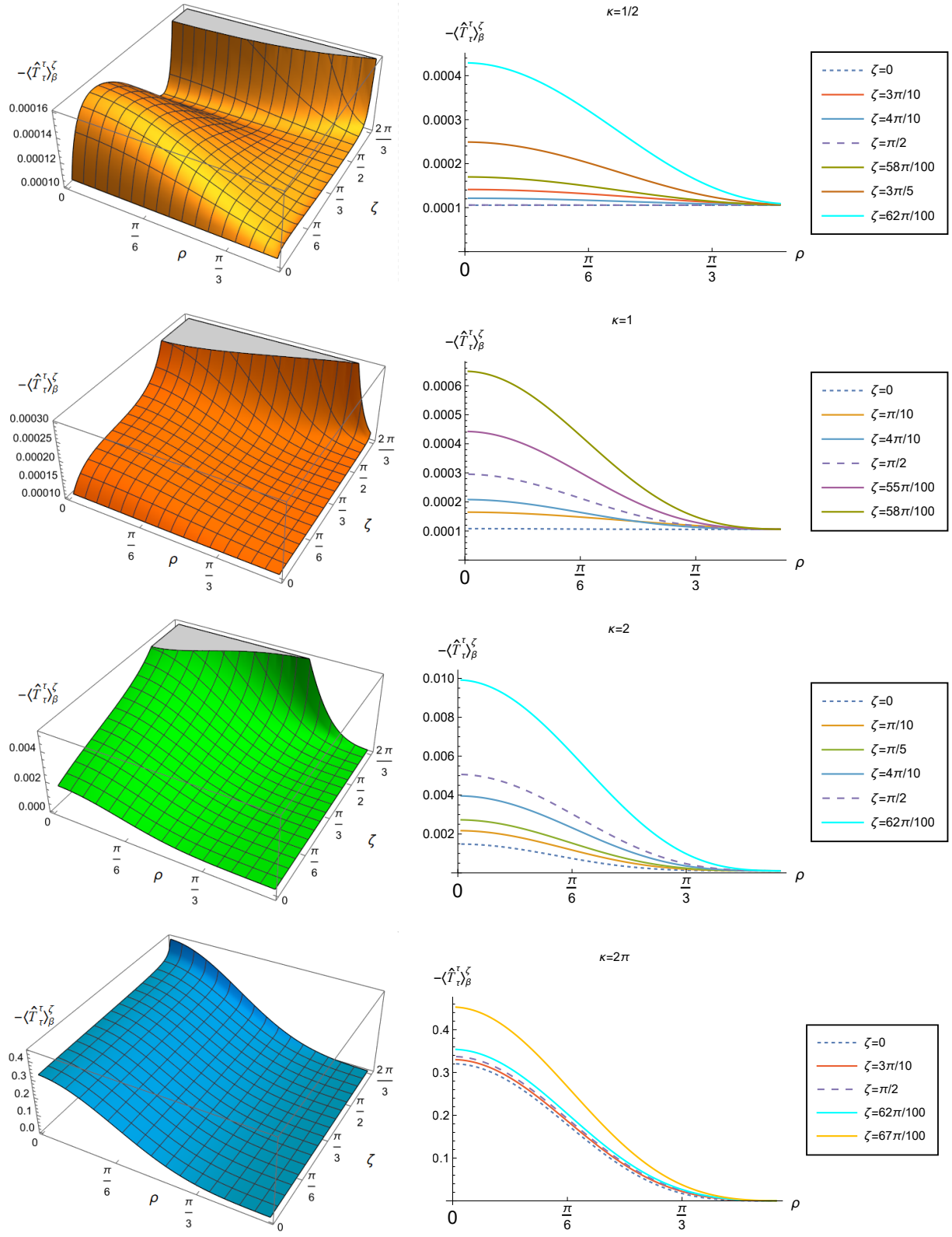

Figure 3.8: Renormalised t.e.v.s of the energy density component of the RSET, $-\langle\hat{T}_t^t\rangle_\beta^\zeta$, with Robin boundary conditions and different values of κ (3.23). On the left are the 3D surface plots showing the variation of $-\langle\hat{T}_t^t\rangle_\beta^\zeta$ with ρ and ζ. The right column shows $-\langle\hat{T}_t^t\rangle_\beta^\zeta$ as a function of ρ for a selection of values of the Robin parameter ζ. Dirichlet and Neumann boundary conditions are shown with dotted lines.

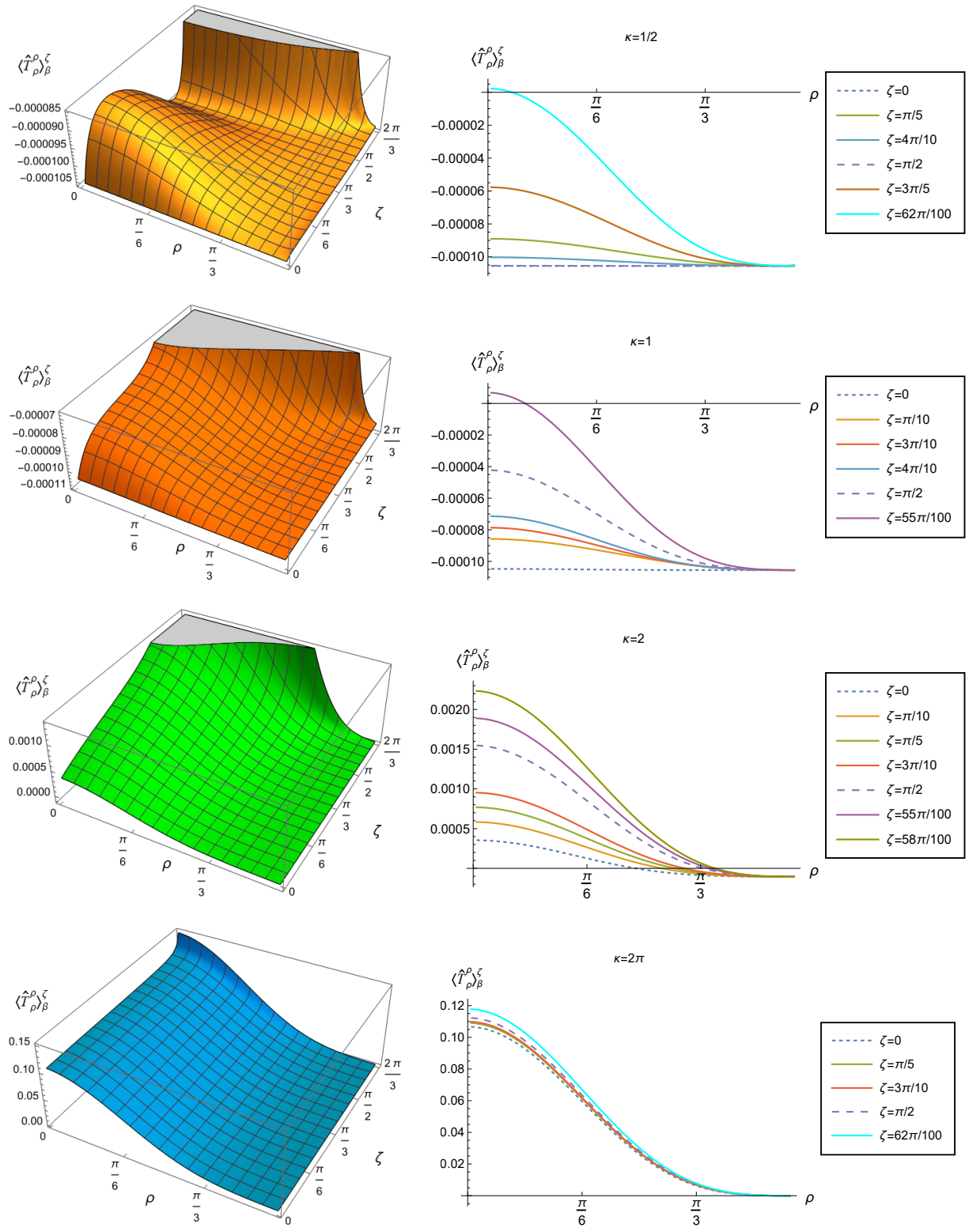

Figure 3.9: Renormalised t.e.v.s of the $\langle \hat{T}^{\rho}_{\rho} \rangle^{\zeta}_{\beta}$ component of the RSET with Robin boundary conditions and different values of κ (3.23). On the left are the 3D surface plots showing the variation of $\langle \hat{T}^{\rho}_{\rho} \rangle^{\zeta}_{\beta}$ with ρ and ζ. The right column shows $\langle \hat{T}^{\rho}_{\rho} \rangle^{\zeta}_{\beta}$ as a function of ρ for a selection of values of the Robin parameter ζ. Dirichlet and Neumann boundary conditions are shown with dotted lines.

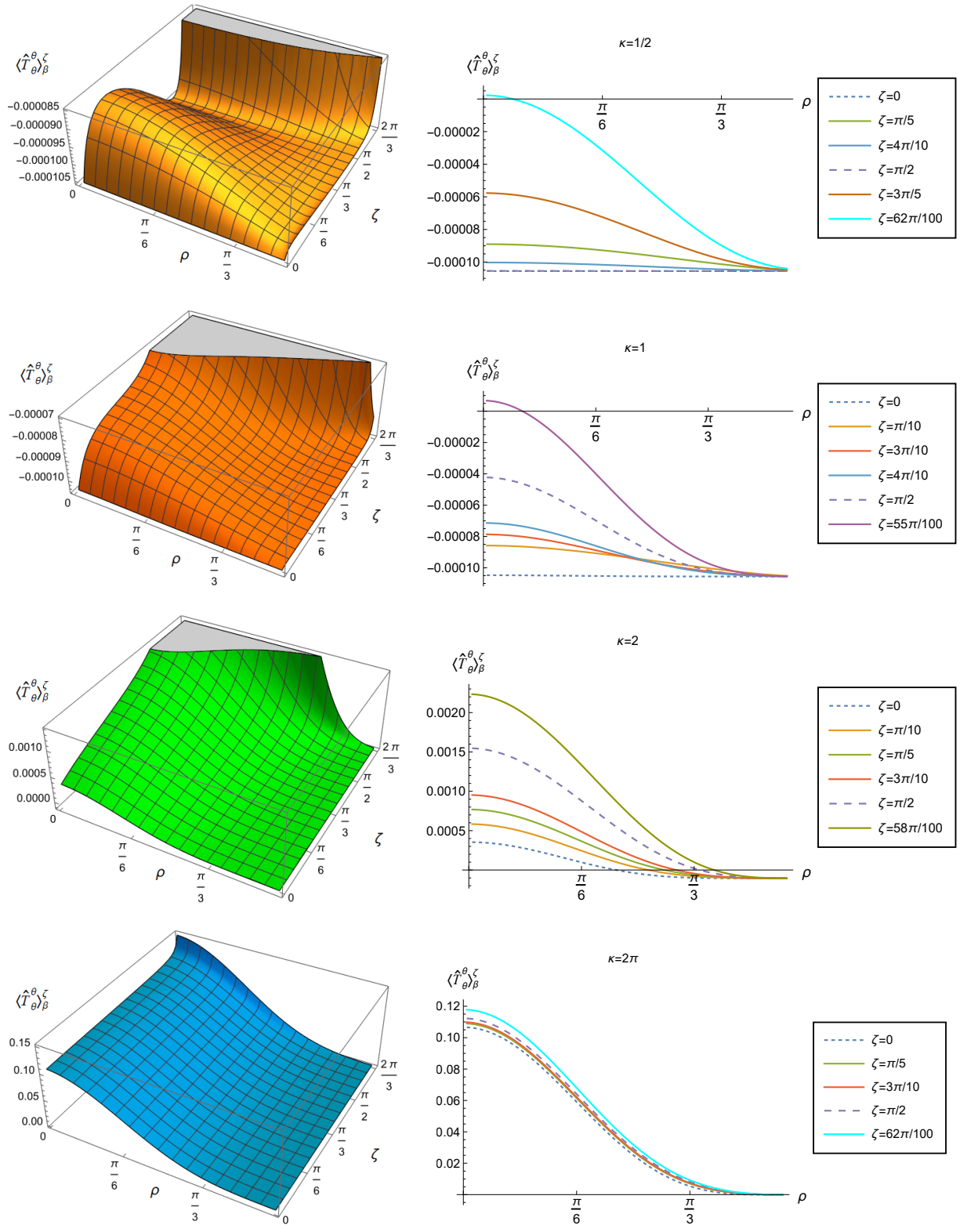

Figure 3.10: Renormalised t.e.v.s of the $\langle \hat{T}^{\theta}_{\theta} \rangle^{\zeta}_{\beta}$ component of the RSET with Robin boundary conditions and different values of κ (3.23). On the left are the 3D surface plots showing the variation of $\langle \hat{T}^{\theta}_{\theta} \rangle^{\zeta}_{\beta}$ with ρ and ζ. The right column shows $\langle \hat{T}^{\theta}_{\theta} \rangle^{\zeta}_{\beta}$ as a function of ρ for a selection of values of the Robin parameter ζ. Dirichlet and Neumann boundary conditions are shown with dotted lines.

component and is not displayed). The nonzero components have very similar qualitative behaviour. Unlike the vacuum case, the t.e.v.s with Dirichlet and Neumann boundary conditions break the underlying symmetry of the adS space-time and their values depend on the space-time location. For each nonzero component of the RSET, the difference between the t.e.v.s with Dirichlet and Neumann boundary conditions is a maximum at the space-time origin and decreases with increasing ρ, converging to their common v.e.v. as the space-time boundary is approached ($\rho \to \pi/2$). At low temperature ($\kappa = 1/2$) the t.e.v.s with Dirichlet and Neumann boundary conditions resemble their common v.e.v.s. As the temperature increases (increasing κ), we see that the absolute difference between the nonzero RSET components for the Dirichlet and Neumann boundary conditions increases.

The energy density component of the RSET, $-\langle \hat{T}^{\tau}_{\tau} \rangle^{\zeta}_{\beta}$, is positive throughout the space-time for all Robin boundary conditions. It achieves its maximum value at the space-time origin and increases with increasing temperature (increasing κ). For all Robin parameters studied, the energy density converges to the common vacuum Dirichlet/Neumann value as the space-time boundary is approached. The other nonzero components of the RSET have similar qualitative behaviour (Figures 3.9 and 3.10). As with the energy density component, the $\langle \hat{T}^{\rho}_{\rho} \rangle^{\zeta}_{\beta}$ and $\langle \hat{T}^{\theta}_{\theta} \rangle^{\zeta}_{\beta}$ components have their maximum at the space-time origin and monotonically decrease as the space-time boundary is approached. The t.e.v.s are mostly negative at low temperature and increase with increasing temperature. For large κ, the t.e.v.s are mostly positive in a neighbourhood of the origin for all Robin parameters studied. For $\kappa = 2\pi$, the t.e.v.s are positive for most of the space-time.

It can be seen that at low temperature ($\kappa = 1/2$), some of the curves for t.e.v.s with Robin boundary conditions lie outside of the curves corresponding to Dirichlet/Neumann boundary conditions. With increasing temperature, the curves for t.e.v.s with Robin boundary conditions increasingly lie within those for Dirichlet/Neumann boundary conditions and are mostly contained within them for $\kappa = 2\pi$. As the temperature increases, the variation in the nonzero components of the RSET with varying Robin parameter ζ becomes much less apparent, as seen in Figures 3.8–3.10. It seems that the effect of the Robin boundary conditions is 'washed out' with increasing temperature.

In Figure 3.11 we plot minus the thermal pressure deviator ($-\Pi^{\zeta}_{\beta}$), which is the difference between the $\langle \hat{T}^{\rho}_{\rho} \rangle^{\zeta}_{\beta}$ and $\langle \hat{T}^{\theta}_{\theta} \rangle^{\zeta}_{\beta}$ components of the t.e.v. of the RSET. With Dirichlet and Neumann boundary conditions we see that the pressure deviator is no longer zero throughout space-time as in the vacuum case (Section 3.5). For these boundary conditions, the pressure deviator is zero at the space-time origin and boundary but attains a maximum magnitude between these, with the maximum magnitude increasing with increasing temperature. We also see from Figure 3.11 that $-\Pi^{\zeta}_{\beta}$ is negative for Dirichlet and positive for Neumann boundary conditions respectively.

For Robin boundary conditions, we see a similar profile for the pressure deviators as with Dirichlet and Neumann boundary conditions. The pressure deviators vanish at the origin and space-time boundary and have a maximum magnitude at some $\rho \in (0, \pi/2)$. At the higher temperatures, the pressure deviator (Π^{ζ}_{β}) is most positive with the Dirichlet boundary condition ($\zeta = 0$) but with increasing Robin parameter, ζ, the pressure deviator becomes increasingly negative. We also notice that as the temperature increases, the thermal pressure deviators, with different Robin boundary conditions, are increasingly 'contained' within the Dirichlet and Neumann curves, as was seen with

the RSET components.

§ 3.8 The RSET at the boundary

In Sections 3.5 and 3.7 we saw that the v.e.v.s and t.e.v.s of the RSET with Robin boundary conditions converged to the Neumann/Dirichlet result at the space-time boundary. In this section we provide an analytical argument to support this finding.

We use the corresponding analysis in [71] for the VP. As the time-like boundary in adS is not part of the space-time and we are considering a massless, conformally coupled scalar field, we can make a conformal transformation to the ESU (see Section 2.1). We then consider a region in ESU for $\rho \in [0, \pi/2]$ and apply Robin boundary conditions to the surface at $\rho = \pi/2$, which is now part of the space-time. Consider a region $V \subset$ ESU for $\rho \in [0, \pi/2]$ which is bounded by a surface S comprised of $\mathcal{I}_0$, $\mathcal{I}_{\pi/2}$, which are time-like hypersurfaces at $\rho = 0$, $\rho = \pi/2$ respectively as well as Σ_1, Σ_2 which are space-like hypersurfaces (see Figure 3.12). We now apply Stokes' theorem to the vacuum Euclidean Green's functions in ESU, $G^{ESU}_{N,0}(x, x')$, $G^{ESU}_{\zeta,0}(x, x')$ in the region V bounded by S to give

$$\begin{aligned}\int_S \Big[G^{ESU}_{N,0}(x,y)\widetilde{\nabla}_\mu G^{ESU}_{\zeta,0}(y,x') - G^{ESU}_{\zeta,0}(x,y)\widetilde{\nabla}_\mu G^{ESU}_{N,0}(y,x')\Big] dS^\mu \\ = \int_V \Big[G^{ESU}_{N,0}(x,y)\ \widetilde{\Box}\ G^{ESU}_{\zeta,0}(y,x') - G^{ESU}_{\zeta,0}(x,y)\ \widetilde{\Box}\ G^{ESU}_{N,0}(y,x')\Big] dV\end{aligned} \tag{3.64}$$

where $\widetilde{\nabla}$ and $\widetilde{\Box}$ are the covariant derivatives and D'Alembertian operator with respect to the Euclidean ESU metric

$$ds^2 = L^2\left(d\tau^2 + d\rho^2 + \sin^2\rho\,[d\theta^2 + \sin^2\theta\, d\phi^2]\right), \tag{3.65}$$

and all integrals in (3.64) are taken with respect to y. The Euclidean Green's functions on ESU, $G^{ESU}_{\zeta,0}(x, x')$ satisfy (1.54)

$$\left(\widetilde{\Box} - \frac{1}{6}\widetilde{R}\right) G^{ESU}_{\zeta,0}(x,x') = \left(\widetilde{\Box} - \frac{1}{L^2}\right) G^{ESU}_{\zeta,0}(x,x') = -\frac{1}{\sqrt{\tilde{g}}}\delta^4(x,x') \tag{3.66}$$

where the tilde denotes the quantities on the ESU metric and $\delta^4(x, x')$ is the four-dimensional Dirac delta function. Using (3.66), the right hand side of (3.64) becomes

$$\int_V \Big[G^{ESU}_{N,0}(x,y)\ \widetilde{\Box}\ G^{ESU}_{\zeta,0}(y,x') - G^{ESU}_{\zeta,0}(x,y)\ \widetilde{\Box}\ G^{ESU}_{N,0}(y,x')\Big] dV = G^{ESU}_{\zeta,0}(x,x') - G^{ESU}_{N,0}(x,x'). \tag{3.67}$$

It now remains to compute the surface integrals on the boundary $S = \mathcal{I}_0 \cup \mathcal{I}_{\pi/2} \cup \Sigma_1 \cup \Sigma_2$ in the left hand side of (3.64). The part of the radial component of the Green's function on ESU (3.27), which is regular on $\mathcal{I}_0\,(\rho \to 0)$, is given by (3.31), and can be written as [39, §14.8.1]

$$p_{\omega\ell}(\rho) \sim \frac{(\sin\rho)^{-1/2}}{\Gamma(\ell + 3/2)}\left(\frac{2}{1-\cos\rho}\right)^{-1/2(\ell+1/2)}. \tag{3.68}$$

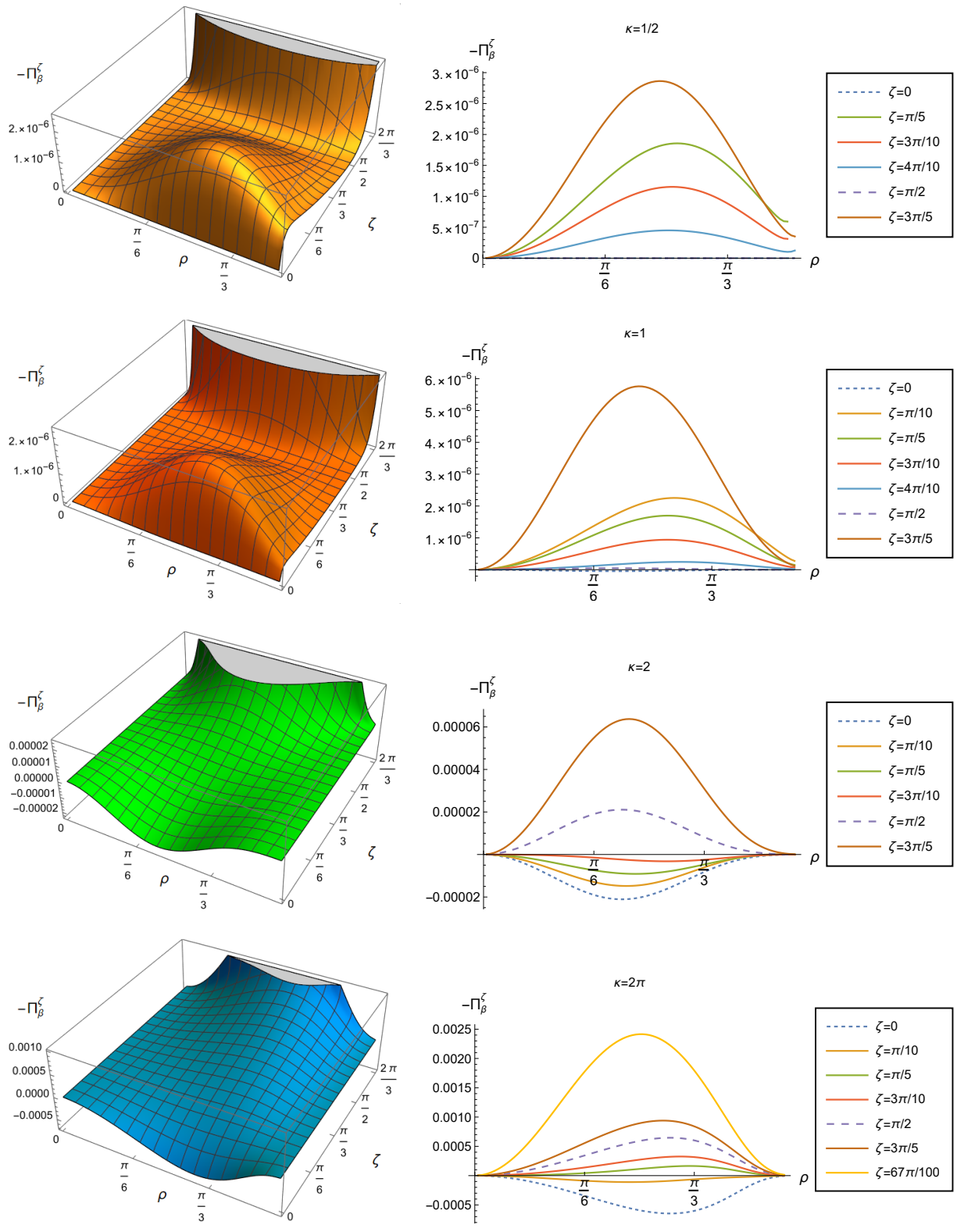

Figure 3.11: Thermal pressure deviators $-\Pi_\beta^\zeta$ (3.55) with Robin boundary conditions and a selection of values of κ (3.23). On the left are 3D surface plots showing the variation of $-\Pi_\beta^\zeta$ with ρ and ζ. On the right is $-\Pi_\beta^\zeta$ as a function of ρ for a selection of values of the Robin parameter ζ. Dirichlet and Neumann boundary conditions are shown with dotted lines.

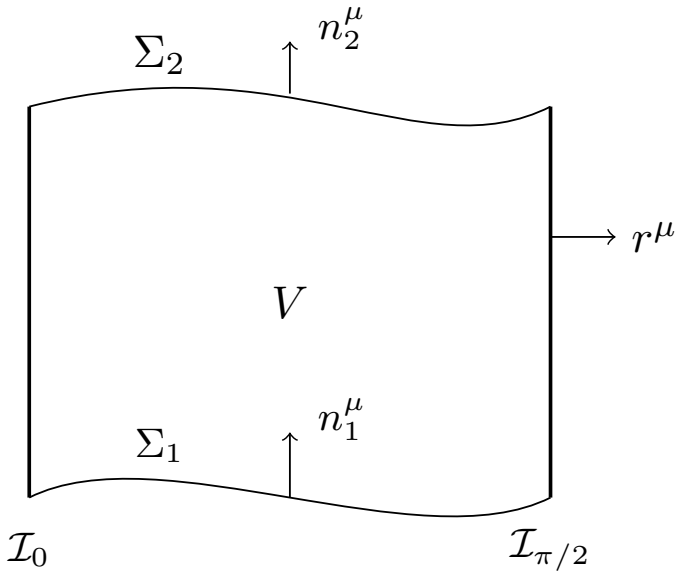

Figure 3.12: Schematic showing the application of Stokes' theorem. The volume V is bounded by the surface $S = \mathcal{I}_0 \cup \Sigma_1 \cup \Sigma_2 \cup \mathcal{I}_{\pi/2}$. The surfaces Σ_1 and Σ_2 are space-like hypersurfaces with unit future-pointing normals n_1^μ and n_2^μ respectively, whilst r^μ is the unit normal to the surface $\mathcal{I}_{\pi/2}$ (adapted from [71]).

Using the Taylor expansion of (3.68), we have

$$p_{\omega\ell}(\rho) \sim \frac{\rho^\ell}{2^{(\ell/2+1/4)}} + \mathcal{O}(\rho^{2\ell+1/2}), \tag{3.69}$$

from which it is clear that only the $\ell = 0$ mode will contribute and, as it is a constant, its derivative vanishes at $\mathcal{I}_0$. Also it can be shown that the contributions to the surface integrals at Σ_1 and Σ_2 cancel each other out so we are left with the surface integral over $\mathcal{I}_{\pi/2}$. The vacuum Euclidean Green's functions at $\mathcal{I}_{\pi/2}$ satisfy the boundary conditions

$$G^{ESU}_{\zeta,0}(x,x')\cos\zeta + \frac{\partial\, G^{ESU}_{\zeta,0}(x,x')}{\partial\rho}\sin\zeta = 0, \tag{3.70}$$

whilst the normal derivative to the boundary is $\mathcal{I}_{\pi/2}$ is $L^{-1}\partial/\partial\rho$. Using (3.70), the left hand side of (3.64) becomes

$$\int_S \Big[G^{ESU}_{N,0}(x,y)\widetilde{\nabla}_\mu G^{ESU}_{\zeta,0}(y,x') - G^{ESU}_{\zeta,0}(x,y)\widetilde{\nabla}_\mu G^{ESU}_{N,0}(y,x')\Big]dS^\mu = \\ -\frac{1}{L}\cot\zeta\int_{\mathcal{I}_{\pi/2}} G^{ESU}_{N,0}(x,y)\, G^{ESU}_{\zeta,0}(y,x')dS. \tag{3.71}$$

Using (3.67, 3.71) we arrive at

$$G^{ESU}_{\zeta,0}(x,x') - G^{ESU}_{N,0}(x,x') = -\frac{1}{L}\cot\zeta\int_{\mathcal{I}_{\pi/2}} G^{ESU}_{N,0}(x,y)\, G^{ESU}_{\zeta,0}(y,x')\, dS. \tag{3.72}$$

This is applicable for all Robin parameters except Dirichlet ($\zeta = 0$). We can now use an iterative procedure on (3.72), given in [36], whereby the Green's function for the scalar field on ESU with Robin boundary conditions applied can be written as an asymptotic series in terms of the Green's function on ESU with Neumann boundary conditions applied. This procedure gives the following asymptotic series for the vacuum Euclidean Green's function on ESU, $G^{ESU}_{\zeta,0}$, with Robin boundary conditions applied:

$$G^{ESU}_{\zeta,0}(x,x') = G^{ESU}_{N,0}(x,x') - \frac{1}{L}G^{(1)}_{\zeta,0}(x,x')\cot\zeta + \frac{1}{L^2}G^{(2)}_{\zeta,0}(x,x')\cot^2\zeta + \dots \tag{3.73}$$

where the first two terms in the series are given by

$$G^{(1)}_{\zeta,0}(x,x') = \int_{\mathcal{I}_{\pi/2}} G^{ESU}_{N,0}(x,y)G^{ESU}_{N,0}(y,x')\,dS, \tag{3.74}$$

$$G^{(2)}_{\zeta,0}(x,x') = \int_{\mathcal{I}_{\pi/2}} G^{ESU}_{N,0}(x,y)\left[\int_{\mathcal{I}_{\pi/2}} G^{ESU}_{N,0}(y,z)G^{ESU}_{N,0}(z,x')\,dS\right]\,dS. \tag{3.75}$$

Here the integrals are performed over the space-times points y, z on the surface $\mathcal{I}_{\pi/2}$ in ESU. Higher-order terms in the series can be found iteratively [36].

The Green's function on ESU with Neumann boundary conditions applied has a compact closed-form expression [71]

$$G^{ESU}_{N,0}(x,x') = \frac{1}{8\pi^2L^2}\left\{\frac{1}{\cosh\Delta\tau + \cos\Psi} + \frac{1}{\cosh\Delta\tau + \cos\Psi^*},\right\} \tag{3.76}$$

where $\Delta\tau = \tau - \tau'$ is the separation of the points in the τ-direction,

$$\begin{aligned}\Psi &= \arccos\left[-\cos\rho\cos\rho' - \cos\gamma\sin\rho\sin\rho'\right],\\ \Psi^* &= \pi + \arccos\left[-\cos\rho\cos\rho' + \cos\gamma\sin\rho\sin\rho'\right]\end{aligned} \tag{3.77}$$

and γ is the angular separation of the points (2.23). Applying the differential operator $\mathcal{T}_{\mu\nu}(x,x')$ (3.44) to the Green's function (3.73) and bringing the space-time points together gives

$$\begin{aligned}\langle\hat{T}_{\mu\nu}\rangle^{ESU}_{\zeta,0} = \langle\hat{T}_{\mu\nu}\rangle^{ESU}_{N,0} &- \frac{\cot\zeta}{L}\lim_{x'\to x}\left\{\mathcal{T}_{\mu\nu}(x,x')\left[G^{(1)}_{\zeta,0}(x,x')\right]\right\}\\ &+ \frac{\cot^2\zeta}{L^2}\lim_{x'\to x}\left\{\mathcal{T}_{\mu\nu}(x,x')\left[G^{(2)}_{\zeta,0}(x,x')\right]\right\} + \dots\end{aligned} \tag{3.78}$$

As we are considering a conformally invariant scalar field in four dimensions, we can relate the RSET on ESU to that on adS using [17]

$$\langle\hat{T}^{\nu}_{\mu}\rangle^{adS}_{\zeta,0} = \langle\hat{T}^{\nu}_{\mu}\rangle^{ESU}_{\zeta,0}\frac{\sqrt{\tilde{g}}}{\sqrt{g}} - \frac{1}{2880\pi^2}\left[\frac{1}{6}\,{}^{(1)}H^{\nu}_{\mu} - {}^{(3)}H^{\nu}_{\mu}\right], \tag{3.79}$$

where $\tilde{g}$ and g are the determinants of the metrics on ESU and adS respectively. The tensors ${}^{(1)}H_{\mu\nu}$ and ${}^{(3)}H_{\mu\nu}$ are given by

$${}^{(1)}H_{\mu\nu} = 2R_{;\mu\nu} - 2g_{\mu\nu}\Box R - \frac{1}{2}g_{\mu\nu}R^2 + 2RR_{\mu\nu}, \tag{3.80}$$

$$ {}^{(3)}H_{\mu\nu} = R^{\rho}_{\mu} R_{\rho\nu} - \frac{2}{3} R R_{\mu\nu} - \frac{1}{2} R_{\rho\sigma} R^{\rho\sigma} g_{\mu\nu} + \frac{1}{4} R^2 g_{\mu\nu}. \tag{3.81} $$

Using (2.19, 2.20), it can be seen that on adS space-time ${}^{(1)}H_{\mu\nu}$ vanishes identically because R is a constant. We also note that ${}^{(3)}H_{\mu\nu} = 3g_{\mu\nu}/L^2$. Using (3.78, 3.79) and noting that $\sqrt{\widetilde{g}}\,/\sqrt{g} = \cos^4\rho$, we can write

$$ \langle \hat{T}^{\nu}_{\mu} \rangle^{adS}_{\zeta,0} = \langle \hat{T}^{\nu}_{\mu} \rangle^{adS}_{\mathrm{N},0} - \frac{\cot\zeta}{L} \lim_{x'\to x} \left\{ \mathcal{T}_{\mu\nu}(x,x') \left[G^{(1)}_{\zeta,0}(x,x') \right] \right\} \cos^4\rho \\ + \frac{\cot^2\zeta}{L^2} \lim_{x'\to x} \left\{ \mathcal{T}_{\mu\nu}(x,x') \left[G^{(2)}_{\zeta,0}(x,x') \right] \right\} \cos^4\rho + \ldots \tag{3.82} $$

Using the analysis in [36], the RSET on ESU (3.78) can be expressed as an asymptotic series at an arbitrarily small distance, ϵ, from the boundary at $\rho = \pi/2$. In flat space-time the asymptotic series is

$$ \langle \hat{T}_{\mu\nu} \rangle^{ESU}_{\zeta,0} \sim \epsilon^{-4} T^{(4)}_{\mu\nu} + \epsilon^{-3} T^{(3)}_{\mu\nu} + \epsilon^{-2} T^{(2)}_{\mu\nu} + O(\epsilon^{-1}). \tag{3.83} $$

In a curved space-time, the $T^{(i)}_{\mu\nu}$ components also depend on the curvature of the space-time but we can still express $\langle \hat{T}_{\mu\nu} \rangle^{ESU}_{\zeta,0}$ as an asymptotic expansion at an arbitrarily small distance, ϵ, from the boundary as [36]

$$ \langle \hat{T}_{\mu\nu} \rangle^{ESU}_{\zeta,0} \sim g^{\alpha'}_{\mu} g^{\beta'}_{\nu} \left(\epsilon^{-4} T^{(4)}_{\alpha'\beta'} + \epsilon^{-3} T^{(3)}_{\alpha'\beta'} + \epsilon^{-2} T^{(2)}_{\alpha'\beta'} \right) + O(\epsilon^{-1}). \tag{3.84} $$

The leading order term in (3.84) is $\epsilon^{-4} g^{\alpha'}_{\mu} g^{\beta'}_{\nu} T^{(4)}_{\alpha'\beta'}$ and when this is substituted into (3.79), together with the contribution from ${}^{(3)}H_{\mu\nu}$, we obtain $\langle \hat{T}_{\mu\nu} \rangle^{adS}_{N,0}$ in (3.82). The next-to-leading order quantity in (3.84), $\epsilon^{-3} g^{\alpha'}_{\mu} g^{\beta'}_{\nu} T^{(3)}_{\alpha'\beta'}$, corresponds to the second term in the expansion (3.82), and the quantity $\epsilon^{-2} g^{\alpha'}_{\mu} g^{\beta'}_{\nu} T^{(2)}_{\alpha'\beta'}$ to the third term in (3.82). The term $T^{(3)}_{\mu\nu}$ is given by [36]

$$ T^{(3)}_{\mu\nu} = \mathscr{A} \left(3\Upsilon_{\mu\nu} - \Upsilon h_{\mu\nu} \right), \tag{3.85} $$

where $\mathscr{A}$ is a constant, $h_{\mu\nu}$ is the boundary metric on ESU, which is given by

$$ h_{\mu\nu} = \begin{pmatrix} -L^2 & 0 & 0 & 0 \\ 0 & 0 & 0 & 0 \\ 0 & 0 & L^2 \sin^2\rho & 0 \\ 0 & 0 & 0 & L^2 \sin^2\rho \sin^2\theta \end{pmatrix}, \tag{3.86} $$

and $\Upsilon_{\mu\nu} = n_{\mu;\alpha}\, h^{\alpha}_{\nu}$, with n^{μ} a unit vector normal to the boundary which is normalised to have unit length $n_{\mu} n^{\mu} = 1$.

Using (3.86) it can be shown that the only nonzero Christoffel components of the boundary metric (3.86) are

$$ \Gamma^{\rho}_{\theta\theta} = -\sin\rho\cos\rho \quad \text{and} \quad \Gamma^{\rho}_{\phi\phi} = -\sin^2\theta \sin\rho\cos\rho, \tag{3.87} $$

giving the non-zero components of $\Upsilon_{\mu\nu}$ as

$$ \Upsilon_{\theta\theta} = L\cos\rho\sin\rho \quad \text{and} \quad \Upsilon_{\phi\phi} = L\cos\rho\sin\rho\sin^2\theta \tag{3.88} $$

and $\Upsilon = 2\cot\rho/L$. Therefore, as we approach the boundary ($\rho \to \pi/2$), $\Upsilon_{\mu\nu} = 0 = \Upsilon$, giving $T^{(3)}_{\mu\nu} = 0$. Therefore the second term in (3.84) is zero and subsequent terms in the expansion are of lower order in ϵ, showing that as we approach the boundary, $\langle\hat{T}^{\nu}_{\mu}\rangle^{adS}_{\zeta,0} = \langle\hat{T}^{\nu}_{\mu}\rangle^{adS}_{N,0}$ as seen numerically in Section 3.5. This analysis can be extended trivially to the t.e.v.s.

§ 3.9 Conclusions

In this chapter we have determined the renormalised v.e.v.s and t.e.v.s of the nonzero components of the stress energy tensor for a massless, conformally coupled scalar field propagating on a background global adS4 space-time. We have used Euclidean methods (Section 1.4), which give a unique Green's function and we find that the numerical calculations are tractable. As a result, we were able to apply Robin boundary conditions to all the field modes. As a check of our methods, we were able to reproduce the results in [12] where the authors remained in Lorentzian space-time and applied Robin boundary conditions to only the $\ell = 0$ modes.

When Dirichlet and Neumann boundary conditions are applied, we find that the v.e.v.s of the RSET, with mixed indices, respect the underlying maximal symmetry of the adS space-time and are constant. As we are considering a massless, conformally coupled field, this constant is fixed by the trace anomaly (3.20) and as a result it is the same for both Dirichlet and Neumann boundary conditions. This finding of a common value for the v.e.v. of the RSET with both Dirichlet and Neumann boundary conditions differs from that seen with the vacuum polarisation, where we find different results of the v.e.v.s for Dirichlet and Neumann boundary conditions in adS4 [71] and also in adS3 (see chapter 5). The maximal symmetry seen with either Dirichlet or Neumann boundary conditions is broken when Robin boundary conditions are applied, with the v.e.v.s depending on the space-time location. However, for all Robin boundary conditions, the v.e.v.s of the nonzero components of the RSET converge to the common v.e.v. for Dirichlet and Neumann boundary conditions as the space-time boundary is approached.

This symmetry breaking is also seen with the t.e.v.s, even for Dirichlet and Neumann boundary conditions. For the thermal states, the boundary conditions have a significant effect on the expectation values of all components of the RSET, most apparent near the origin, but this effect is diluted with increasing temperature (Figures 3.8–3.10). When computing the t.e.v.s, we used values of κ (3.23) between $1/2$ and 2π. These values are based on setting the radius of curvature of adS, L, to unity and are thus in units of L.

The t.e.v.s with either Dirichlet or Neumann boundary conditions are no longer constant and depend on the spatial location with the maximum difference between them being found at the space-time origin. With increasing temperature we find that the t.e.v.s with different Robin boundary conditions are increasingly 'contained' within the Dirichlet and Neumann curves, with the difference between all boundary conditions decreasing with increasing temperature. However, for all temperatures and Robin parameters, the t.e.v.s of the nonzero components of the RSET converge to the common v.e.v. found, with Dirichlet and Neumann boundary conditions, as we approach the space-time boundary. This is consistent with the results for the vacuum polarisation (VP) [71] where the vacuum and thermal expectation values for all Robin parameters (except Dirichlet) converged to the Neumann result. In the case of the RSET, both Dirichlet and Neumann boundary conditions have the same v.e.v.s and so in this case, all boundary conditions, including Dirichlet, converge to

the same result. This supports the conclusion in [71] that Neumann boundary conditions reflect the generic behaviour of the field at the boundary.

In Chapter 6 we move away from the massless, conformally coupled case and examine the effects on the RSET when we change the mass and coupling constant of the field. First, however, we discuss aspects of quantum scalar field theory on adS3 which is the subject of the next chapter.

Chapter 4

Quantum scalar field theory on adS3

In Chapter 3 we determined the RSET for a massless, conformally coupled, quantum scalar field on adS4. We now consider what happens when we consider a scalar field with general mass and coupling to the background curvature and this is the focus of Chapters 4, 5 and 6. Allowing the field mass and coupling constant to vary presents additional complexities to the underlying mathematics and therefore we work in three-dimensional anti-de Sitter space-time (adS3). The reduced number of space-time dimensions simplifies the angular component of the scalar field Green's function, thereby avoiding the use of conical (Mehler) functions which were required in [71] and Chapter 3.

This chapter is laid out as follows. In Section 4.1 we determine the mode solutions to the Klein-Gordon equation for a scalar field with general mass and coupling on adS3. These are formulated in terms of hypergeometric functions. In Section 4.2 we examine the regularity of the solutions found in Section 4.1 at the space-time origin and boundary. In Section 4.3 we apply boundary conditions of Robin type to the scalar field modes, parameterised by the Robin parameter ζ. In Section 4.4 we establish quantisation conditions on the frequency ω and in Section 4.5 we derive an upper bound on ζ to obtain stable mode solutions for the scalar field. Finally we conclude our findings in Section 4.6

§ 4.1 Mode solutions to the Klein-Gordon equation

In this thesis we consider a real, free quantum scalar field, Φ satisfying the Klein-Gordon equation (1.22). As the coupling constant and the Ricci scalar terms in (1.22) are constants we can write

$$m^2 + \xi R = \mu^2 = \text{constant}, \tag{4.1}$$

where $R = -6/L^2$ in adS3 and $L > 0$ is the radius of curvature of adS (Section 2.1). The μ term in (4.1) contains the information about the mass and coupling constant of the scalar field. Using the adS3 metric (2.9) the curved space D'Alembertian operator becomes

$$\Box = \frac{1}{L^2 \sec^2\rho}\left(-\frac{\partial^2}{\partial t^2} + \frac{\partial^2}{\partial \rho^2} + \frac{1}{\sin\rho\,\cos\rho}\frac{\partial}{\partial\rho} + \frac{1}{\sin^2\rho}\frac{\partial^2}{\partial\theta^2}\right). \tag{4.2}$$

Solutions to the Klein-Gordon equation (1.22) take the form

$$\Phi = e^{-i\omega t}e^{ik\theta}f(\rho), \tag{4.3}$$

where ω is the frequency, $k \in \mathbb{Z}$ and $f(\rho)$ is the radial function. Using (4.1, 4.3), the Klein-Gordon equation (1.22) becomes

$$\cos^2\rho\,\frac{\partial^2 f(\rho)}{\partial^2\rho} + \cot\rho\,\frac{\partial f(\rho)}{\partial\rho} + (\omega^2\cos^2\rho - k^2\cot^2\rho - \mu^2L^2)f(\rho) = 0. \tag{4.4}$$

This is the radial equation for the scalar field with general mass and coupling.

To solve the radial equation (4.4) we use a substitution of the form

$$f(\rho) = [\cos\rho]^A[\sin\rho]^B F(z), \tag{4.5}$$

where

$$z = \cos^2\rho \tag{4.6}$$

and A, B are parameters to be determined later. Substituting (4.5) into (4.4) gives, after much algebra,

$$\begin{aligned} 0 = z(1-z)\frac{d^2F}{dz^2} + \{A - (A+B+1)z\}\frac{dF}{dz} \\ + \frac{1}{4}\left\{\frac{B(B-1)z}{1-z} - B(A+1) + \frac{A(A-1)(1-z)}{z}\right. \\ \left. -A(B+1) + \frac{B}{1-z} - \frac{A}{z} + \omega^2 - \frac{k^2}{1-z} - \frac{\mu^2L^2}{z}\right\}F(z). \end{aligned} \tag{4.7}$$

By appropriate choices of A and B, (4.7) can be transformed into a hypergeometric differential equation [39, §15.10]

$$z(1-z)\frac{d^2F(z)}{dz^2} + [\gamma - (\alpha+\beta+1)z]\frac{dF(z)}{dz} - \alpha\beta F(z) = 0 \tag{4.8}$$

the solutions of which are the hypergeometric functions ${}_2F_1(\alpha,\beta,\gamma;z)$ given by [39, §15.2.1]

$${}_2F_1(\alpha,\beta,\gamma;z) = \sum_{s=0}^{\infty}\frac{(\alpha)_s\,(\beta)_s}{(\gamma)_s}\,\frac{z^s}{s!} = 1 + \frac{\alpha\,\beta}{\gamma}z + \frac{\alpha(\alpha+1)\beta(\beta+1)}{\gamma(\gamma+1)2!}z^2 + \ldots \tag{4.9}$$

for parameters α, β, γ to be determined. The 2,1 subscripts in the hypergeometric functions will be omitted in the future for clarity. Comparing (4.7) to (4.8) gives

$$-4\alpha\beta = \left\{\frac{B^2-k^2}{1-z} + \frac{A^2-2A-\mu^2L^2}{z} + \omega^2 - (B+A)^2\right\}. \tag{4.10}$$

As α, β are constants we have

$$\begin{aligned} B^2 - k^2 = 0, \\ A^2 - 2A - \mu^2L^2 = 0 \end{aligned} \tag{4.11}$$

the solutions of which give

$$B = \pm k \quad \text{and} \quad A = 1 \pm \sqrt{1+\mu^2L^2}. \tag{4.12}$$

row	A, B	α	β	γ
1	$A = 1-\nu;\ B = +\lvert k\rvert$	$\frac{1}{2}(1+\lvert k\rvert-\nu-\omega)$	$\frac{1}{2}(1+\lvert k\rvert-\nu+\omega)$	$1-\nu$
2	$A = 1-\nu;\ B = -\lvert k\rvert$	$\frac{1}{2}(1-\lvert k\rvert-\nu-\omega)$	$\frac{1}{2}(1-\lvert k\rvert-\nu+\omega)$	$1-\nu$
3	$A = 1+\nu;\ B = +\lvert k\rvert$	$\frac{1}{2}(1+\lvert k\rvert+\nu-\omega)$	$\frac{1}{2}(1+\lvert k\rvert+\nu+\omega)$	$1+\nu$
4	$A = 1+\nu;\ B = -\lvert k\rvert$	$\frac{1}{2}(1-\lvert k\rvert+\nu-\omega)$	$\frac{1}{2}(1-\lvert k\rvert+\nu+\omega)$	$1+\nu$

Table 4.1: Possible coefficients of the hypergeometric functions representing the solutions to the radial equation of the scalar field (4.7).

Equation (4.7) can now be written as

$$z(1-z)\frac{d^2F}{dz^2} + \{A-(A+B+1)z\}\frac{dF}{dz} + \frac{1}{4}[\omega^2-(B+A)^2]F(z) = 0. \tag{4.13}$$

Comparing (4.8) and (4.13) we have

$$\begin{aligned} \omega^2-(B+A)^2 &= -4\alpha\beta, \\ \alpha+\beta &= A+B, \\ \gamma &= A. \end{aligned} \tag{4.14}$$

From (4.14) we find the following expressions for α, β and γ

$$\begin{aligned} \alpha &= \frac{1}{2}(A+B) \pm \frac{1}{2}\omega, \\ \beta &= \frac{1}{2}(A+B) \mp \frac{1}{2}\omega, \\ \gamma &= 1 \pm \sqrt{1+\mu^2L^2}. \end{aligned} \tag{4.15}$$

From now on it will be more convenient to define the quantity

$$\nu = \sqrt{1+\mu^2L^2}, \tag{4.16}$$

where the ν parameter contains the information about the mass and coupling of the field. For the time being we consider $0 < \nu < 1$ (see Section 4.3 for more detailed discussion on this).

As the α and β terms in the hypergeometric function (4.9) are interchangeable, we can arbitrarily choose β to have the $+1/2\,\omega$ term and α to have the $-1/2\,\omega$ term in (4.15). Table 4.1 shows the possible values of A and B from (4.14) and the corresponding values of the hypergeometric parameters α, β, γ.

Regular singularities of the hypergeometric differential equation (4.8) occur at $z = 0$, $z = 1$ and $z = \infty$ [39, §15.10] . However as $0 \le \rho \le \pi/2$ the singularity at $z = \infty$ is not relevant. Consider now the solutions to (4.13) in the neighbourhood of the following singular points:

Neighbourhood of $z = 0$, $\rho = \pi/2$: For $0 < \nu < 1$, we have $\gamma \notin \mathbb{Z}$ and hence the solutions of (4.13) are given by [39, §15.10]

$$F_1(z) = F(\alpha, \beta, \gamma; z),$$
$$F_2(z) = z^{1-\gamma} F(\alpha - \gamma + 1,\, \beta - \gamma + 1,\, 2 - \gamma; z). \tag{4.17}$$

If $\gamma \in \mathbb{Z}$, then we use [39, §15.2.5] for the second solution. The solutions $F_1(z)$ and $F_2(z)$ are two linearly independent solutions of (4.13) in the neighbourhood of $z = 0$, $\rho = \pi/2$. The parameters in the hypergeometric functions in (4.17) are related pairs from Table 4.1. For instance they can be from the first and third rows of coefficients in Table 4.1 or indeed the second and fourth rows. For example, if we take the parameters from row three in Table 4.1 for the hypergeometric parameters in $F_1(z)$, then the parameters for the hypergeometric function in $F_2(z)$ will be from row one and *vice versa*. We can now write the general solution to the radial equation (4.4), in the neighbourhood of $z = 0$, $\rho = \pi/2$, as

$$f(\rho) = [\cos\rho]^A [\sin\rho]^B \left\{ \mathcal{C}_1 F(\alpha, \beta, \gamma; z) + \mathcal{C}_2\; z^{1-\gamma} F(\alpha - \gamma + 1, \beta - \gamma + 1, 2 - \gamma; z) \right\} \tag{4.18}$$

where $\mathcal{C}_1$ and $\mathcal{C}_2$ are arbitrary constants.

Neighbourhood of $z = 1$, $\rho = 0$: To examine the form of the solutions to the hypergeometric differential equation (4.13) in the neighbourhood of $z = 1$, $\rho = 0$, we employ a substitution of the form $u = 1 - z$ into (4.8) to obtain

$$u(1-u)\frac{d^2F}{du^2} + \Big[(\alpha + \beta - \gamma + 1) - (\alpha + \beta + 1)u\Big]\frac{dF}{du} - \alpha\beta F = 0. \tag{4.19}$$

Equation (4.19) is now in the form of (4.8) but with the γ term replaced by $\alpha + \beta - \gamma + 1$. Using (4.17) we can write the solution of (4.13) in the neighbourhood of $z = 1$ as

$$F_3(u) = F(\alpha, \beta, \alpha + \beta - \gamma + 1; u) \tag{4.20}$$

But as $u = 1 - z$ we can express this solution in terms of z as

$$F_3(z) = F(\alpha, \beta, \alpha + \beta - \gamma + 1; 1 - z) \tag{4.21}$$

The second linearly independent solution to (4.13) has a logarithmic singularity at $z = 1$, $\rho = 0$ and hence we ignore this solution [39, §15.2.5]. Therefore, we can write the solution to the radial equation (4.4) regular near $z = 1$, $\rho = 0$ as

$$f(\rho) = \mathcal{C}_3\, [\cos\rho]^A [\sin\rho]^B F(\alpha, \beta, \alpha + \beta - \gamma + 1; 1 - z), \tag{4.22}$$

where $\mathcal{C}_3$ is a constant. Equations (4.18) and (4.22) give two possible forms of the solution to the radial equation (4.9) for $z \in (0, 1)$.

§ 4.2 Regularity of the solutions

It is worthwhile at this point considering the regularity of the solutions (4.18) and (4.22) at $z = 0$, $\rho = \pi/2$ and $z = 1$, $\rho = 0$ respectively. Consider first equation (4.18) reproduced here

for convenience with z replaced by $\cos^2\rho$ in the hypergeometric functions and $z^{1-\gamma}$ replaced by $[\cos\rho]^{2(1-A)}$

$$f(\rho) = [\cos\rho]^A[\sin\rho]^B\Big\{\mathcal{C}_1 F(\alpha,\beta,\gamma;\cos^2\rho) + \mathcal{C}_2\ [\cos\rho]^{2(1-A)}F(\alpha-\gamma+1,\beta-\gamma+1,2-\gamma;\cos^2\rho)\Big\}. \quad (4.23)$$

To establish a possible range for the parameter A, we note that if $A < 0$ we must have $\mathcal{C}_1 = 0$ and for $A > 2$ we must have $\mathcal{C}_2 = 0$. We will see in Section 4.3 that the constants $\mathcal{C}_1$, $\mathcal{C}_2$ are used in the definitions of the boundary conditions applied at the space-time boundary ($\rho = \pi/2$). Hence we must have $\mathcal{C}_1 \neq 0$, $\mathcal{C}_2 \neq 0$ in order to have a choice of boundary conditions. Therefore, for (4.23) to be regular at $z = 0$, $\rho = \pi/2$ and to have a choice of boundary conditions we require that $0 \leq A \leq 2$.

For (4.22) to be regular at $z = 1,\ \rho = 0$ we require that $B > 0$ i.e. that $B = |k|$. Therefore we must choose the coefficients of the hypergeometric functions from rows one or three in Table 4.1. In summary for regular solutions of (4.18) and (4.22) and for a choice of boundary conditions at $\rho = \pi/2$ we require

$$B = |k| \quad \text{and} \quad 0 \leq A \leq 2. \quad (4.24)$$

Without loss of generality, we can choose the coefficients from row 3. Equations (4.24) and (4.16) together with (4.16) imply we consider $0 \leq \nu \leq 1$. Also, in order to satisfy the Breitenlohner-Freedman bound [19], we require $\nu \geq 0$ for the field to be classically stable. Thus our range of ν is

$$0 \leq \nu \leq 1, \quad (4.25)$$

and this applies to the scalar field with general mass and coupling. In the particular case of the massless, conformally coupled scalar field where $m = 0$, $\xi = 1/8$ and $R = -6/L^2$ we have $\nu = 1/2$ and the inequality (4.25) is satisfied.

Using (4.1, 4.16, 4.25) we can establish a relationship between the mass m of our quantum scalar field and the coupling constant ξ as

$$\frac{1}{L^2}(6\xi - 1) \leq\ m^2\ \leq \frac{6\xi}{L^2}. \quad (4.26)$$

The lower bound of (4.26) corresponds to the Breitenlohner-Freedman bound [19] and also the mass constraints in [29]. Using (4.1, 4.16) we can plot m^2 as a function of the coupling constant ξ for various values of the parameter ν as shown in Figure 4.1. Each fixed value of ν represents a range of possible values of m^2 and ξ. All values on m^2 in the blue shaded region ($\nu \in [0,1]$), including $m^2 < 0$, satisfy the Breitenlohner-Freedman bound [19], although the physical significance of $m^2 < 0$ on a background adS is unclear.

We now determine the constants $\mathcal{C}_1$, $\mathcal{C}_2$, $\mathcal{C}_3$ in (4.18, 4.22). The three hypergeometric functions in (4.18, 4.22) are related by Kummer's connection formulae [39, §15.10(ii)]. Letting

$$\begin{aligned} w_1 &= F_1(\alpha,\beta,\gamma;z), \\ w_2 &= z^{1-\gamma}\,F_3(\alpha-\gamma+1,\beta-\gamma+1,2-\gamma;z), \\ w_3 &= F_2(\alpha,\beta,\alpha+\beta-\gamma+1;1-z), \end{aligned} \quad (4.27)$$

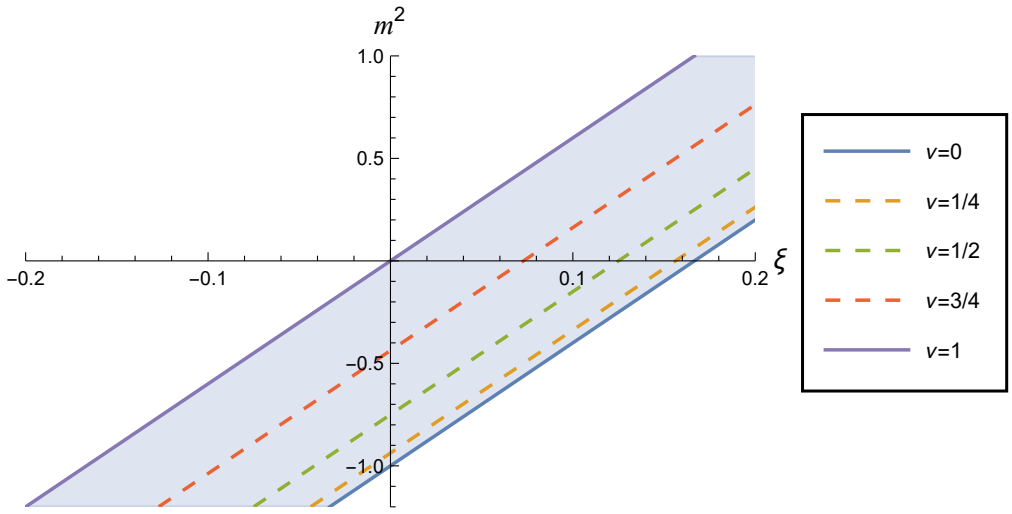

Figure 4.1: Plot of m^2 against ξ for different values of fixed ν (4.16). For clarity, only a limited range of ξ is shown. The dotted lines represent three values of ν studied in Chapters 5–7. The adS length scale L has been set to one.

we have [39, §15.10.17]

$$w_3(z) = \frac{\Gamma(1-\gamma)\Gamma(\alpha+\beta-\gamma+1)}{\Gamma(\alpha-\gamma+1)\Gamma(\beta-\gamma+1)} w_1(z) + \frac{\Gamma(\gamma-1)\Gamma(\alpha+\beta-\gamma+1)}{\Gamma(\alpha)\Gamma(\beta)} w_2(z). \tag{4.28}$$

Comparing (4.27) and (4.28) the constants $\mathcal{C}_1$ and $\mathcal{C}_2$ in (4.18) can be written in terms of the constant $\mathcal{C}_3$ in (4.22) as

$$\mathcal{C}_1 = \mathcal{C}_3 \, \frac{\Gamma(1-\gamma)\Gamma(\alpha+\beta-\gamma+1)}{\Gamma(\alpha-\gamma+1)\Gamma(\beta-\gamma+1)} = \mathcal{C}_3 \, \mathcal{P} \tag{4.29}$$

and

$$\mathcal{C}_2 = \mathcal{C}_3 \, \frac{\Gamma(\gamma-1)\Gamma(\alpha+\beta-\gamma+1)}{\Gamma(\alpha)\Gamma(\beta)} = \mathcal{C}_3 \, \mathcal{Q}, \tag{4.30}$$

where

$$\mathcal{P} = \frac{\Gamma(1-\gamma)\Gamma(\alpha+\beta-\gamma+1)}{\Gamma(\alpha-\gamma+1)\Gamma(\beta-\gamma+1)} \quad \text{and} \quad \mathcal{Q} = \frac{\Gamma(\gamma-1)\Gamma(\alpha+\beta-\gamma+1)}{\Gamma(\alpha)\Gamma(\beta)}. \tag{4.31}$$

Using (4.28, 4.29, 4.30), we can express the solution to the radial equation at $z = 1$, $\rho = 0$ (4.22) in the alternative form

$$f(\rho) = \mathcal{C}_{\omega k} \, [\cos\rho]^A [\sin\rho]^B \{\mathcal{P} F(\alpha, \beta, \gamma; z) + \mathcal{Q} \; z^{1-\gamma} F(\alpha-\gamma+1, \beta-\gamma+1, 2-\gamma; z)\}, \tag{4.32}$$

where the constant $\mathcal{C}_3$ has been absorbed into an overall normalisation constant $\mathcal{C}_{\omega k}$.

§ 4.3 Boundary conditions on adS

Formulating a QFT on adS space-time has some advantages and disadvantages. Having maximum symmetry is certainly beneficial, as outlined in Section 2.3, but the possession of a time-like boundary at spatial infinity presents a problem. Information is able to enter and leave at the boundary [8],

meaning we have to impose boundary conditions on the field in order to have a well-posed QFT. Whilst many boundary conditions have been studied on an adS background (see Section 2.4), our focus in this thesis are the three boundary conditions of Dirichlet, Neumann and Robin.

For Dirichlet boundary conditions we require that the value of the field falls to zero as rapidly as possible at the boundary. Imposing Neumann boundary conditions, however, presents more of a challenge for the scalar field with general mass and curvature coupling. In the case of the massless, conformally coupled field ($\nu = 1/2$), the Neumann boundary condition can be defined naturally [8], as we can map the field onto the globally hyperbolic Einstein static universe (ESU) (see Sections 2.1 and 2.4). As the boundary of adS is not part of the space-time we establish boundary conditions on the conformally invariant field on ESU instead.

If the scalar field is not conformally invariant, the above method of mapping to ESU no longer applies, and we have a choice as to how 'Neumann' boundary conditions are defined [29]. In [59], the authors studied the possible boundary conditions that can be imposed at spatial infinity for different values of ν. For $\nu < 0$, no boundary conditions are possible, whilst for $\nu = 0$ both Dirichlet and Neumann are simultaneously imposed and characterised by a one-parameter family of boundary conditions. For $\nu \geq 1$, we only have Dirichlet boundary conditions. For $0 < \nu < 1$, 'generalised' Neumann boundary conditions were defined [59], which corresponded to the vanishing of the derivative of the products of the field with trigonometric functions of the radial coordinate.

We can define the Robin boundary condition for a massless, conformally coupled field (2.28) as a linear combination of Dirichlet and Neumann boundary conditions [59, 71]. To apply Robin boundary conditions we need to first map the conformal scalar field to the ESU (Section 2.1). Using (4.32), the radial function on ESU $\widetilde{f}(\rho)$ becomes

$$\widetilde{f}(\rho) = [\cos\rho]^{(A-\frac{1}{2})}[\sin\rho]^{B}\Big\{\mathcal{P}F(\alpha,\beta,\gamma;\cos^2\rho) + \mathcal{Q}\,[\cos\rho]^{2(1-A)}F(\alpha-\gamma+1,\beta-\gamma+1,2-\gamma;\cos^2\rho)\Big\}, \quad (4.33)$$

where the $\mathcal{C}_{\omega k}$ constant has been set to one and the tilde notation on $\widetilde{f}(\rho)$ denotes that we are on ESU. In the case of the massless conformally coupled scalar field in adS3 we have $\nu = 1/2$. Using the values of $A = 3/2$ and $B = |k|$ from row three in Table 4.1 we have

$$\widetilde{f}(\rho) \;=\; [\sin\rho]^{|k|}\Big\{\mathcal{P}\cos\rho\,F(\alpha,\beta,\gamma;\cos^2\rho) \,+\, \mathcal{Q}\,F(\alpha-\gamma+1,\beta-\gamma+1,2-\gamma;\cos^2\rho)\Big\}, \quad (4.34)$$

and

$$\begin{aligned}\frac{d\tilde{f}}{d\rho} = &-[\sin\rho]^{|k|+1}\mathcal{P}F(\alpha,\beta,\gamma;\cos^2\rho) + |k|[\cos\rho][\sin\rho]^{|k|-1}\Big\{\mathcal{P}[\cos\rho]F(\alpha,\beta,\gamma;\cos^2\rho) \\ &+ \mathcal{Q}F(\alpha-\gamma+1,\beta-\gamma+1,2-\gamma;\cos^2\rho)\Big\} \\ &- 2\cos\rho[\sin\rho]^{|k|+1}\left\{\mathcal{P}\cos\rho\frac{d}{dz}F(\alpha,\beta,\gamma;\cos^2\rho) + \mathcal{Q}\,\frac{d}{dz}F(\alpha-\gamma+1,\beta-\gamma+1,2-\gamma;\cos^2\rho)\right\}.\end{aligned} \quad (4.35)$$

It is clear that at $\rho = \pi/2$ both (4.34) and (4.35) are regular and their hypergeometric functions tend to unity at $z = 0$, $\rho = \pi/2$ (and hence their derivatives vanish). Therefore applying Robin boundary conditions to the scalar field on the ESU for the massless conformally coupled field gives

$$\mathcal{P} \sin\zeta - \mathcal{Q} \cos\zeta = 0. \tag{4.36}$$

When the scalar field is not massless and conformally coupled, i.e. when $\nu \neq 1/2$ the above approach is no longer applicable. In [29], trigonometric functions of the Robin parameter were equated with the constants of the solutions of the Klein-Gordon equation. In keeping with [29] we can define the Robin parameter $\zeta \in [0, \pi]$ for the scalar field with general mass and coupling as

$$\cos\zeta = \mathcal{P} \qquad \text{and} \qquad \sin\zeta = \mathcal{Q}, \tag{4.37}$$

which is consistent with (4.36) obtained for the massless, conformally coupled field. The Dirichlet boundary condition is given by $\zeta = 0$, whilst for Neumann $\zeta = \pi/2$.

Using (4.37) and inserting the values of α, β, γ from row three Table 4.1 gives

$$\tan\zeta = \frac{\Gamma(\nu)\,\Gamma(\frac{1}{2}(|k|+1-\nu-\omega))\,\Gamma(\frac{1}{2}(|k|+1-\nu+\omega))}{\Gamma(-\nu)\,\Gamma(\frac{1}{2}(|k|+1+\nu-\omega))\,\Gamma(\frac{1}{2}(|k|+1+\nu+\omega))}. \tag{4.38}$$

This equation provides us with a useful relationship between the frequency ω and the Robin parameter ζ. We will use this to establish an upper bound for the Robin parameter ζ in Section 4.5 and also in the establishment of quantisation conditions for the mode frequency ω which is the subject of the next section.

§ 4.4 Quantisation condition on ω

Let $\mathcal{J}$ represent the right hand side of (4.38), namely

$$\mathcal{J} = \frac{\Gamma(\nu)\,\Gamma(\frac{1}{2}(|k|+1-\nu-\omega))\,\Gamma(\frac{1}{2}(|k|+1-\nu+\omega))}{\Gamma(-\nu)\,\Gamma(\frac{1}{2}(|k|+1+\nu-\omega))\,\Gamma(\frac{1}{2}(|k|+1+\nu+\omega))}. \tag{4.39}$$

We can plot $\mathcal{J}$ as a function of ω for fixed ν and a selection of values of $|k|$ as shown in Figure 4.2. Each value of the Robin parameter ζ corresponds to a discrete set of quantised frequencies. For example for the Dirichlet boundary condition with $\zeta = 0$ we have $\mathcal{J} = 0$ corresponding to the $\omega-$axis in Figure 4.2. Considering the form of the gamma function, $\Gamma(x)$ (Figure 4.3), we note that the argument of one of the Gamma functions in the denominator of the right hand side of (4.38) must be 0 or a negative integer. Therefore, we can write

$$\pm\,\omega_{nk} = 2n + 1 + \nu + |k| \quad \text{for} \quad n \in \mathbb{Z}^-, \tag{4.40}$$

where we have used ω_{nk} to represent the set of quantised frequencies. Similarly for the Neumann boundary condition we have $\zeta = \pi/2$ and so require that the argument of one of the Gamma functions in the numerator of (4.38) is a negative integer or zero which gives the quantisation condition on ω for the Neumann boundary condition as

$$\pm\,\omega_{nk} = 2n + 1 - \nu + |k| \quad \text{for} \quad n \in \mathbb{Z}^-. \tag{4.41}$$

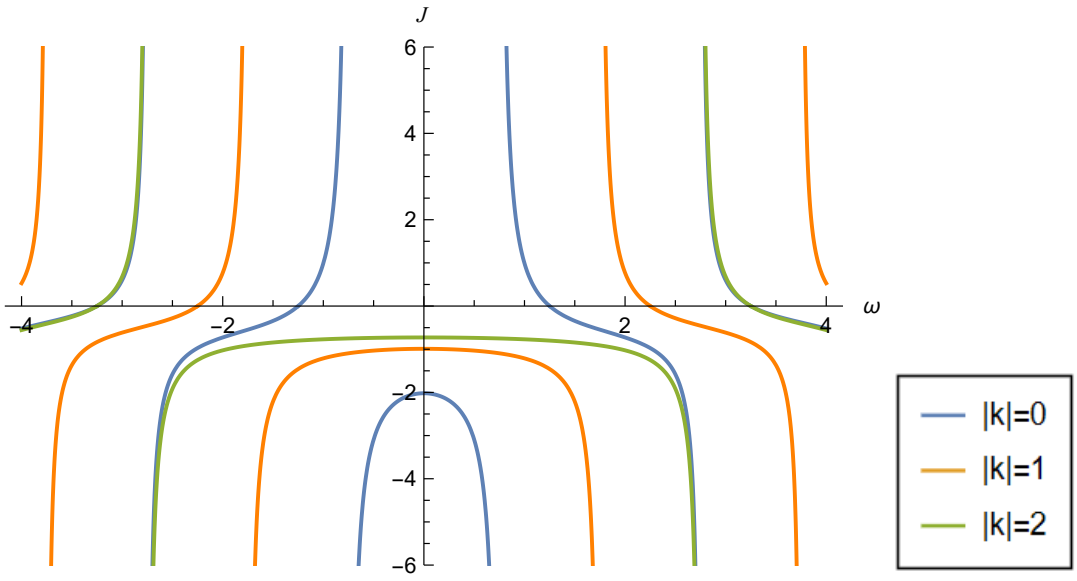

Figure 4.2: Right hand side of (4.38), $\mathcal{J}$ against ω for a selection of values of $|k|$ and an example value of $\nu = 1/4$. Noninteger values of ω are shown for Dirichlet ($\zeta = 0$) and Neumann ($\zeta = \pi/2$) given by the vertical asymptotes. Qualitatively similar plots are seen for $\nu = 1/2$ and $\nu = 3/4$ with noninteger values of ω for Dirichlet and Neumann boundary conditions.

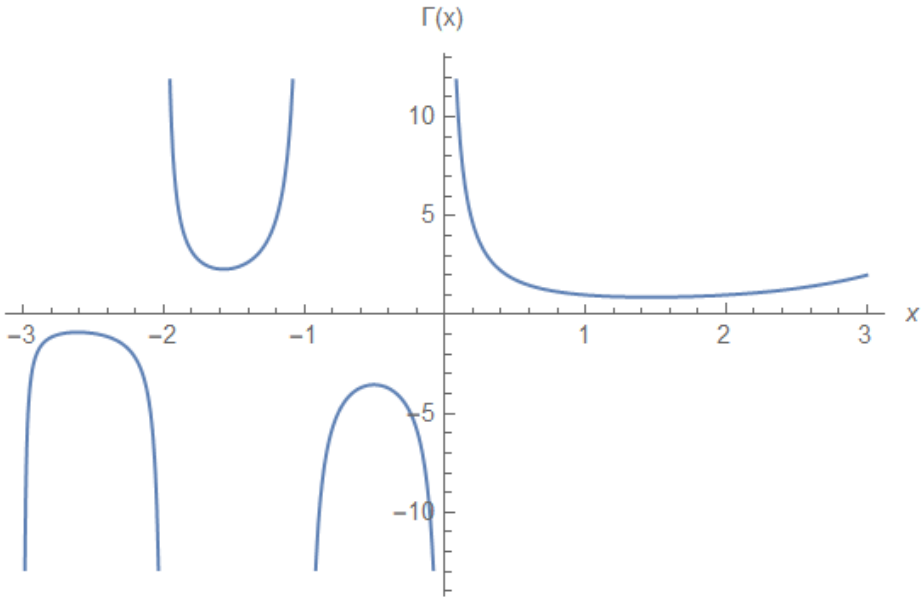

Figure 4.3: The Gamma function, $\Gamma(x)$, showing singularities at negative integer values of its argument.

For $0 < \nu < 1$ we will not obtain integer values for the ω_{nk} for Dirichlet, Neumann or general ζ but from (4.40, 4.41) we see that the quantised frequencies ω_{nk} are evenly spaced. This is in contrast to the case for the massless, conformally coupled scalar field in adS4 [12] where integer quantisation of the mode frequency was found in Lorentzian space-time. The quantisation condition for ω in (4.38) matches that in [29] for the scalar field in adS3.

§ 4.5 Stability analysis

In this section we show that there is a critical value of the Robin parameter, ζ_{crit}, beyond which we obtain unstable mode solutions. This corresponds to the presence of solutions of (4.38) with purely imaginary frequency. To examine this we consider $\omega \to i\Omega$ for $\Omega \in \mathbb{R}$ in which case (4.38) becomes

$$\tan\zeta = \frac{\Gamma(\nu)|\Gamma(\frac{|k|}{2}+\frac{1}{2}-\frac{\nu}{2}-\frac{i\Omega}{2})|^2}{\Gamma(-\nu)|\Gamma(\frac{|k|}{2}+\frac{1}{2}+\frac{\nu}{2}-\frac{i\Omega}{2})|^2}. \tag{4.42}$$

We consider only purely imaginary values of ω rather than complex following on from the work of Ishibashi and Wald [58, 59]. As discussed in Section 2.4, the possible choices of dynamics of the scalar field correspond to having self-adjoint extensions of the spatial component of the wave operator. For this to happen we require that $\omega^2 \in \mathbb{R}$. We look for values of the Robin parameter ζ which result in values of Ω which satisfy (4.42) and such values of Ω will produce unstable, exponentially growing modes of the scalar field. Let $\mathcal{F}$ represent the right hand side of (4.42)

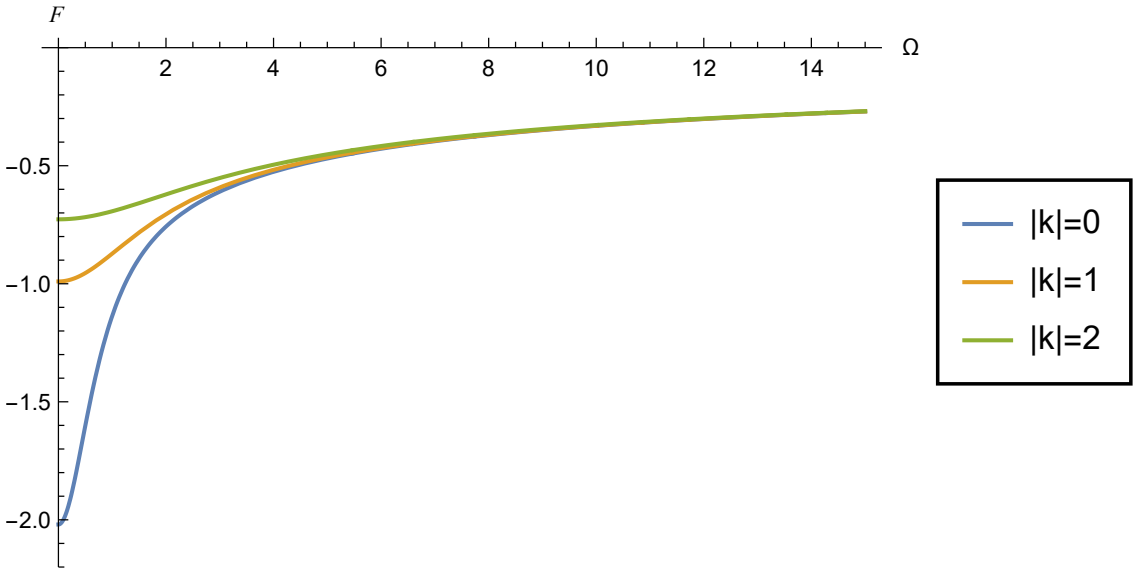

Figure 4.4: Plot of $\mathcal{F}(|k|,\Omega)$ (4.43), as a function of Ω for three different values of $|k|$ and fixed $\nu = 1/4$.

$$\mathcal{F}(|k|,\Omega) = \frac{\Gamma(\nu)|\Gamma(\frac{|k|}{2}+\frac{1}{2}-\frac{\nu}{2}-\frac{i\Omega}{2})|^2}{\Gamma(-\nu)|\Gamma(\frac{|k|}{2}+\frac{1}{2}+\frac{\nu}{2}-\frac{i\Omega}{2})|^2}. \tag{4.43}$$

Figure 4.4 shows $\mathcal{F}$ plotted as a function of Ω for three values of $|k|$ and fixed $\nu = 1/4$. As $\mathcal{F}$ is an even function of Ω we only show $\Omega > 0$.

As we have $\Gamma(\nu)/\Gamma(-\nu) < 0$ for $0 < \nu < 1$, we can see that for $0 \leq \zeta \leq \pi/2$ ($\tan\zeta > 0$) there are no values of Ω that are solutions to (4.42) and hence no unstable modes. However, there are values of $\tan\zeta < 0$ which result in unstable modes. We now investigate the possible values of ζ for which this occurs. Firstly it appears from Figure 4.4 that $\tan\zeta$ attains a minimum at $k = 0$, $\Omega = 0$ and increases monotonically for increasing Ω. We show this analytically as follows: differentiating the right hand side of (4.42) with respect to Ω gives

$$\frac{\partial\mathcal{F}}{\partial\Omega} = \frac{i\Gamma(\nu)\left|\Gamma(\frac{|k|}{2}+\frac{1}{2}-\frac{\nu}{2}+\frac{i\Omega}{2})\right|^2}{2\Gamma(-\nu)\left|\Gamma(\frac{|k|}{2}+\frac{1}{2}+\frac{\nu}{2}+\frac{i\Omega}{2})\right|^2}\Bigg\{\Psi\left(\frac{|k|}{2}+\frac{1}{2}+\frac{\nu}{2}-\frac{i\Omega}{2}\right)-\Psi\left(\frac{|k|}{2}+\frac{1}{2}+\frac{\nu}{2}+\frac{i\Omega}{2}\right)$$
$$+\Psi\left(\frac{|k|}{2}+\frac{1}{2}-\frac{\nu}{2}+\frac{i\Omega}{2}\right)-\Psi\left(\frac{|k|}{2}+\frac{1}{2}-\frac{\nu}{2}-\frac{i\Omega}{2}\right)\Bigg\}, \quad (4.44)$$

where Ψ is the digamma function defined as [76]

$$\Psi(\mathrm{w}) = \frac{d}{d\mathrm{w}}\ln\left[\Gamma(\mathrm{w})\right], \quad (4.45)$$

for complex argument $\mathrm{w} = x + iy$. It can be seen from (4.44) that a stationary point exists at $\Omega = 0\ \forall\,|k|$. The digamma function with complex argument can be split into its real and imaginary parts using [76]

$$\Psi(x+iy) = -\varsigma - \frac{x}{x^2+y^2} + \sum_{j=1}^{\infty}\frac{jx+x^2+y^2}{j[(j+x)^2+y^2]} + i\sum_{j=0}^{\infty}\frac{y}{(j+x)^2+y^2} \quad (4.46)$$

where ς is used to represent the Euler constant. Using (4.46) we can write the difference between two digamma functions with complex conjugate arguments as

$$\Psi(x+iy) - \Psi(x-iy) = 2i\sum_{j=0}^{\infty}\frac{y}{(j+x)^2+y^2}. \quad (4.47)$$

We can now write (4.44) as

$$\frac{\partial\mathcal{F}}{\partial\Omega} = \frac{\Gamma(\nu)\,\Omega\left|\Gamma(\frac{|k|}{2}+\frac{1}{2}-\frac{\nu}{2}+\frac{i\Omega}{2})\right|^2}{2\Gamma(-v)\left|\Gamma(\frac{|k|}{2}+\frac{1}{2}+\frac{\nu}{2}+\frac{i\Omega}{2})\right|^2}\sum_{j=0}^{\infty}\left\{\frac{1}{(j+k_1)^2+\frac{\Omega^2}{4}}-\frac{1}{(j+k_2)^2+\frac{\Omega^2}{4}}\right\}, \quad (4.48)$$

where we have defined

$$k_1 = \frac{1}{2}(1+|k|+\nu),$$
$$k_2 = \frac{1}{2}(1+|k|-\nu). \quad (4.49)$$

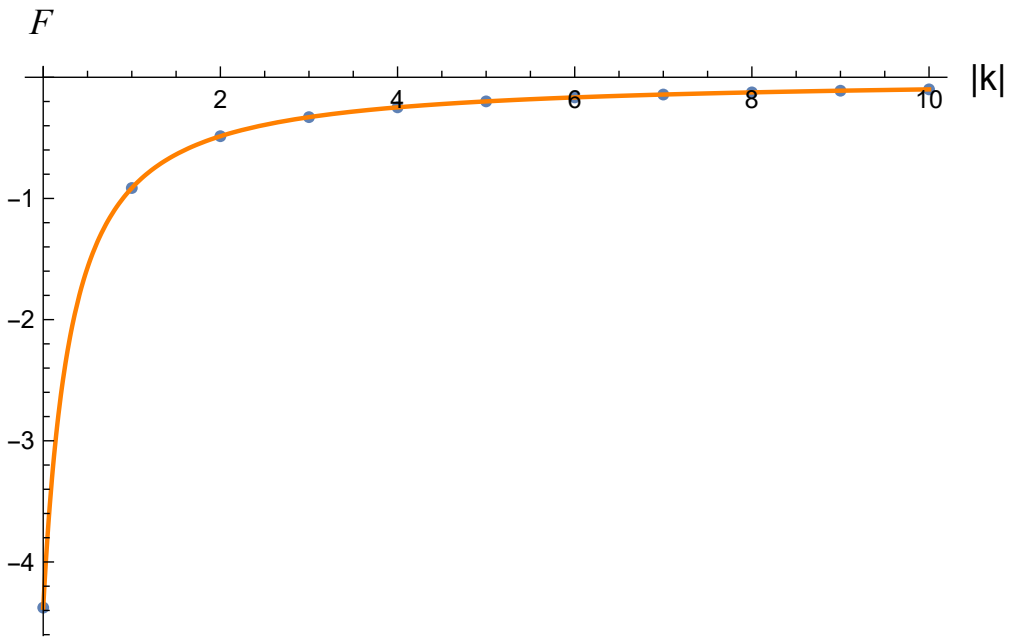

Figure 4.5: Plot of $\mathcal{F}(|k|,0)$ (4.50), as a function of $|k| \in \mathbb{Z}$ with $\Omega = 0$ for the massless, conformally coupled scalar field ($\nu = 1/2$). The discrete plot, shown in dots, is superimposed by a line plot to more clearly demonstrate the asymptotic behaviour of $\mathcal{F}(|k|,0)$ for large $|k|$.

Although $k_1 > k_2$, we have $\Gamma(\nu)/\Gamma(-\nu) < 0$ for $0 < \nu < 1$ and thus it can be seen that (4.48) is positive for all $\Omega > 0$ and $\mathcal{F}$ increases monotonically as Ω increases.

As the minimum of $\mathcal{F}$ for fixed $|k|$ occurs for $\Omega = 0$, we now study the behaviour of $\mathcal{F}$ for general values of $|k|$ at $\Omega = 0$. From (4.42), we have

$$\mathcal{F}(|k|,0) = \frac{\Gamma(\nu)\Gamma\left(\frac{|k|}{2}+\frac{1}{2}-\frac{\nu}{2}\right)^2}{\Gamma(-\nu)\Gamma\left(\frac{|k|}{2}+\frac{1}{2}+\frac{\nu}{2}\right)^2}. \tag{4.50}$$

For $0 < \nu < 1$, we have $\mathcal{F} < 0 \quad \forall\, |k|$. For large $|k|$ we have [39, §5.11.12]

$$\frac{\Gamma(\nu)\Gamma\left(\frac{|k|}{2}+\frac{1}{2}-\frac{\nu}{2}\right)^2}{\Gamma(-\nu)\Gamma\left(\frac{|k|}{2}+\frac{1}{2}+\frac{\nu}{2}\right)^2} \sim -\frac{1}{|k|}. \tag{4.51}$$

Therefore as $|k| \to \infty$ we have $\mathcal{F} \to 0^-$ as demonstrated in figure 4.5 which shows $\mathcal{F}$ (4.50) plotted as a function of $|k|$ for $\Omega = 0$. This is essentially the plot of the $\mathcal{F}$-axis intercept of the profiles in Figure 4.4 with increasing values of $|k|$.

Consider now the derivative of $\mathcal{F}$ with respect to $|k|$ (for $\Omega = 0$) given by

$$\left.\frac{\partial \mathcal{F}}{\partial k}\right|_{\Omega=0} = \frac{\Gamma(\nu)\Gamma\left(\frac{|k|}{2}+\frac{1}{2}-\frac{\nu}{2}\right)^2}{\Gamma(-\nu)\Gamma\left(\frac{|k|}{2}+\frac{1}{2}+\frac{\nu}{2}\right)^2}\left\{\Psi\left(\frac{|k|}{2}+\frac{1}{2}-\frac{\nu}{2}\right)-\Psi\left(\frac{|k|}{2}+\frac{1}{2}+\frac{\nu}{2}\right)\right\}, \tag{4.52}$$

where Ψ is the digamma function (4.45). The difference between two digamma functions with real arguments x_1, x_2 is given by [76]

$$\Psi(x_1) - \Psi(x_2) = (x_1 - x_2) \sum_{j=0}^{\infty} \frac{1}{(j + x_1)(j + x_2)}. \tag{4.53}$$

Therefore, (4.52) becomes

$$\left.\frac{\partial \mathcal{F}}{\partial k}\right|_{\Omega=0} = -\nu \frac{\Gamma(\nu)\Gamma\left(\frac{|k|}{2} + \frac{1}{2} - \frac{\nu}{2}\right)^2}{\Gamma(-\nu)\Gamma\left(\frac{|k|}{2} + \frac{1}{2} + \frac{\nu}{2}\right)^2} \left\{ \sum_{j=0}^{\infty} \frac{1}{\left(j + \frac{|k|}{2} + \frac{1}{2} - \frac{\nu}{2}\right)\left(j + \frac{|k|}{2} + \frac{1}{2} + \frac{\nu}{2}\right)} \right\}. \tag{4.54}$$

For $0 < \nu < 1$, the right hand side of (4.54) is positive for all $|k|$.

We can now conclude that the right hand side of (4.38), $\mathcal{F}$, has its minimum value at $\Omega = 0 = |k|$ for fixed $\nu \in (0, 1)$ (Figure 4.4). Therefore, from (4.42) we will have unstable mode solutions for

$$\frac{\Gamma(\nu)\Gamma\left(\frac{1}{2} - \frac{\nu}{2}\right)^2}{\Gamma(-\nu)\Gamma\left(\frac{1}{2} + \frac{\nu}{2}\right)^2} < \tan\zeta < 0. \tag{4.55}$$

Thus for $\zeta \in [0, \pi)$ we have

$$\zeta_{\text{crit}} = \pi + \tan^{-1}\left[\frac{\Gamma(\nu)\Gamma\left(\frac{1}{2} - \frac{\nu}{2}\right)^2}{\Gamma(-\nu)\Gamma\left(\frac{1}{2} + \frac{\nu}{2}\right)^2}\right]. \tag{4.56}$$

In the case of the massless, conformally coupled field $\nu = 1/2$, we have $\zeta_{\text{crit}} \sim 0.57\pi$. This differs from the corresponding value in four dimensions [71] which is $\zeta_{\text{crit}} \sim 0.68\pi$. For values of $\zeta_{\text{crit}} < \zeta < \pi$ we will have mode solutions that are classically unstable and the semi-classical approximation breaks down. Therefore, we must consider the Robin parameter within the range $\zeta \in [0, \zeta_{\text{crit}})$. From (4.55) it can be seen that the values of ζ_{crit} is dependent on the parameter ν. Figure 4.6 shows a plot of ζ_{crit} against ν, showing that as $\nu \to 1$ we have $\zeta_{\text{crit}} \to \pi/2$. This shows that at $\nu = 1$ the mode solutions with the Neumann boundary condition are unstable (see Chapter 5). For $\nu \to 0$, from (4.55), we have $\zeta_{\text{crit}} = 0.75\pi$ (Figure 4.6).

§ 4.6 Conclusions

In this chapter we have highlighted some of the keys aspects of a quantum field theory on adS3 for a massive, real scalar field Φ. We have found mode solutions to the Klein-Gordon equation in terms of hypergeometric functions (Section 4.1) and have examined the regularity of the solutions near the space-time origin and boundary (Section 4.2).

As adS is not a globally hyperbolic space-time, we need to impose boundary conditions on the scalar field at the space-time boundary in order to have a well-posed quantum field theory. We have discussed how boundary conditions of Dirichlet, Neumann and Robin type can be applied. For the massless, conformally coupled field ($\nu = 1/2$), Robin boundary conditions can be defined as (2.28). For the scalar field with general mass and coupling ($\nu \neq 1/2$), we adopt the approach

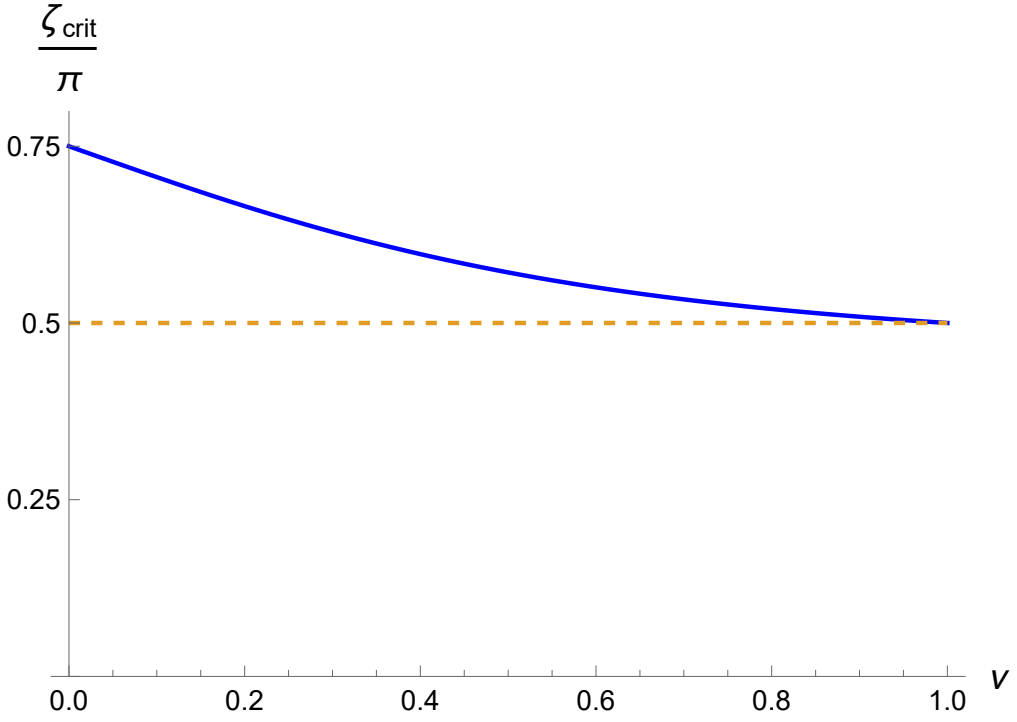

Figure 4.6: Variation of ζ_{crit} with ν for the scalar field with general mass and coupling.

of [29] and define the parameter ζ governing the Robin boundary condition in terms of constants of the mode solutions (4.37). This definition provides a useful relationship (4.38) between the Robin parameter ζ and the mode frequency ω, which is used to establish quantisation conditions on ω. Examples of the quantisation condition for ω with Dirichlet and Neumann boundary conditions are given in (4.40, 4.41).

Perhaps the key result in this chapter is in Section 4.5, where we show analytically that there is an upper limit for the Robin parameter ζ_{crit} (4.55), beyond which we obtain unstable mode solutions of the scalar field equation. The value of ζ_{crit} depends on ν (4.16) and for the massless conformally coupled field ($\nu = 1/2$) on adS3, we have $\zeta_{\text{crit}} \sim 0.57\pi$. This differs from the corresponding value on adS4 (Section 3.2), which is $\zeta_{\text{crit}} \sim 0.68\pi$. Thus, when applying Robin boundary conditions in Chapters 5 and 6 we use $0 \leq \zeta < \zeta_{\text{crit}}$.

Chapter 5

Vacuum polarisation on adS3

In this chapter we determine the v.e.v.s and t.e.v.s of the vacuum polarisation (VP) of a quantum scalar field on adS3. We study a scalar field with general mass and coupling to the background curvature subject to Dirichlet, Neumann and Robin boundary conditions applied to the scalar field at the space-time boundary. In [12], the v.e.v.s of the VP for a massless, conformally coupled scalar field was studied in adS4. When Robin boundary conditions were applied to just the $s-$wave modes, it was found that the v.e.v. of the VP approached that of the Dirichlet value at the space-time boundary. In contrast, if Robin boundary conditions are applied to all field modes, the v.e.v.s and t.e.v.s approach the Neumann value for all Robin boundary conditions (except Dirichlet) [71].

The work of [12, 71] considers the case of a massless, conformally coupled scalar field in adS4. In this chapter we examine what happens when we have a scalar field with general mass and coupling constant and examine whether the results in [71] hold in this case. Allowing the field mass and coupling constant to vary presents additional complexities to the underlying mathematics and therefore we work in three-dimensional adS. The reduced number of space-time dimensions simplifies the angular component of the scalar field Green's function, thereby avoiding the use of conical (Mehler) functions which were required in [71]. In [29], the ground state Green's function for a quantum scalar field with arbitrary mass and coupling has been constructed on n-dimensional anti-de Sitter space-time (adS_n) using Robin boundary conditions. However, the resulting renormalised expectation values have yet to be computed.

This chapter is laid out as follows. In Section 5.1 we describe the construction of the vacuum and thermal Feynman Green's functions and use Hadamard renormalisation to compute the v.e.v.s and t.e.v.s of the VP with Dirichlet and Neumann boundary conditions. In Section 5.2 we transform to Euclidean space to construct the vacuum and thermal Green's functions, which we then use to compute the renormalised v.e.v.s and t.e.v.s of the VP with Robin boundary conditions. In Section 5.3 we explore the VP at the space-time boundary and provide an analytical argument for some of the conclusions made in this chapter. Finally, in Section 5.4 we summarise our key results.

§ 5.1 Vacuum polarisation with Dirichlet and Neumann boundary conditions

5.1.1 Vacuum expectation values

Expectation values of the product of field operators can be determined using Green's functions [17]. We consider the Feynman Green's function, $G_F(x, x')$ (Section 1.3) which satisfies the inhomoge-

neous scalar field equation (1.36)

$$\left[g^{\alpha\beta}\nabla_\alpha\nabla_\beta - \mu^2\right] G_F(x,x') = -\frac{1}{\sqrt{|g|}}\delta^3(x-x') \tag{5.1}$$

in three dimensions, where g is the determinant of the metric (2.9), $\delta^3(x-x')$ is the three-dimensional Dirac delta function and μ is given by (4.1). Allen and Jacobson [3] have studied vector and scalar two-point functions in maximally symmetric spaces, including anti-de Sitter space-time. They showed that for states respecting this maximum symmetry, Green's functions can be expressed as functions of the unique geodesic distance $s(x,x')$ between the points x and x'. In this case they showed that $g^{\alpha\beta}\nabla_\alpha\nabla_\beta$ can be given as a second order differential operator in $s(x,x')$.

As the vacuum state with Dirichlet or Neumann boundary conditions respects the underlying adS symmetry [8, 61], for space-like separated points where $s \in \mathbb{R}$, equation (5.1) can be expressed as [3]

$$\left[\frac{d^2}{ds^2} + \frac{2}{L}\coth\left(\frac{s}{L}\right)\frac{d}{ds} - \mu^2\right] G_F = 0. \tag{5.2}$$

Using the change of variable [61]

$$z_1 = -\sinh^2\left(\frac{s}{2L}\right), \tag{5.3}$$

we find that (5.2) can be expressed as

$$z_1(1-z_1)\frac{d^2G_F}{dz_1^2} + \left\{\frac{3}{2} - 3z_1\right\}\frac{dG_F}{dz_1} + \mu^2\,L^2 G_F = 0. \tag{5.4}$$

This is now in the form of a hypergeometric differential equation

$$z_1(1-z_1)\frac{d^2G_F(z_1)}{dz_1^2} + [c-(a+b+1)z_1]\frac{dG_F(z_1)}{dz_1} - ab\,G_F(z_1) = 0 \tag{5.5}$$

whose solutions are hypergeometric functions ${}_2F_1(a,b,c;z_1)$ for parameters a, b, c to be determined. The 2,1 subscripts in the hypergeometric functions will be omitted from henceforth for brevity. Comparing (5.4) with (5.5) gives the parameters to be

$$a = 1+\nu, \quad b = 1-\nu \quad \text{and} \quad c = \frac{3}{2} \tag{5.6}$$

where ν is given by (4.16). From [39, §15.10.2] we can write the solution to (5.5) in a neighbourhood of $z_1 = 0$, $s = 0$ as

$$G_F(x,x') = CF\left(1+\nu, 1-\nu, \frac{3}{2}; z_1\right) + Dz_1^{-\frac{1}{2}}F\left(\frac{1}{2}+\nu, \frac{1}{2}-\nu, \frac{1}{2}; z_1\right) \tag{5.7}$$

where C and D are arbitrary constants. This solution is valid for $\nu \in [0,1]$ but for now we focus on $\nu \in (0,1)$ and return to the special cases of $\nu = 0, 1$ later. In the coincidence limit where

$s \to 0, z_1 \to 0$ both hypergeometric functions tend to unity so, using (5.3), we can write the leading order behaviour of $G_F(s)$ as

$$G_F(s) \sim C - \frac{iD}{\sinh\left(\frac{s}{2L}\right)} \quad \text{as} \quad s \to 0 \tag{5.8}$$

from whence it can be seen that the $D-$ term on the right hand side is clearly divergent in the coincidence limit.

As the Feynman Green's function, and hence $\langle\hat{\Phi}^2\rangle$, is formally divergent when the spacetime points x, x' are brought together, we use Hadamard renormalisation (Section 1.5) to extract a physically meaningful result. We match the divergent term in (5.8) to the divergent term in the corresponding Hadamard parametrix, G_H, which in three dimensions is given by (1.75) and reproduced here for convenience

$$G_H(x,x') = \frac{i}{4\sqrt{2}\pi}\left[\frac{U(x,x')}{\sigma^{1/2}} + W(x,x')\right]. \tag{5.9}$$

Here $U(x,x')$ and $W(x,x')$ are biscalars, regular in the coincidence limit (Section 1.5) and σ is Synge's world function (1.57). As we are dealing with a maximally symmetric state with Dirichlet or Neumann boundary conditions, we can write $U(x,x') = U(s)$, which has an expansion of the form [35]

$$\begin{aligned} U(s) &= \sum_{n=0}^{\infty} U_n(s)\sigma^n(s) \\ &= U_0 + U_1\sigma^1 + U_2\sigma^2 + \ldots. \end{aligned} \tag{5.10}$$

with $U_0 = \Delta^{1/2}$ and Δ is the van Vleck Morette determinant (1.61) which satisfies the boundary condition [35]

$$\lim_{s\to 0}\Delta(s) = 1. \tag{5.11}$$

Therefore as we approach the coincidence limit, the divergent part of the Hadamard parametrix, $\tilde{G}_H$ (5.9) is given by

$$\tilde{G}_H = \frac{i}{4\pi s}, \tag{5.12}$$

which is in agreement with the findings in [61]. It now remains to fix the constants C and D in (5.7). For the latter, we match the divergent term in (5.8) with (5.12). Using the Maclaurin expansion of $\sinh(s/2L)$ to first order gives

$$D = -\frac{1}{8\pi L}. \tag{5.13}$$

The other constant C is determined by considering the form of the Green's function (5.7) at the boundary as $s \to \infty$ and applying the appropriate boundary condition. This is achieved by applying Kummer's connection formulae [39, §15.10 (ii)] to the hypergeometric functions in (5.7) to give

$$G_F(s) = \left\{ \frac{C\sqrt{\pi}}{2\Gamma(1-\nu)} + \frac{i\sqrt{\pi}}{8\pi L\,\Gamma(-\nu)} \right\} \frac{\Gamma(-2\nu)}{\Gamma(\frac{1}{2}-\nu)} \left[\cosh\left(\frac{s}{2L}\right)\right]^{-2(1+\nu)} F\left(1+\nu, \frac{1}{2}+\nu, 1+2\nu; \frac{1}{1-z_1}\right)$$
$$+ \left\{ \frac{C\sqrt{\pi}}{2\Gamma(1+\nu)} + \frac{i\sqrt{\pi}}{8\pi L\,\Gamma(\nu)} \right\} \frac{\Gamma(2\nu)}{\Gamma(\frac{1}{2}+\nu)} \left[\cosh\left(\frac{s}{2L}\right)\right]^{-2(1-\nu)} F\left(1-\nu, \frac{1}{2}-\nu, 1-2\nu; \frac{1}{1-z_1}\right). \tag{5.14}$$

For Dirichlet boundary conditions, we require that $G_F(s) \to 0$ as $s \to \infty$. It is evident from (5.14) that both the hypergeometric functions converge to unity as $s \to \infty$, $z_1 \to -\infty$. Also, as we consider $0 < \nu < 1$, it is clear that both terms in (5.14) converge to zero but the second term converges more slowly. Using the analysis in [29] we can define our Dirichlet boundary condition by requiring that $G_F(s) \to 0$ as rapidly as possible. Therefore, for rapid convergence to zero, we require

$$\frac{C\sqrt{\pi}}{2\Gamma(1+\nu)} + \frac{i\sqrt{\pi}}{8\pi L\,\Gamma(\nu)} = 0, \tag{5.15}$$

giving

$$C = -\frac{i\Gamma(1+\nu)}{4\pi L\Gamma(\nu)}. \tag{5.16}$$

Using the relation $\Gamma(1+\nu) = \nu\Gamma(\nu)$ [39, §5.1.1], we have for the Dirichlet boundary condition

$$C = -\frac{i\nu}{4\pi L}. \tag{5.17}$$

Using the values of the constants C and D, we can now write the vacuum Feynman Green's function with Dirichlet boundary conditions as

$$G_0^D(s) = -\frac{i\nu}{4\pi L} F\left(1+\nu, 1-\nu, \frac{3}{2}; -\sinh^2\left(\frac{s}{2L}\right)\right)$$
$$+ \frac{i}{8\pi L\,\sinh\left(\frac{s}{2L}\right)} F\left(\frac{1}{2}+\nu, \frac{1}{2}-\nu, \frac{1}{2}; -\sinh^2\left(\frac{s}{2L}\right)\right). \tag{5.18}$$

Calculation of the vacuum Green's functions with Neumann boundary conditions presents a greater challenge. In the case of the massless, conformally coupled field ($\nu = 1/2$), the Neumann boundary condition can be defined naturally [8], as we can map the field onto the globally hyperbolic ESU, whose line element is given by [55]

$$ds^2 = L^2[-dt^2 + d\rho^2 + \sin^2\rho\, d\theta^2]. \tag{5.19}$$

The metric in adS is conformally related to that in ESU by

$$\tilde{g}_{\mu\nu} = \Omega^2 g_{\mu\nu}, \tag{5.20}$$

where $\tilde{g}_{\mu\nu}$ is the metric in ESU, $g_{\mu\nu}$ is the metric in adS and

$$\Omega^2 = \cos^2\rho \tag{5.21}$$

is the conformal factor. As the boundary of adS is not part of the space-time we establish boundary conditions on the conformally invariant field on ESU instead. For the massless, conformally coupled field we can write (5.7) as

$$G_F = C(1-z_1)^{-1/2} + Dz_1^{-1/2} = \frac{C}{\cosh\left(\frac{s}{2L}\right)} - \frac{iD}{\sinh\left(\frac{s}{2L}\right)}, \tag{5.22}$$

which is valid for all $s \in [0,\infty)$. Transforming to the ESU, the Feynman Green's function of the massless, conformally coupled field takes the form

$$G_F^{ESU}(t,\theta,\rho\,;t',\rho',\theta') = \frac{\sqrt{2}}{\sqrt{\cos\rho\cos\rho'}}\left\{C\left[\frac{\cos\Delta t}{\cos\rho\cos\rho'} - \tan\rho\tan\rho'\cos\Delta\theta + 1\right]^{-1/2}\right.$$
$$\left. -iD\left[\frac{\cos\Delta t}{\cos\rho\cos\rho'} - \tan\rho\tan\rho'\cos\Delta\theta - 1\right]^{-1/2}\right\}, \tag{5.23}$$

where we have used

$$\cosh\left(\frac{s}{L}\right) = \frac{\cos\Delta\tau}{\cos\rho\cos\rho'} - \tan\rho\tan\rho'\cos\Delta\theta, \tag{5.24}$$

with $\Delta\tau = \tau - \tau'$ and $\Delta\theta = \theta - \theta'$. For the Neumann boundary condition we require that

$$\frac{\partial G_F^{ESU}}{\partial\rho'}(\rho,\rho') \to 0 \quad \text{as} \quad \rho' \to \pi/2. \tag{5.25}$$

The derivative in (5.25) can be calculated using MATHEMATICA and then expanded to first order in $(\rho' - \pi/2)$ to give

$$\begin{aligned}\frac{\partial G_F^{ESU}}{\partial\rho'} &= \frac{(C+iD)\cos\rho}{\sqrt{2}(\cos\Delta\tau - \cos\Delta\theta\sin\rho)^{3/2}} \\ &+ \frac{(C-iD)(3\cos^2\rho - 2\cos\Delta\tau\cos\Delta\theta\sin\rho + 2\cos^2\Delta\theta\sin^2\rho)(\rho'-\pi/2)}{2\sqrt{2}(\cos\Delta\tau - \cos\Delta\theta\sin\rho)^{5/2}} \\ &+ \mathcal{O}(\rho'-\pi/2)^{9/2},\end{aligned} \tag{5.26}$$

from whence it can be readily seen that in order to satisfy the Neumann boundary condition as $\rho' \to \pi/2$, we require that $C = -iD$.

For the scalar field with general mass and coupling, the above method of mapping to ESU is no longer applicable, and we can choose how 'Neumann' boundary conditions are defined [29] (see Section 4.3). In keeping with [29, 59], we now choose the relationship $C = -iD$ between C and D for the Neumann boundary condition for general ν, yielding

$$C = \frac{i\nu}{4\pi L}. \tag{5.27}$$

With this value of the constant C, together with (5.13), we can write the Feynman's Green's function for the scalar field with general mass and coupling, subject to Neumann boundary conditions, as

$$G_0^N(s) = + \frac{i\nu}{4\pi L} F\left(1+\nu, 1-\nu, \frac{3}{2}; -\sinh^2\left(\frac{s}{2L}\right)\right) + \frac{i}{8\pi L \sinh\left(\frac{s}{2L}\right)} F\left(\frac{1}{2}+\nu, \frac{1}{2}-\nu, \frac{1}{2}; -\sinh^2\left(\frac{s}{2L}\right)\right), \tag{5.28}$$

which differs from the Dirichlet form (5.18) only in the sign of the first term.

Having constructed the vacuum Feynman Green's functions for Dirichlet and Neumann boundary conditions (5.18, 5.28), we are now in a position to determine the renormalised v.e.v. of the VP, denoted by $\langle\hat{\Phi}^2\rangle_{0,\text{ren}}$, which is given by

$$\langle\hat{\Phi}^2\rangle_{0,\text{ren}} = \lim_{s\to 0}[-iG_0^{D/N} - (-i\widetilde{G}_H)], \tag{5.29}$$

where $\widetilde{G}_H$ is the divergent part of the Hadamard parametrix given by (5.12). The expansions of (5.18, 5.28) for small s are

$$G_0^{N/D}(s) \sim \pm\frac{\nu}{4\pi L}\left(1-\mathcal{O}(s^2)\right) + \frac{1}{8\pi L}\left(\frac{2L}{s} - \frac{s}{12L} + \mathcal{O}(s^3)\right)\left(1-\mathcal{O}(s^2)\right), \tag{5.30}$$

where the +/- refers to Neumann and Dirichlet respectively. Thus in the limit as $s \to 0$ we have, for the Dirichlet boundary condition,

$$\langle\hat{\Phi}^2\rangle_{0,\text{ren}}^D = -\frac{\nu}{4\pi L}. \tag{5.31}$$

This matches the result found in [61] in three dimensions. From now on the 'ren' subscript will be omitted and it will be assumed that all expectation values are renormalised. Likewise, the renormalised vacuum expectation value of the VP with Neumann boundary conditions is

$$\langle\hat{\Phi}^2\rangle_0^N = \frac{\nu}{4\pi L}. \tag{5.32}$$

This has the same magnitude as the Dirichlet case but opposite sign. It can be seen that in the case $\nu = 0$ both boundary conditions give the same result (see Section 5.1.3 where we consider this case in more detail). With both Dirichlet and Neumann boundary conditions, we note that the v.e.v.s depend only on ν and are independent of the radial coordinate. Therefore they respect the maximal symmetry of the background space-time.

5.1.2 Thermal expectation values

We now determine the thermal Green's function, $G_\beta(t, \mathbf{x}; t', \mathbf{x}')$, for inverse temperature β, where $\mathbf{x} = (\rho, \theta)$. The thermal Green's functions are periodic in imaginary time and can be expressed as an infinite sum involving the vacuum Green's function $G_0(x, x')$ [17] (see Section 1.3). The thermal Green's function appearing in the sum in (1.49) depends on the proper distance between the space-time points $(t + ij\beta, \mathbf{x})$ and $(t', \mathbf{x}')$, which can be found using (5.24). However, as the divergent part of the Hadamard parametrix is independent of the state (see Section 1.5), we consider the difference

between the thermal and vacuum Green's functions. Bringing the space-time points together, that is, in the limit $t' \to t$, $\mathbf{x}' \to \mathbf{x}$, we have for the Dirichlet boundary condition

$$G^D_\beta(\rho) - G^D_0(\rho) = \frac{1}{4\pi L} \sum_{j=-\infty, j\neq 0}^{j=\infty} \Bigg\{ -i\nu F\left(1+\nu, 1-\nu, \frac{3}{2}; \frac{1-\cosh(j\beta)}{2\cos^2\rho}\right) + \frac{i\sqrt{2}\cos\rho}{2\sqrt{\cosh(j\beta)-1}} F\left(\frac{1}{2}+\nu, \frac{1}{2}-\nu, \frac{1}{2}; \frac{1-\cosh(j\beta)}{2\cos^2\rho}\right)\Bigg\}. \quad (5.33)$$

Likewise for the Neumann boundary condition we use (5.24, 5.28) to give

$$G^N_\beta(\rho) - G^N_0(\rho) = \frac{1}{4\pi L} \sum_{j=-\infty, j\neq 0}^{j=\infty} \Bigg\{ i\nu F\left(1+\nu, 1-\nu, \frac{3}{2}; \frac{1-\cosh(j\beta)}{2\cos^2\rho}\right) + \frac{i\sqrt{2}\cos\rho}{2\sqrt{\cosh(j\beta)-1}} F\left(\frac{1}{2}+\nu, \frac{1}{2}-\nu, \frac{1}{2}; \frac{1-\cosh(j\beta)}{2\cos^2\rho}\right)\Bigg\}. \quad (5.34)$$

Both (5.33, 5.34) are finite and we observe that the thermal Green's functions depend on ρ and so break the maximum symmetry of the background adS, in contrast to the maximally symmetric vacuum Green's functions [3, 4].

We are now in a position to calculate the t.e.v.s of the VP. As the renormalised v.e.v. has already been calculated, we do not need to repeat the renormalisation process for the t.e.v. Instead we can look at the difference between the t.e.v. and the v.e.v. using the result

$$\langle\hat{\Phi}^2\rangle_\beta - \langle\hat{\Phi}^2\rangle_0 = -i \sum_{j=-\infty, j\neq 0}^{\infty} G_\beta(t+ij\beta, \mathbf{x}, t, \mathbf{x}). \quad (5.35)$$

We then simply add the already determined renormalised v.e.v. to the result to give the final t.e.v. Noting that (5.33, 5.34) are even functions of j gives, for the Dirichlet boundary condition,

$$\langle\hat{\Phi}^2\rangle^D_\beta - \langle\hat{\Phi}^2\rangle^D_0 = \frac{1}{2\pi L} \sum_{j=1}^{\infty} \Bigg\{ -\nu F\left(1+\nu, 1-\nu, \frac{3}{2}; \frac{1-\cosh(j\beta)}{2\cos^2\rho}\right) + \frac{\sqrt{2}\cos\rho}{2\sqrt{\cosh(j\beta)-1}} F\left(\frac{1}{2}+\nu, \frac{1}{2}-\nu, \frac{1}{2}; \frac{1-\cosh(j\beta)}{2\cos^2\rho}\right)\Bigg\}, \quad (5.36)$$

and for the Neumann boundary condition we have

$$\langle\hat{\Phi}^2\rangle^N_\beta - \langle\hat{\Phi}^2\rangle^N_0 = \frac{1}{2\pi L} \sum_{j=1}^{\infty} \Bigg\{ \nu F\left(1+\nu, 1-\nu, \frac{3}{2}; \frac{1-\cosh(j\beta)}{2\cos^2\rho}\right) + \frac{\sqrt{2}\cos\rho}{2\sqrt{\cosh(j\beta)-1}} F\left(\frac{1}{2}+\nu, \frac{1}{2}-\nu, \frac{1}{2}; \frac{1-\cosh(j\beta)}{2\cos^2\rho}\right)\Bigg\}. \quad (5.37)$$

The t.e.v.s of the VP, $\langle\hat{\Phi}^2\rangle_\beta$, with both Dirichlet and Neumann boundary conditions (5.36, 5.37) are calculated numerically using MATHEMATICA. We were able to consider values of the radial

coordinate, ρ in the interval $\rho \in [0, 99\pi/200]$ and found that the $j-$sums in (5.36, 5.37) converge exponentially, so the $j-$sum was performed in the interval $|j| \leq 20$. The relative error in truncating the $j-$sum to 20 was very low. For instance, away from the space-time boundary at $\rho = 30\pi/200$ (with $\nu = 1/2, \beta = 1$), the relative error of truncating the $j-$sum to 20 compared to 100 was $\sim 7.3 \times 10^{-14}$. This did not change appreciably when we move closer to the space-time boundary with the relative error at $\rho = 99\pi/200$ being $\sim 2.7 \times 10^{-14}$.

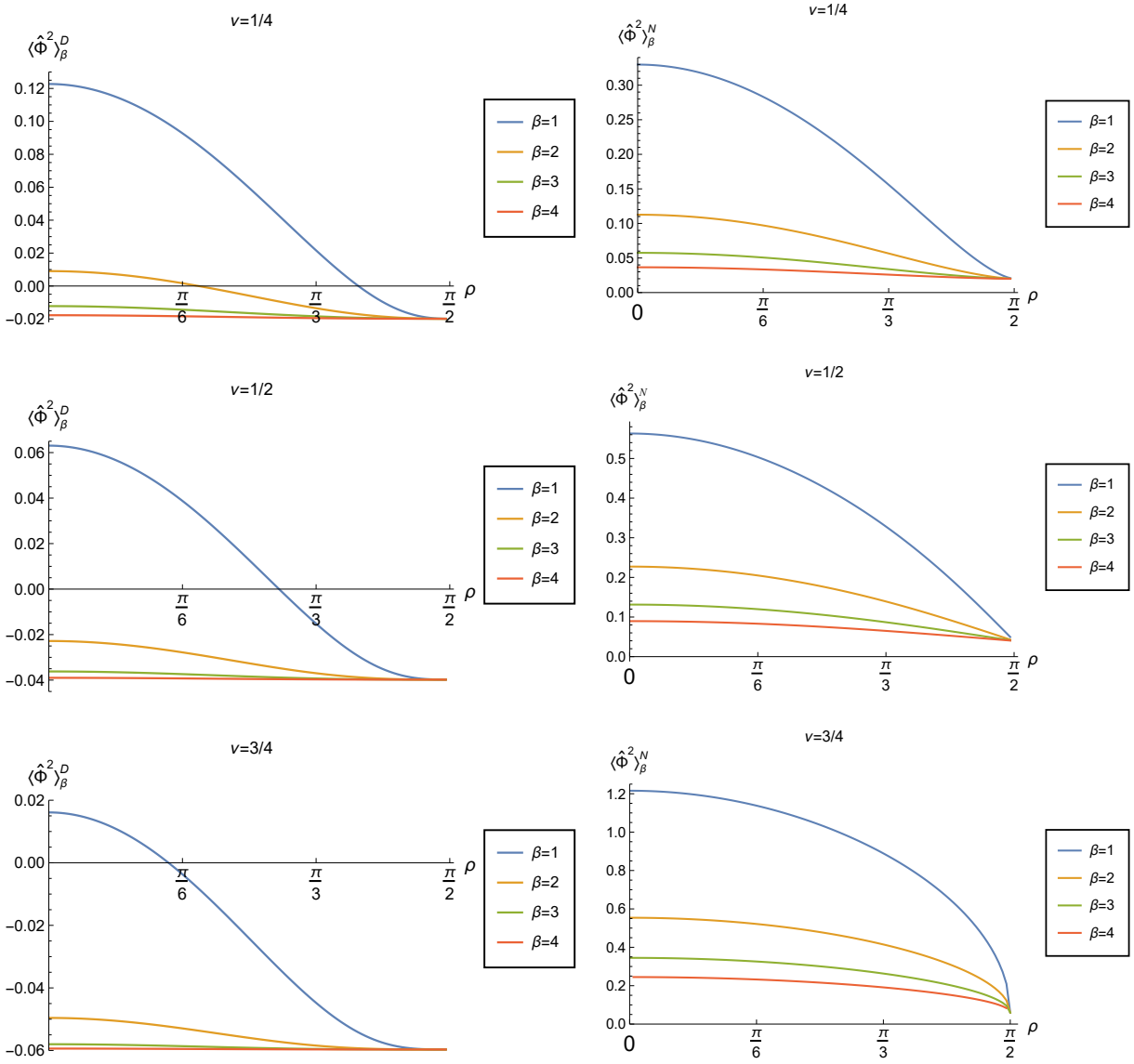

Figure 5.1: Renormalised t.e.v.s of the VP $\langle\hat{\Phi}^2\rangle_\beta$ as a function of ρ, with Dirichlet (left) and Neumann (right) boundary conditions, for a range of values of the inverse temperature, β. Top row shows $\nu = 1/4$, middle row shows $\nu = 1/2$ and bottom row shows $\nu = 3/4$.

The results for the t.e.v.s are shown in Figures 5.1–5.3 for different values of the inverse temperature β. Figure 5.1 shows $\langle\hat{\Phi}^2\rangle_\beta$ for Dirichlet (left) and Neumann (right) boundary conditions, for four different values of the inverse temperature β and for three values of ν ($\nu = 1/4$, $1/2$, and $3/4$).

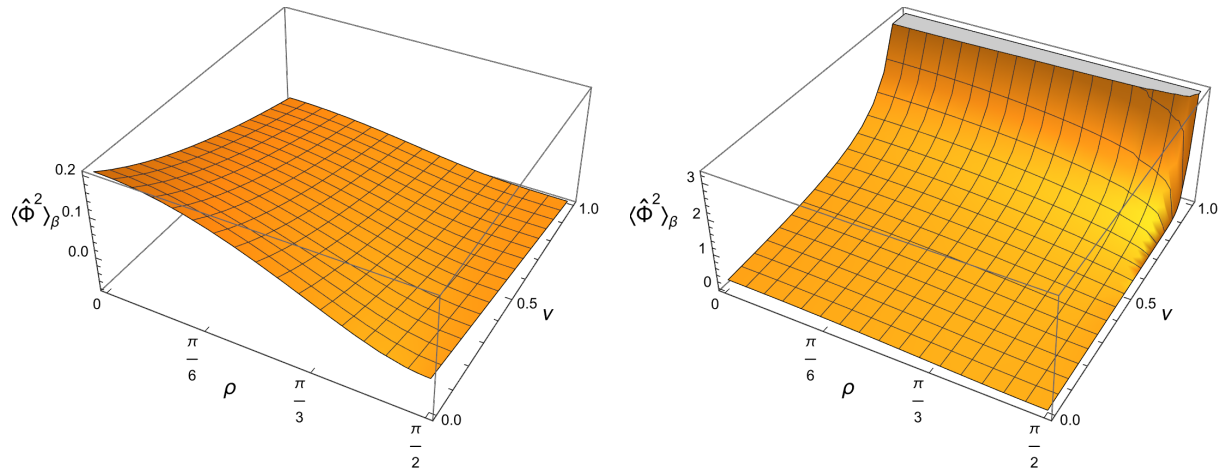

Figure 5.2: Renormalised t.e.v.s of the VP $\langle\hat{\Phi}^2\rangle_\beta$, as a function of ρ and ν, with Dirichlet (left) and Neumann (right) boundary conditions. In both cases $\beta = 1$.

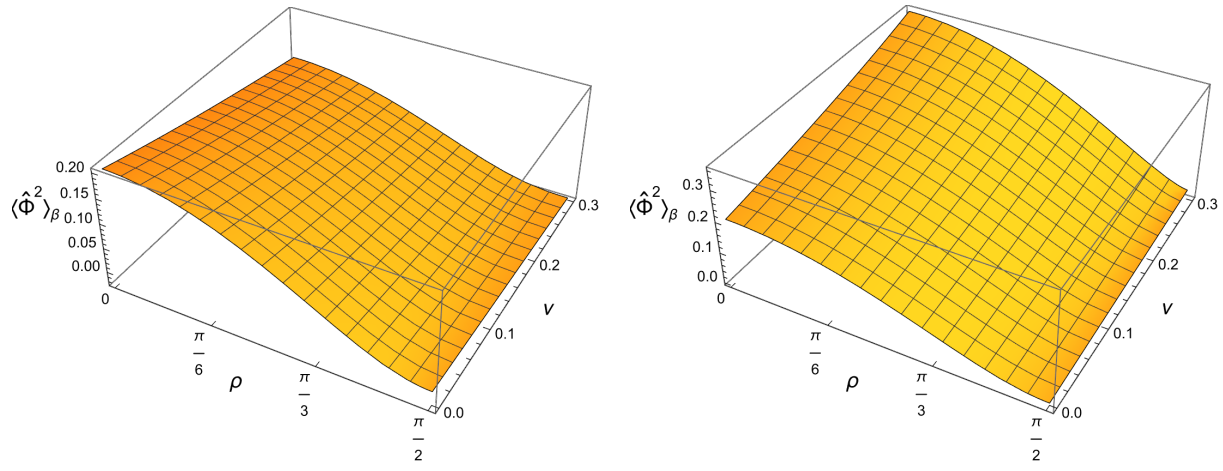

Figure 5.3: Close up view of Figure 5.2 showing $\langle\hat{\Phi}^2\rangle_\beta$, for Dirichlet (left) and Neumann (right) boundary conditions, for $\nu \in (0, 0.3)$ and $\beta = 1$.

Figure 5.2 shows the three-dimensional surface plots of $\langle\hat{\Phi}^2\rangle_\beta$ as a function of ρ and ν, for Dirichlet (left) and Neumann (right) boundary conditions. The plots in Figure 5.1 are qualitatively similar to those in [4], showing that the thermal energy of the field concentrates in a region close to the origin, thereby breaking the translational symmetry of the background adS space-time. For all values of the inverse temperature and $\nu \in (0,1)$, the t.e.v.s of the VP attain their maximum value at the origin, and are monotonically decreasing towards the boundary. We also see that for increasing β (decreasing temperature), the t.e.v.s approach the v.e.v.s, as observed in [71] for the four-dimensional, massless, conformally coupled scalar field. Approaching the space-time boundary as $\rho \to \pi/2$, we recover the zero temperature v.e.v. for all β and ν. For the Neumann boundary condition, the convergence to the vacuum result, as $\rho \to \pi/2$, occurs less rapidly than in the Dirichlet case.

Although the t.e.v.s for the cases of $\nu = 0, 1$ have not specifically been determined in the above analysis (see Section 5.1.3 for analysis of these values of ν), Figure 5.3, which shows an expanded view of Figure 5.2 for $\nu \in (0, 0.3)$, suggests that $\langle\hat{\Phi}^2\rangle_\beta$ reaches the same value for both Dirichlet and Neumann boundary conditions as $\nu \to 0$ for all ρ. For the Dirichlet boundary condition, at fixed ρ the t.e.v. $\langle\hat{\Phi}^2\rangle_\beta$ has its maximum value at $\nu = 0$ and decreases for increasing ν. For the Neumann boundary condition, however, at fixed ρ the t.e.v. $\langle\hat{\Phi}^2\rangle_\beta$ has its minimum value at $\nu = 0$, and increases steadily for increasing ν. As $\nu \to 1$, it appears to be the case that $\langle\hat{\Phi}^2\rangle_\beta$ diverges, in accordance with the result in [59] that there is no generalized Neumann boundary condition for $\nu = 1$ (see discussion at the end of Section 4.5).

5.1.3 Vacuum and thermal expectation values for $\nu = 0, 1$

The analysis in the previous subsections was valid for $\nu \in (0,1)$. We now consider the particular cases $\nu = 0, 1$. First, for $\nu = 0$, the vacuum Green's function (5.7) simplifies to

$$G_F(z_1) = \frac{C \sin^{-1}\sqrt{z_1}}{\sqrt{z_1}\sqrt{1-z_1}} + \frac{D}{\sqrt{z_1}\sqrt{1-z_1}}. \tag{5.38}$$

Using the Taylor expansion of $\sin^{-1}\sqrt{z_1}$, as $z_1 \to 0$ we have

$$G_F(z_1) \sim C + \frac{D}{\sqrt{z_1}}, \tag{5.39}$$

the second term of which is clearly divergent. Matching the $D-$term to the divergent part of the Hadamard parametrix (5.12) gives the same value of D as in (5.13). To obtain the value of the constant C, we adopt the same procedure used earlier, namely we consider the form of the Green's function (5.38) at the space-time boundary. Using (5.3) and the series expansion for $\sin^{-1}\sqrt{z_1}$ as $z_1 \to -\infty$ ($s \to \infty$), we obtain

$$G_F(s) \sim \frac{-Cs}{2L\sinh^2(\frac{s}{2L})} + \frac{iD}{\sinh^2(\frac{s}{2L})} \quad \text{as} \quad s \to \infty. \tag{5.40}$$

Equation (5.40) shows that $G_F(s) \to 0$ as $s \to \infty$ for all values of C. However, applying Dirichlet boundary conditions and demanding rapid convergence to zero requires $C = 0$, as in Section 5.1.1.

Applying the results of Section 5.1.1 for $\nu = 0$, we find from (5.17) that $C = 0$ for Neumann boundary conditions also. Therefore, for $\nu = 0$, the Neumann boundary condition corresponds to the Dirichlet boundary condition, and so we cannot consider Robin (mixed) boundary conditions. However, in this case there still remains a one-parameter family of boundary conditions leading to consistent classical dynamics [59]. We can construct a one-parameter family of maximally symmetric vacuum Green's functions by choosing a nonzero value of the constant C. In order to obtain a real expectation value for the v.e.v., we define $C = i\widetilde{C}$ for $\widetilde{C} \in \mathbb{R}$. Thus (5.39) becomes

$$\begin{aligned} G_F(z_1) &\sim i\widetilde{C} + \frac{D}{\sqrt{z_1}}, \\ &\sim i\widetilde{C} + \frac{i}{8\pi L}\left(\frac{2L}{s} + \mathcal{O}(s)\right), \end{aligned} \tag{5.41}$$

where in the second line we have used the Maclaurin series expansion of $\sqrt{z_1}$ and the value of the D constant in (5.13). Using (5.29) and (5.12), the renormalised v.e.v. of the VP is then

$$\langle \hat{\Phi}^2 \rangle_0 = \widetilde{C}. \tag{5.42}$$

Varying the constant $\widetilde{C}$ therefore results simply in a constant shift of the v.e.v. of the VP.

For $\nu = 1$, the vacuum Green's function (5.7) simplifies to

$$G_F(z_1) = C + \frac{D(1 - 2z_1)}{\sqrt{z_1}\sqrt{1 - z_1}}. \tag{5.43}$$

Matching the divergent term in (5.43) with the corresponding term in the Hadamard parametrix (5.12), as $z_1 \to 0$, reveals the same value of the constant D in (5.13). To find the constant C, we use the same analysis as previously and consider the form of (5.43) at the space-time boundary as $z_1 \to -\infty$, giving

$$G_F \sim C - 2iD. \tag{5.44}$$

Thus, for the Dirichlet boundary condition with $\nu = 1$, the constant C is

$$C = -\frac{i}{4\pi L}, \tag{5.45}$$

giving the same result as in (5.17). We can therefore write the vacuum Feynman Green's function (5.43), with Dirichlet boundary condition, for $\nu = 1$, as

$$G_F(s) = -\frac{i}{4\pi L} + \frac{i\cosh(\frac{s}{L})}{8\pi L \sinh^2(\frac{s}{2L})\cosh^2(\frac{s}{2L})}. \tag{5.46}$$

Using (5.29, 5.46) gives the v.e.v. of the VP for $\nu = 1$, with Dirichlet boundary conditions, to be

$$\langle \hat{\Phi}^2 \rangle_0 = -1/4\pi L, \tag{5.47}$$

consistent with the value found for $\nu \in (0, 1)$ in (5.31). As discussed in Section 4.5 we do not have Neumann boundary conditions for $\nu = 1$.

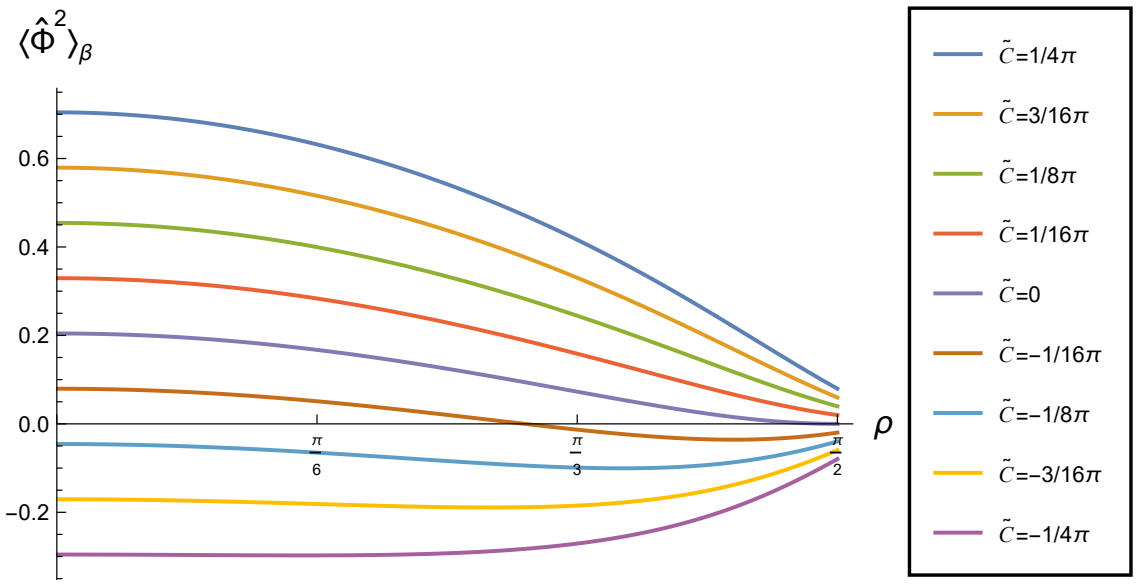

Figure 5.4: Renormalised t.e.v.s of the VP, $\langle\hat{\Phi}^2\rangle_\beta$, as functions of the radial coordinate ρ, for $\nu = 0$ and different values of $\tilde{C}$ with $\beta = 1$.

We can calculate the t.e.v. for the VP, for $\nu = 0, 1$, along the same lines as we did for $\nu \in (0, 1)$ previously. For $\nu = 0$, we express the difference between the t.e.v. and the v.e.v. of the VP as

$$\langle\hat{\Phi}^2\rangle_\beta - \langle\hat{\Phi}^2\rangle_0 = \sum_{j=1}^{j=\infty}\left\{\frac{2\sqrt{2}\,\widetilde{C}\cos\rho}{\sqrt{\cosh j\beta + \cos 2\rho}} + \frac{\cos^2\rho}{2\pi L\sqrt{(\cosh j\beta - 1)(\cosh j\beta + \cos 2\rho)}}\right\}, \tag{5.48}$$

where $\langle\hat{\Phi}^2\rangle_0$ is given in (5.42). Figure 5.4 shows the t.e.v.s for various different values of $\widetilde{C}$ and inverse temperature $\beta = 1$. As we approach the space-time boundary ($\rho \to \pi/2$), the t.e.v.s converge to the v.e.v.s (which depend on $\widetilde{C}$ (5.42)). For $\widetilde{C} = 0$, the t.e.v.s match those seen in Figure 5.3 for $\nu \to 0$. A feature of the t.e.v.s in Figure 5.4 is that the profiles of the t.e.v.s depend on the value of the constant $\widetilde{C}$. For $\widetilde{C} > 0$, the t.e.v. profiles are similar to those in Figure 5.1, in that they have their maximum at the space-time origin and then monotonically decrease as the space-time boundary is approached. However, for $\widetilde{C} < 0$, the t.e.v.s are monotonically increasing close to the boundary. For small and negative $\widetilde{C}$, there is still a maximum at the origin, but for sufficiently negative $\widetilde{C}$ the t.e.v.s have a minimum at the origin and monotonically increase with increasing ρ.

Using the same method for $\nu = 1$, the t.e.v. of the VP, with Dirichlet boundary conditions applied, is found to be

$$\langle\hat{\Phi}^2\rangle^D_\beta - \langle\hat{\Phi}^2\rangle^D_0 = \frac{1}{2\pi L}\sum_{j=1}^{j=\infty}\left\{\frac{(\cosh j\beta - \sin^2\rho)}{\sqrt{\cosh j\beta - 1}\sqrt{\cosh j\beta + \cos 2\rho}} - 1\right\}, \tag{5.49}$$

from which it can be readily seen that at $\rho = \pi/2$, we obtain $\langle\hat{\Phi}^2\rangle^D_\beta = -1/4\pi L$ consistent with Figure 5.2. If we try to find the t.e.v. of the VP with Neumann boundary conditions (by using the

value (5.27) for C), we obtain

$$\langle\hat{\Phi}^2\rangle^N_\beta - \langle\hat{\Phi}^2\rangle^N_0 = \frac{1}{2\pi L}\sum_{j=1}^{j=\infty}\left\{\frac{(\cosh j\beta - \sin^2\rho)}{\sqrt{\cosh j\beta - 1}\sqrt{\cosh j\beta + \cos 2\rho}} + 1\right\}. \tag{5.50}$$

For large j, it can be seen that the summand in (5.49) tends to zero, whereas the sum in (5.50) is divergent. This shows that for $\nu = 1$, we only have Dirichlet boundary conditions (Section 4.5).

§ 5.2 Vacuum polarisation with Robin boundary conditions

Having computed the renormalised t.e.v.s and v.e.v.s of the VP for a scalar field with general mass and coupling, when either Dirichlet or Neumann boundary conditions are applied, we now turn our attention to more general mixed (Robin) boundary conditions. As in the case for the RSET on adS4, Section 3.2, we employ Euclidean methods, so that the Green's function is unique and to circumvent the requirement to use an $i\epsilon$-prescription.

5.2.1 Euclidean Green's functions

The Euclidean Green's function, $G_E(x, x')$, for the scalar field on adS3 satisfies the inhomogeneous PDE

$$\begin{aligned}\underbrace{\left(\Box_E - \mu^2\right)}_{\mathcal{L}_x} G_E(x,x') &= -\frac{1}{\sqrt{g_E}}\delta^3(x,x') \\ &= -\frac{1}{L^3\sec^3\rho\sin\rho}\delta(\tau-\tau')\delta(\rho-\rho')\delta(\theta-\theta'),\end{aligned} \tag{5.51}$$

where μ is given in (4.1), g_E is the determinant of the Euclidean adS3 metric

$$ds^2 = L^2\sec^2\rho\,[d\tau^2 + d\rho^2 + \sin^2\rho\, d\theta^2], \tag{5.52}$$

and $\mathcal{L}_x$ is a differential operator given by

$$\mathcal{L}_x = \frac{1}{L^2\sec^2\rho}\left(\frac{\partial^2}{\partial\tau^2} + \frac{\partial^2}{\partial\rho^2} + \frac{1}{\sin^2\rho}\frac{\partial^2}{\partial\theta^2} + \frac{1}{\sin\rho\,\cos\rho}\frac{\partial}{\partial\rho} - \mu^2L^2\sec^2\rho\right). \tag{5.53}$$

For vacuum and thermal states we use the Fourier representation of $\delta(\theta - \theta')$ as

$$\delta(\theta-\theta') = \frac{1}{2\pi}\sum_{\ell=-\infty}^{\infty} e^{i\ell\Delta\theta}, \tag{5.54}$$

where $\Delta\theta$ represents the separation of the angular coordinate. For the vacuum Green's function we use

$$\delta(\tau-\tau') = \frac{1}{2\pi}\int_{-\infty}^{\infty} e^{i\omega\Delta\tau}d\omega, \tag{5.55}$$

where $\Delta\tau$ represents the separation of the time coordinate. Using (5.54, 5.55), we can write an ansatz for the vacuum Euclidean Green's function, $G_E^0(x,x')$, as

$$G_E^0(x,x') = \frac{1}{4\pi^2}\int_{-\infty}^{\infty} e^{i\omega\Delta\tau}d\omega \sum_{\ell=-\infty}^{\infty} e^{i\ell\Delta\theta} g_{\omega\ell}(\rho,\rho'), \tag{5.56}$$

where $g_{\omega\ell}(\rho,\rho')$ is the vacuum radial Green's function. Applying the differential operator (5.53) to (5.56), we find that $g_{\omega\ell}(\rho,\rho')$ satisfies

$$\cos^2\rho\,\frac{\partial^2 g_{\omega\ell}}{\partial\rho^2}(\rho,\rho') + \cot\rho\,\frac{\partial g_{\omega\ell}}{\partial\rho}(\rho,\rho') + (-\omega^2\cos^2\rho - \ell^2\cot^2\rho - \mu^2L^2)g_{\omega\ell}(\rho,\rho') = -\frac{\cot\rho\cos^2\rho}{L}\delta(\rho-\rho'). \tag{5.57}$$

For the thermal Green's functions, with inverse temperature β, we use the mode sum representation of $\delta(\tau-\tau')$

$$\delta(\tau-\tau') = \frac{\kappa}{2\pi}\sum_{n=-\infty}^{\infty} e^{in\kappa\Delta\tau}, \tag{5.58}$$

where

$$\kappa = \frac{2\pi}{\beta}, \tag{5.59}$$

and ω is replaced by $n\kappa$ (where $n\in\mathbb{Z}$). A suitable ansatz for the thermal Green's function is then

$$G_E^\beta(x,x') = \frac{\kappa}{4\pi^2}\sum_{n=-\infty}^{\infty}\sum_{\ell=-\infty}^{\infty} e^{in\kappa\Delta\tau}e^{i\ell\Delta\theta} g_{n\ell}(\rho,\rho'), \tag{5.60}$$

where $g_{n\ell}(\rho,\rho')$ is the thermal radial Green's function which also satisfies (5.57) with ω^2 replaced by $n^2\kappa^2$.

We now consider the solution of the homogeneous version of (5.57). Using the substitution

$$z = \cos^2\rho, \tag{5.61}$$

our analysis mirrors that for the mode solutions of the Klein-Gordon equation (4.4) in Lorentzian space-time, Section 4.1. We find that the general solution $q_{\omega\ell}$ of the homogeneous version of (5.57) is

$$q_{\omega\ell}(\rho) = [\cos\rho]^A[\sin\rho]^B\left\{\mathscr{C}_1 F(a,b,c;z) + \mathscr{C}_2\, z^{1-c}F(a-c+1,b-c+1,2-c;z)\right\}, \tag{5.62}$$

where $\mathscr{C}_1$ and $\mathscr{C}_2$ are arbitrary constants. The list of the possible parameters for the hypergeometric functions in (5.62) are given in Table 5.1. As in Section 4.1 we are free to choose the parameters from rows one or three in Table 5.1. Choosing row three gives

$$a = \frac{1}{2}(A+B) - \frac{1}{2}i\omega, \qquad b = \frac{1}{2}(A+B) + \frac{1}{2}i\omega, \qquad c = 1+\nu, \tag{5.63}$$

row	A, B	a	b	c
1	$A = 1-\nu;\ B = +\lvert\ell\rvert$	$\frac{1}{2}(1+\lvert\ell\rvert-\nu-i\omega)$	$\frac{1}{2}(1+\lvert\ell\rvert-\nu+i\omega)$	$1-\nu$
2	$A = 1-\nu;\ B = -\lvert\ell\rvert$	$\frac{1}{2}(1-\lvert\ell\rvert-\nu-i\omega)$	$\frac{1}{2}(1-\lvert\ell\rvert-\nu+i\omega)$	$1-\nu$
3	$A = 1+\nu;\ B = +\lvert\ell\rvert$	$\frac{1}{2}(1+\lvert\ell\rvert+\nu-i\omega)$	$\frac{1}{2}(1+\lvert\ell\rvert+\nu+i\omega)$	$1+\nu$
4	$A = 1+\nu;\ B = -\lvert\ell\rvert$	$\frac{1}{2}(1-\lvert\ell\rvert+\nu-i\omega)$	$\frac{1}{2}(1-\lvert\ell\rvert+\nu+i\omega)$	$1+\nu$

Table 5.1: Possible parameters for the hypergeometric solutions to (5.57). For thermal states, ω is replaced by $n\kappa$.

and

$$A = 1+\nu, \quad B = |\ell| \quad \text{for} \quad \ell \in \mathbb{Z}. \tag{5.64}$$

The a and b coefficients are complex conjugates. For the thermal Green's function we substitute $n\kappa$ for ω in (5.63).

Since we are considering $\nu \in (0,1)$, the solution (5.62) is regular at $z=0$ (which corresponds to the space-time boundary $\rho = \pi/2$) for all values of $\mathscr{C}_1$, $\mathscr{C}_2$. This is a manifestation of the requirement to impose boundary conditions on the scalar field at $z=0$. In general, $q_{\omega\ell}(\rho)$ is divergent at the origin $\rho = 0$ ($z=1$). The solution $p_{\omega\ell}$ of the homogeneous version of (5.57) which is regular at the origin is

$$p_{\omega\ell}(\rho) = \mathscr{C}_3[\cos\rho]^A[\sin\rho]^B\, F(a,b,a+b-c+1;1-z), \tag{5.65}$$

where $\mathscr{C}_3$ is another arbitrary constant. The second, linearly independent, solution of the radial equation has a logarithmic singularity at $z=1$, $\rho=0$ [39, §15.10(i)] and hence we eliminate this solution [29]. The hypergeometric functions in (5.62, 5.65) are related by Kummer's connection formulae [39, §15.10(ii)]. This enables us to write $p_{\omega\ell}(\rho)$ (5.65) in the alternative form

$$p_{\omega\ell}(\rho) = [\cos\rho]^A[\sin\rho]^B\{\mathcal{P}F(a,b,c;z) + \mathcal{Q}\ z^{1-c}F(a-c+1,b-c+1,2-c;z)\}, \tag{5.66}$$

where $\mathcal{P}$ and $\mathcal{Q}$ are given by (4.31) (by replacing α,β,γ by a,b,c respectively) and we have set $\mathscr{C}_3 = 1$.

The vacuum radial Green's function, $g_{\omega\ell}(\rho,\rho')$, can be constructed from $q_{\omega\ell}(\rho)$ and $p_{\omega\ell}(\rho)$ by

$$g_{\omega\ell}(\rho,\rho') = \mathscr{N}_{\omega\ell}\, p_{\omega\ell}(\rho_<)\, q_{\omega\ell}(\rho_>) \tag{5.67}$$

where $\mathscr{N}_{\omega\ell}$ is a normalisation constant and

$$\begin{aligned}\rho_< &= \min\{\rho,\rho'\},\\ \rho_> &= \max\{\rho,\rho'\}.\end{aligned} \tag{5.68}$$

We determine the normalisation constant $\mathscr{N}_{\omega\ell}$ as follows: First we multiply both sides of (5.57) by $\tan\rho\sec^2\rho$ and then integrate with respect to ρ over the interval $\rho'-\delta<\rho<\rho'+\delta$, for fixed ρ'.

This gives

$$\int_{\rho'-\delta}^{\rho'+\delta}\Bigg\{-\omega^2\tan\rho-\frac{\ell^2}{\cos\rho\sin\rho}-\mu^2L^2\tan\rho\sec^2\rho \\ +\tan\rho\frac{\partial^2}{\partial\rho^2}+\sec^2\rho\,\frac{\partial}{\partial\rho}\Bigg\}g_{\omega\ell}(\rho,\rho')\,d\rho=-\frac{1}{L}. \tag{5.69}$$

The first three terms in the integrand (5.69) and $g_{\omega\ell}$ are continuous and therefore the magnitude of these terms is bounded by a positive constant $\mathcal{K}$. So we can write

$$\begin{aligned}\Bigg|\int_{\rho'-\delta}^{\rho'+\delta}\Bigg\{-\omega^2\tan\rho-\frac{\ell^2}{\cos\rho\sin\rho}-\mu^2L^2\tan\rho\sec^2\rho\Bigg\}g_{\omega\ell}(\rho,\rho')\,d\rho\Bigg| \\ \leq\int_{\rho'-\delta}^{\rho'+\delta}\max\Bigg[\Bigg\{-\omega^2\tan\rho-\frac{\ell^2}{\cos\rho\sin\rho}-\mu^2L^2\tan\rho\sec^2\rho\Bigg\}g_{\omega\ell}(\rho,\rho')\Bigg]\,d\rho \\ \leq\int_{\rho'-\delta}^{\rho'+\delta}\mathcal{K}d\rho=2\delta\mathcal{K}.\end{aligned} \tag{5.70}$$

Therefore in the limit $\delta\to0$, the integral of the first three terms in the integrand in (5.69) vanishes. The resulting integral is then

$$\int_{\rho'-\delta}^{\rho'+\delta}\left\{\tan\rho\frac{\partial^2}{\partial\rho^2}+\sec^2\rho\frac{\partial}{\partial\rho}\right\}g_{\omega\ell}(\rho,\rho')\,d\rho=-\frac{1}{L}. \tag{5.71}$$

This can be expressed as

$$-\frac{1}{L}=\int_{\rho'-\delta}^{\rho'+\delta}\left\{\frac{\partial}{\partial\rho}\left(\tan\rho\frac{\partial}{\partial\rho}\right)\right\}g_{\omega\ell}(\rho,\rho')\,d\rho=\left[\tan\rho\,\frac{\partial g_{\omega\ell}(\rho,\rho')}{\partial\rho}\right]_{\rho'-\delta}^{\rho'+\delta}. \tag{5.72}$$

Using (5.67) and (5.72) we can write

$$\begin{aligned}-\frac{1}{L}&=\lim_{\delta\to0}\left\{\tan(\rho'+\delta)\mathscr{N}_{\omega\ell}\,p_{\omega\ell}(\rho')\frac{dq_{\omega\ell}(\rho)}{d\rho}-\tan(\rho'-\delta)\mathscr{N}_{\omega\ell}\,\frac{dp_{\omega\ell}(\rho)}{d\rho}q_{\omega\ell}(\rho')\right\} \\ &=\mathscr{N}_{\omega\ell}\tan\rho'\,\mathcal{W}_\rho\left\{p_{\omega\ell},q_{\omega\ell}\right\},\end{aligned} \tag{5.73}$$

where $\mathcal{W}$ is the Wronskian of $p_{\omega\ell},q_{\omega\ell}$ given by

$$\mathcal{W}\{p_{\omega\ell},q_{\omega\ell}\}=p_{\omega\ell}\frac{dq_{\omega\ell}}{d\rho}-q_{\omega\ell}\frac{dp_{\omega\ell}}{d\rho}. \tag{5.74}$$

Therefore, from (5.73), we have

$$\mathscr{N}_{n\ell}=-\frac{1}{L\tan\rho\,\mathcal{W}_\rho\left\{p_{n\ell},q_{n\ell}\right\}}. \tag{5.75}$$

Using [39, §15.10.2] as well as (5.62, 5.65), the Wronskian is given by

$$\mathcal{W}\{p_{\omega\ell},q_{\omega\ell}\}=2(1-c)(\mathscr{C}_1\mathcal{Q}-\mathscr{C}_2\mathcal{P})\cot\rho, \tag{5.76}$$

where $\mathscr{C}_1$, $\mathscr{C}_2$ are the constants appearing in (5.62). The thermal radial Green's function, $g_{n\ell}(\rho,\rho')$, is constructed similarly:

$$g_{n\ell}(\rho,\rho') = \mathscr{N}_{n\ell}\, p_{n\ell}(\rho_<)\, q_{n\ell}(\rho_>), \tag{5.77}$$

where $\mathscr{N}_{n\ell}$, $p_{n\ell}$ and $q_{n\ell}$ are found by making the substitution $\omega = n\kappa$ in $\mathcal{N}_{\omega\ell}$, $p_{\omega\ell}$ and $q_{\omega\ell}$ respectively.

The Robin boundary condition (2.28) has been defined for a massless, conformally coupled scalar field on ESU [71]. This is a linear combination of Dirichlet and Neumann boundary conditions at the time-like boundary at $\rho = \pi/2$, parametrised by the Robin parameter, $\zeta \in [0,\pi)$. The values $\zeta = 0$ and $\zeta = \pi/2$ correspond to Dirichlet and Neumann boundary conditions respectively. As we are dealing with a scalar field with general mass and coupling ($\nu \neq 1/2$), we cannot transform to the ESU so we consider instead generalised Robin boundary conditions [59] (Section 4.3). We adopt the approach in [29] and define the arbitrary constants $\mathscr{C}_1$ and $\mathscr{C}_2$ in terms of the Robin parameter ζ as follows:

$$\mathscr{C}_1 = \cos\zeta \quad \text{and} \quad \mathscr{C}_2 = \sin\zeta. \tag{5.78}$$

For Dirichlet boundary conditions we have $\mathscr{C}_1 = 1$ and $\mathscr{C}_2 = 0$. Then, using (4.31, 5.75, 5.76) the normalisation constant in this case is

$$\mathscr{N}^D_{\omega\ell} = -\frac{\Gamma(a)\Gamma(b)}{2L(1-c)\Gamma(c-1)\Gamma(a+b-c+1)} = -\frac{1}{2L(1-c)\mathcal{Q}}. \tag{5.79}$$

Likewise, for Neumann boundary conditions we have $\mathscr{C}_1 = 0$ and $\mathscr{C}_2 = 1$ in which case we have from (4.31, 5.75, 5.76)

$$\mathscr{N}^N_{\omega\ell} = \frac{\Gamma(a-c+1)\Gamma(b-c+1)}{2L(1-c)\Gamma(1-c)\Gamma(a+b-c+1)} = \frac{1}{2L(1-c)\mathcal{P}}. \tag{5.80}$$

For general Robin boundary conditions we find

$$\begin{aligned}\mathscr{N}^\zeta_{\omega\ell} &= \left[2L(1-c)\left\{\sin\zeta\frac{\Gamma(1-c)\Gamma(a+b-c+1)}{\Gamma(a-c+1)\Gamma(b-c+1)} - \cos\zeta\frac{\Gamma(c-1)\Gamma(a+b-c+1)}{\Gamma(a)\Gamma(b)}\right\}\right]^{-1} \\ &= \frac{1}{2L(1-c)\left[\mathcal{P}\sin\zeta - \mathcal{Q}\cos\zeta\right]}.\end{aligned} \tag{5.81}$$

The denominator of (5.81) becomes zero if ζ satisfies

$$\tan\zeta = \frac{\mathcal{Q}}{\mathcal{P}} = \frac{\Gamma(\nu)|\Gamma(\frac{|\ell|}{2}+\frac{1}{2}-\frac{\nu}{2}-\frac{i\omega}{2})|^2}{\Gamma(-\nu)|\Gamma(\frac{|\ell|}{2}+\frac{1}{2}+\frac{\nu}{2}-\frac{i\omega}{2})|^2}, \tag{5.82}$$

resulting in divergent values of (5.81) and a divergent Euclidean Green's function. Following the analysis in Section 4.5 in Lorentzian space-time, we use (5.82) to determine an upper bound for the Robin parameter ζ_{crit} beyond which our scalar field develops a classical instability. The analysis proceeds along the same lines as in Section 4.5 and we obtain the expression for ζ_{crit} given in (4.56).

5.2.2 Vacuum expectation values

Following on from the analysis in Section 5.2.1, we can now explicitly state the radial Euclidean Green's functions using (5.62, 5.65, 5.67, 5.79–5.81). The vacuum radial Green's function with Dirichlet boundary conditions, $g^D_{\omega\ell}(\rho,\rho')$, is

$$\begin{aligned} g^D_{\omega\ell}(\rho,\rho') = \mathscr{N}^D_{\omega\ell}\ &[\cos\rho]^{1+\nu}[\cos\rho']^{1+\nu}[\sin\rho]^{|\ell|}\ [\sin\rho']^{|\ell|} \\ &\times F\Big(\frac{1}{2}(1+|\ell|+\nu-i\omega),\frac{1}{2}(1+|\ell|+\nu+i\omega),1+|\ell|;\sin^2\rho_<\Big) \\ &\times F\Big(\frac{1}{2}(1+|\ell|+\nu-i\omega),\frac{1}{2}(1+|\ell|+\nu+i\omega),1+\nu;\cos^2\rho_>\Big). \end{aligned} \tag{5.83}$$

Likewise, with Neumann boundary conditions, the vacuum radial Green's function, $g^N_{\omega l}(\rho,\rho')$ is

$$\begin{aligned} g^N_{\omega\ell}(\rho,\rho') = \mathscr{N}^N_{\omega\ell}\ &[\cos\rho_<]^{1+\nu}\ [\cos\rho_>]^{1-\nu}[\sin\rho]^{|\ell|}\ [\sin\rho']^{|\ell|} \\ &\times F\Big(\frac{1}{2}(1+|\ell|+\nu-i\omega),\frac{1}{2}(1+|\ell|+\nu+i\omega),1+|\ell|;\sin^2\rho_<\Big) \\ &\times F\Big(\frac{1}{2}(1+|\ell|-\nu-i\omega),\frac{1}{2}(1+|\ell|-\nu+i\omega),1-\nu;\cos^2\rho_>\Big). \end{aligned} \tag{5.84}$$

Similarly, the vacuum radial Green's function with Robin boundary conditions $g^\zeta_{\omega\ell}(\rho,\rho')$ is

$$\begin{aligned} g^\zeta_{\omega\ell}(\rho,\rho') = \mathscr{N}^\zeta_{\omega\ell}\ &[\cos\rho]^{1+\nu}\ [\cos\rho']^{1+\nu}[\sin\rho]^{|\ell|}\ [\sin\rho']^{|\ell|} \\ &\times F\Big(\frac{1}{2}(1+|\ell|+\nu-i\omega),\frac{1}{2}(1+|\ell|+\nu+i\omega),1+|\ell|;\sin^2\rho_<\Big) \\ &\times \Bigg\{ \cos\zeta\, F\Big(\frac{1}{2}(1+|\ell|+\nu-i\omega),\frac{1}{2}(1+|\ell|+\nu+i\omega),1+\nu;\cos^2\rho_>\Big) \\ &+ \sin\zeta\ [\cos\rho_>]^{-2\nu} F\Big(\frac{1}{2}(1+|\ell|-\nu-i\omega),\frac{1}{2}(1+|\ell|-\nu+i\omega),1-\nu;\cos^2\rho_>\Big)\Bigg\}. \end{aligned} \tag{5.85}$$

As the divergent part of the Hadamard parametrix (5.12) is state-independent, we have a simple method to calculate the renormalised v.e.v. of the VP with Robin boundary conditions. We consider the difference between the unrenormalised v.e.v.s with Robin and Neumann boundary conditions. This removes the singularities common to both. Following this, we simply add the v.e.v. with Neumann boundary conditions (5.32) determined in Section 5.1.1. Using (5.56, 5.84, 5.85) we can therefore write the v.e.v. with Robin boundary conditions as

$$\langle\hat{\Phi}^2\rangle^\zeta_0 = \lim_{\rho'\to\rho}\frac{1}{4\pi^2}\sum_{\ell=-\infty}^{\infty}\int_{-\infty}^{\infty}\Big[g^\zeta_{\omega\ell}(\rho,\rho') - g^N_{\omega\ell}(\rho,\rho')\Big]\,d\omega + \frac{\nu}{4\pi L}. \tag{5.86}$$

Using (5.86), we have computed the v.e.v.s of the VP with Robin boundary conditions using MATHEMATICA. The $\omega-$integration and $\ell-$sum and in (5.86) converge very rapidly (Figures 5.5, 5.6). To reduce computation time, we were able to limit the $\ell-$sum to 50 and the $\omega-$integration to 30. The associated error, in the computation of the v.e.v., was small compared to performing the $\ell-$sum and $\omega-$integration to 100 for both. For instance, close to the origin at $\rho = \pi/200$ (and for a

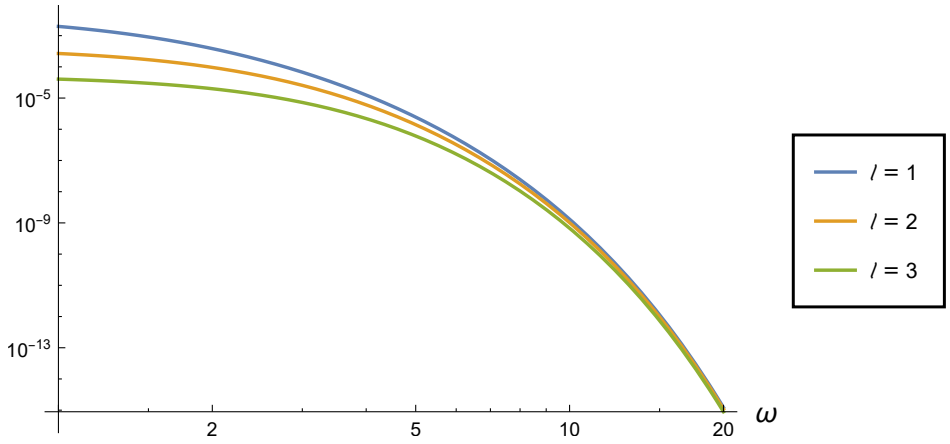

Figure 5.5: Loglog plot of the integrand in (5.86) as a function of ω for fixed $\rho = 3\pi/10, \zeta = \pi/3$ and $\nu = 1/2$ for three values of ℓ.

representative value of the Robin parameter $\zeta = \pi/10$), we find the relative error is $\sim 2.45 \times 10^{-24}$. Closer to the space-time boundary at $\rho = 90\pi/200$ we find the relative error to be greater but still acceptable at $\sim 2.83 \times 10^{-7}$. The sum over ℓ demonstrates nonuniform convergence with respect to the radial coordinate ρ Figure 5.6, as was seen for the VP [71] and RSET (Section 3.4) in adS4.

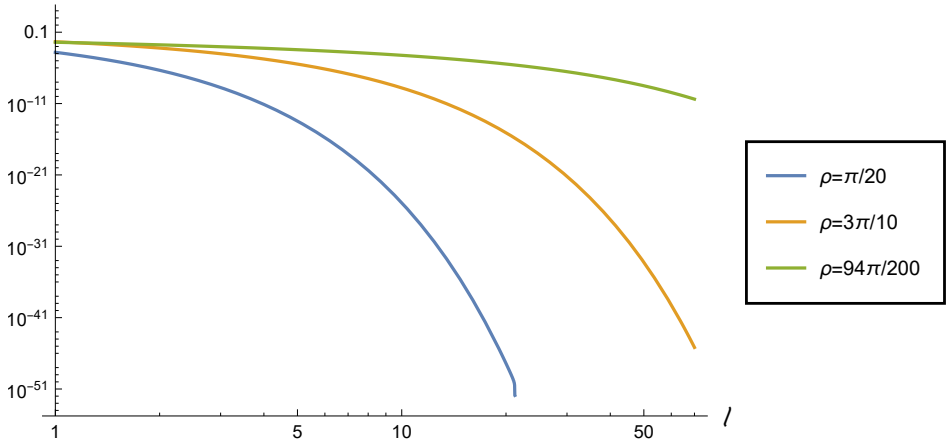

Figure 5.6: Loglog plot of the summand in (5.86) as a function of ℓ, for three values of the radial coordinate ρ, demonstrating non-uniform convergence of the $\ell-$sum. For each plot $\zeta = \pi/3$, $\nu = 1/2$ and the $\omega-$integration has been performed up to $|\omega| = 30$.

The v.e.v.s of the VP with Robin boundary conditions are displayed in Figure 5.7 for three values of ν and a range of values of the Robin parameter ζ. It can be seen that unlike the Dirichlet/Neumann case (5.31, 5.32), the v.e.v.s with Robin parameters are not constant and vary with the radial coordinate ρ. This symmetry breaking with Robin boundary conditions was also noted for the VP [71] and the RSET (Section 3.5) for the massless, conformally coupled scalar field on adS4. For all Robin parameters except Dirichlet and Neumann ($\zeta \neq 0, \pi/2$), the v.e.v.s are either monotonically decreasing or monotonically increasing functions of ρ, dependent on the value of the Robin parameter used. For all values of ν studied, the v.e.v.s are monotonically increasing as ρ

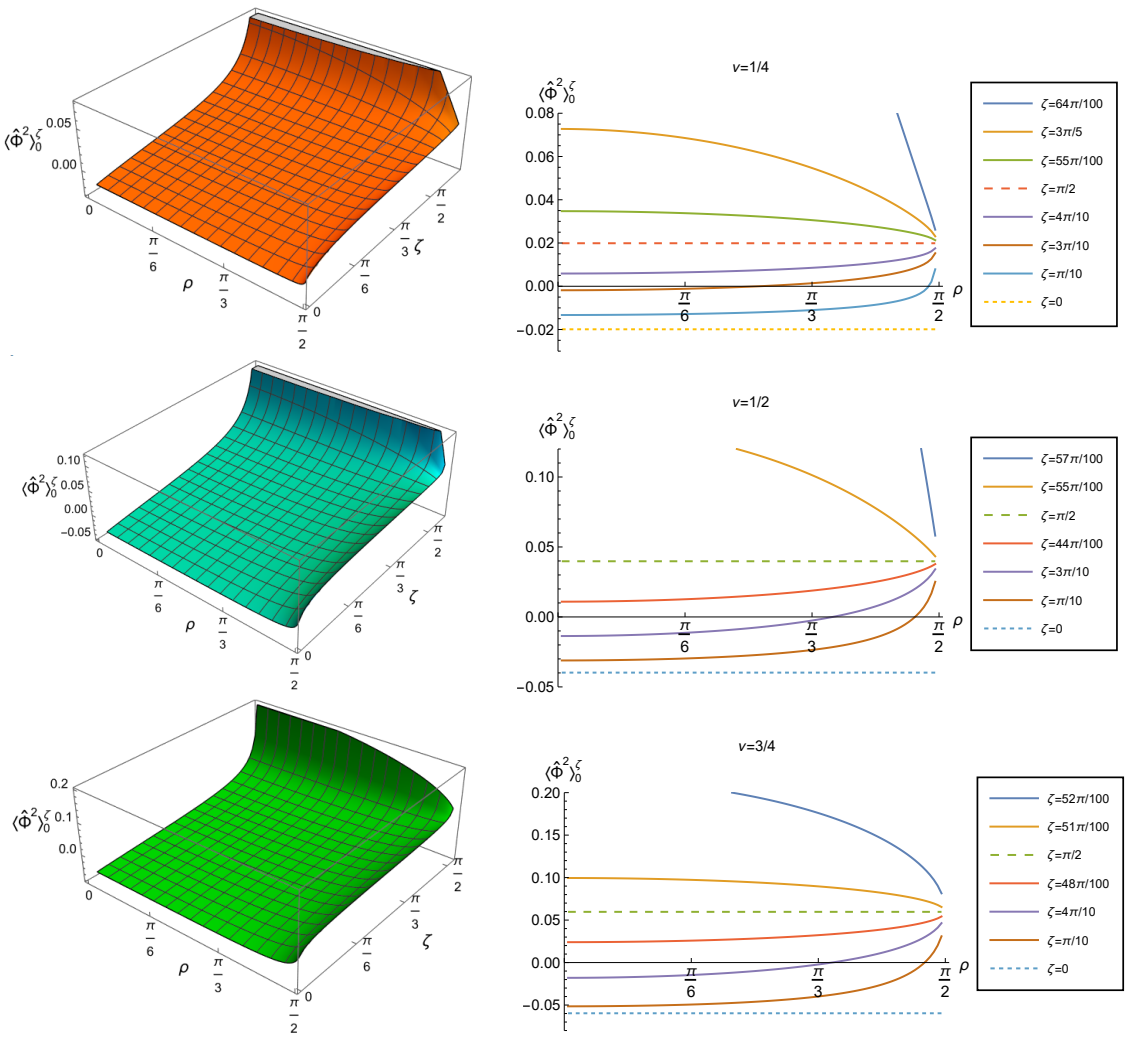

Figure 5.7: Renormalised v.e.v.s of the VP, $\langle\hat{\Phi}^2\rangle_0^\zeta$, for $\nu = 1/4,\ 1/2,\ 3/4$. On the left is shown 3D surface plots of $\langle\hat{\Phi}^2\rangle_0^\zeta$ as a function of ρ and ζ. On the right is shown $\langle\hat{\Phi}^2\rangle_0^\zeta$ as a function of ρ for a selection of values of the Robin parameter ζ. Dirichlet ($\zeta = 0$) and Neumann ($\zeta = \pi/2$) profiles are shown dotted.

increases if $0 < \zeta < \pi/2$, but monotonically decreasing for $\zeta > \pi/2$. It can also be seen from the 3D surface plots in Figure 5.7 that, for fixed ρ, the v.e.v.s are monotonically increasing functions of the Robin parameter ζ. Their have their minimum at $\zeta = 0$, corresponding to the Dirichlet boundary condition and increase steadily with increasing ζ, eventually diverging as $\zeta \to \zeta_{\text{crit}}$. Furthermore, for fixed ρ, ζ, we see that the v.e.v.s increase in magnitude with increasing ν. For each ν, the variation in the v.e.v.s with different Robin boundary conditions is greatest at the space time origin. As we approach the space-time boundary, the v.e.v.s of the VP for all Robin boundary conditions (except Dirichlet, $\zeta = 0$) converge to the Neumann result, generalising the finding of [71] in the massless, conformally coupled case in four dimensions.

5.2.3 Thermal expectation values

The thermal Euclidean Green's functions (5.60) are obtained from (5.83–5.85) by replacing ω with $n\kappa$ for $n \in \mathbb{N}$ and κ given in (5.59). We calculate the t.e.v.s of the VP using the same method

used in Section 5.2.2 and consider the difference between the unrenormalised thermal expectation values with Robin and Neumann boundary conditions. Following this we simply add the thermal expectation value of the VP with the Neumann boundary condition, previously determined in (5.37). We can therefore write

$$\langle\hat{\Phi}^2\rangle^{\zeta}_{\beta} = \frac{1}{2\pi\beta}\lim_{\rho'\to\rho}\sum_{\ell=-\infty}^{\infty}\sum_{n=-\infty}^{\infty}\left[g^{\zeta}_{n\ell}(\rho,\rho') - g^{N}_{n\ell}(\rho,\rho')\right] + \frac{\nu}{4\pi L} + \frac{1}{2\pi L}\sum_{j=1}^{\infty}\left\{\nu F\left(1+\nu, 1-\nu, \frac{3}{2}; \frac{1-\cosh(j\beta)}{2\cos^2\rho}\right) + \frac{\sqrt{2}\cos\rho}{2\sqrt{\cosh(j\beta)-1}}F\left(\frac{1}{2}+\nu, \frac{1}{2}-\nu, \frac{1}{2}; \frac{1-\cosh(j\beta)}{2\cos^2\rho}\right)\right\}. \quad (5.87)$$

The t.e.v.s of the VP, with Robin boundary conditions, have been calculated with MATHEMATICA. The $n-$ and $\ell-$sums in the summand in (5.87) converge rapidly and were performed to $|n|$, $|\ell| \leq 20$. The relative errors in curtailing the sums to 20 compared to 30 was $\sim 3\times10^{-9}$ away from the space-time bundary at $\rho = 3\pi/20$ with parameter values of $\nu = 1/2$, $\zeta = 3\pi/100$, $\beta = 1$. Closer to the boundary at $\rho = 90\pi/200$, the relative error was greater but still acceptable at $\sim 7\times10^{-5}$.

The t.e.v.s of the VP for three different values of ν and a range of the Robin parameter $0 \leq \zeta < \zeta_{\text{crit}}$ and are displayed in Figures 5.8 and 5.9. Figure 5.8 shows the t.e.v.s for different inverse temperatures β, with fixed $\nu = 1/4$ and a range of values of the Robin parameter ζ. It can be seen that with increasing temperature (decreasing β) the t.e.v.s increase in magnitude for all Robin parameters studied. With decreasing temperature (increasing β), we see that the plots approach those of the v.e.v.s as was noted for the VP on adS4 [71]. Figure 5.9 shows the t.e.v.s for three different values of ν and fixed inverse temperature $\beta = 1$. For all ρ we find that the the t.e.v.s increase in magnitude with increasing ν as was seen in the vacuum case. From the 3D surface plots in Figures 5.8 and 5.9 it can be seen that for fixed ν, β, ρ, the t.e.v.s increase with increasing ζ eventually diverging as ζ_{crit} is reached. Furthermore it can be seen that the maximum separation of the plots for the different Robin parameters is found at the space-time origin. As we approach the space-time boundary, the t.e.v.s for all Robin boundary conditions (except Dirichlet) approach the Neumann result as was seen in the vacuum case (Figure 5.7). Similar results were found in [71] for the massless, conformally coupled scalar field in adS4. Our results therefore support the key finding in [71] that near the boundary the Neumann v.e.v.s are generic whilst those for Dirichlet boundary conditions are a special case. This applies to scalar fields with general mass and coupling constant for all applicable Robin boundary conditions.

§ 5.3 Vacuum polarisation at the space-time boundary

In Sections 5.2.2, 5.2.3 we found that the VP with Robin boundary conditions converges to the Neumann v.e.v. at the space-time boundary for all values of the Robin parameter $0 < \zeta < \zeta_{\text{crit}}$. This result was also demonstrated in [71] for a massless, conformally coupled scalar field in four dimensions. In this section we seek to extend the analysis in [71] to the scalar field with general

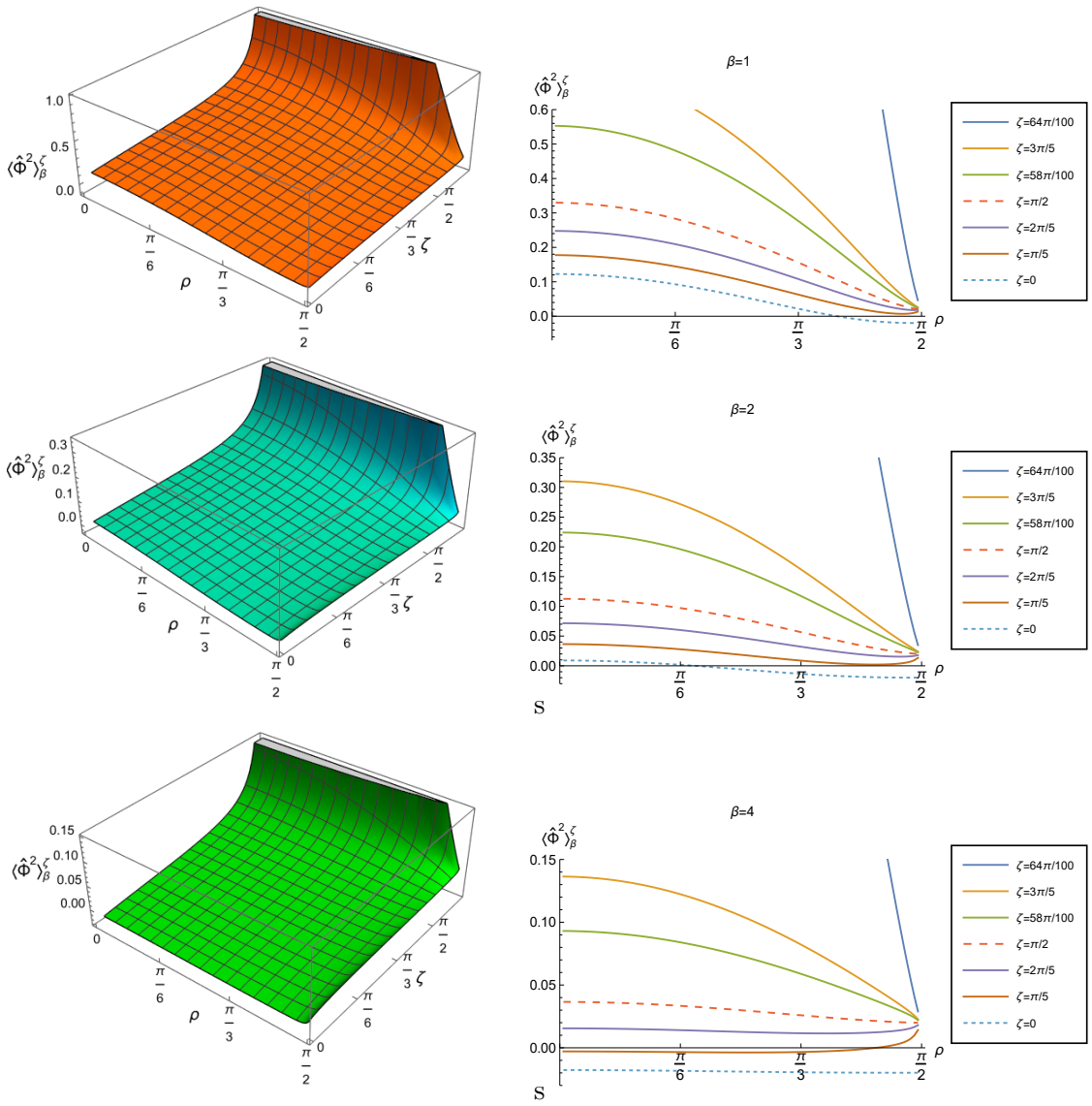

Figure 5.8: Renormalised t.e.v.s of the VP, $\langle\hat{\Phi}^2\rangle^{\zeta}_{\beta}$, for $\nu = 1/4$ and a selection of values of the inverse temperature β: $\beta = 1$ (top), $\beta = 2$ (middle) and $\beta = 4$ (bottom). On the left are 3D surface plots of $\langle\hat{\Phi}^2\rangle^{\zeta}_{\beta}$ as a function of ρ and ζ. On the right is shown $\langle\hat{\Phi}^2\rangle^{\zeta}_{\beta}$ as a function of ρ for a selection of values of the Robin parameter ζ. The Dirichlet and Neumann plots are shown dotted.

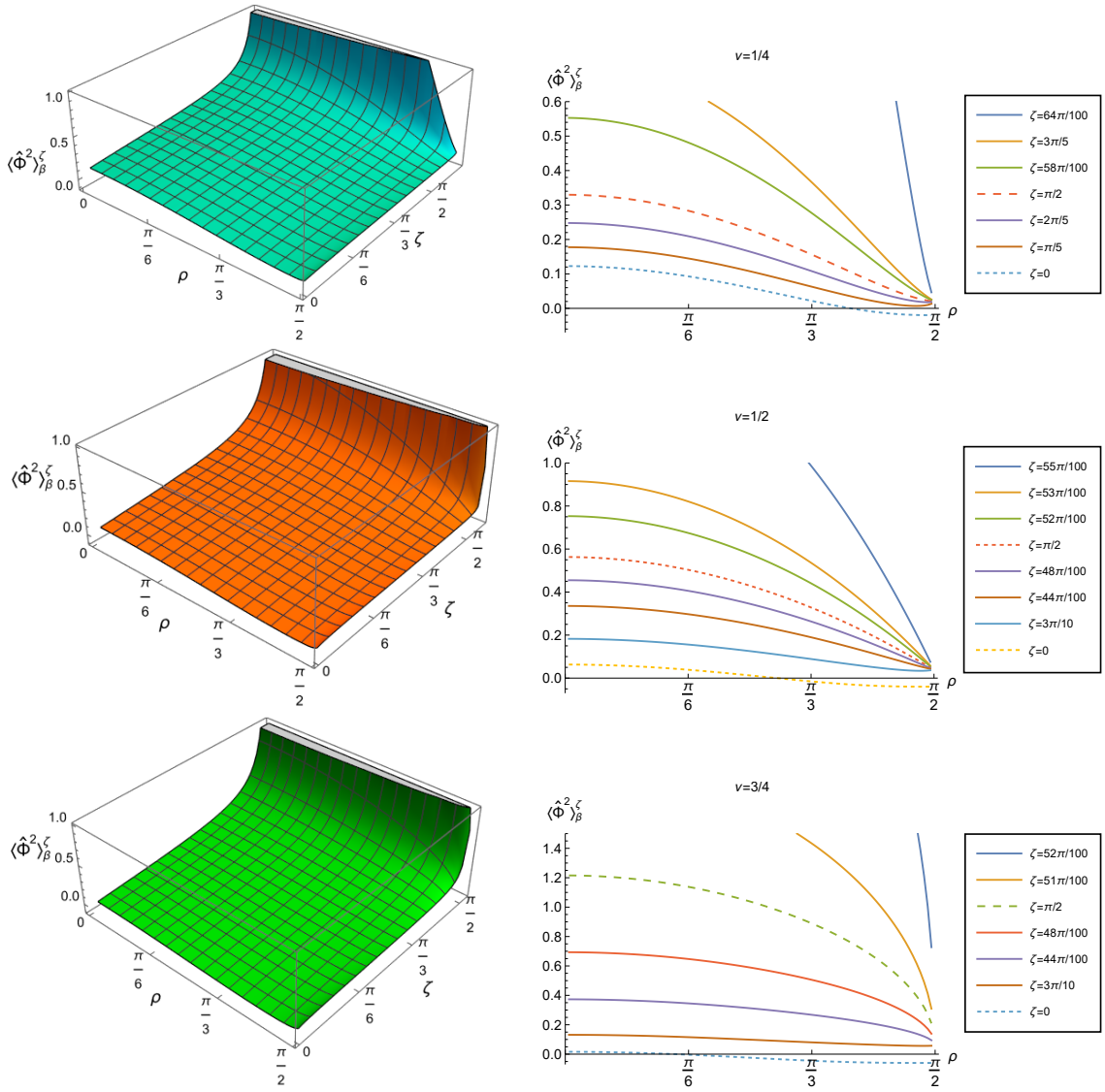

Figure 5.9: Renormalised t.e.v.s of the VP, $\langle\hat{\Phi}^2\rangle^{\zeta}_0$, with $\beta = 1$ and a selection of values of ν: $\nu = 1/4$ (top), $\nu = 1/2$ (middle) and $\nu = 3/4$ (bottom). On the left are 3D surface plots of $\langle\hat{\Phi}^2\rangle^{\zeta}_0$ as a function of ρ and ζ. On the right is shown $\langle\hat{\Phi}^2\rangle^{\zeta}_0$ as a function of ρ for a selection of values of the Robin parameter, ζ. The Dirichlet and Neumann plots are shown dotted.

mass and coupling in adS3.

Consider first the v.e.v.s, with Robin boundary conditions, determined using (5.86). The first part of the right hand side of (5.86) is the difference between v.e.v.s with Robin and Neumann boundary conditions applied, which we can express as

$$\langle\hat{\Phi}^2\rangle_0^\zeta - \langle\hat{\Phi}^2\rangle_0^N = \frac{1}{4\pi^2}\sum_{\ell=-\infty}^{\infty}\int_{-\infty}^{\infty} p_{\omega\ell}(\rho)\left[\mathscr{N}_{\omega\ell}^\zeta\, q_{\omega\ell}^\zeta(\rho) - \mathscr{N}_{\omega\ell}^N\, q_{\omega\ell}^N(\rho)\right] d\omega, \tag{5.88}$$

where we have used (5.62, 5.65, 5.67). As before, the ζ, N superscripts refer to the Robin and Neumann boundary conditions respectively. Using (5.80, 5.81, 5.84, 5.85), we can express (5.88) as

$$\langle\hat{\Phi}^2\rangle_0^\zeta - \langle\hat{\Phi}^2\rangle_0^N = -\frac{L\nu\cos\zeta}{2\pi^2}\sum_{\ell=-\infty}^{\infty}\int_{-\infty}^{\infty} \mathscr{N}_{\omega\ell}^\zeta\ \mathscr{N}_{\omega\ell}^N\ [p_{\omega\ell}(\rho)]^2\, d\omega. \tag{5.89}$$

To analyse the behaviour of this quantity as $\rho \to \pi/2$, it is helpful to use the form (5.66) for the radial function $p_{\omega\ell}(\rho)$. As the space-time boundary is approached, the hypergeometric functions in (5.66) tend to unity. Therefore the second term in (5.66) is dominant, giving the following leading-order behaviour of (5.89):

$$\langle\hat{\Phi}^2\rangle_0^\zeta - \langle\hat{\Phi}^2\rangle_0^N \sim -\frac{L\nu[\cos\rho]^{2-2\nu}\cos\zeta}{2\pi^2}\sum_{\ell=-\infty}^{\infty}\int_{-\infty}^{\infty} \mathscr{N}_{\omega\ell}^\zeta\ \mathscr{N}_{\omega\ell}^N\ [\sin\rho]^{2|\ell|}\mathcal{Q}^2\, d\omega, \tag{5.90}$$

where $\mathcal{Q}$ is given in (4.31).

The integral over ω and sum over ℓ in (5.90) cannot be performed analytically. However, whether or not this quantity is convergent or divergent (and the rate at which it diverges) depends only on the large $|\ell|$, $|\omega|$ behaviour. Using the expressions (5.80, 5.81) for the normalization constants, and considering only the dominant behaviour of $\mathscr{N}_{\omega\ell}^\zeta\mathscr{N}_{\omega\ell}^N\,\mathcal{Q}^2$ for large $|\ell|$, $|\omega|$ gives

$$\mathscr{N}_{\omega\ell}^\zeta\mathscr{N}_{\omega\ell}^N\,\mathcal{Q}^2 \sim \frac{1}{4L^2\nu^2}\frac{\Gamma(\nu)^2}{\Gamma(-\nu)^2}\frac{|\Gamma(1/2-\nu/2+|\ell|/2+i\omega/2)|^4}{|\Gamma(1/2+\nu/2+|\ell|/2+i\omega/2)|^4}\csc\zeta, \tag{5.91}$$

which is valid only for $\zeta > 0$, that is for all boundary conditions except Dirichlet. Consider first the quantity

$$\Sigma_0 = \sum_{\ell=-\infty}^{\infty}\int_{-\infty}^{\infty}\frac{|\Gamma(1/2-\nu/2+|\ell|/2+i\omega/2)|^4}{|\Gamma(1/2+\nu/2+|\ell|/2+i\omega/2)|^4}[\sin\rho]^{2|\ell|}\, d\omega. \tag{5.92}$$

Although we are still unable to perform the sum over ℓ and integral over ω in (5.92) analytically, from [39, §5.11.12] we have, for large $|\ell|$ and $|\omega|$, the following approximation

$$\frac{|\Gamma(1/2-\nu/2+|\ell|/2+i\omega/2)|^4}{|\Gamma(1/2+\nu/2+|\ell|/2+i\omega/2)|^4} \sim \frac{2^{4\nu}}{(|\ell|^2+|\omega|^2)^{2\nu}}. \tag{5.93}$$

Using this approximation, the expression

$$\Sigma_1 = \sum_{\ell=1}^{\infty}\int_0^{\infty}\frac{2^{4\nu}[\sin\rho]^{2\ell}}{(\ell^2+\omega^2)^{2\nu}}d\omega \tag{5.94}$$

is amendable to exact evaluation. The integral over ω in (5.94) is convergent for $\nu > 1/4$, leading to

$$\Sigma_1 = \frac{\sqrt{\pi}\,\nu\Gamma(2\nu - 1/2)}{2^{-4\nu}\Gamma(2\nu+1)} \sum_{\ell=1}^{\infty} \frac{[\sin\rho]^{2\ell}}{\ell^{(4\nu-1)}} = \frac{\sqrt{\pi}\nu\Gamma(2\nu-1/2)}{2^{-4\nu}\Gamma(2\nu+1)} \mathrm{Li}_{(4\nu-1)}(\sin^2\rho), \tag{5.95}$$

where $\mathrm{Li}_{4\nu-1}[\sin^2\rho]$ is the polylogarithm function [39, §25.12.10]. To find the behaviour of (5.95) as $\rho \to \pi/2$, we use the relationship between the polylogarithm and Lerch's transcendental function Φ_L [39, §25.14.1]

$$\mathrm{Li}_{(4\nu-1)}(\sin^2\rho) = (\sin^2\rho)\Phi_L(\sin^2\rho, 4\nu-1, 1), \tag{5.96}$$

together with the result in [76, §64:12.6]:

$$\lim_{\rho\to\pi/2}\left[\frac{\Phi_L(\sin^2\rho, 4\nu-1, 1)}{(\cos^2\rho)^{4\nu-2}}\right] = \Gamma(2-4\nu). \tag{5.97}$$

However, (5.97) is only valid for $\nu < 1/2$. So, for $1/4 < \nu < 1/2$, we have, as $\rho \to \pi/2$,

$$\Sigma_1 \sim \frac{\sqrt{\pi}\nu\Gamma(2\nu-1/2)\Gamma(2-4\nu)2^{4\nu}}{\Gamma(2\nu+1)}[\cos\rho]^{8\nu-4}. \tag{5.98}$$

We can recover the dominant behaviour of $\langle\hat{\Phi}^2\rangle_0^\zeta - \langle\hat{\Phi}^2\rangle_0^N$ at the space-time boundary by substituting $4\Sigma_1$ for the sum and integral (to account for both positive and negative values of ω and ℓ) in (5.92) and subsequently in (5.90), which gives

$$\langle\hat{\Phi}^2\rangle_0^\zeta - \langle\hat{\Phi}^2\rangle_0^N \sim \ -\frac{\Gamma(\nu)^2\Gamma(2\nu-1/2)\Gamma(2-4\nu)\cot\zeta}{2\pi^{3/2}2^{-4\nu}\,L\,\Gamma(-\nu)^2\Gamma(2\nu+1)}[\cos\rho]^{6\nu-2}, \tag{5.99}$$

which vanishes in the limit $\rho \to \pi/2$ when $\nu > 1/3$. Therefore for $1/3 < \nu < 1/2$ we have $\langle\hat{\Phi}^2\rangle_0^\zeta = \langle\hat{\Phi}^2\rangle_0^N$ at the space-time boundary.

For the case of $\nu > 1/2$ we note that polylogarithm function in (5.95) becomes the Riemann zeta function, as $\rho \to \pi/2$ [39, §25.12.10], which is itself convergent to a finite value for $\nu > 1/2$. When we then substitute (5.95) back into (5.90) we see that the RHS of (5.90) vanishes owing to the $(\cos\rho)^{2-2\nu}$ term. Therefore, from our analysis of the quantity Σ_1, we deduce that $\langle\hat{\Phi}^2\rangle_0^\zeta = \langle\hat{\Phi}^2\rangle_0^N$ at the space-time boundary for $\nu > 1/3$, $\nu \neq 1/2$.

While the above discussion is for v.e.v.s for $\nu > 1/3$, $\nu \neq 1/2$, similar considerations apply to t.e.v.s. In that case the integral over ω in (5.94) is replaced by a sum over n (from replacing ω by $n\kappa$), leading us to consider the quantity

$$\Sigma_\beta = \sum_{\ell=1}^{\infty}\sum_{n=1}^{\infty} \frac{[\sin\rho]^{2\ell}}{(\ell^2+n^2\kappa^2)^{2\nu}}. \tag{5.100}$$

While the sum is convergent for $\nu > 1/4$, it cannot be performed analytically. However, using the Euler-Maclaurin formula [39, §2.10.1], we have the asymptotic approximation

$$\sum_{n=0}^{\infty}\frac{1}{(\ell^2+n^2\kappa^2)^{2\nu}} \sim \int_0^\infty \frac{1}{(\ell^2+y^2\kappa^2)^{2\nu}}dy + \frac{1}{\ell^{4\nu}} + \ldots, \tag{5.101}$$

where ... denotes terms which vanish more rapidly as $\ell \to \infty$. Therefore the dominant behaviour in Σ_β, for large ℓ, arises from the integral in (5.101). Therefore we can write

$$\Sigma_\beta \sim \sum_{\ell=1}^{\infty} \int_0^\infty \frac{[\sin\rho]^{2\ell}}{(\ell^2 + y^2\kappa^2)^{2\nu}} dy. \tag{5.102}$$

We now use the same analysis as that performed for the v.e.v.s to deduce that $\langle\hat{\Phi}^2\rangle_\beta^\zeta = \langle\hat{\Phi}^2\rangle_\beta^N$ at the space-time boundary for $\nu > 1/3$.

When $\nu = 1/2$ we have the massless, conformally coupled case and our argument follows along the same line as in [71] and Section 3.8 on adS4. We first make a conformal transformation to the ESU (see Section 2.1). We then consider a region, V, in ESU for $\rho \in [0, \pi/2]$ (Figure 3.12) and apply Robin boundary conditions to the surface at $\rho = \pi/2$, which is now part of the space-time. We start with (3.72), reproduced here for convenience

$$G_\zeta^{ESU}(x,x') - G_N^{ESU}(x,x') = -\frac{\cot\zeta}{L} \int_{\mathcal{I}_{\pi/2}} G_N^{ESU}(x,y) G_\zeta^{ESU}(y,x') dS, \tag{5.103}$$

where $\mathcal{I}_{\pi/2}$ is a time-like hypersurface at $\rho = \pi/2$ (Figure 3.12). Using the results of [36], we can express (5.103) as an asymptotic expansion to obtain

$$G_\zeta^{ESU}(x,x') - G_N^{ESU}(x,x') = -\frac{\cot\zeta}{L} \int_{\widetilde{I}_{\pi/2}} G_N^{ESU}(x,y) G_N^{ESU}(y,x') dS + ... \tag{5.104}$$

where +... represents additional integrals over the space-time boundary (see Section 3.8).

To find the vacuum Euclidean Green's function on ESU, with Neumann boundary conditions, we start with (5.23) formulated on Lorentzian space-time and use (5.27) for the constant $C = iD$. Making a Wick rotation to the Euclidean section gives (for $\nu = 1/2$)

$$G_N^{ESU}(x,x') = \frac{\sqrt{2}}{8\pi L} \Big\{ \big[\cosh\Delta\tau - \cos\Delta\theta \sin\rho\sin\rho' + \cos\rho\cos\rho'\big]^{-\frac{1}{2}} + \big[\cosh\Delta\tau - \cos\Delta\theta\sin\rho\sin\rho' - \cos\rho\cos\rho'\big]^{-\frac{1}{2}} \Big\}, \tag{5.105}$$

which differs from the equivalent expression on adS4 [71] given in (3.76). The difference between (3.76) and (5.105) is primarily in the angular separation given by γ on adS4 (2.23) and $\cos\Delta\theta$ on adS3.

To perform the integral in (5.104), which is performed over the space-time point y, we set $\rho' = \pi/2$ on the boundary to obtain

$$G_N^{ESU}(\tau,\rho,\theta;\tau',\pi/2,\theta') = \frac{\sqrt{2}}{4\pi L\sqrt{\cosh\Delta\tau - \cos\Delta\theta\sin\rho}}. \tag{5.106}$$

Using (5.104), and in the limit $x' \to x$, we can now write

$$G_\zeta^{ESU}(x,y) - G_N^{ESU}(x,y) = -\frac{\cot\zeta}{L} \int_{\widetilde{I}_{\pi/2}} \frac{1}{8\pi^2 L^2(\cosh\Delta\tau_y - \cos\Delta\theta_y \sin\rho)} dS. \tag{5.107}$$

Here x is a general point in ESU with coordinates (τ, ρ, θ) and the integral is performed over the space-time point $y = (\tau_y, \pi/2, \theta_y)$ on the time-like hypersurface $\mathscr{I}_{\pi/2}$ with $\Delta\tau_y = \tau_y - \tau$ and $\Delta\theta_y = \theta_y - \theta$.

The determinant of the induced metric, h, on the surface of integration is L^2. Performing the integral over $\Delta\theta$, gives

$$G_\zeta^{ESU}(x,y) - G_N^{ESU}(x,y) = -\frac{\cot\zeta}{L}\int_{\Delta\tau=-\infty}^{\infty} \frac{1}{4\pi\sqrt{\cosh^2\Delta\tau_y - \sin^2\rho}} d\Delta\tau. \tag{5.108}$$

This is divergent for $\Delta\tau_y = 0$ as $\rho \to \pi/2$, but we can perform the integral over $\Delta\tau_y$ for $0 < \rho < \pi/2$ to give

$$G_\zeta^{ESU}(\rho) - G_N^{ESU}(\rho) = -\frac{\cot\zeta}{2\pi L} K[-\tan^2\rho]\sec\rho, \tag{5.109}$$

where $K[m]$ is the complete elliptic integral of the first kind [39, 19.2.8]. It can be seen that the divergent term in (5.109) is $\sec\rho$ as $\rho \to \pi/2$. However, we now transform back to CadS by multiplying (5.109) by $\cos\rho$ to obtain

$$\langle\hat{\Phi}^2\rangle_0^\zeta - \langle\hat{\Phi}^2\rangle_0^N = -\frac{\cot\zeta}{2\pi L} K[-\tan^2\rho] + \ldots, \tag{5.110}$$

where $\ldots$ denotes terms which vanish as $\rho \to \pi/2$. In the limit $\rho \to \pi/2$, the elliptic integral vanishes [39, 19.2.8] and the right hand side of (5.110) tends to zero. We can therefore conclude that in the massless conformally coupled case, $\nu = 1/2$, we have that $\langle\hat{\Phi}^2\rangle_0^\zeta = \langle\hat{\Phi}^2\rangle_0^N$ as we approach the space-time boundary. The above argument can be extended trivially to the t.e.v.s for the massless, conformally coupled case.

The above analytic argument is valid only for $\nu > 1/3$. However, our numerical results in Section 5.2 indicate that $\langle\hat{\Phi}^2\rangle^\zeta = \langle\hat{\Phi}^2\rangle^N$ on the space-time boundary for both v.e.v.s and t.e.v.s and values of ν less than or equal to $1/3$. However, although we have been unable to show this analytically, we can provide additional numerical evidence for v.e.v.s (similar results are obtained for t.e.v.s). Using the form (5.65) for the radial function $p_{\omega\ell}(\rho)$, and applying [39, §15.8.1], we consider the quantity

$$\Sigma_2 = \sum_{\ell=-\infty}^{\infty}\int_{-\infty}^{\infty} d\omega\, \mathscr{N}_{\omega\ell}^\zeta\, \mathscr{N}_{\omega\ell}^N\, (\sin\rho)^{2|\ell|}[F(b-c+1, a-c+1, a+b-c+1; \sin^2\rho)]^2, \tag{5.111}$$

where the parameters a, b and c are given in (5.63). The quantity Σ_2 will be multiplied by a factor $[\cos\rho]^{2-2\nu}$ (plus some numerical factors) to give $\langle\hat{\Phi}^2\rangle^\zeta - \langle\hat{\Phi}^2\rangle^N$ (see (5.90)). Therefore, if we can demonstrate that Σ_2 is finite as the boundary is approached, it must be the case that $\langle\hat{\Phi}^2\rangle^\zeta - \langle\hat{\Phi}^2\rangle^N$ vanishes on the boundary, as required.

For fixed ℓ and $\rho < \pi/2$, the integral over ω in (5.111) converges very rapidly for large ω, as can be seen in Figure 5.10. We compute the integral over ω numerically for fixed ℓ, for $|\omega| \leq 200$. The integral for larger values of $|\omega|$ is estimated by fitting a sum of exponentials to the integrand in the region $\omega \in [201, 700]$ and then integrating the fitting functions. We thereby estimate that the relative error in truncating the integral at $|\omega| = 200$ is of the order of 10^{-6}.

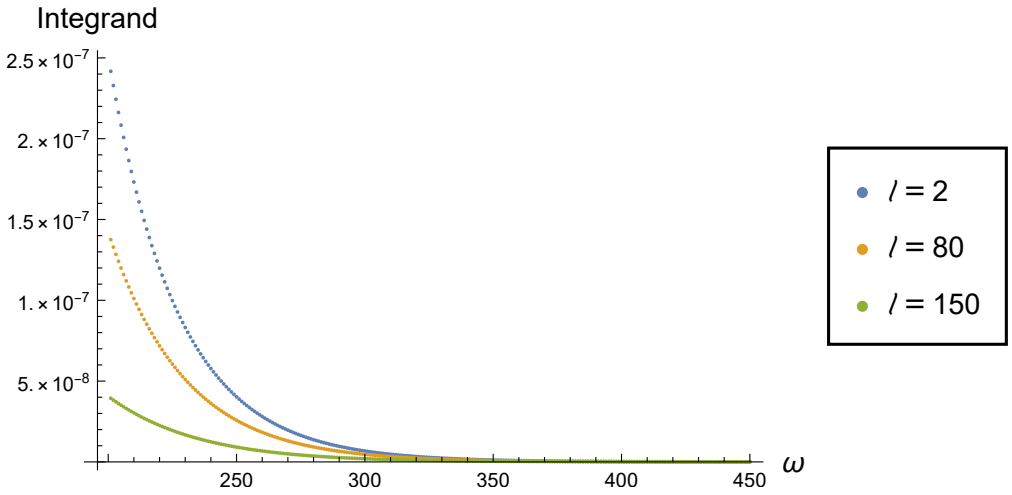

Figure 5.10: The integrand in (5.111) for $\rho = 99\pi/200$, $\nu = 1/8$, $\zeta = \pi/3$, $\omega \in [201, 450]$ and a selection of values of ℓ.

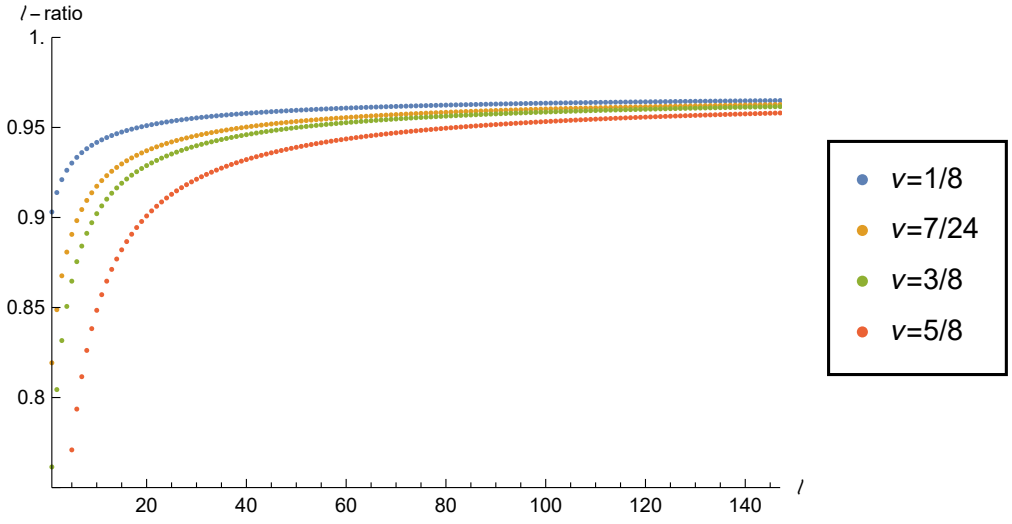

Figure 5.11: Ratio of successive terms in the sum over ℓ in (5.111) for four different values of ν with $\rho = 99\pi/200$ and $\zeta = \pi/3$. In each case the integral over ω has been performed for $|\omega| \leq 200$.

We then use the ratio test to show that the sum over ℓ converges. Our results for $\rho = 99\pi/200$ and four different values of ν are shown in Figure 5.11. We plot the ratio of successive terms in the sum over ℓ for $\ell \leq 150$. For all values of ν, the ratio of successive terms in the sum over ℓ, as ℓ increases, tends to a limit which is below unity. Our numerical investigations reveal that the limit is below unity for all $0 < \rho < \pi/2$, but that the limit increases towards unity as $\rho \to \pi/2$. This provides evidence that the sum over ℓ converges to a finite value for $0 < \rho < \pi/2$.

To find $\langle\hat{\Phi}^2\rangle_0^\zeta - \langle\hat{\Phi}^2\rangle_0^N$ at the space-time boundary, we multiply the finite value of Σ_2 obtained from (5.111) by $[\cos\rho]^{2-2\nu}$, which vanishes as $\rho \to \pi/2$ (there are also some irrelevant numerical factors). We therefore conclude that $\langle\hat{\Phi}^2\rangle_0^\zeta = \langle\hat{\Phi}^2\rangle_0^N$ as the space-time boundary is approached for all values of $\nu \in (0, 1)$.

§ 5.4 Conclusions

In this chapter we have determined the v.e.v.s and t.e.v.s of the VP of a real quantum scalar field with general mass and curvature coupling on a background adS3. We have constructed the vacuum and thermal Feynman Green's functions and have used Hadamard renormalisation to compute the v.e.v.s and t.e.v.s of the scalar field subject to Dirichlet and Neumann boundary conditions applied at the time-like boundary. We have found that in the vacuum state, both Dirichlet and Neumann boundary conditions respect the maximal symmetry of the background space-time, whilst this symmetry is lost with the addition of a nonzero temperature, where the t.e.v.s depend on the radial coordinate ρ. As the space-time boundary is approached ($\rho \to \pi/2$), we find that the t.e.v.s with Dirichlet and Neumann boundary conditions converge towards their respective v.e.v.s for all values of the inverse temperature β.

We have also determined the renormalised v.e.v.s and t.e.v.s of the VP with Robin boundary conditions applied at the space-time boundary. We studied the scalar field in Euclidean space where the Green's functions are unique. We find that both the v.e.v.s and t.e.v.s break the underlying symmetry of adS3 and have values dependent on the space-time location. The t.e.v.s increase with increasing temperature (decreasing β). Both v.e.v.s and t.e.v.s increase in magnitude with increasing ν which itself is dependent on the mass and coupling constant (4.16).

The key finding from this chapter is that for all Robin parameters (except Dirichlet) both the v.e.v.s and t.e.v.s converge towards the Neumann result as the space-time boundary is approached, extending the work in [71] to the scalar field with general mass and coupling in adS3. This suggests that the Neumann boundary condition gives the generic behaviour of the scalar field at the space-time boundary whilst the Dirichlet boundary condition is a special case, even though it is the most widely studied in the literature. We have supplemented this finding by giving analytical and numerical arguments as to why the v.e.v.s and t.e.v.s with Robin boundary conditions converge to the Neumann result at the space-time boundary. In the next chapter we extend the work on the scalar field with general mass and coupling and determine the RSET on adS3. We will examine whether the findings in Chapter 3 are applicable to the RSET when the mass and coupling constant of the field are allowed to vary.

Chapter 6

Renormalised stress energy tensor on adS3

In Chapter 3, we determined the v.e.v.s and t.e.v.s of the RSET of a massless, conformally coupled scalar field on adS4. It was found that both the v.e.v.s and t.e.v.s of the nonzero components of the RSET approached the common Dirichlet/Neumann v.e.v. result at the space-time boundary for all Robin boundary conditions. This is consistent with the findings seen with the vacuum polarisation (VP) of a massless, conformally coupled scalar field in adS4 [71] and also for a scalar field with general mass and curvature coupling on adS3 (Chapter 5). In [71] and Chapter 5, the v.e.v.s and t.e.v.s of the VP converged to the Neumann result at the space-time boundary for all Robin boundary conditions except Dirichlet which had its own limit.

In this chapter we seek to determine whether the findings in [71] and Chapter 5 for the VP extend to the RSET of a quantum scalar field with general mass and coupling. We use three dimensional anti-de Sitter space-time (adS3) as our background as this simplifies the angular component of the Green's function and avoids the use of conical (Mehler) functions that were used in [71] and Chapter 3. We consider the coupling constant in the range $\xi \in [-1, 1]$ as this includes the minimal ($\xi = 0$) and conformal ($\xi = 1/8$) cases. It will be shown that when the scalar field is no longer massless and conformally coupled, the v.e.v.s with Dirichlet and Neumann boundary conditions have different values. Therefore, a natural question to ask is whether the expectation values with Robin boundary conditions converge towards the Neumann result at the space-time boundary as we saw with the VP.

In Sections 6.1 and 6.2 we consider the v.e.v.s and t.e.v.s of the RSET with Dirichlet and Neumann boundary conditions, followed in Sections 6.3 and 6.4 by the v.e.v.s and t.e.v.s when Robin boundary conditions are applied. In the study of the expectation values of the RSET of a massless, conformally coupled scalar field on adS4 (Chapter 3) we examined the effects on the RSET of different Robin boundary conditions and temperatures (for the t.e.v.s). Allowing the field mass and coupling constant to vary means there are additional parameters to consider, namely ν, defined in (4.16), the coupling constant ξ and the mass squared of the scalar field (m^2). In addition, for the t.e.v.s, we consider different values of the inverse temperature, β. For each expectation value we plot the components of the RSET as functions of the radial coordinate ρ, allowing one or two of the parameters to vary at a time whilst keeping the others fixed at some chosen value.

In Section 6.5 we summarise the key findings in this chapter and in Section 6.6 we present the mathematical expressions of the components of the RSET used in the numerical calculations.

§ 6.1 Vacuum expectation values with Dirichlet and Neumann boundary conditions

For the Dirichlet and Neumann boundary conditions we remain in Lorentzian space-time with the metric given by (2.9). In the vacuum state, Dirichlet and Neumann boundary conditions respect the maximal symmetry of the underlying space-time [2, 3, 61] (see also Chapters 3, 5) and so we can express the vacuum Dirichlet and Neumann Green's functions in terms of $s(x, x')$ (2.22), the proper distance between the space-time points x, x' connected by a unique geodesic [3]. The vacuum Green's functions with Dirichlet and Neumann boundary conditions are given in (5.18, 5.28).

As the Green's functions in (5.18, 5.28) represent Hadamard states (Section 1.5), we can extract the regular state-dependent component $W(x, x')$, given in (1.77). We follow the approach in Chapter 3 and calculate the RSET using [35],

$$\langle \hat{T}_{\mu\lambda} \rangle = \frac{1}{4\sqrt{2}\pi} \left[-w_{\mu\lambda} + \frac{1}{2}(1-2\xi) w_{;\mu\lambda} + \frac{1}{2}\left(2\xi - \frac{1}{2}\right) g_{\mu\lambda} \Box w + \xi R_{\mu\lambda}\, w \right] \tag{6.1}$$

where

$$\begin{aligned} w(x) &= \lim_{x' \to x} W(x, x') \\ w_{\mu\lambda}(x) &= \lim_{x' \to x} W_{;\mu\lambda}\,(x, x'). \end{aligned} \tag{6.2}$$

As we are in three dimensions, there is no v_1 term which was needed to compute the RSET in four dimensions (1.88).

In the vacuum state, when Dirichlet/Neumann boundary conditions are applied, we can write $W(x, x') \to W(s)$. Using (5.18, 5.28) and (5.12), we can derive an expression for $W(s)$ to second order in s, with Dirichlet/Neumann boundary conditions applied. Using the Taylor expansion of $-\sinh^2(s/2L)$ we can obtain a second order expansion of the hypergeometric functions in (5.18, 5.28) as

$$\begin{aligned} F\left(1+\nu, 1-\nu, \frac{3}{2}; -\sinh^2\left(\frac{s}{2L}\right)\right) &= 1 - \frac{(1+\nu)(1-\nu)s^2}{6L^2} + \mathcal{O}(s^3), \\ F\left(\frac{1}{2}+\nu, \frac{1}{2}-\nu, \frac{1}{2}; -\sinh^2\left(\frac{s}{2L}\right)\right) &= 1 - \frac{(1/2+\nu)(1/2-\nu)s^2}{2L^2} + \mathcal{O}(s^3). \end{aligned} \tag{6.3}$$

Using the expansion of $\sinh(s/2L)^{-1}$ and (6.3), we can now express (5.18, 5.28) as

$$\begin{aligned} G_0^{D/N}(s) = \pm\frac{i\nu}{4\pi L}\left(1 - \frac{(1+\nu)(1-\nu)s^2}{6L^2} + \mathcal{O}(s^3)\right) + \frac{i}{4\pi s}\left(1 - \frac{s^2}{24L^2} + \mathcal{O}(s^4)\right) \\ \times \left(1 - \frac{(1/2+\nu)(1/2-\nu)s^2}{2L^2} + \mathcal{O}(s^3)\right). \end{aligned} \tag{6.4}$$

Finally, using (1.77), we can write $W(s)^{D/N}$ to second order in s as

$$W(s)^{D/N} = \frac{\sqrt{2}}{L^3}\left\{ \pm\nu L^2 + \frac{1}{6}(3\nu^2 - 1)sL + \frac{1}{6}(\nu - \nu^3)s^2 + \mathcal{O}(s^3) \right\}, \tag{6.5}$$

with the $+/-$ terms corresponding to Neumann/Dirichlet boundary conditions respectively. This matches the second order expansion of $W(s)$ given in [61] except for the first order term in s. However, bearing in mind that the calculation of the RSET involves second order derivatives of $W(s)$, the $\mathcal{O}(s)$ term in (6.5) is not relevant for the calculation of the RSET.

As the w term in (6.1) is a constant, we can express (6.1) as

$$\langle \hat{T}_{\mu\lambda} \rangle = \frac{1}{4\sqrt{2}\pi} \Big[- w_{\mu\lambda} + \xi R_{\mu\lambda}\, w \Big]. \tag{6.6}$$

Using (6.5) and (6.6), the v.e.v. of the RSET with the Dirichlet boundary condition is

$$\langle T_{\mu\lambda} \rangle_0^D = \frac{1}{12\pi L^3} \left\{ \nu^3 + (6\xi - 1)\nu \right\} g_{\mu\lambda}, \tag{6.7}$$

in agreement with the corresponding result in [61]. The v.e.v. with the Neumann boundary condition is

$$\langle T_{\mu\lambda} \rangle_0^N = -\frac{1}{12\pi L^3} \left\{ \nu^3 + (6\xi - 1)\nu \right\} g_{\mu\lambda}. \tag{6.8}$$

Both $\langle T_{\mu\lambda} \rangle_0^D$ and $\langle T_{\mu\lambda} \rangle_0^N$ depend on the parameter ν (4.16) and the coupling constant ξ. From now on we consider the components of the RSET with mixed indices and this will be useful in Sections 6.3 and 6.4 when we study the RSET with Robin boundary conditions using Euclidean methods. It is noteworthy that for both Dirichlet and Neumann boundary conditions, the v.e.v.s of the RSET with mixed indices are independent of the space-time location and are the same for all three components. Using the definition of ν (4.16) we can write the v.e.v. as

$$\langle T_{\mu}^{\lambda} \rangle_0^{D/N} = \pm \frac{m^2 \nu}{12\pi L}\, \delta_{\mu}^{\lambda}, \tag{6.9}$$

which is written in a similar format to the corresponding results for the vacuum polarisation (5.31, 5.32). As in the four-dimensional case (Section 3.1), the v.e.v. of the RSET in three-dimensions is fixed by the trace given by

$$\langle T_{\mu}^{\mu} \rangle_0^{D/N} = \pm \frac{m^2 \nu}{4\pi L}. \tag{6.10}$$

Unlike the case for the VP, we note that $\langle T_{\mu}^{\lambda} \rangle_0^{D/N}$ is zero for $m = 0$, regardless of the value of ν (or indeed the coupling constant ξ), whereas the VP is zero for $m = 0$ only in the conformally coupled case ($\xi = 1/8$). The finding of a zero v.e.v. of the RSET (6.9), for a massless scalar field (independent of ξ) is not seen in adS4 (Chapter 3), where the v.e.v. is nonzero for both Dirichlet and Neumann boundary conditions for the massless, conformally coupled scalar field as this is fixed by the trace anomaly (3.20). Using the definition of ν (4.16), we can rewrite (6.9) as

$$\langle T_{\mu}^{\lambda} \rangle_0^{D/N} = \pm \frac{m^2}{12\pi L} \sqrt{m^2 L^2 + 1 - 6\xi}\, \delta_{\mu}^{\lambda}. \tag{6.11}$$

So for $\langle T_{\mu}^{\lambda} \rangle_0^{D/N}$ to be real, we require

$$m^2 \geq \frac{1}{L^2}(6\xi - 1), \tag{6.12}$$

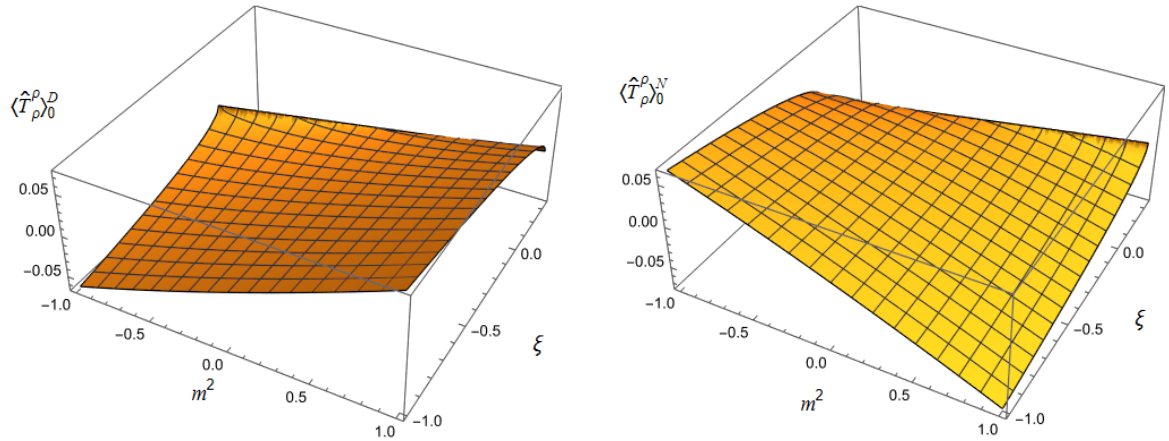

Figure 6.1: 3D surface plot of $\langle T^{\rho}_{\rho}\rangle^{D/N}_{0}$, as a function of m^2 and ξ, with Dirichlet (left) and Neumann (right) boundary conditions, using the range of $m^2 \in [-1, 1]$.

which corresponds to the Breitenlohner-Freedman bound [19]. As the nonzero components of $\langle T^{\lambda}_{\mu}\rangle^{D/N}_{0}$ are equal, in Figure 6.1 we plot $\langle T^{\rho}_{\rho}\rangle^{D/N}_{0}$ as a function of m^2 and ξ for values of $-1 \leq m^2 \leq 1$. Figure 6.1 shows how $\langle T^{\rho}_{\rho}\rangle^{D/N}_{0}$ depends on m^2 and ξ as well as the boundary conditions. We see that with the Dirichlet boundary condition, $\langle T^{\rho}_{\rho}\rangle^{D/N}_{0}$ increases monotonically with m^2 for all ξ. However, when Neumann boundary conditions are applied, we see that $\langle T^{\rho}_{\rho}\rangle^{D/N}_{0}$ decreases monotonically with increasing m^2. The variation of $\langle T^{\rho}_{\rho}\rangle^{D/N}_{0}$ with m^2 is more marked for $\xi < 0$.

§ 6.2 Thermal expectation values with Dirichlet and Neumann boundary conditions

The thermal Green's functions, $G^{D/N}_{\beta}(x, x')$, for inverse temperature β, can be expressed as an infinite sum involving the vacuum Green's function $G^{D/N}_{0}(x, x')$ (1.49) giving

$$G^{D/N}_{\beta}(x, x') = \sum_{j=-\infty}^{\infty} \left\{ \pm \frac{i\nu}{4\pi L} F\left(1+\nu, 1-\nu, \frac{3}{2}; -\sinh^2\left(\frac{s_\beta}{2L}\right)\right) \right.$$
$$\left. + \frac{i}{8\pi L \sinh\left(\frac{s_\beta}{2L}\right)} F\left(\frac{1}{2}+\nu, \frac{1}{2}-\nu, \frac{1}{2}; -\sinh^2\left(\frac{s_\beta}{2L}\right)\right) \right\}, \tag{6.13}$$

with the $+/-$ signs corresponding to the Dirichlet/Neumann boundary conditions respectively and where s_β given by

$$\cosh\left(\frac{s_\beta}{L}\right) = \frac{\cos(\Delta t + ij\beta)}{\cos\rho\cos\rho'} - \tan\rho\tan\rho'\cos\Delta\theta. \tag{6.14}$$

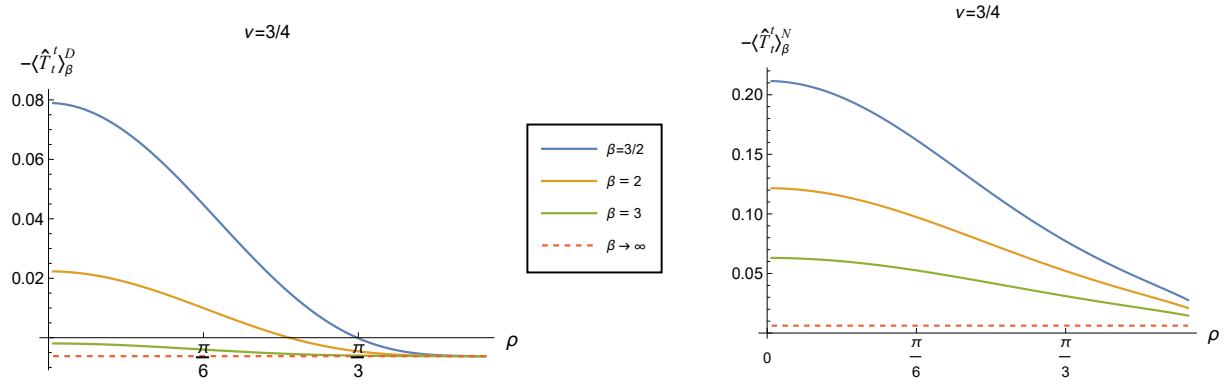

Figure 6.2: Renormalised t.e.v.s of the energy density component of the RSET, $-\langle\hat{T}_t^t\rangle_\beta^{D/N}$ with Dirichlet (left) and Neumann (right) boundary conditions, for a selection of inverse temperatures, β ($\beta \to \infty$ represents the vacuum state). For both plots $\nu = 3/4$ and $\xi = 1/8$.

To determine the t.e.v.s of the RSET we consider first the difference between the thermal and the vacuum states giving

$$G_\beta^{D/N}(x,x') - G_0^{D/N}(x,x') = \sum_{j=-\infty, j\neq 0}^{\infty} \left\{ \pm \frac{i\nu}{4\pi L} F\left(1+\nu, 1-\nu, \frac{3}{2}; -\sinh^2\left(\frac{s_\beta}{2L}\right)\right) \right.$$
$$\left. + \frac{i}{8\pi L \sinh\left(\frac{s_\beta}{2L}\right)} F\left(\frac{1}{2}+\nu, \frac{1}{2}-\nu, \frac{1}{2}; -\sinh^2\left(\frac{s_\beta}{2L}\right)\right) \right\}. \tag{6.15}$$

Using (6.15), we calculate $W(x,x')$, from which we can find the components in the right hand side of (6.1) using (6.2). For the computation of the t.e.v.s of the RSET, we consider (6.1) with mixed indices, giving

$$\langle\hat{T}_\mu^\lambda\rangle = \frac{1}{4\sqrt{2}\pi}\left[-w_\mu^\lambda + \frac{1}{2}(1-2\xi)w_{;\mu}^{;\lambda} + \frac{1}{2}\left(2\xi - \frac{1}{2}\right)\delta_\mu^\lambda \Box w - 2\xi\, w\, \delta_\mu^\lambda\right]. \tag{6.16}$$

The lengthy expressions for the w, w_μ^λ, $w_{;\mu}^{;\lambda}$, $\Box w$ terms in the right hand side of (6.16) are displayed in Section 6.6.1 and were computed numerically by performing the sum over j (see below). This method of constructing the t.e.v.s of the RSET allows us to vary the coupling constant ξ independently. As the computed expectation values are the differences between the t.e.v.s and v.e.v.s ($\langle\hat{T}_\mu^\lambda\rangle_\beta^{D/N} - \langle\hat{T}_\mu^\lambda\rangle_0^{D/N}$), to determine the renormalised t.e.v. we simply add the relevant v.e.v. to the result.

For the numerical computations of the components in (6.16), it is found that the sum over j converges very quickly for each term. As a result, the $j-$sum was limited to $|j| \leq 30$. The relative error using this limit for the $j-$sum was calculated for the Neumann boundary condition at two values of the radial coordinate, at $\rho = 30\pi/200$ and close to the boundary at $\rho = 94\pi/200$. Representative values of $\nu = 1/4$ and $\beta = 2$ were chosen. For each of the components in (6.16), the relative error of performing the $j-$sum to 30 compared to 100 was of the order of 10^{-20} for both values of the radial coordinate. It is reasonable to assume that similarly low relative errors would be obtained for other parameter values and the Dirichlet boundary condition.

The results for the energy density component of the t.e.v.s of the RSET for different values of the inverse temperature β and fixed ν, ξ, are shown in Figure 6.2 for Dirichlet and Neumann boundary conditions.

It can be seen that for both boundary conditions, the t.e.v.s of the energy density component of the RSET $-\langle\hat{T}_t^t\rangle_\beta$, not surprisingly, increase with decreasing β (increasing temperature). The maximum difference between the profiles is seen towards the space-time origin ($\rho = 0$), whilst for all β and both boundary conditions, the t.e.v.s tend to their respective v.e.v. at the space-time boundary. However, with the Neumann boundary condition, the plots convergence more slowly approaching the space-time boundary compared with Dirichlet. The significantly greater magnitude of $-\langle\hat{T}_t^t\rangle_\beta^N$ seen when Neumann boundary conditions are applied (compared to Dirichlet) can be appreciated by examining the corresponding behaviour of the vacuum polarisation (VP) shown in Figure 5.2. It can be seen from Figure 5.2 that the difference between the VP with Dirichlet and that with Neumann boundary conditions increases with increasing ν, with the VP eventually diverging for Neumann boundary conditions as $\nu \to 1$. It is not surprising, therefore, that with a value of $\nu = 3/4$ the energy density component of the RSET with the Neumann boundary condition is nearly an order of magnitude greater than its Dirichlet counterpart.

Figure 6.3 shows 3D surface plots of the t.e.v. of the energy density component of the RSET $-\langle T_t^t\rangle_\beta^{D/N}$, as a function of the radial coordinate ρ and the coupling constant ξ. A selection of inverse temperatures is used ($\beta = 1$, $\beta = 2$, $\beta = 3$) and either Dirichlet or Neumann boundary conditions. Interestingly it can be seen that with either boundary condition and for certain values of $\xi < 0$, the energy density is negative close to the space-time origin (except for Dirichlet with $\beta = 3$, where it is close to zero) and *decreases* with increasing temperature (decreasing β). With values of $\xi > 0$ we see that the energy density is positive near the space-time origin and increases with increasing temperature (decreasing β). The dependence of $-\langle T_t^t\rangle_\beta^{D/N}$ on the radial coordinate ρ is very much dependent on the coupling constant ξ. With $\xi \lesssim -1/2$ we see that $-\langle T_t^t\rangle_\beta^{D/N}$ monotonically increases with increasing ρ, whilst with $\xi > 1/2$, we find $-\langle T_t^t\rangle_\beta^{D/N}$ monotonically decreases with increasing ρ. This is seen with either boundary condition. However, for all ξ, we see that $-\langle T_t^t\rangle_\beta$ converges towards the respective v.e.v. result at the space-time boundary, which is dependent on the value of ξ (6.7, 6.8). The behaviour of $-\langle T_t^t\rangle_\beta^{D/N}$ with other values of ν (and fixed $\beta = 1$) is shown in Figures 6.4– 6.6.

It must be remembered, however, from our definition of ν in (4.16), that for fixed ν varying the coupling constant ξ will also change the squared mass of the scalar field. As we have only studied three values of $\nu = 1/4$, $1/2$, $3/4$, we are unable to study the components of the RSET when we vary ξ and m^2 independently for arbitrary values of these parameters. Instead we approach this in a different way. Figure 4.1 shows the relationship between m^2 and ξ for various fixed values of ν. Using Figure 4.1 we can choose fixed values of $\xi \in [-1, 1]$ and, for each value of ξ, find the three corresponding values of m^2 which correspond to the three values of ν studied in this chapter ($\nu = 1/4$, $1/2$, $3/4$). We adopt a similar approach with fixed m^2 and three values of ξ.

Figure 6.7 shows the energy density component of the RSET as a function of the radial coordinate ρ, for a selection of fixed coupling constants $\xi \in [-1, 1]$ and different values of m^2. It can be seen

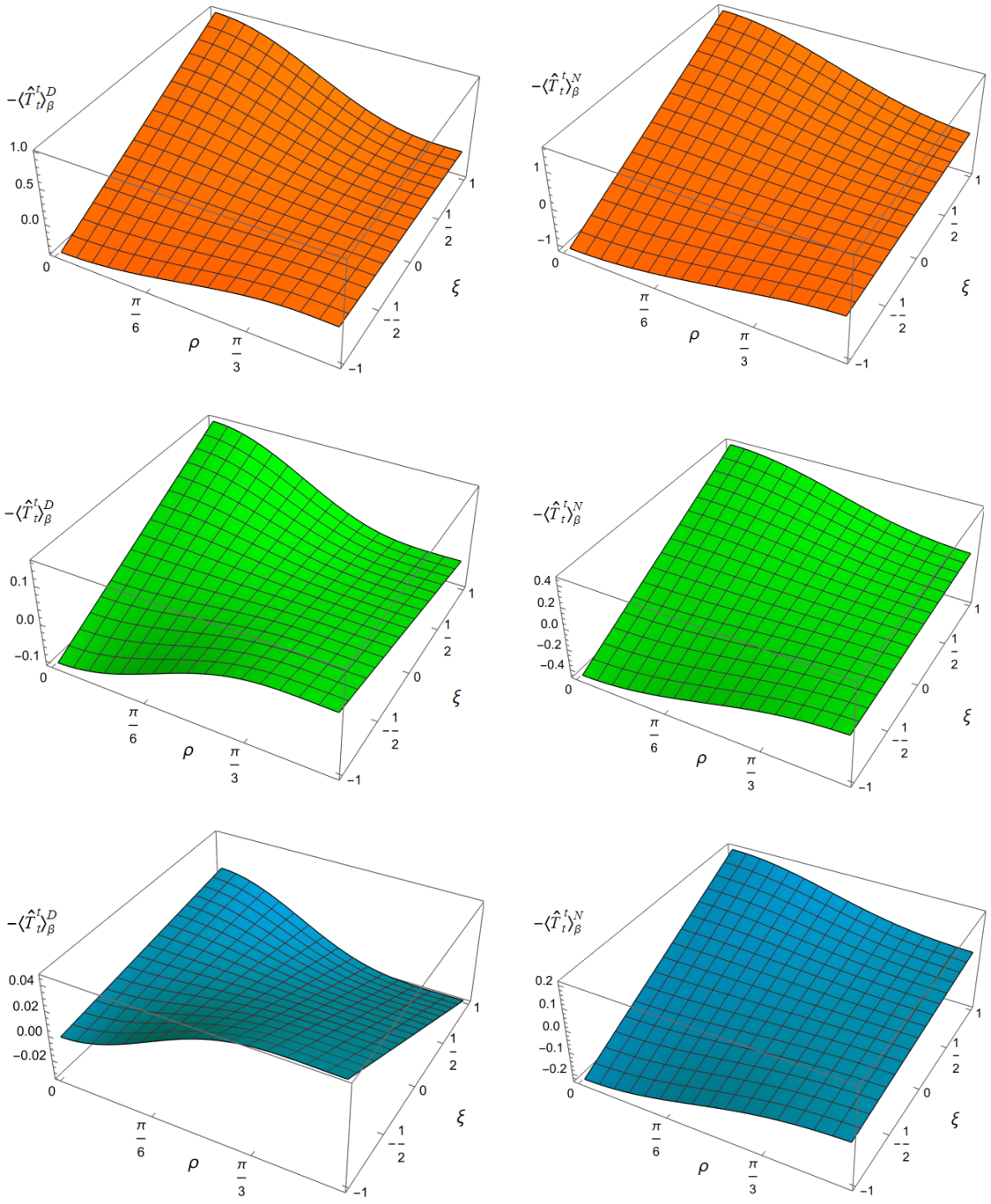

Figure 6.3: 3D surface plots of the energy density component $-\langle T^t_t\rangle_\beta$ of the RSET as functions of the radial coordinate ρ and the coupling constant ξ, for different values of the inverse temperature β. The left column has the Dirichlet boundary condition and the right column has Neumann boundary condition, with $\beta = 1$ (top), $\beta = 2$ (middle) and $\beta = 3$ (bottom). For all plots, $\nu = 1/4$.

that $-\langle\hat{T}_t^t\rangle_\beta^{D/N}$ depends significantly on the coupling constant ξ, and also on whether Dirichlet or Neumann boundary conditions are used. With Dirichlet boundary conditions, we see that for values of $\xi \geq 0$ the energy densities of the scalar field have their maximum at the space-time origin, following which they decrease monotonically with increasing ρ, and converge to their corresponding v.e.v. as the space-time boundary is approached. For $\xi = -1$, and the Dirichlet boundary condition, the energy densities are negative at the space-time origin, for the three values of m^2 considered, and increase to reach a positive maximum at $\rho \sim \pi/3$ before converging towards their respective v.e.v. at the space-time boundary. With $\xi = -1$, we also see that $-\langle\hat{T}_t^t\rangle_\beta^D$ increases with increasing m^2 as one would expect intuitively. However, a coupling constant of $\xi \geq 0$ results in the energy density decreasing with increasing m^2. This finding was also noted in [94], where the authors studied a quantum scalar field on a Schwarzschild black hole space-time.

A somewhat different picture is seen when Neumann boundary conditions are applied (right column of Figure 6.7). As with the Dirichlet boundary condition, for $\xi \geq 0$, the energy density has its maximum at the space-time origin and decreases monotonically towards its v.e.v. as the space-time boundary is approached. For $\xi = -1$, the energy densities are entirely negative throughout the space-time. They have their maximum magnitude at the space-time origin and increase monotonically towards the space-time boundary. With $\xi = 0$ (minimal coupling), we see that the energy densities are all positive at the space-time origin but are no longer monotonic functions of ρ. With the Neumann boundary condition, the energy density increases with increasing m^2 for values of $\xi \geq 1/8$ and decreases with increasing m^2 for $\xi = -1$. Only for the minimally coupled case, $\xi = 0$, do the two boundary conditions exhibit the same behaviour with the energy density increasing with decreasing m^2. For both boundary conditions, we see the maximum variation in the t.e.v.s at $\xi = \pm 1$ and at their minimum when $\xi = 0$ for Dirichlet (where the plots almost coincide) and $\xi = 1/8$ for Neumann boundary conditions.

Figure 6.8 shows $-\langle\hat{T}_t^t\rangle_\beta^{D/N}$ for a selection of fixed values of $m^2 \in [-1/2, 1/2]$ and different coupling constants ξ. The values of m^2 used in the plot all satisfy the Breitenlohner-Freedman bound [19]. The plots with the Dirichlet boundary condition are quite similar for the different values of m^2. All plots are monotonic functions of the radial coordinate ρ, except for the plots with $m^2 = -1/2$ and the Neumann boundary condition. Comparing with Figure 6.7, it would appear that the different values of the coupling constant have a greater effect on $-\langle\hat{T}_t^t\rangle_\beta^{D/N}$ than m^2.

The behaviour of the t.e.v. of the energy density component of the RSET, for fixed $\nu = 1/4$ and a range of different inverse temperatures β, was shown in Figure 6.3. We now examine the effects of different values of the parameter ν (4.16) on the t.e.v.s of all the nonzero components of the RSET with fixed inverse temperature, $\beta = 1$. These are displayed in Figures 6.4, 6.5, 6.6 where the three values of $\nu = 1/4$, $\nu = 1/2$, and $\nu = 3/4$ are used respectively. The behaviour of the t.e.v.s of the RSET components is similar for the three values of ν considered. As with the energy density, the $\langle\hat{T}_\rho^\rho\rangle_\beta^{D/N}$ and $\langle\hat{T}_\theta^\theta\rangle_\beta^{D/N}$ components depend significantly on the radial coordinate ρ, and the coupling constant ξ. For $\xi < 0$, the $\langle\hat{T}_\rho^\rho\rangle_\beta^{D/N}$ and $\langle\hat{T}_\theta^\theta\rangle_\beta^{D/N}$ components are monotonically decreasing from the origin towards the space-time boundary. The behaviour of the RSET components is qualitatively similar for Dirichlet and Neumann boundary conditions. However, the magnitudes of the RSET

components are greater with the Neumann boundary condition, especially for $\nu = 3/4$ where there is an order of magnitude difference between the respective plots.

For both Dirichlet and Neumann boundary conditions (and the three values of ν) it appears at first glance that the t.e.v.s of the $\langle \hat{T}^{\rho}_{\rho} \rangle_{\beta}$ and $\langle \hat{T}^{\theta}_{\theta} \rangle_{\beta}$ components of the RSET are the same, but there are in fact subtle differences which can be appreciated when we examine the thermal pressure deviator Π_{β}, in much the same way as we did for the RSET in adS4 (Chapter 3). The pressure deviator Π_{β}, represents the difference between the $\langle \hat{T}^{\rho}_{\rho} \rangle_{\beta}$ and $\langle \hat{T}^{\theta}_{\theta} \rangle_{\beta}$ components of the RSET, and is a measure of the difference between the quantum state and its classical counterpart [4]. For a classical gas of particles, $\Pi_{\beta} = 0$. In three dimensions we can write the Landau decomposition [66] of the SET as

$$\langle \hat{T}^{\nu}_{\mu} \rangle_{\beta} = \text{Diag}\Big\{ -E_{\beta},\, P_{\beta} + \Pi_{\beta}, P_{\beta} - \Pi_{\beta} \Big\}, \tag{6.17}$$

where E_{β} is the energy density, P_{β} the pressure and Π_{β} is the shear stress or pressure deviator. Figure 6.9 shows the thermal pressure deviators plotted as a function of the radial coordinate ρ for different values of the coupling constant ξ, with Dirichlet or Neumann boundary conditions applied. As the $\langle \hat{T}^{\theta}_{\theta} \rangle^{D/N}_{\beta}$ component of the RSET is greater than the $\langle \hat{T}^{\rho}_{\rho} \rangle^{D/N}_{\beta}$ component, in Figure 6.9 we plot $-\Pi^{D/N}_{\beta}$. For both boundary conditions and all values of ν and ξ, we find that $-\Pi^{D/N}_{\beta}$ is zero at the space-time origin and attains its maximum magnitude between the space-time origin and the boundary. As the space-time boundary is approached, however, the difference between the two boundary conditions is noticeable. For the Dirichlet boundary condition, $-\Pi^{D}_{\beta}$ converges to zero as the space-time boundary is reached (as was seen in the massless, conformally coupled case in Chapter 3, Figure 3.11). For the Neumann boundary condition, $-\Pi^{N}_{\beta}$ converges more slowly as we approach the space-time boundary, for all ξ. The convergence of $-\Pi^{N}_{\beta}$ occurs more slowly with increasing ν. However, it is notable that for both boundary conditions, $-\Pi^{D/N}_{\beta}$ attains its minimum magnitude (for all ρ) when conformal coupling ($\xi = 1/8$), rather than minimal coupling ($\xi = 0$) is employed, suggesting that in this case, the quantum scalar field most closely resembles its classical counterpart. This is in keeping with the findings of [4] where the authors studied massless, quantum scalar and fermionic fields with minimal ($\xi = 0$) and conformal ($\xi = 1/6$) coupling on adS4. They found that the pressure deviators for the scalar field with conformal coupling was an order of magnitude smaller than the minimally coupled case.

§ 6.3 Vacuum expectation values with Robin boundary conditions

To determine the RSET with Robin boundary conditions we employ Euclidean methods as in Chapters 3, 5 and [71], by performing a Wick rotation of the time coordinate (1.52). Moving to Euclidean space-time has the advantage that the Green's function is unique without the need for an '$i\epsilon$' prescription. The vacuum and thermal Euclidean Green's functions in adS3 with Dirichlet, Neumann and Robin boundary conditions were determined in Chapter 5. As discussed in Section 4.5, when using Robin boundary conditions, we only consider values of the Robin parameter ζ below a critical value ζ_{crit} ie $0 \leq \zeta < \zeta_{\text{crit}}$. The value of ζ_{crit} (4.56) is dependent on the value of the

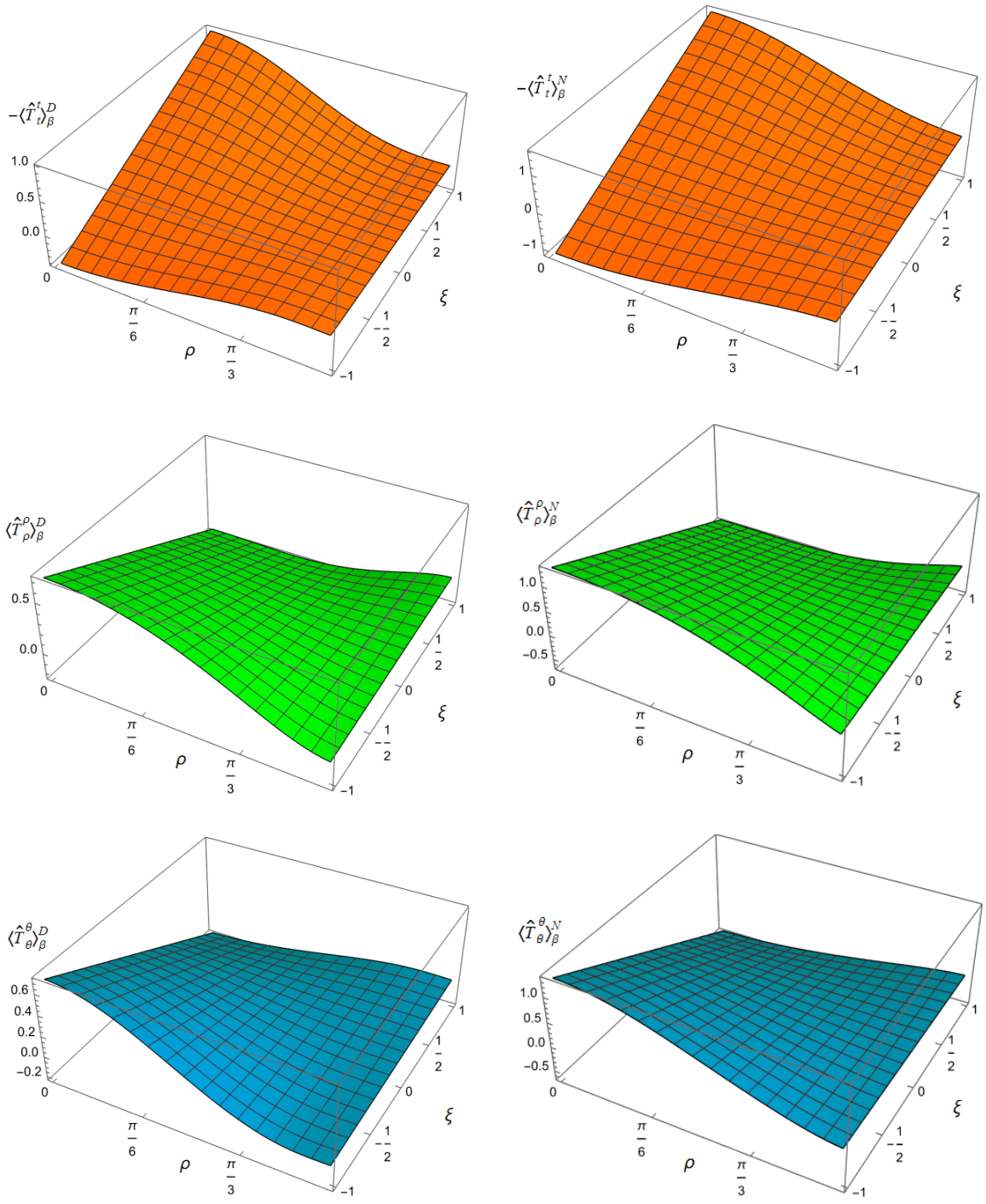

Figure 6.4: 3D surface plots of the t.e.v.s of the nonzero components of the RSET, as functions of the radial coordinate ρ and the coupling constant ξ. The left column shows Dirichlet and the right column Neumann boundary conditions. For all plots, $\nu = 1/4$ and $\beta = 1$.

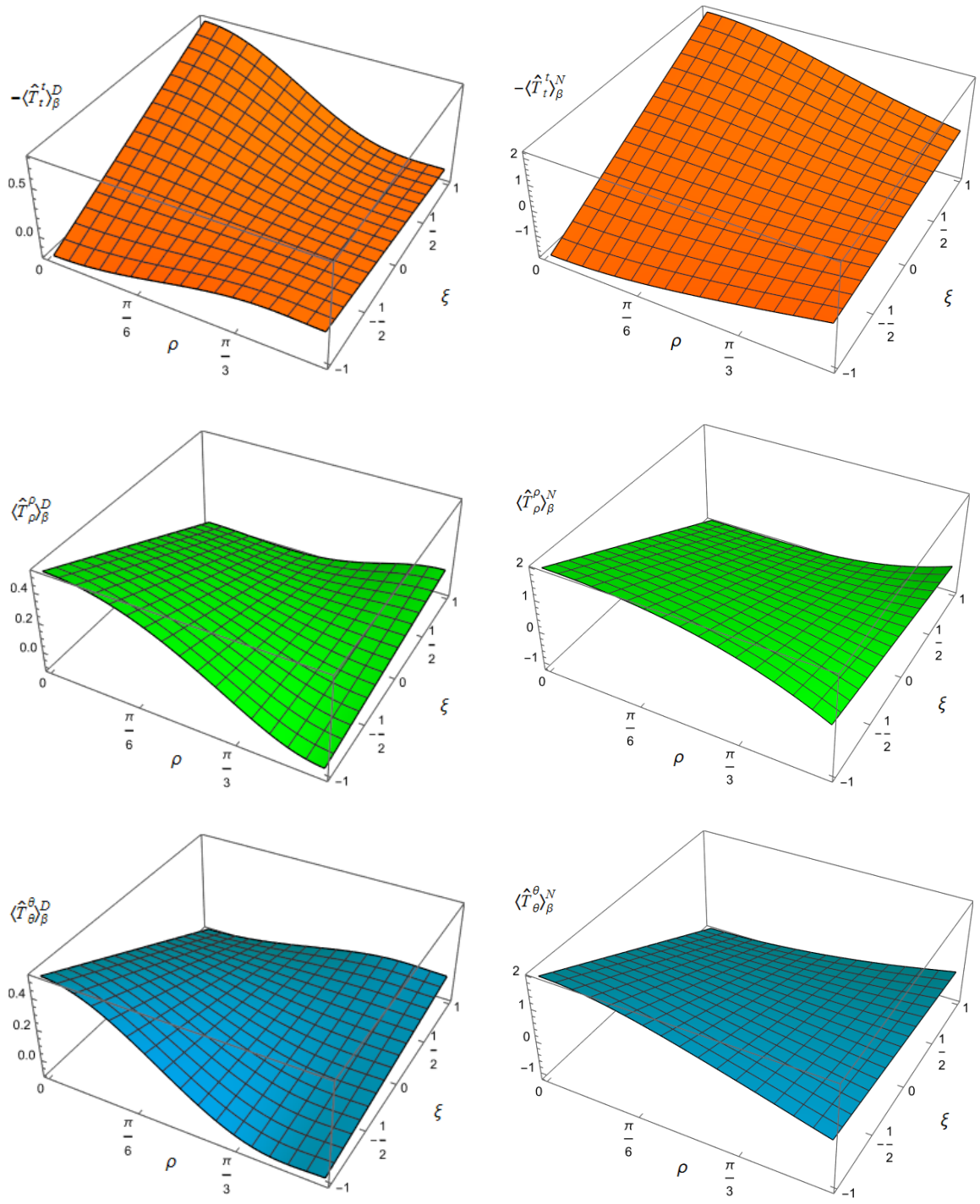

Figure 6.5: 3D surface plots of the t.e.v.s of the nonzero components of the RSET as functions of the radial coordinate ρ and the coupling constant ξ. The left column shows Dirichlet and the right column Neumann boundary conditions. For all plots, $\nu = 1/2$ and $\beta = 1$.

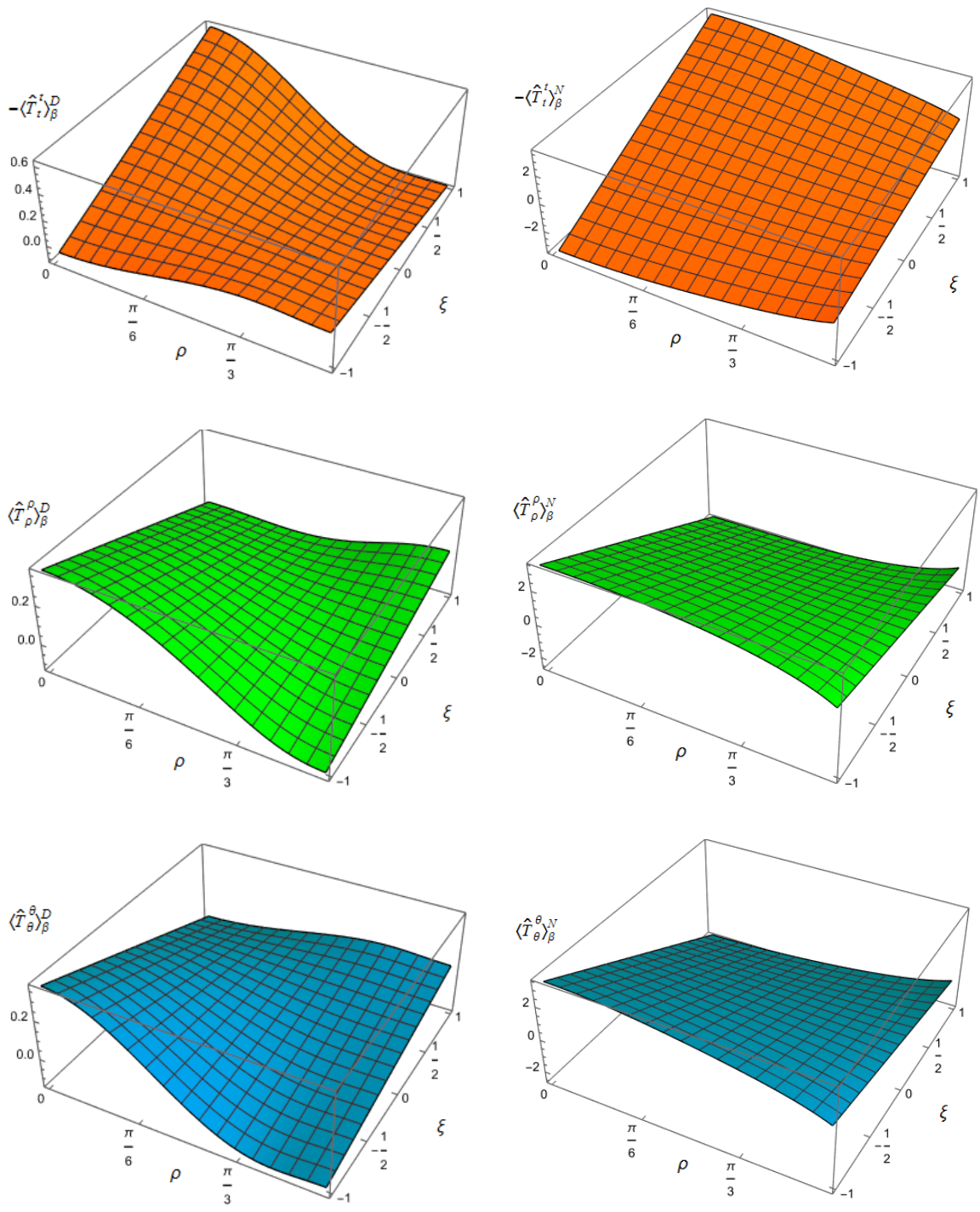

Figure 6.6: 3D surface plots of the t.e.v.s of the nonzero components of the RSET as functions of the radial coordinate ρ and the coupling constant ξ. The left column shows Dirichlet and the right column Neumann boundary conditions. For all plots, $\nu = 3/4$ and $\beta = 1$.

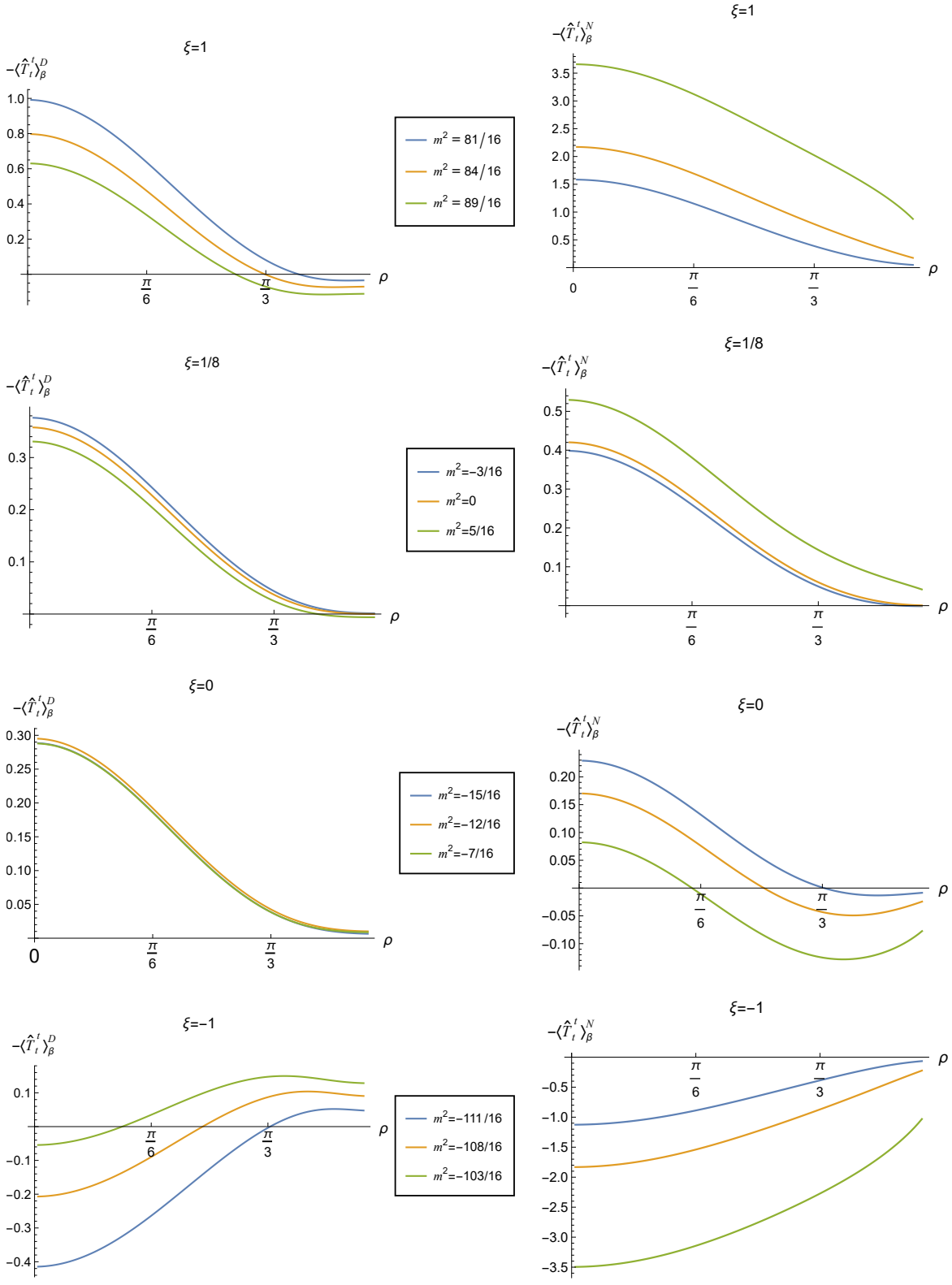

Figure 6.7: Renormalised t.e.v.s of $-\langle\hat{T}_t^t\rangle_\beta^{D/N}$ as a function of ρ, with different values of m^2 and fixed coupling constant, ξ. Left column shows Dirichlet and right column Neumann boundary conditions. For all plots $\beta = 1$.

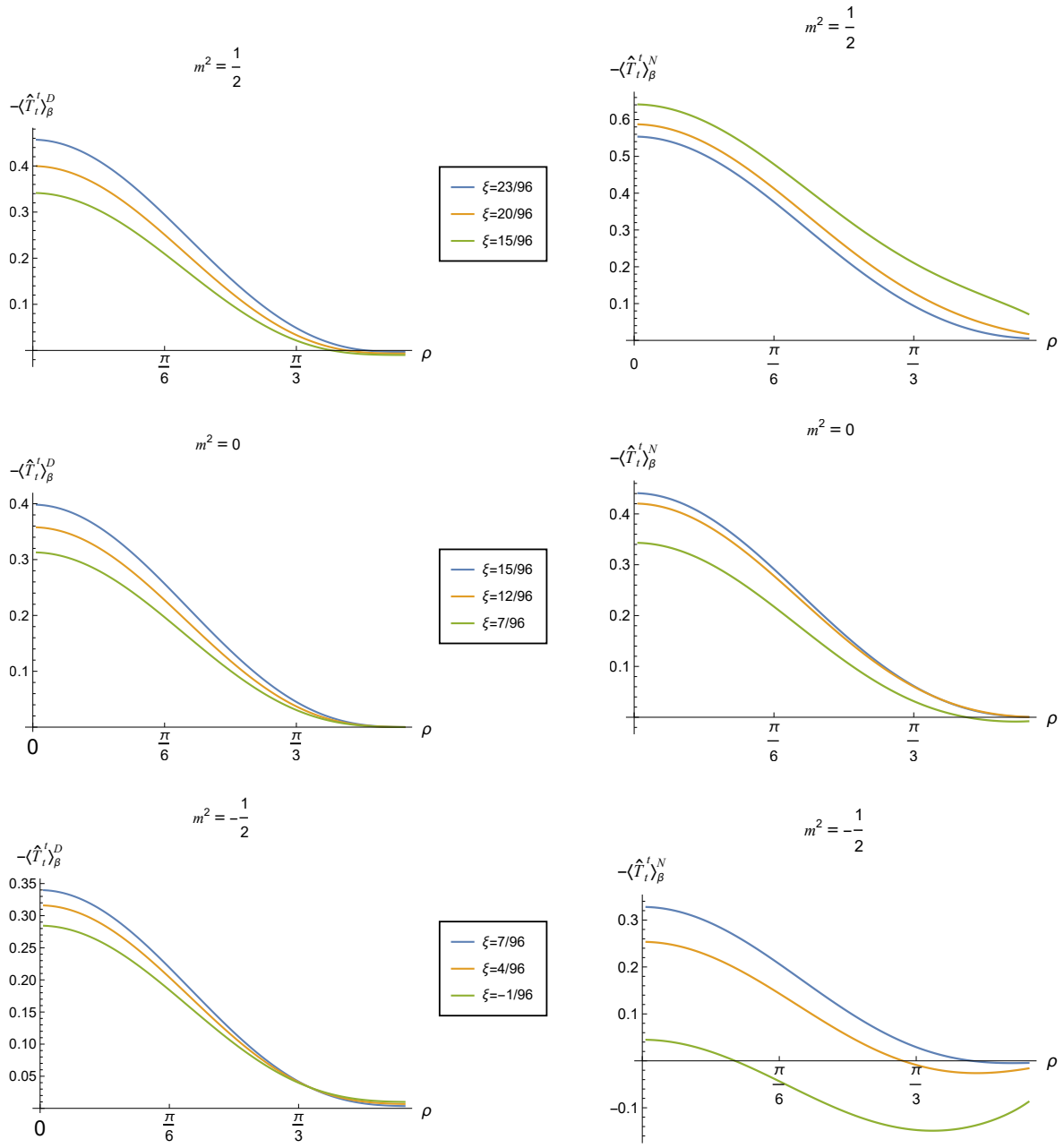

Figure 6.8: Renormalised t.e.v.s of the energy density component of the RSET, $-\langle \hat{T}_t^t \rangle_\beta^{D/N}$ with Dirichlet (left) and Neumann (right) boundary conditions, for different values of the coupling constant, ξ and fixed m^2. For all plots $\beta = 1$.

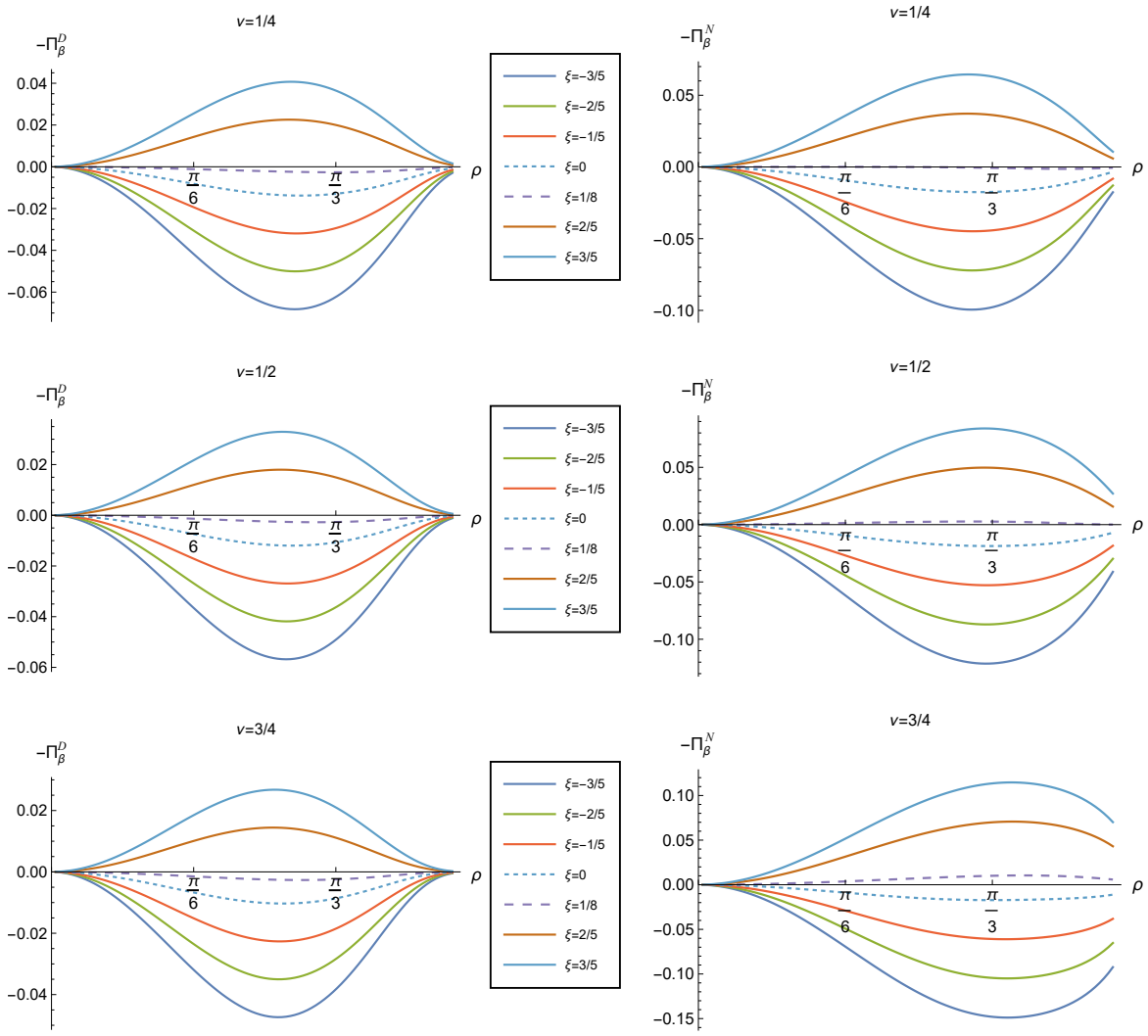

Figure 6.9: Negative thermal pressure deviators $-\Pi_\beta^{D/N}$ as functions of the radial coordinate ρ, for different values of ν and ξ with Dirichlet (left) and Neumann (right) boundary conditions. For all plots, $\beta = 1$.

parameter ν defined in (4.16). For the different values of ν used in this thesis we have (Figure 4.6)

$$\zeta_{\text{crit}} \sim \begin{cases} 0.64\pi & \text{for} \quad \nu = 1/4, \\ 0.57\pi & \text{for} \quad \nu = 1/2, \\ 0.52\pi & \text{for} \quad \nu = 3/4. \end{cases} \tag{6.18}$$

To determine the renormalised v.e.v.s of the RSET with Robin boundary conditions, we adopt the same procedure used for the VP (Chapter 5) and in Sections 6.1, 6.2 and consider the difference between the v.e.v. with Robin boundary conditions and the already renormalised Neumann v.e.v. (6.9). Following this we simply add the renormalised Neumann v.e.v. to the result. So, for the v.e.v. we start with the difference between the Robin and Neumann vacuum Green's functions (5.56, 5.84, 5.85)

$$G_E^{\zeta,0}(x,x') - G_E^{N,0}(x,x') = \frac{1}{4\pi^2}\int_{-\infty}^{\infty} e^{i\omega\Delta\tau} d\omega \sum_{\ell=-\infty}^{\infty} e^{i\ell\Delta\theta}\Big[g_{\omega\ell}^{\zeta}(\rho,\rho') - g_{\omega\ell}^{N}(\rho,\rho')\Big]. \tag{6.19}$$

We follow the same approach outlined in Section 6.2 and compute the components of (6.16) using (6.19) as $W(x,x')$. The lengthy expressions of the terms in (6.16) are displayed in Section 6.6.2 and are computed numerically using MATHEMATICA. As in the case of the RSET on adS4 (Chapter 3) the $\ell-$sum and $\omega-$integration in (6.19) is performed to 100.

Figure 6.10 shows the v.e.v.s of the energy density component of the RSET with Robin boundary conditions for the different values of ν studied and fixed $\xi = 1/8$. Unlike the case with Dirichlet and Neumann boundary conditions (6.9), when Robin boundary conditions are applied, the underlying space-time symmetry is broken. The v.e.v.s are no longer constant but depend on the radial coordinate ρ. The value of $\nu = 1/2$ corresponds to the massless, conformally coupled scalar field and the profiles seen are comparable to those in the adS4 case (Figure 3.4), with the energy density being positive throughout the space-time for all Robin parameters studied ($\zeta < \zeta_{\text{crit}}$). For $\nu = 1/4$ and $\nu = 3/4$ there are values of the Robin parameter ζ for which the energy density is negative for at least some values of ρ. However, for all values of ν, we find that $-\langle\hat{T}_\tau^\tau\rangle_0^\zeta$ appears to converge towards the Neumann result at the space-time boundary for all Robin parameters studied (except Dirichlet). This convergence is seen more clearly in the massless, conformally coupled case ($\nu = 1/2$) where $-\langle\hat{T}_\tau^\tau\rangle_0^\zeta$ with Dirichlet and Neumann boundary conditions are both zero. Similar profiles are seen for the $\langle\hat{T}_\rho^\rho\rangle_0^\zeta$ and $\langle\hat{T}_\theta^\theta\rangle_0^\zeta$ components, Figures 6.11 and 6.12, where again the components converge towards the Neumann result as the space-time boundary is approached, except Dirichlet which has its own limit. The dependence of the RSET components on the radial coordinate ρ also depends nontrivially on the Robin boundary condition as well as the value of ν. This is more easily appreciated in the 3D surface plots in the right column of Figures 6.10–6.12. In the massless, conformally coupled case ($\nu = 1/2$, $\xi = 1/8$) each RSET component has a similar profile, attaining its maximum at the space-time origin and monotonically decreasing with increasing ρ before converging to the common (zero) Dirichlet/Neumann v.e.v. at the space-time boundary. For the other values of ν, we see different behaviours for the three components of the RSET. For $\nu = 1/4$, we find that $-\langle\hat{T}_\tau^\tau\rangle_0^\zeta$ is either a monotonically increasing (for $\zeta > \pi/2$) or monotonically decreasing ($\zeta < \pi/2$) function of ρ, whilst the opposite is seen for $\langle\hat{T}_\rho^\rho\rangle_0^\zeta$ and $\langle\hat{T}_\theta^\theta\rangle_0^\zeta$. For $\nu = 3/4$, we find that $-\langle\hat{T}_\tau^\tau\rangle_0^\zeta$ is either a

monotonically decreasing (for $\zeta > \pi/2$) or monotonically increasing ($\zeta < \pi/2$) function of ρ, whilst again the opposite is seen for $\langle \hat{T}^{\rho}_{\rho} \rangle^{\zeta}_{0}$ and $\langle \hat{T}^{\theta}_{\theta} \rangle^{\zeta}_{0}$.

The profiles of the RSET components as functions of the Robin parameter ζ also depend on the value of ν. For $\nu = 1/2$, similar profiles are seen in the massless, conformally coupled case. The RSET components increase with increasing ζ and attain a maximum at some value of $\zeta \in (0, \pi/2)$ before decreasing to zero again at $\zeta = \pi/2$. Following this the RSET components steadily increase with increasing ζ and diverge as $\zeta \to \zeta_{\text{crit}}$. For the other values of ν, the v.e.v.s with Dirichlet and Neumann boundary conditions are no longer the same and as a result we see that the RSET components are either monotonically increasing or decreasing functions of ζ and also diverge as $\zeta \to \zeta_{\text{crit}}$.

When we consider the massless, conformally coupled case ($\nu = 1/2$, $\xi = 1/8$), there is a notable difference between the $\langle \hat{T}^{\rho}_{\rho} \rangle^{\zeta}_{0}$ and $\langle \hat{T}^{\theta}_{\theta} \rangle^{\zeta}_{0}$ plots seen in adS3 (Figures 6.11 and 6.12), and those seen in adS4 (Figure 3.4). In Figures 6.11 and 6.12, the $\langle \hat{T}^{\rho}_{\rho} \rangle^{\zeta}_{0}$ and $\langle \hat{T}^{\theta}_{\theta} \rangle^{\zeta}_{0}$ components, for $\nu = 1/2$, $\xi = 1/8$, are entirely positive throughout the space-time, converging to the common zero v.e.v. as the space-time boundary is approached. In contrast, the corresponding plot in adS4 (Figure 3.4) shows that the $\langle \hat{T}^{\rho}_{\rho} \rangle^{\zeta}_{0}$ and $\langle \hat{T}^{\theta}_{\theta} \rangle^{\zeta}_{0}$ components are entirely negative throughout the space-time and converge towards the negative common v.e.v. at the space-time boundary. The reason for this difference in behaviour of the $\langle \hat{T}^{\rho}_{\rho} \rangle^{\zeta}_{0}$ and $\langle \hat{T}^{\theta}_{\theta} \rangle^{\zeta}_{0}$ components is likely due to the different values of the v.e.v.s in adS3 and adS4, as the 3D surface plots are similar in appearance in each case.

The (negative) pressure deviators for the v.e.v.s of the RSET are shown in Figure 6.13 with the same parameter values used in Figures 6.11 and 6.12. The magnitudes of $-\Pi^{\zeta}_{0}$ are very small especially for $\nu = 1/4, 1/2$ where they are $\sim \mathcal{O}(10^{-5})$. This is likely to be a reflection of using conformal coupling, ($\xi = 1/8$) where $-\Pi^{\zeta}_{0}$ is at its minimum for Dirichlet and Neumann boundary conditions (Figure 6.9). There are significant differences in the pressure deviators when different values of ν are used. For each ν, we see that $-\Pi^{\zeta}_{0}$ is zero at the space-time origin and reaches its maximum magnitude between the origin and space-time boundary (left hand plots). However, it is at the space-time boundary where the differences between the different values of ν are more evident. For $\nu = 1/2$, it can be seen that $-\Pi^{\zeta}_{0}$ tends to zero at the space-time boundary consistent with the massless, conformally coupled field on adS4 (Figure 3.5). However, for the case of $\nu = 1/4$ and $\nu = 3/4$, the pressure deviators converge more slowly as they approach the space-time boundary, and still show considerable separation between the different Robin parameters studied as the space-time boundary is approached. For $\zeta = 0, \pi/2$ (Dirichlet and Neumann boundary conditions), we note that $-\Pi^{\zeta}_{0} = 0$ (see (6.9) and preceding discussion). For a given value of $\rho > 0$, the profiles of $-\Pi^{\zeta}_{0}$ with increasing ζ are best appreciated from the 3D surface plots (right column of Figure 6.13) and are strikingly different for the different values of ν studied. For $\nu = 1/2$, we see that $-\Pi^{\zeta}_{0}$ increases with ζ, attains a maximum at some value of $\rho \in (0, \pi/2)$ before decreasing back to zero for $\zeta = \pi/2$. Subsequently, $-\Pi^{\zeta}_{0}$ diverges as $\zeta \to \zeta_{\text{crit}}$. For $\nu = 1/4$, we can see that $-\Pi^{\zeta}_{0}$ increases with increasing ζ, attains a maximum at some $\zeta \in (0, \pi/2)$ and then diverges in a negative direction as $\zeta \to \zeta_{\text{crit}}$. The opposite picture is seen with $\nu = 3/4$.

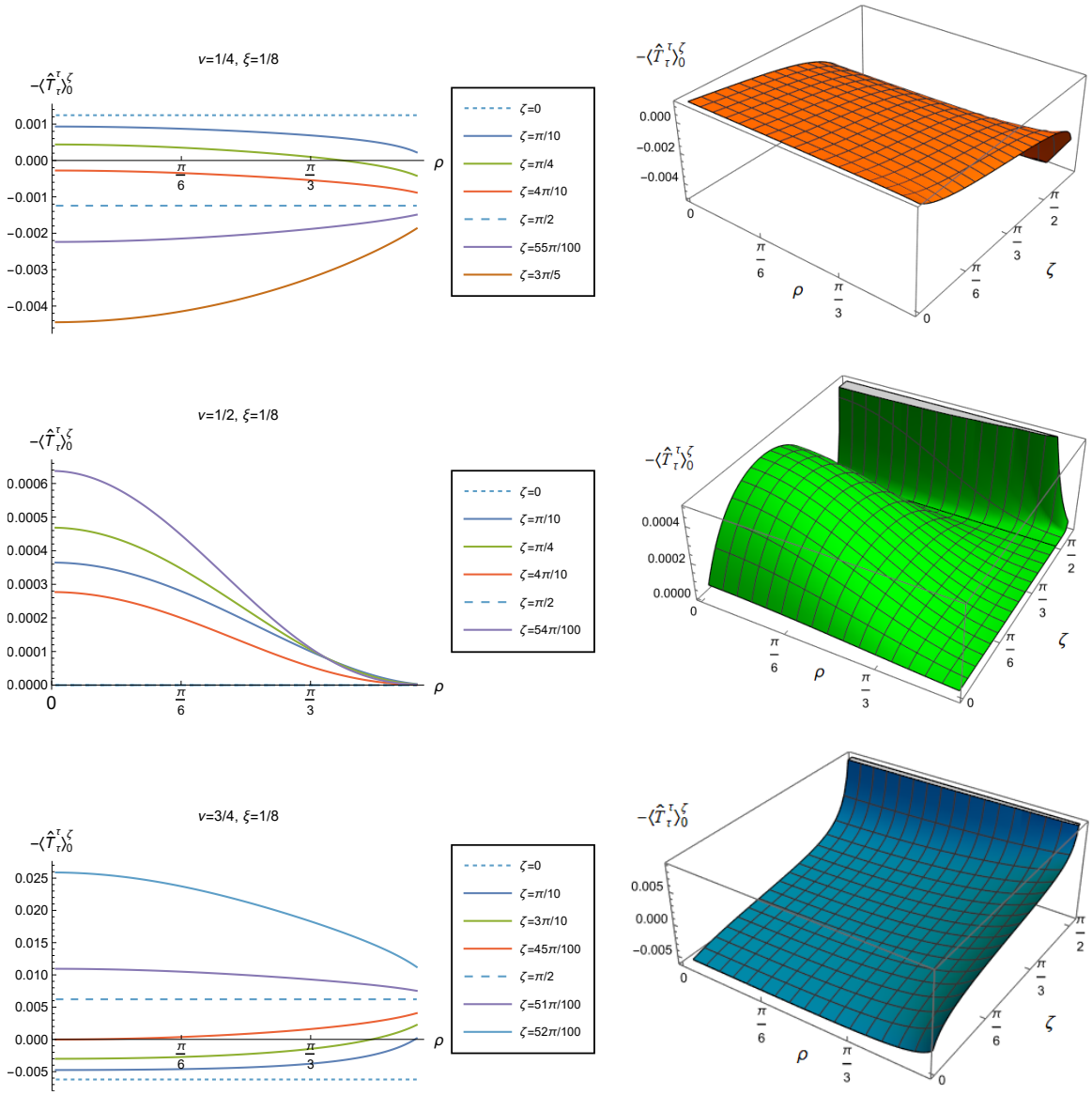

Figure 6.10: Renormalised v.e.v.s of the energy density component of the RSET, $-\langle\hat{T}^{\tau}_{\tau}\rangle^{\zeta}_{0}$, with Robin boundary conditions and different values of ν. Plots in the left column show $-\langle\hat{T}^{\tau}_{\tau}\rangle^{\zeta}_{0}$ as a function of the radial coordinate ρ for a range of Robin parameters, ζ. The right column shows the 3D-surface plots of the energy density as functions of ρ and ζ. For all plots, $\xi = 1/8$.

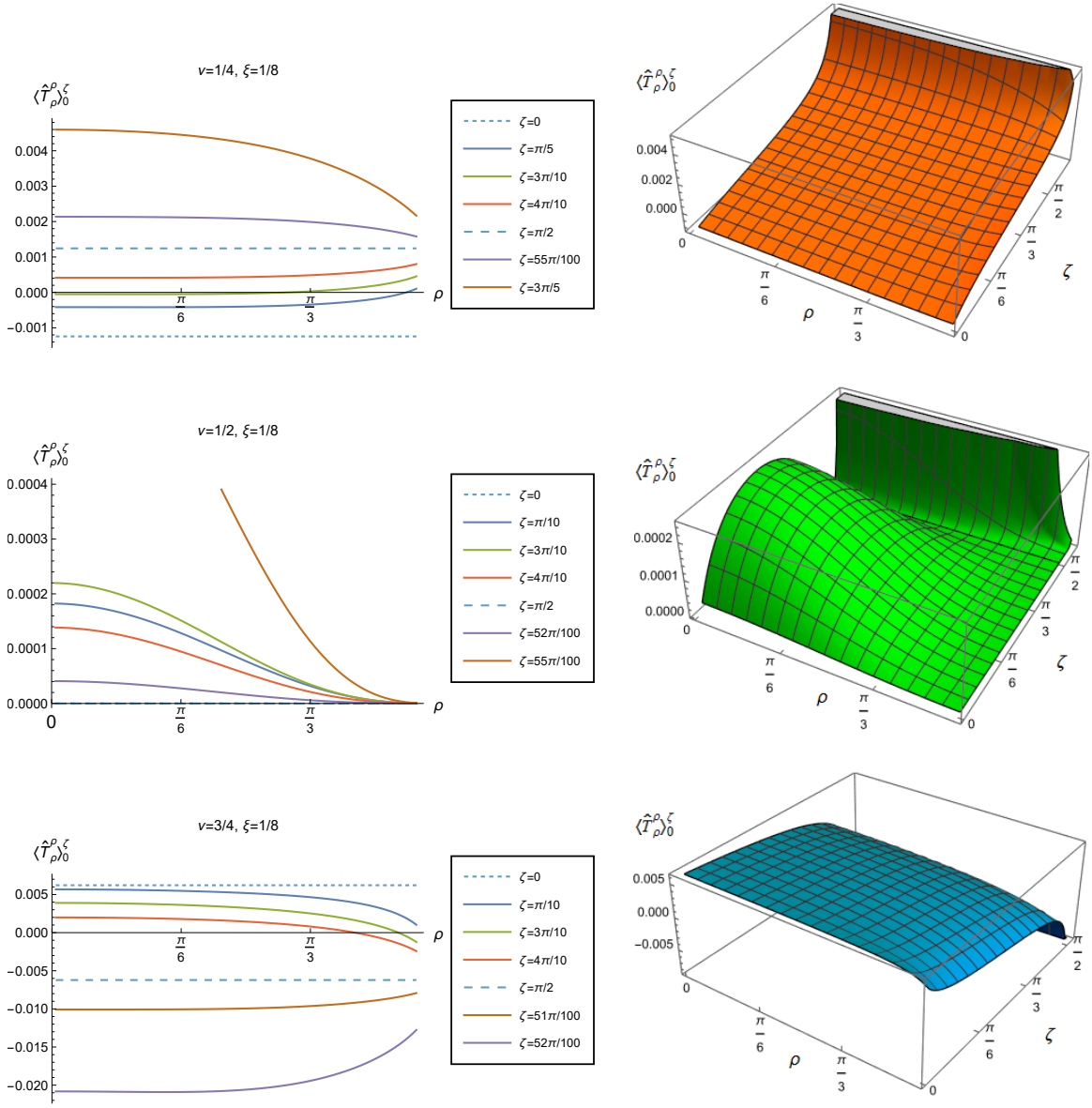

Figure 6.11: Renormalised v.e.v.s of the $\langle \hat{T}^{\rho}_{\rho} \rangle^{\zeta}_{0}$ component of the RSET with Robin boundary conditions and different values of ν. Plots in the left column show $\langle \hat{T}^{\rho}_{\rho} \rangle^{\zeta}_{0}$ as a function of the radial coordinate ρ for a range of Robin parameters, ζ. The right column shows the 3D-surface plots of $\langle \hat{T}^{\rho}_{\rho} \rangle^{\zeta}_{0}$ as functions of ρ and ζ. For all plots, $\xi = 1/8$.

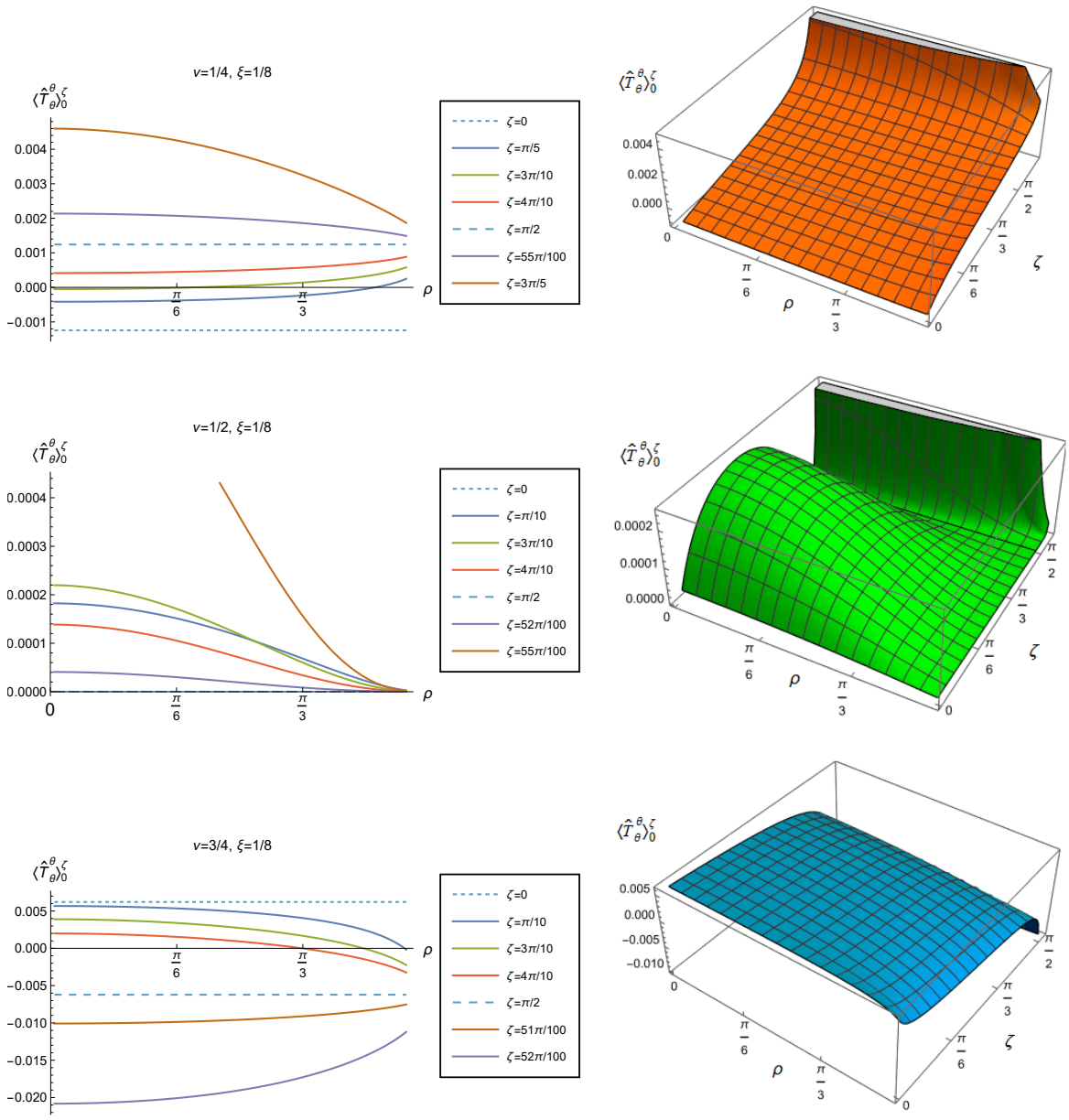

Figure 6.12: Renormalised v.e.v.s of the $\langle \hat{T}^{\theta}_{\theta} \rangle^{\zeta}_{0}$ component of the RSET with Robin boundary conditions and different values of ν. Plots in the left column show $\langle \hat{T}^{\theta}_{\theta} \rangle^{\zeta}_{0}$ as a function of the radial coordinate ρ for a range of Robin parameters, ζ. The right column shows the 3D-surface plots of $\langle \hat{T}^{\theta}_{\theta} \rangle^{\zeta}_{0}$ as functions of ρ and ζ. For all plots, $\xi = 1/8$.

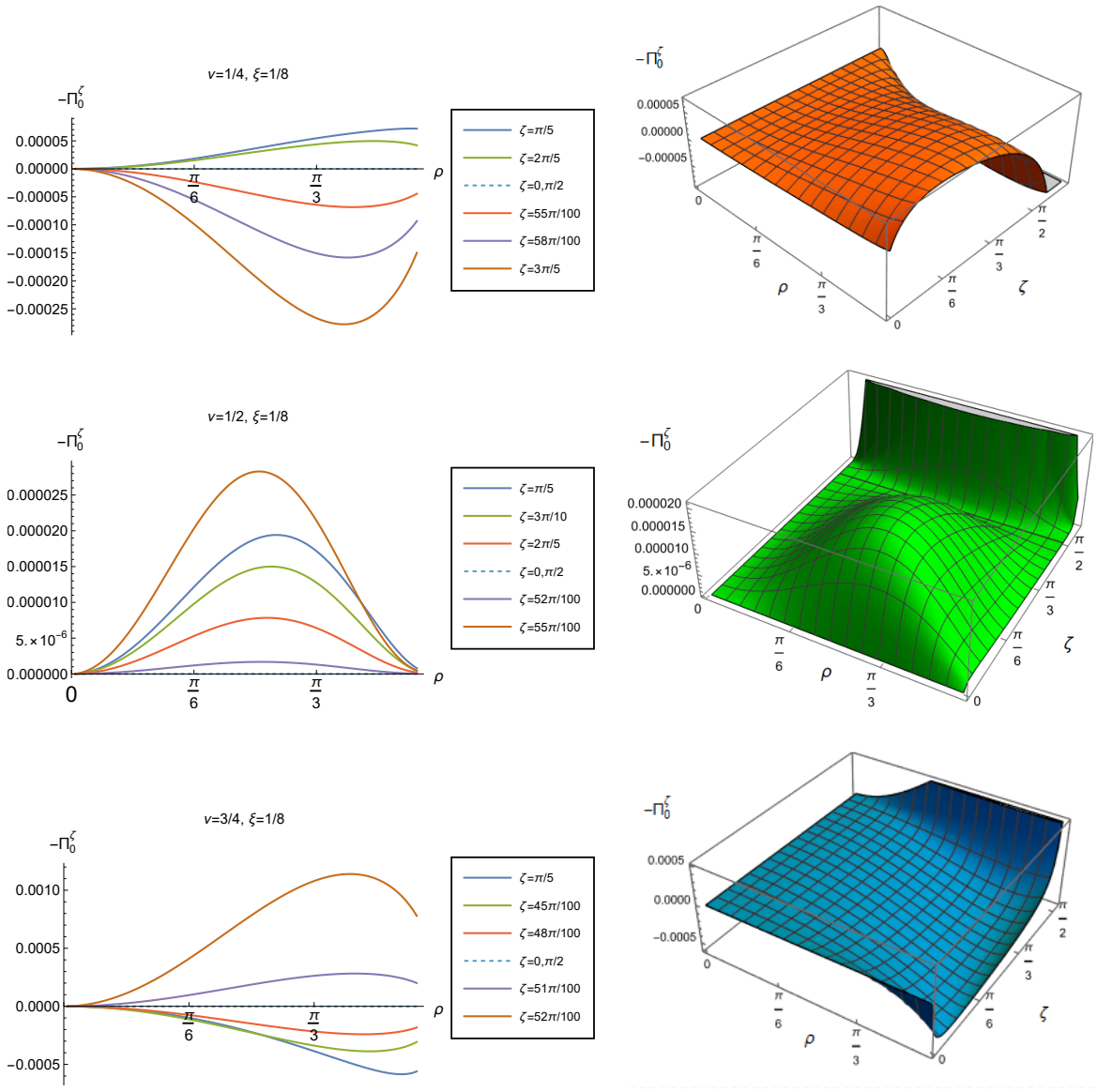

Figure 6.13: Negative vacuum pressure deviators, $-\Pi_0^\zeta$, with Robin boundary conditions and different values of ν. The left column shows $-\Pi_0^\zeta$ as a function of the radial coordinate ρ for a range of Robin parameters ζ. The right column shows the 3D surface plots of $-\Pi_0^\zeta$ as functions of ρ and ζ. For all plots, $\xi = 1/8$.

We now study the behaviour of the components of the RSET when we vary the coupling constant ξ, for a range of values of ν and ζ (Figures 6.14–6.19). Figure 6.14 shows the v.e.v.s of the RSET components as functions of the radial coordinate ρ with different values of the coupling constant ξ and fixed Robin parameter $\zeta = 3\pi/10$. The plot shows the results with $\nu = 1/4$ and $\nu = 3/4$. The behaviour of the v.e.v.s with respect to ξ depends significantly on the value of the parameter ν. For $\nu = 1/4$, the profiles for the energy density component $-\langle\hat{T}^{\tau}_{\tau}\rangle^{\zeta}_{0}$ show a wide variation at the space-time origin for the different values of ξ considered and converge to a common near-zero value for some $\rho \in (\pi/3, \pi/2)$. Following this the different $-\langle\hat{T}^{\tau}_{\tau}\rangle^{\zeta}_{0}$ diverge again as the space-time boundary is approached. The finding of a common cross-over point of the energy density component of the RSET with different values of ξ is also seen in [94], where the authors studied a quantum scalar field on a Schwarzschild black hole space-time. Interestingly in [94], it can be seen that $\langle\hat{T}^{\tau}_{\tau}\rangle$ profiles with different ξ diverge away from each other after the common cross-over point (much like the case in Figure 6.14) but following this the $\langle\hat{T}^{\tau}_{\tau}\rangle$ profiles converge to a common non-zero value further away from the black hole.

It can also be seen in Figure 6.14 that for $\xi \leq 0$ the energy density is positive at the space-time origin and becomes negative after the common cross-over point, whilst the opposite is seen for $\xi > 0$. The common cross-over point for $-\langle\hat{T}^{\tau}_{\tau}\rangle^{\zeta}_{0}$ is pushed further towards the space-time boundary when we increase the value of ν to 3/4. A similar picture is seen with the $\langle\hat{T}^{\rho}_{\rho}\rangle^{\zeta}_{0}$ and $\langle\hat{T}^{\theta}_{\theta}\rangle^{\zeta}_{0}$ components but the cross-over point is further towards the space-time boundary for $\langle\hat{T}^{\rho}_{\rho}\rangle^{\zeta}_{0}$ compared to $\langle\hat{T}^{\theta}_{\theta}\rangle^{\zeta}_{0}$. When we consider $\nu = 3/4$, we see that the cross-over point is seemingly pushed 'beyond' the space-time boundary and is therefore not evident, resulting in profiles of $\langle\hat{T}^{\rho}_{\rho}\rangle^{\zeta}_{0}$ and $\langle\hat{T}^{\theta}_{\theta}\rangle^{\zeta}_{0}$ that are almost parallel throughout the space-time.

Figure 6.15 focuses further on the effects of the coupling constant ξ on the energy density component $-\langle\hat{T}^{\tau}_{\tau}\rangle^{\zeta}_{0}$ with different values of ν and fixed ζ. We can see that increasing ν not only pushes the common cross-over point further towards the space-time boundary but also increases the magnitude of $-\langle\hat{T}^{\tau}_{\tau}\rangle^{\zeta}_{0}$, as evidenced by the increase in scale on the vertical axis. Of interest is the finding that before the cross-over point, increasing the coupling constant ξ results in a decrease in the energy density. This seems perhaps somewhat counter-intuitive, as increasing ξ with fixed ν results in an increase in the square of the mass (m^2) from (4.16). However, beyond the cross-over point, the opposite is seen with the energy density increasing with increasing ξ and therefore m^2.

Figure 6.16 shows the (negative) pressure deviators corresponding to Figure 6.14 with different values of ξ, fixed $\zeta = 3\pi/10$ and two values of ν. The pressure deviators show significant differences between the different values of ξ. For these parameter values, the pressure deviators are all zero close to the space-time origin and attain their maximum magnitude just before the space-time boundary is reached. Following this they appear to start to converge towards each other but still demonstrate wide separation, near the space-time boundary, with the different values of the coupling constant. The 3D surface plots in Figure 6.16 show that $-\Pi^{\zeta}_{0}$ is a monotonically decreasing function of ξ, for fixed $\rho > 0$, and this is more evident as we move towards the space-time boundary.

The finding of a common cross-over point in the values of the RSET components with different values of the coupling constant ξ, in Figures 6.14 and 6.15 is very much dependent on the chosen

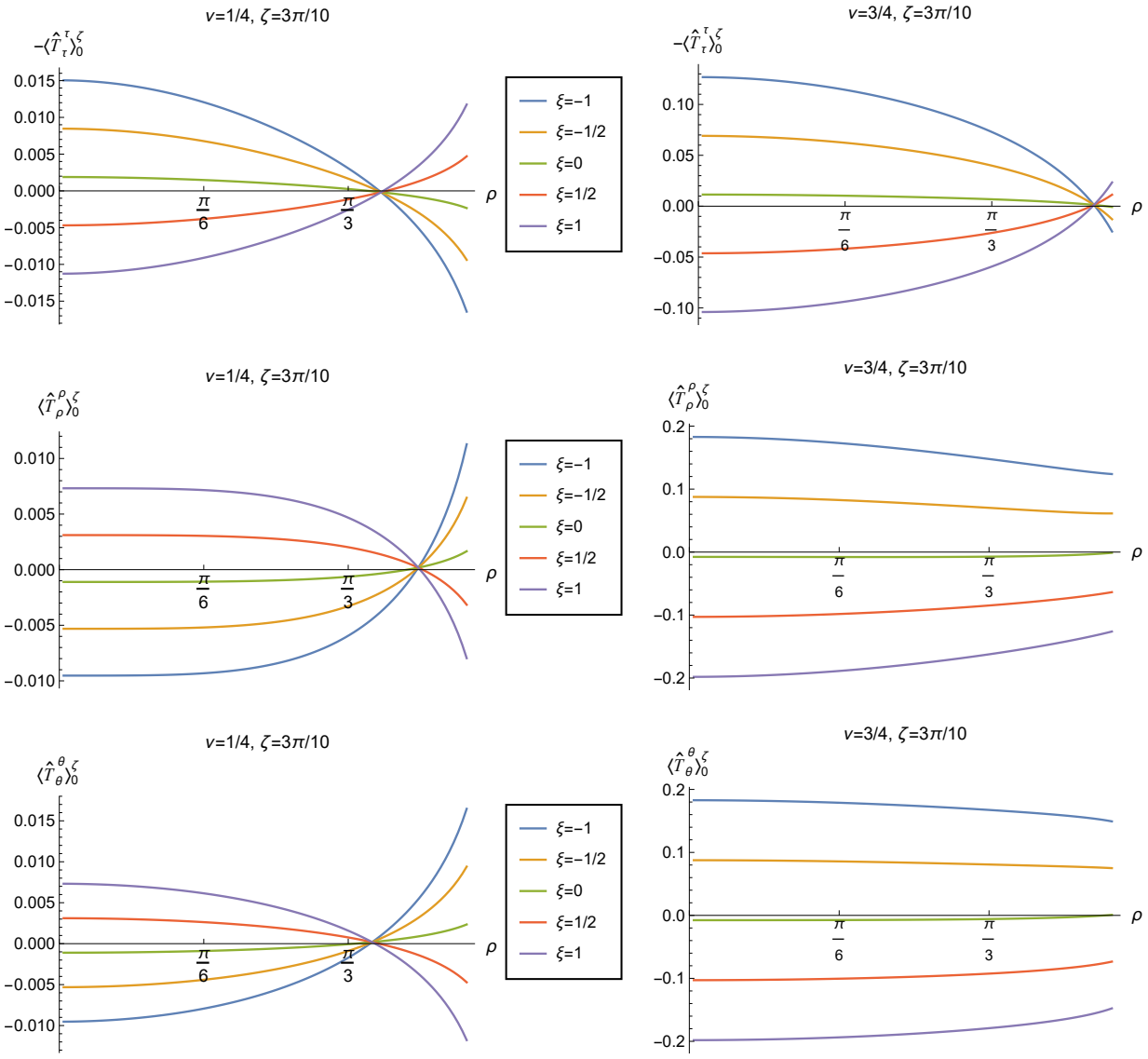

Figure 6.14: Renormalised v.e.v.s of the different components of the RSET for a selection of coupling constants ξ. In left column $\nu = 1/4$ and in the right column $\nu = 3/4$. For all plots, $\zeta = 3\pi/10$.

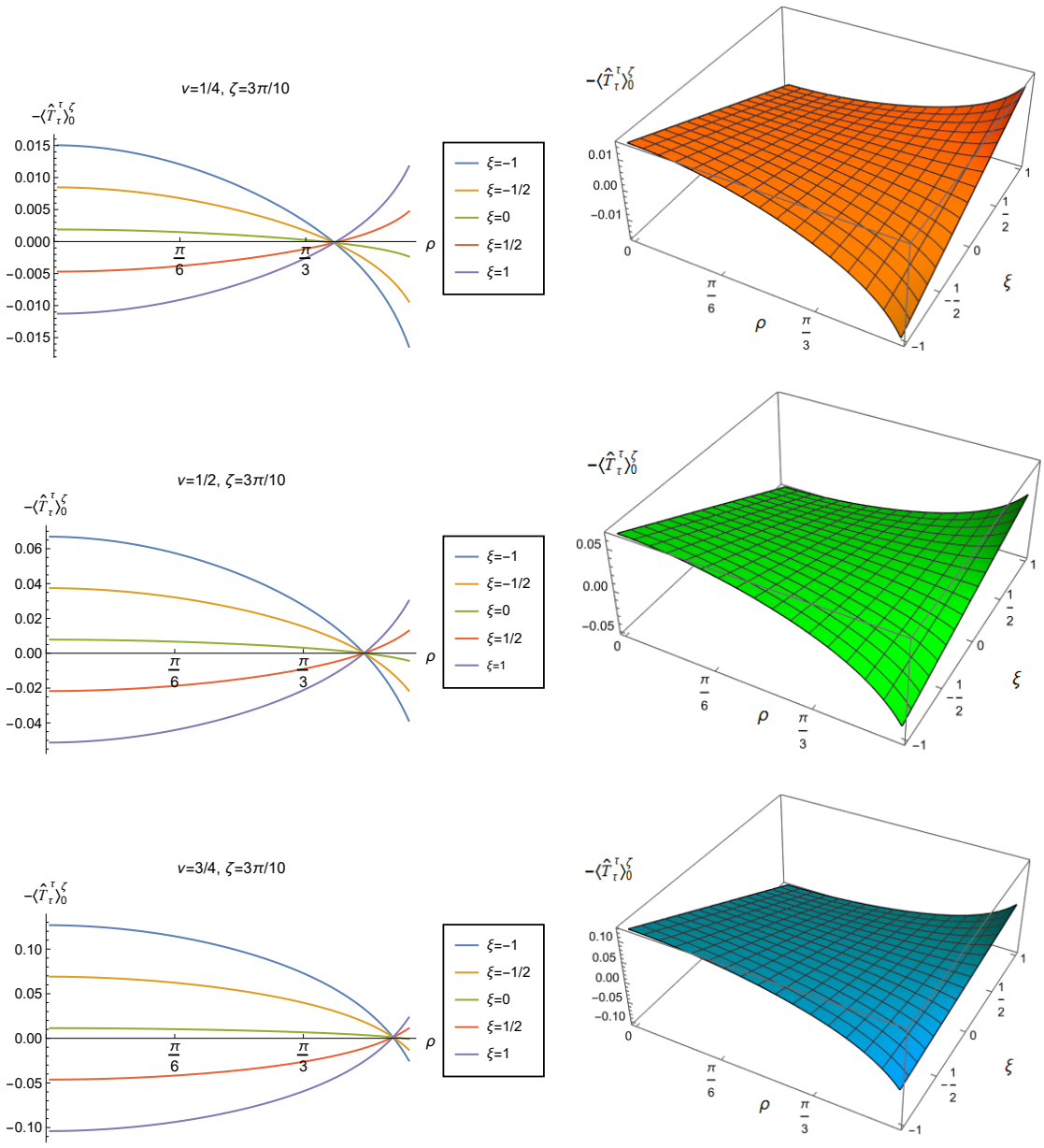

Figure 6.15: Renormalised v.e.v.s of the energy density component of the RSET, $-\langle\hat{T}_\tau{}^\tau\rangle_0^\zeta$, with a selection of coupling constants ξ. Top $\nu = 1/4$, middle $\nu = 1/2$ and bottom $\nu = 3/4$. Right column shows 3D surface plots of $-\langle\hat{T}_\tau{}^\tau\rangle_0^\zeta$ as functions of ρ and ξ. For all plots, $\zeta = 3\pi/10$.

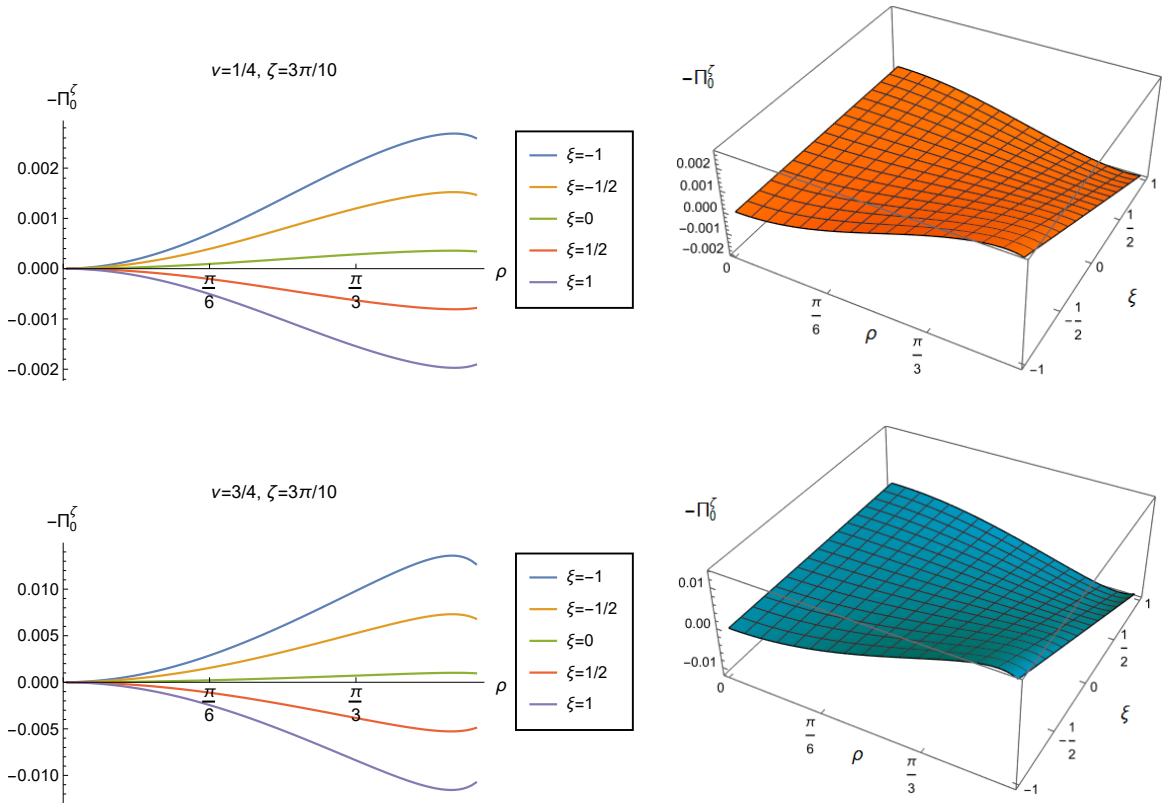

Figure 6.16: Negative vacuum pressure deviator $-\Pi_0^\zeta$, with different values of the coupling constant ξ and two values of ν, with fixed Robin parameter ζ (left). The right column shows 3D-surface plots for $-\Pi_0^\zeta$ as a function of the radial coordinate ρ and coupling constant ξ. For all plots $\zeta = 3\pi/10$.

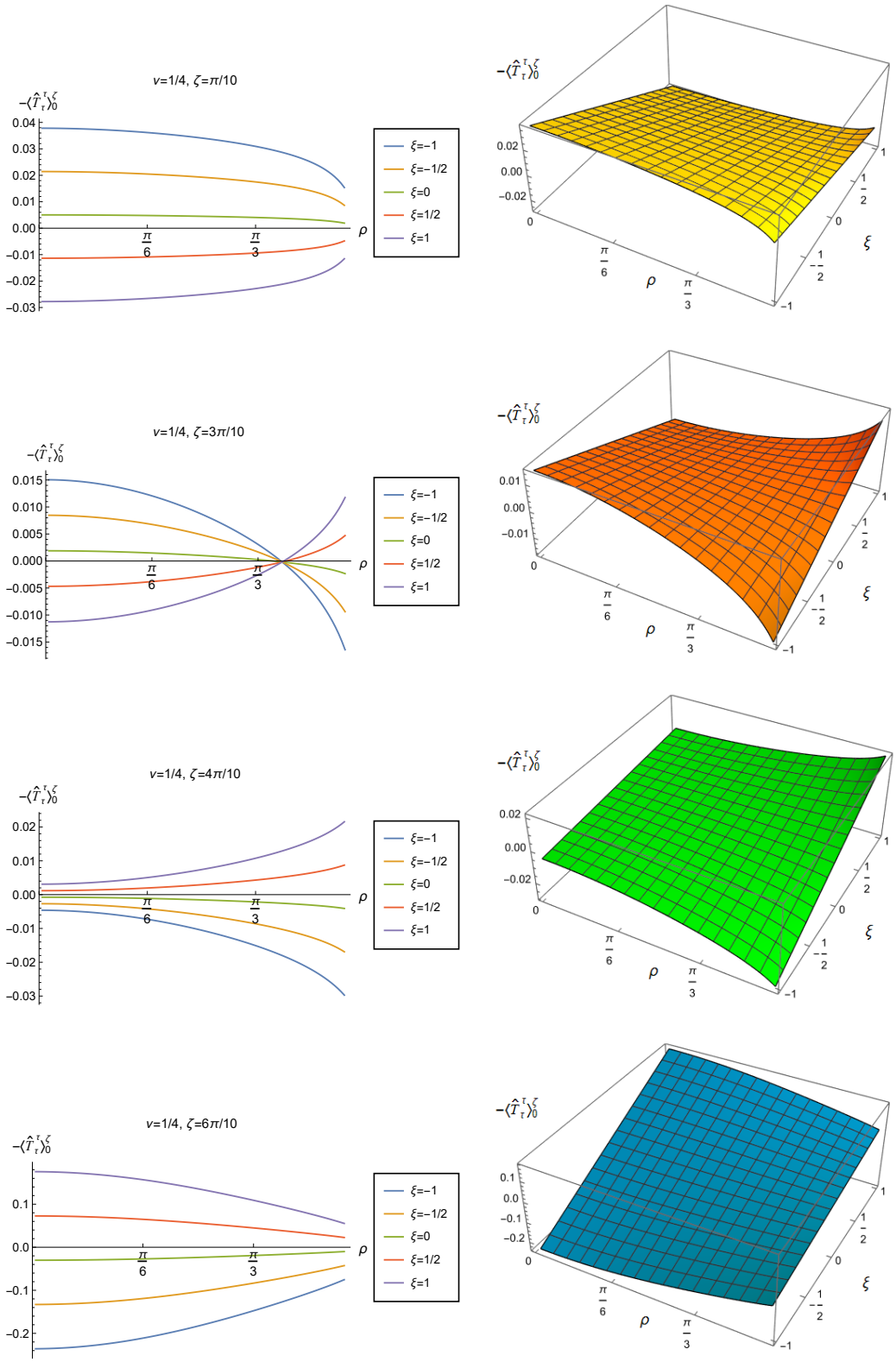

Figure 6.17: Renormalised v.e.v.s of the energy density component of the RSET, $-\langle\hat{T}_\tau^{\ \tau}\rangle_0^\zeta$, with different values of the coupling constant ξ and Robin parameter ζ. Top row $\zeta = \pi/10$, second row $\zeta = 3\pi/10$, third row $\zeta = 4\pi/10$ and bottom row $\zeta = 6\pi/10$. The right column shows 3D surface plots of $-\langle\hat{T}_\tau^{\ \tau}\rangle_0^\zeta$ as functions of ρ and ξ. For all plots $\nu = 1/4$.

value of the Robin parameter ζ. This is demonstrated in Figure 6.17, which shows $-\langle\hat{T}_\tau^{\ \tau}\rangle_0^\zeta$ with different values of ξ and ζ for fixed $\nu = 1/4$. We see that with $\zeta = \pi/10$, a cross-over point is not evident, although the plots appear to be converging towards each other as the space-time boundary is approached. With increasing ν, the cross-over point appears to be moving progressively towards the space-time origin such that with $\zeta = 4\pi/10$, the cross-over point is seemingly at or 'beyond' the space-time origin and the energy density increases with increasing ξ throughout the space-time. The behaviour of $-\langle\hat{T}_\tau^{\ \tau}\rangle_0^\zeta$ with different values of the Robin parameter ζ is perhaps more evident in the 3D surface plots in Figure 6.17. With $\zeta = \pi/10$, we see that $-\langle\hat{T}_\tau^{\ \tau}\rangle_0^\zeta$ is monotonically decreasing with increasing ξ for all $\rho \in (0, \pi/2)$. With $\zeta = 3\pi/10$, we see that $-\langle\hat{T}_\tau^{\ \tau}\rangle_0^\zeta$ monotonically decreases with increasing ξ before the cross-over point beyond which it monotonically increases with increasing ξ. For $\zeta = 4\pi/10$ and $\zeta = 3\pi/5$, we see that $-\langle\hat{T}_\tau^{\ \tau}\rangle_0^\zeta$ is now a monotonically increasing function of ξ for all $\rho \in (0, \pi/2)$. For $\zeta = 4\pi/10$, the rate of increase is maximum towards the space-time boundary, whilst for $\zeta = 3\pi/5$, the rate of increase is maximum towards the origin.

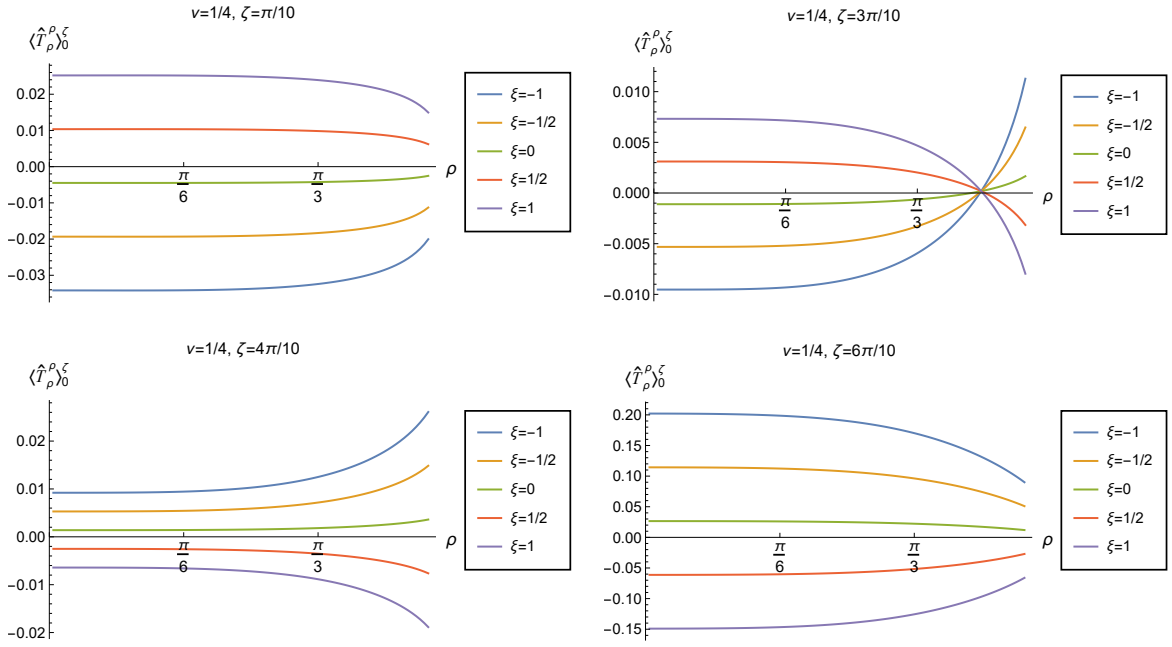

Figure 6.18: Renormalised v.e.v.s of the $\langle\hat{T}_\rho^{\ \rho}\rangle_0^\zeta$ component of the RSET with different values of the coupling constant ξ and Robin parameter ζ. Top left $\zeta = \pi/10$, top right $\zeta = 3\pi/10$, bottom left $\zeta = 4\pi/10$ and bottom right $\zeta = 6\pi/10$. For all plots $\nu = 1/4$.

Figure 6.18 shows the $\langle\hat{T}_\rho^{\ \rho}\rangle_0^\zeta$ component of the RSET with different values of the coupling constant ξ and Robin parameter ζ. The behaviour of $\langle\hat{T}_\rho^{\ \rho}\rangle_0^\zeta$ with respect to ξ differs from that seen in Figure 6.17 for the energy density component. With $\zeta = \pi/10$, we can see that $\langle\hat{T}_\rho^{\ \rho}\rangle_0^\zeta$ monotonically increases with increasing ξ throughout the space-time, whilst for $\zeta = 3\pi/5$, it monotonically decreases with increasing ξ. The plot for the $\langle\hat{T}_\theta^{\ \theta}\rangle_0^\zeta$ component is similar to that of $\langle\hat{T}_\rho^{\ \rho}\rangle_0^\zeta$ and is not displayed. Instead we show the (negative) pressure deviator, $-\Pi_0^\zeta$ in Figure 6.19, with the same parameters used in Figures 6.18. Figure 6.19 shows that the Robin parameter ζ has a noticeable

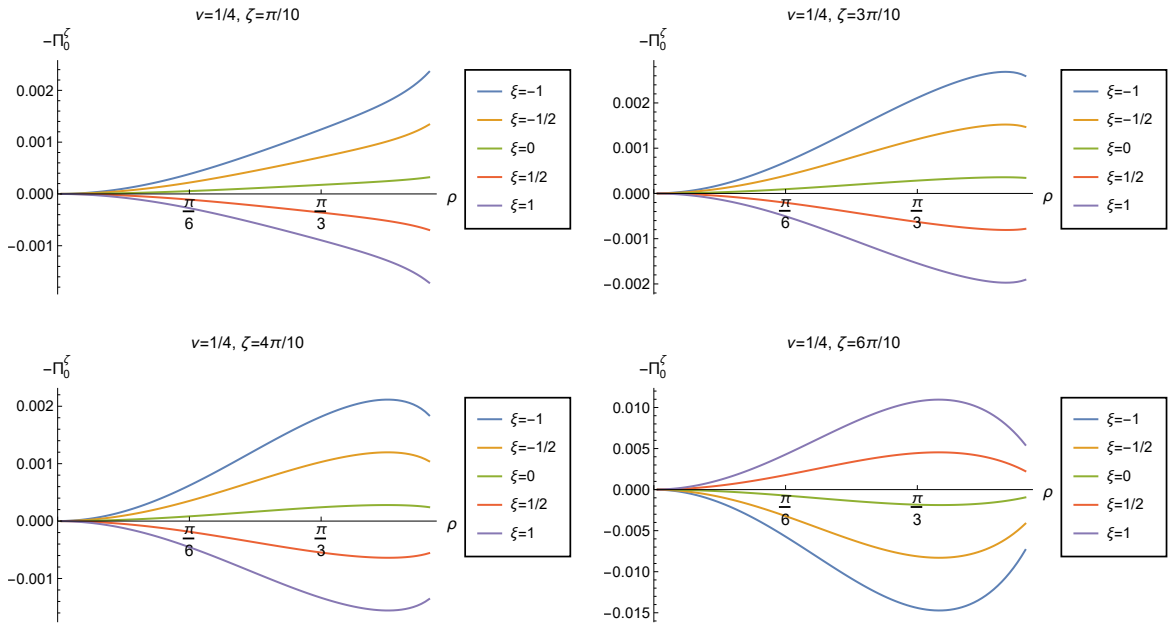

Figure 6.19: Negative vacuum pressure deviators, $-\Pi_0^\zeta$, with different values of the coupling constant ξ and Robin parameter ζ. Top left $\zeta = \pi/10$, top right $\zeta = 3\pi/10$, bottom left $\zeta = 4\pi/10$ and bottom right $\zeta = 3\pi/5$. For all plots $\nu = 1/4$.

effect on the pressure deviator. With these parameters, $-\Pi_0^\zeta$ is zero at the space-time origin following which it increases in magnitude steadily towards the space-time boundary. For $\zeta = \pi/10$, the pressure deviators increase in magnitude with increasing ρ and the plots continue to move apart as the space-time boundary is approached. With larger values of ζ, the plots attain their maximum magnitude at some value of $\rho \in (\pi/3, \pi/2)$ following which they appear to slowly move towards each other, more so with $\zeta = 6\pi/10$.

Having examined the v.e.v.s of the RSET with Robin boundary conditions, we now turn our attention to the t.e.v.s using a selection of values of the inverse temperature β.

§ 6.4 Thermal expectation values with Robin boundary conditions

To determine the t.e.v.s of the RSET with Robin boundary conditions, we again consider the difference between the t.e.v.s with Robin and Neumann boundary conditions and then add the renormalised t.e.v. with the Neumann boundary condition. So for the t.e.v. we start with the difference between the Robin and Neumann thermal Green's functions

$$G_E^{\zeta,\beta}(x,x') - G_E^{N,\beta}(x,x') = \frac{\kappa}{4\pi^2} \sum_{n=-\infty}^{\infty} \sum_{\ell=-\infty}^{\infty} e^{in\kappa\Delta\tau} e^{i\ell\Delta\theta} \Big[g_{n\ell}^{\zeta}(\rho,\rho') - g_{n\ell}^{N}(\rho,\rho') \Big]. \tag{6.20}$$

We follow the same approach outlined in Section 6.3, and use (6.20) as $W(x,x')$. The lengthy expressions of the terms in (6.16) are displayed in Section 6.6.3 and are computed numerically using MATHEMATICA. In order to make the numerical computations tractable, the $\ell-$ and $n-$ sums in (6.16) are performed to 50 and 20 respectively and with this the relative error for the individual

components of the RSET range between $\sim 10^{-5}$ and $\sim 10^{-7}$ compared to if the $\ell-$ and $n-$sums were performed to 150 each. This relative error was found for representative parameter values of $\zeta = \pi/10$, $\nu = 1/2$, $\beta = 1$ and near the space-time boundary at $\rho = 94\pi/200$. Whilst these relative errors are acceptable, it is likely that they represent an upper limit as it was noted in Section 3.4 that the relative errors incurred in curtailing summations were in fact better further away from the space-time boundary.

Figure 6.20 shows the renormalised t.e.v.s of the energy density component of the RSET $-\langle\hat{T}^{\tau}_{\tau}\rangle^{\zeta}_{\beta}$ with different Robin boundary conditions, three different values of ν ($\nu = 1/4$, $\nu = 1/2$ and $\nu = 3/4$), fixed $\xi = 1/8$ and $\beta = 1$. The value of $\beta = 1$ is the highest temperature studied in this chapter and, as discussed in Section 3.9, is based on setting the radius of curvature of adS, L, to unity and is thus in units of L. It can be seen that for these parameter values, $-\langle\hat{T}^{\tau}_{\tau}\rangle^{\zeta}_{\beta}$ is a monotonically decreasing function of ρ. We also see that $-\langle\hat{T}^{\tau}_{\tau}\rangle^{\zeta}_{\beta}$ is monotonically increasing with increasing ζ, eventually diverging as we approach ζ_{crit} (see Section 4.5). This is more easily appreciated in the 3D surface plots in the right column of Figure 6.20. It should be remembered that the value of ζ_{crit} depends on the value of ν (see Section 4.5). It can also be seen that for $\nu = 1/4$ and $\nu = 1/2$, the plots of $-\langle\hat{T}^{\tau}_{\tau}\rangle^{\zeta}_{\beta}$, with the different Robin boundary conditions, are quite close together, more so with $\nu = 1/4$. All plots (except Dirichlet, $\zeta = 0$) converge towards the Neumann v.e.v. at the space-time boundary. In the case of $\nu = 1/2$, $\xi = 1/8$ (massless, conformally coupled), both the Neumann and Dirichlet v.e.v. are equal to zero. For $\nu = 3/4$, the plots are more widely separated but still appear to be converging to the Neumann v.e.v. at the space-time boundary albeit more slowly than with $\nu = 1/4$, $1/2$.

Figure 6.21 shows the $\langle\hat{T}^{\rho}_{\rho}\rangle^{\zeta}_{\beta}$ component of the RSET using the same parameters used in Figure 6.20. As with $-\langle\hat{T}^{\tau}_{\tau}\rangle^{\zeta}_{\beta}$, the $\langle\hat{T}^{\rho}_{\rho}\rangle^{\zeta}_{\beta}$ component is also a monotonically decreasing function of ρ, except for $\nu = 3/4$. Also, with $\nu = 3/4$, the $\langle\hat{T}^{\rho}_{\rho}\rangle^{\zeta}_{\beta}$ component monotonically decreases with increasing ζ eventually diverging in the negative direction as $\zeta \to \zeta_{\text{crit}}$. The opposite behaviour is seen for $\nu = 1/4$ and $\nu = 1/2$ where $\langle\hat{T}^{\rho}_{\rho}\rangle^{\zeta}_{\beta}$ monotonically increases with increasing ζ. Furthermore, for $\nu = 1/4$ and $\nu = 1/2$, the plots for different Robin boundary conditions converge towards the Neumann result at the space-time boundary (except for Dirichlet, $\zeta = 0$). For $\nu = 3/4$, there is quite wide separation between the plots and this persists as the space-time boundary is approached. However, it appears that, for $\zeta > 0$, the plots are starting to converge towards the Neumann result as the space-time boundary is approached, albeit quite slowly.

The $\langle\hat{T}^{\theta}_{\theta}\rangle^{\zeta}_{\beta}$ component of the RSET exhibits qualitatively similar behaviour to the $\langle\hat{T}^{\rho}_{\rho}\rangle^{\zeta}_{\beta}$ component and is therefore not shown. Instead we plot the (negative) pressure deviators using the same parameter values used in Figure 6.21, and this is displayed in Figure 6.22. For all values of ν, we see that $-\Pi^{\zeta}_{\beta}$ is zero at the space-time origin. For $\nu = 1/2$ and $\xi = 1/8$, representing the massless, conformally coupled case, we see a similar picture to that seen in adS4 (Figure 3.11), where $-\Pi^{\zeta}_{\beta}$ attains its maximum magnitude for some $\rho \in (0, \pi/2)$, before converging to zero at the space-time boundary. With $\nu = 3/4$, the plots also attain a maximum magnitude at some $\rho \in (0, \pi/2)$ but the subsequent convergence occurs more slowly so the plots are still widely separated close to the

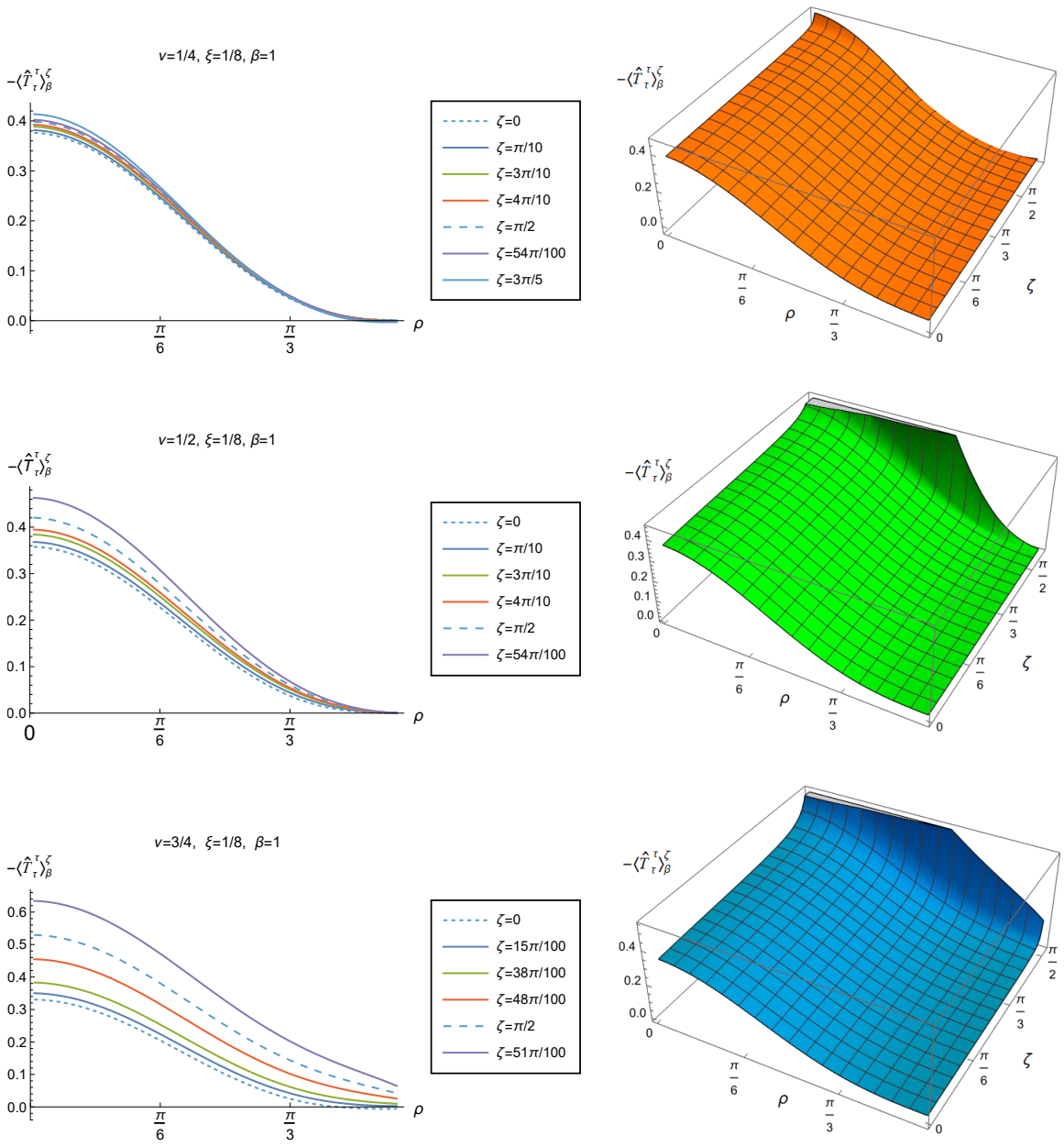

Figure 6.20: Renormalised t.e.v.s of the energy density component of the RSET $-\langle\hat{T}^{\tau}_{\tau}\rangle^{\zeta}_{\beta}$ with Robin boundary conditions. The left column shows $-\langle\hat{T}^{\tau}_{\tau}\rangle^{\zeta}_{\beta}$ for a selection of Robin parameters ζ. For $\nu = 3/4$, the values of ζ have been chosen to produce profiles that are clearly separated. The right column shows the 3D surface plots of $-\langle\hat{T}^{\tau}_{\tau}\rangle^{\zeta}_{\beta}$ as functions of the radial coordinate ρ and Robin parameter ζ. Top $\nu = 1/4$, middle $\nu = 1/2$ and bottom $\nu = 3/4$. For all plots, $\xi = 1/8$ and $\beta = 1$.

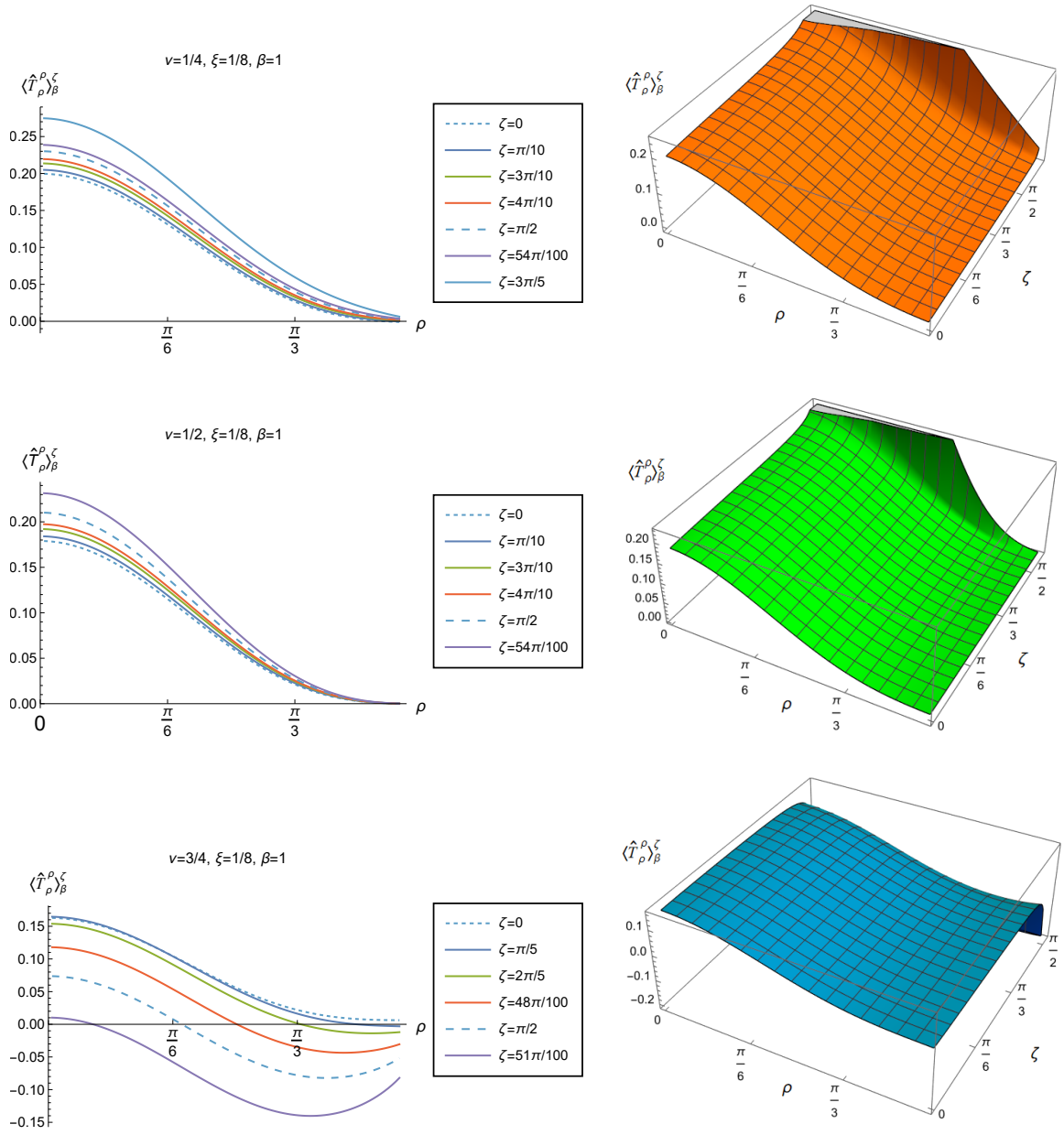

Figure 6.21: Renormalised t.e.v.s of the $\langle \hat{T}^{\rho}_{\rho} \rangle^{\zeta}_{\beta}$ component of the RSET with Robin boundary conditions and different values of ν; top $\nu = 1/4$, middle $\nu = 1/2$ and bottom $\nu = 3/4$. The left column shows $\langle \hat{T}^{\rho}_{\rho} \rangle^{\zeta}_{\beta}$ as a function of the radial coordinate ρ for a selection of Robin parameters ζ. The right column shows the 3D surface plots of $\langle \hat{T}^{\rho}_{\rho} \rangle^{\zeta}_{\beta}$ as functions of ρ and ζ. For all plots, $\xi = 1/8$ and $\beta = 1$.

space-time boundary. For both $\nu = 1/2$ and $\nu = 3/4$, we see that $-\Pi^{\zeta}_{\beta}$ is positive throughout the space-time, for all ζ considered, except for the Dirichlet boundary condition ($\zeta = 0$). The behaviour of $-\Pi^{\zeta}_{\beta}$ with $\nu = 1/4$, however, shows marked differences compared to the other values of ν. Whilst $-\Pi^{\zeta}_{\beta}$ is zero at the space-time origin, most of the plots are negative throughout the space-time, achieving their respective minima at different values of $\rho \in (0, \pi/2)$. Furthermore, away from the space-time origin, we see that $-\Pi^{\zeta}_{\beta}$ is monotonically increasing with increasing ζ, for $\nu = 1/2$ and $\nu = 3/4$. This can be better appreciated in the 3D surface plots. For $\nu = 1/4$, it can be seen that $-\Pi^{\zeta}_{\beta}$ is no longer a monotonic function of ζ. It increases with increasing ζ up to $\zeta \sim \pi/2$ following which it decreases with increasing ζ.

Figure 6.23 demonstrates the effects of temperature on the t.e.v.s of the energy density component of the RSET with Robin boundary conditions. Not surprisingly, the energy density increases in magnitude with increasing temperature (decreasing β). For each value of β studied, the plots for $\nu = 1/4$ are less spread out than for $\nu = 3/4$. Also with $\nu = 1/4$, the plots become closer together with increasing temperature in much the same way as was seen in the massless, conformally coupled case on adS4 (Figure 3.8). However, with $\beta \geq 3/2$ we see there is a cross-over of the plots located between $\rho = \pi/6$ and $\rho = \pi/3$. The cross-over does not appear to occur at a single space-time position as in Figure 6.17 but is spread out with different plots crossing at different places. This cross-over is not seen with the larger $\nu = 3/4$, where the separation between the plots is generally wider compared to $\nu = 1/4$ for all values of β studied. As with $\nu = 1/4$, the plots with $\nu = 3/4$ come together more with increasing temperature, suggesting that the effects of the Robin boundary conditions are 'washed out' with increasing temperature.

Figure 6.24 shows the $\langle \hat{T}^{\rho}_{\rho} \rangle^{\zeta}_{\beta}$ component of the RSET for the same parameter values as in Figure 6.23. Unlike the energy density, there is no cross-over of the plots for any temperature studied. For both values of ν, the Dirichlet and Neumann plots (dotted) converge towards their respective (different) v.e.v. at the space-time boundary. The difference between the Dirichlet and Neumann plots at the boundary is more difficult to appreciate with $\nu = 1/4$ and increasing temperature due to the changing scales involved. The plots for the different Robin boundary conditions are closer together with $\nu = 1/4$ compared to $\nu = 3/4$, with the separation between the plots decreasing with increasing temperature for both values of ν. With $\nu = 1/4$, we find that $\langle \hat{T}^{\rho}_{\rho} \rangle^{\zeta}_{\beta}$ is a monotonically decreasing function of ρ, whilst this is not the case for $\nu = 3/4$. For $\nu = 1/4$ and all temperatures it appears that both $-\langle \hat{T}^{\tau}_{\tau} \rangle^{\zeta}_{\beta}$ and $\langle \hat{T}^{\rho}_{\rho} \rangle^{\zeta}_{\beta}$ converge towards the Neumann result at the space-time boundary. Similar findings are also suggestive for $-\langle \hat{T}^{\tau}_{\tau} \rangle^{\zeta}_{\beta}$ with $\nu = 3/4$. However, for $\langle \hat{T}^{\rho}_{\rho} \rangle^{\zeta}_{\beta}$ and $\nu = 3/4$, convergence at the space-time boundary is less clear owing to the wider separation of the plots. All plots are closer to the Neumann result at the space-time boundary than at the origin and if we were able to perform the numerical computations closer to the space-time boundary, convergence to the Neumann result may be more evident.

Figure 6.25 shows the (negative) pressure deviators corresponding to Figure 6.24 to highlight the difference between the $\langle \hat{T}^{\rho}_{\rho} \rangle^{\zeta}_{\beta}$ and $\langle \hat{T}^{\theta}_{\theta} \rangle^{\zeta}_{\beta}$ components of the RSET. For both $\nu = 1/4$ and $\nu = 3/4$, the pressure deviators are zero at the space-time origin and attain their maximum magnitude

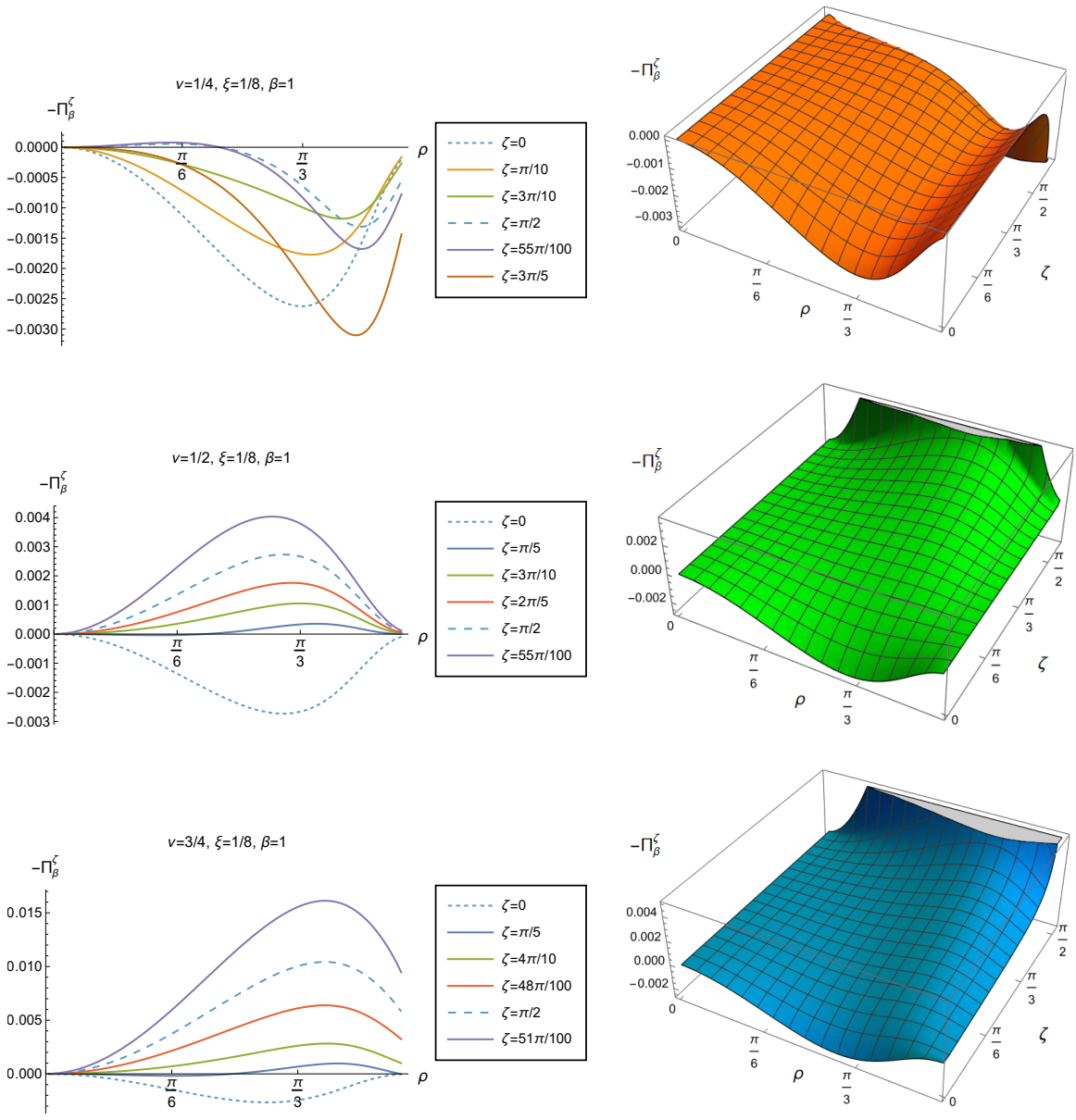

Figure 6.22: Negative thermal pressure deviators $-\Pi_\beta^\zeta$ with Robin boundary conditions and different values of ν; top $\nu = 1/4$, middle $\nu = 1/2$ and bottom $\nu = 3/4$. The left column shows $-\Pi_\beta^\zeta$ as a function of the radial coordinate ρ, for a selection of Robin parameters ζ. The right column shows the 3D surface plots of $-\Pi_\beta^\zeta$ as functions of ρ and ζ. For all plots, $\xi = 1/8$ and $\beta = 1$.

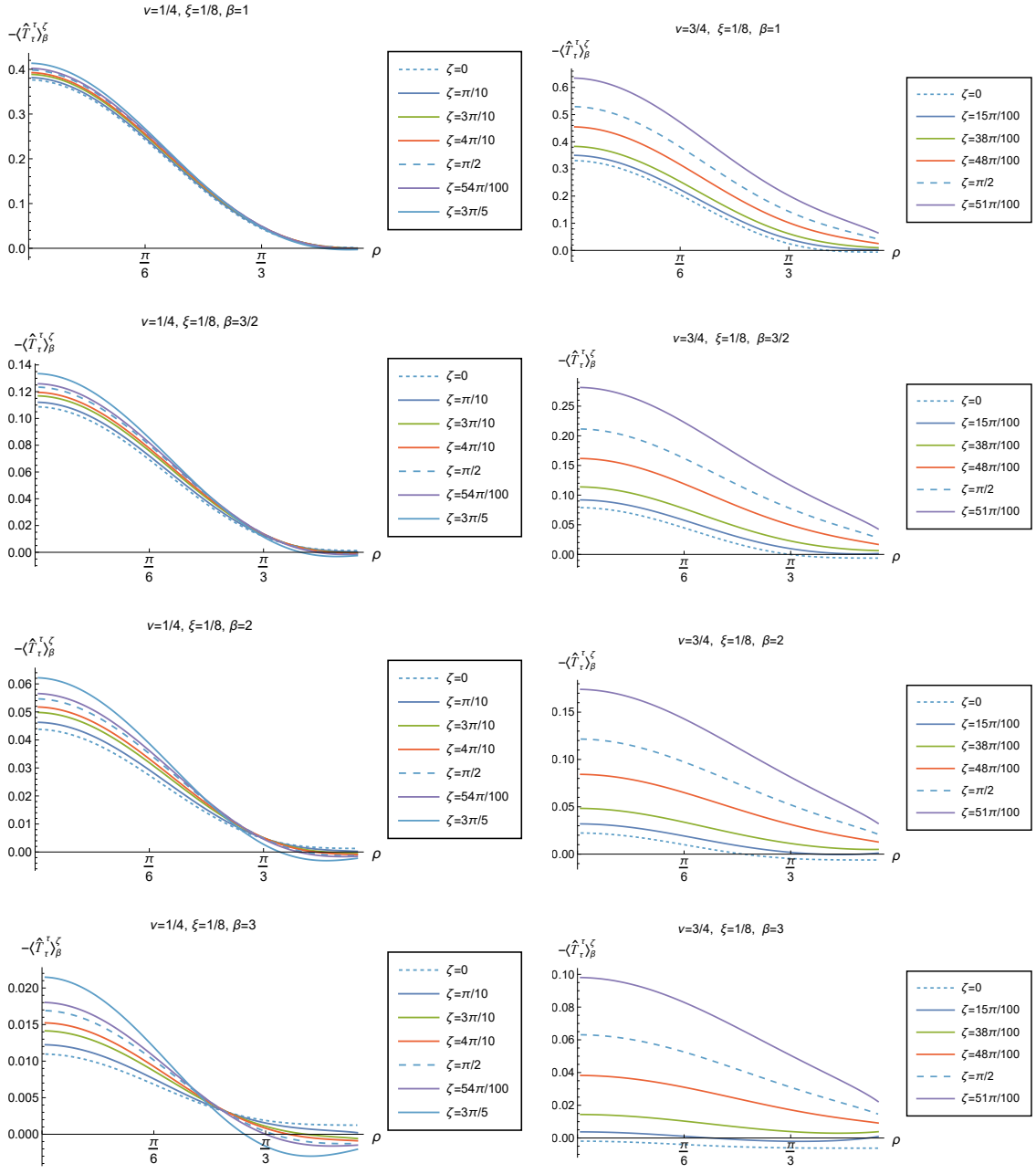

Figure 6.23: Renormalised t.e.v.s of the energy density component of the RSET, $-\langle\hat{T}_\tau^\tau\rangle_\beta^\zeta$, with Robin boundary conditions and different inverse temperatures β. Plots show $-\langle\hat{T}_\tau^\tau\rangle_\beta^\zeta$ as a function of the radial coordinate ρ for a selection of Robin parameters ζ. In the left column we have $\nu = 1/4$ and the right column $\nu = 3/4$. For each column, top row $\beta = 1$, second row $\beta = 3/2$, third row $\beta = 2$ and bottom row $\beta = 3$. For all plots, $\xi = 1/8$.

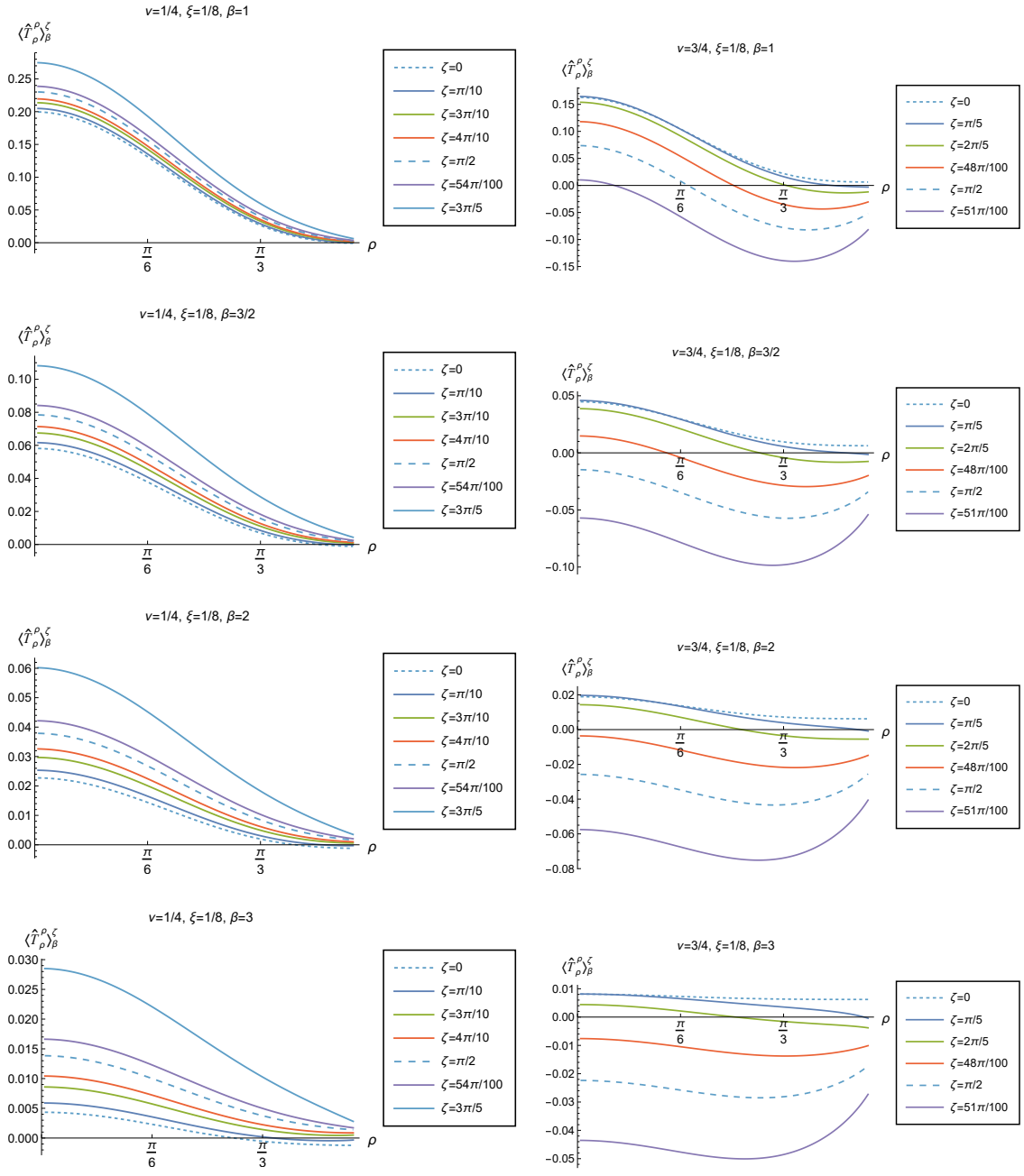

Figure 6.24: Renormalised t.e.v.s of the $\langle \hat{T}^{\rho}_{\rho} \rangle^{\zeta}_{\beta}$ component of the RSET, with Robin boundary conditions and different inverse temperatures β. The plots show $\langle \hat{T}^{\rho}_{\rho} \rangle^{\zeta}_{\beta}$ as a function of the radial coordinate ρ, for a selection of Robin parameters ζ. For the left column we have $\nu = 1/4$ and for the right column $\nu = 3/4$. For each column, top row $\beta = 1$, second row $\beta = 3/2$, third row $\beta = 2$ and bottom row $\beta = 3$. For all plots $\xi = 1/8$.

between the origin and space-time boundary. The value of this magnitude increases with increasing temperature (decreasing β). For $\nu = 1/4$ we see that $-\Pi^{\zeta}_{\beta}$ is negative for all ζ and β except for $\zeta \sim \pi/2$, $\beta = 1$ where the plots become positive for $\rho \sim \pi/6$. For $\nu = 3/4$, the plots are mostly positive for the different Robin boundary conditions, especially with increasing temperature, except for Dirichlet ($\zeta = 0$) which remains entirely negative for all β studied. As the space-time boundary is approached, there remains quite wide separation between the different values of $-\Pi^{\zeta}_{\beta}$, especially for $\nu = 3/4$, and this seems to be independent of the temperature. Overall it can be seen that the magnitudes of the pressure deviators in Figure 6.25 are small, $\sim \mathcal{O}(10^{-4})$ for $\nu = 1/4$ and $\sim \mathcal{O}(10^{-3})$ for $\nu = 3/4$ with $\beta = 3$, increasing approximately three-fold as we increase the temperature to $\beta = 1$.

Figures 6.26, 6.27 and 6.28 show the effects of different coupling constants ξ on the energy density component of the RSET $-\langle\hat{T}^{\tau}_{\tau}\rangle^{\zeta}_{\beta}$ for the different values of ν studied, namely $\nu = 1/4$ (Figure 6.26), $\nu = 1/2$ (Figure 6.27) and $\nu = 3/4$ (Figure 6.28). It can be seen that for each value of ν, the plots are situated closest together for the conformally coupled case ($\xi = 1/8$) and become increasingly spread out as the coupling constant decreases. This is exaggerated for higher values of ν. It can also be seen that when ξ decreases, the energy density becomes progressively more negative. Indeed, for $\xi = -1/2$, the energy density is negative throughout space-time for almost all Robin parameters. We also see that for each value of ν, the $-\langle\hat{T}^{\tau}_{\tau}\rangle^{\zeta}_{\beta}$ profiles are monotonic functions of ρ for $\xi = 1/8$ and $\xi = -1/2$ but not for the minimally coupled case ($\xi = 0$). Furthermore, we see that with conformal coupling, $\xi = 1/8$, the $-\langle\hat{T}^{\tau}_{\tau}\rangle^{\zeta}_{\beta}$ profiles increase with increasing ζ eventually diverging as ζ approaches the relevant ζ_{crit}. This is more easily seen with the 3D plots. With $\xi = 0$ and $\xi = -1/2$, the profiles of $-\langle\hat{T}^{\tau}_{\tau}\rangle^{\zeta}_{\beta}$ become progressively negative with increasing ζ and also diverge as $\zeta \to \zeta_{\text{crit}}$.

Figure 6.29 shows the $\langle\hat{T}^{\rho}_{\rho}\rangle^{\zeta}_{\beta}$ component of the RSET, as a function of the radial coordinate ρ, with different Robin parameters ζ and a choice of coupling constants ξ, with $\nu = 1/4$ and $\nu = 3/4$. It can be seen that for both values of ν, the plots are closest together for the conformally coupled case ($\xi = 1/8$) and spread out more with decreasing ξ. This is more prominent for $\nu = 3/4$. In contrast to the plots of the energy density, with $\nu = 1/4$ (Figure 6.26), the $\langle\hat{T}^{\rho}_{\rho}\rangle^{\zeta}_{\beta}$ component of the RSET is a monotonically decreasing function of ρ for all values of ξ considered, including $\xi = 0$ (minimal coupling). Furthermore, from Figure 6.29, we see that for $\nu = 3/4$, the $\langle\hat{T}^{\rho}_{\rho}\rangle^{\zeta}_{\beta}$ plots are monotonic functions of ρ for $\xi = 0$ and $\xi = -1/2$ but not $\xi = 1/8$, in contrast to that seen for the energy density (Figures 6.26, 6.28).

The plots of the $\langle\hat{T}^{\theta}_{\theta}\rangle^{\zeta}_{\beta}$ component of the RSET are qualitatively similar to those of the $\langle\hat{T}^{\rho}_{\rho}\rangle^{\zeta}_{\beta}$ component in Figure 6.29 and are therefore not shown. Instead we plot the (negative) pressure deviators in Figure 6.30 for the same parameter values as in Figure 6.29. For both values of ν and all coupling constants, the pressure deviators are zero at the space-time origin and achieve their maximum magnitude for some $\rho \in (0, \pi/2)$. Following this the plots converge towards each other although there is still noticeable separation between the plots at the space-time boundary, especially for $\nu = 3/4$. For all plots, $-\Pi^{\zeta}_{\beta}$ is negative throughout most of the space-time apart from $\nu = 3/4$, $\xi = 1/8$ where the profiles are positive, except for $\zeta = 0$ (Dirichlet) which is entirely

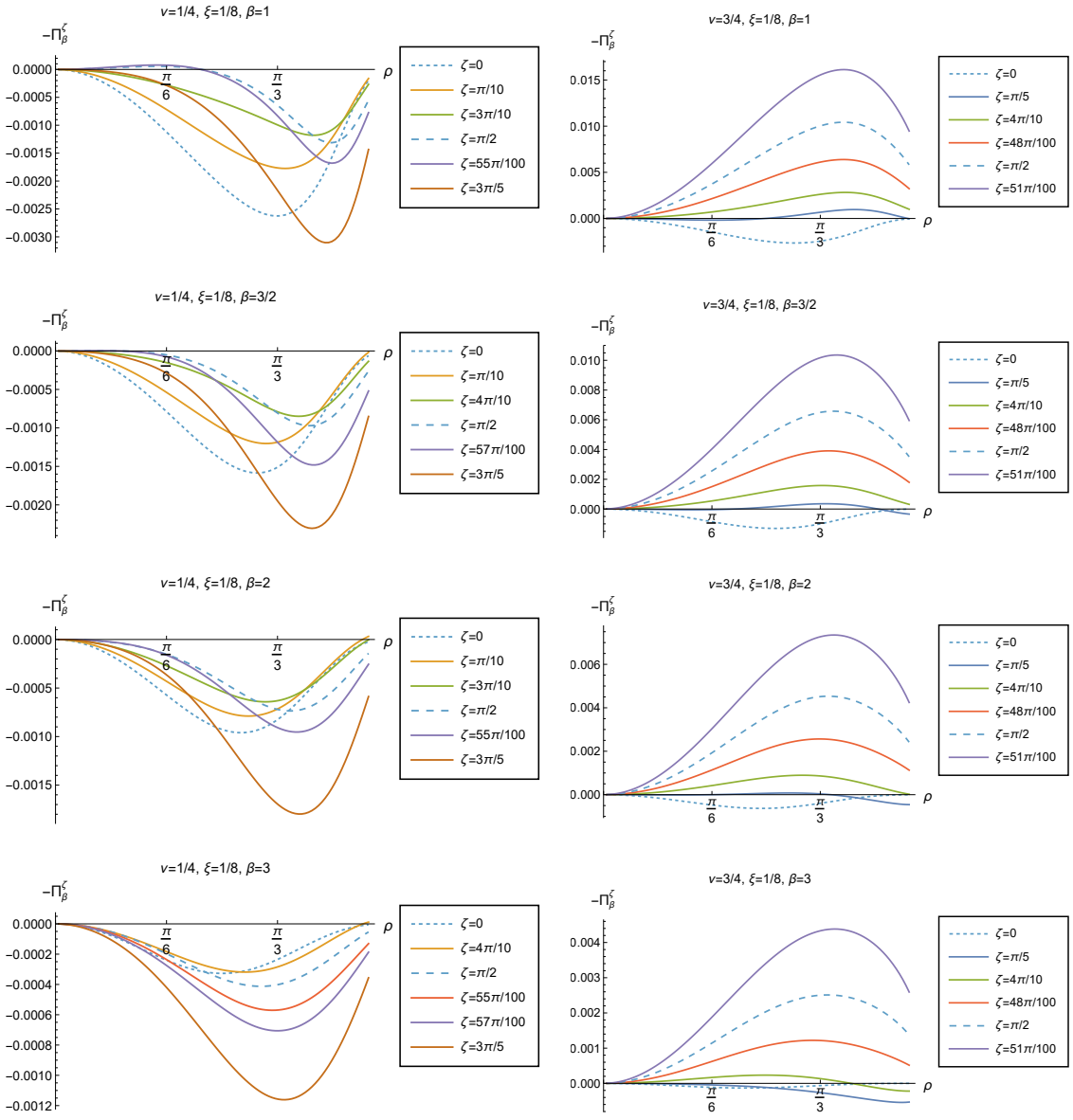

Figure 6.25: Negative thermal pressure deviators $-\Pi_\beta^\zeta$ with Robin boundary conditions and different inverse temperatures β. The plots show $-\Pi_\beta^\zeta$ as a function of the radial coordinate ρ, for a selection of Robin parameters ζ. For the left column we have $\nu = 1/4$ and for the right column $\nu = 3/4$. For each column, top row $\beta = 1$, second row $\beta = 3/2$, third row $\beta = 2$ and bottom row $\beta = 3$. For all plots $\xi = 1/8$.

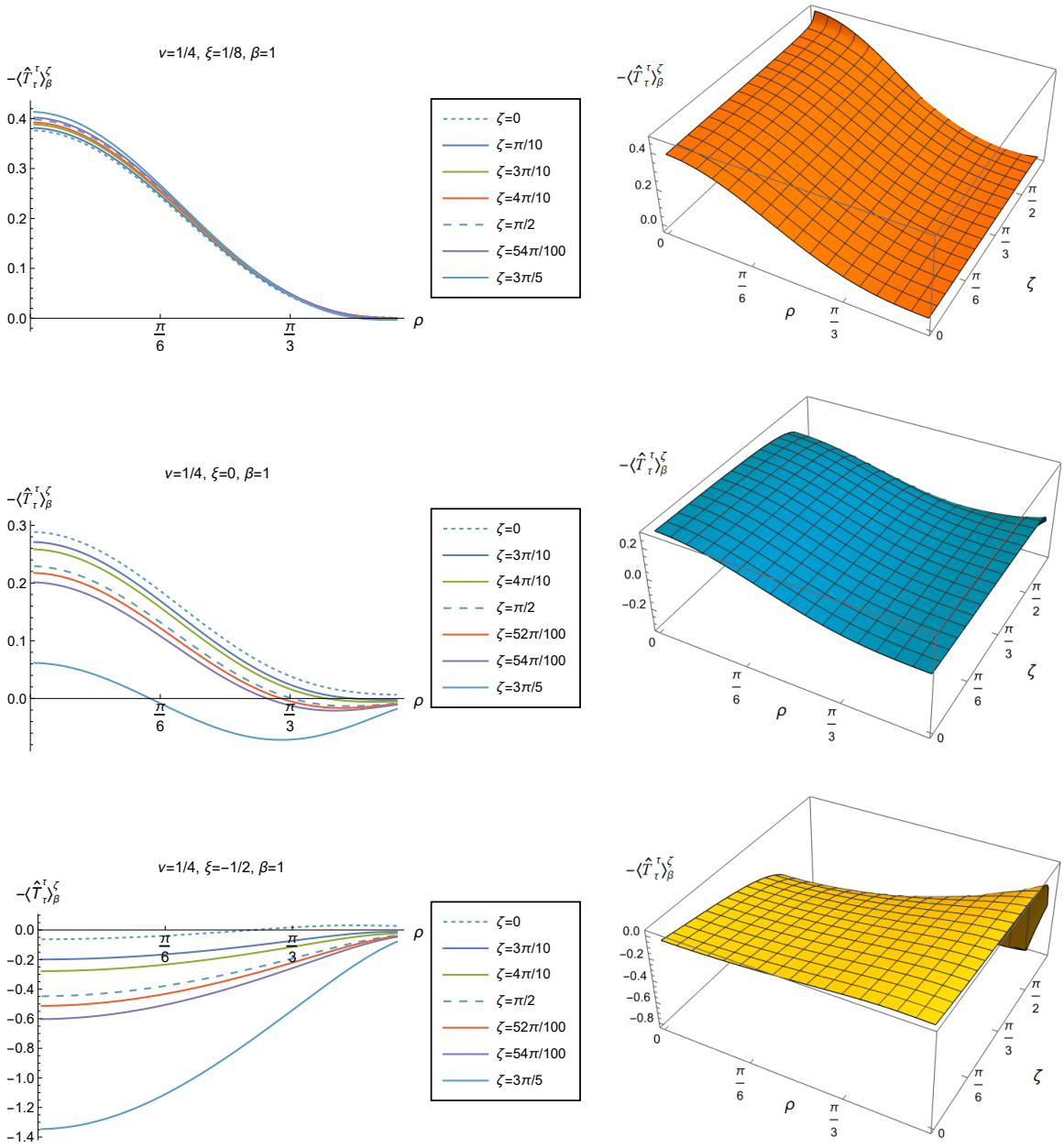

Figure 6.26: Renormalised t.e.v.s of the energy density component of the RSET $-\langle\hat{T}_\tau^\tau\rangle_\beta^\zeta$, with Robin boundary conditions and different coupling constants ξ. The left column shows $-\langle\hat{T}_\tau^\tau\rangle_\beta^\zeta$ as a function of the radial coordinate ρ for a range of Robin parameters ζ. The right column shows 3D surface plots of $-\langle\hat{T}_\tau^\tau\rangle_\beta^\zeta$ as functions of ρ and ζ. Top row $\xi = 1/8$, middle row $\xi = 0$ and bottom row $\xi = -1/2$. For all plots, $\nu = 1/4$, $\beta = 1$.

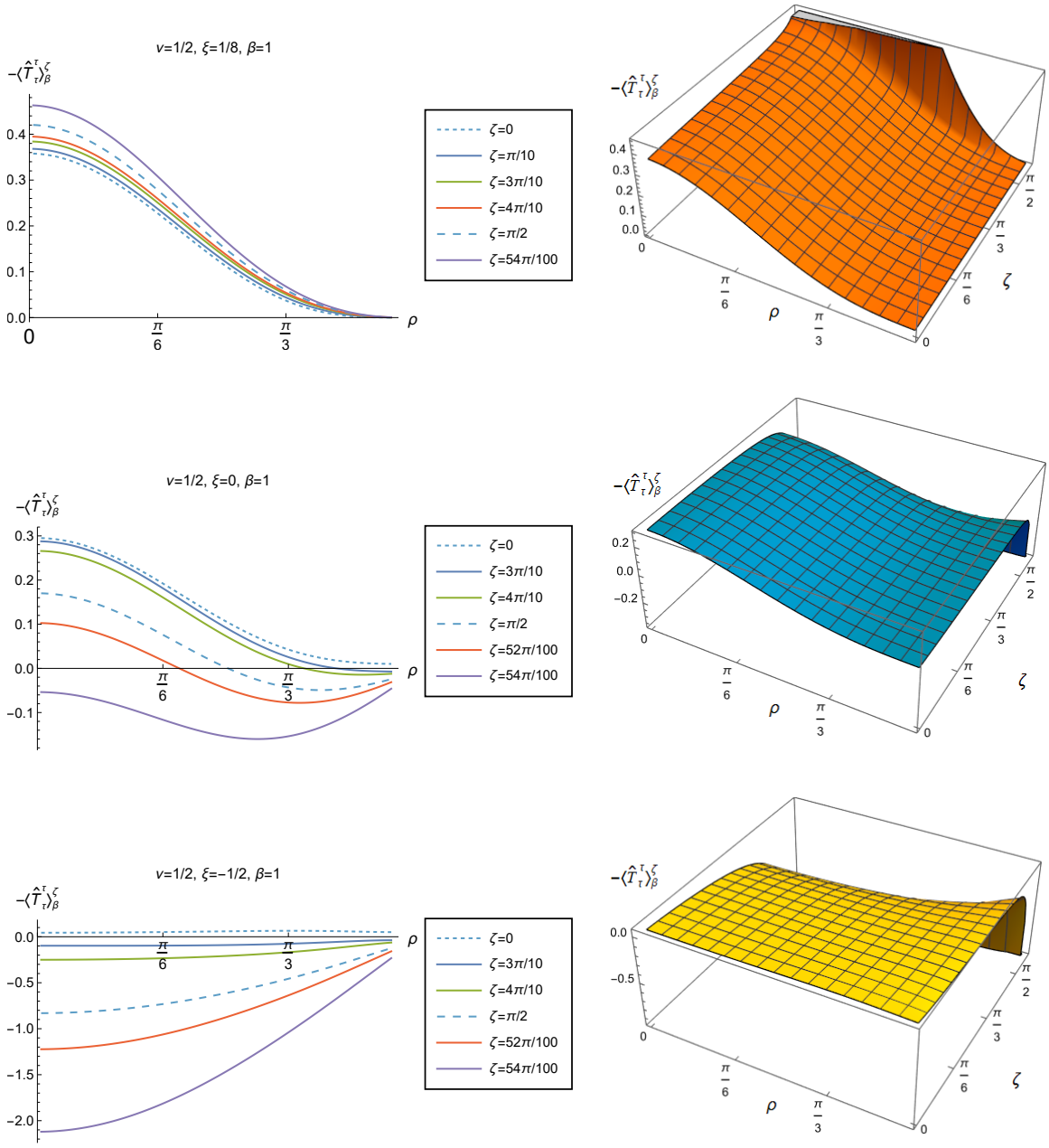

Figure 6.27: Renormalised t.e.v.s of the energy density component of the RSET $-\langle\hat{T}_\tau^{\ \tau}\rangle_\beta^\zeta$, with Robin boundary conditions and different coupling constants ξ. The left column shows $-\langle\hat{T}_\tau^{\ \tau}\rangle_\beta^\zeta$ as a function of the radial coordinate ρ for a range of Robin parameters ζ. The right column shows 3D surface plots of $-\langle\hat{T}_\tau^{\ \tau}\rangle_\beta^\zeta$ as functions of ρ and ζ. Top row $\xi = 1/8$, middle row $\xi = 0$ and bottom row $\xi = -1/2$. For all plots, $\nu = 1/2$, $\beta = 1$.

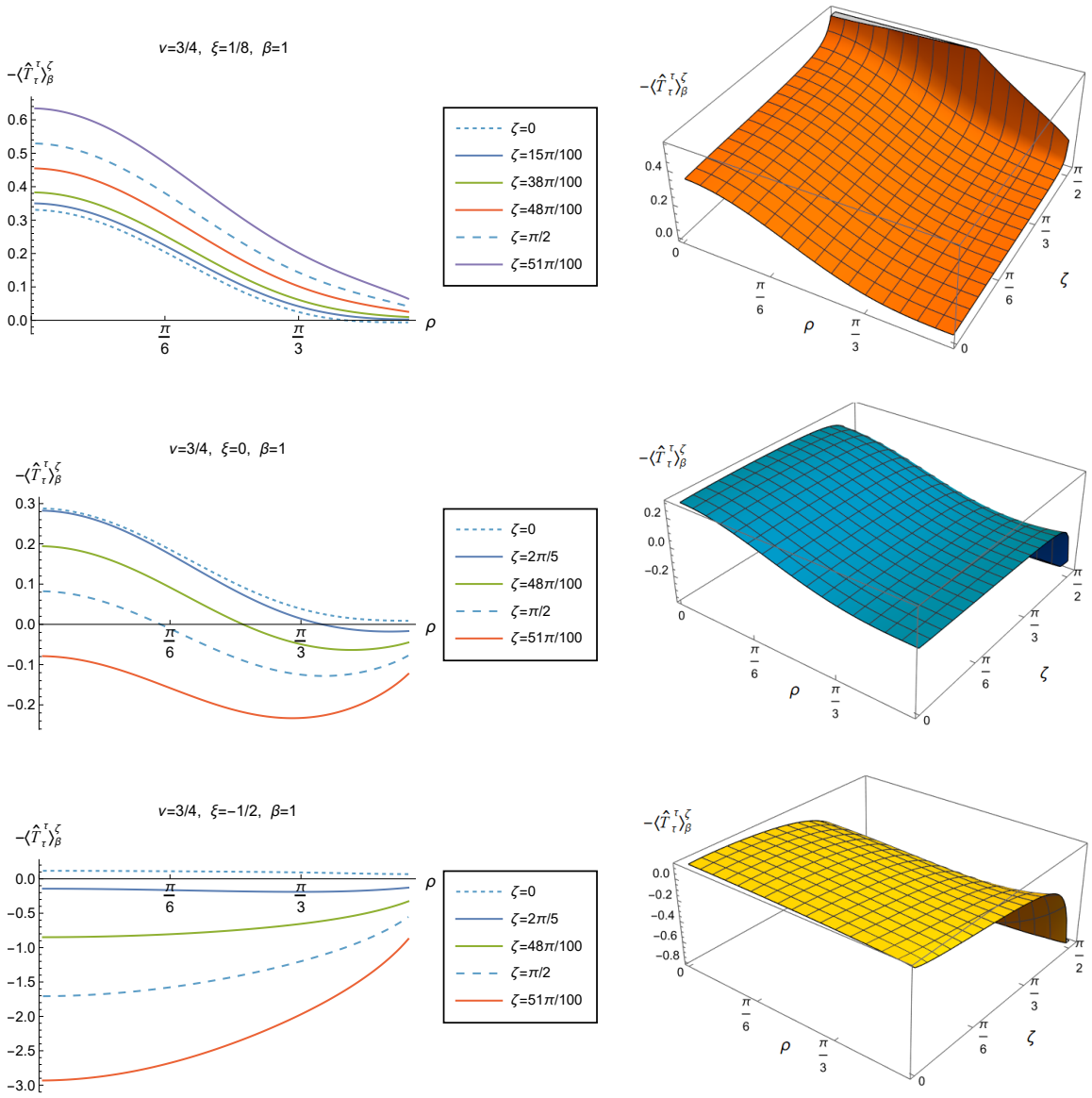

Figure 6.28: Renormalised t.e.v.s of the energy density component of the RSET $-\langle\hat{T}_\tau^{\ \tau}\rangle_\beta^\zeta$, with Robin boundary conditions and different coupling constants ξ. The left column shows $-\langle\hat{T}_\tau^{\ \tau}\rangle_\beta^\zeta$ as a function of the radial coordinate ρ for a range of Robin parameters ζ. The right column shows 3D surface plots of $-\langle\hat{T}_\tau^{\ \tau}\rangle_\beta^\zeta$ as functions of ρ and ζ. Top row $\xi = 1/8$, middle row $\xi = 0$ and bottom row $\xi = -1/2$. For all plots, $\nu = 3/4$, $\beta = 1$.

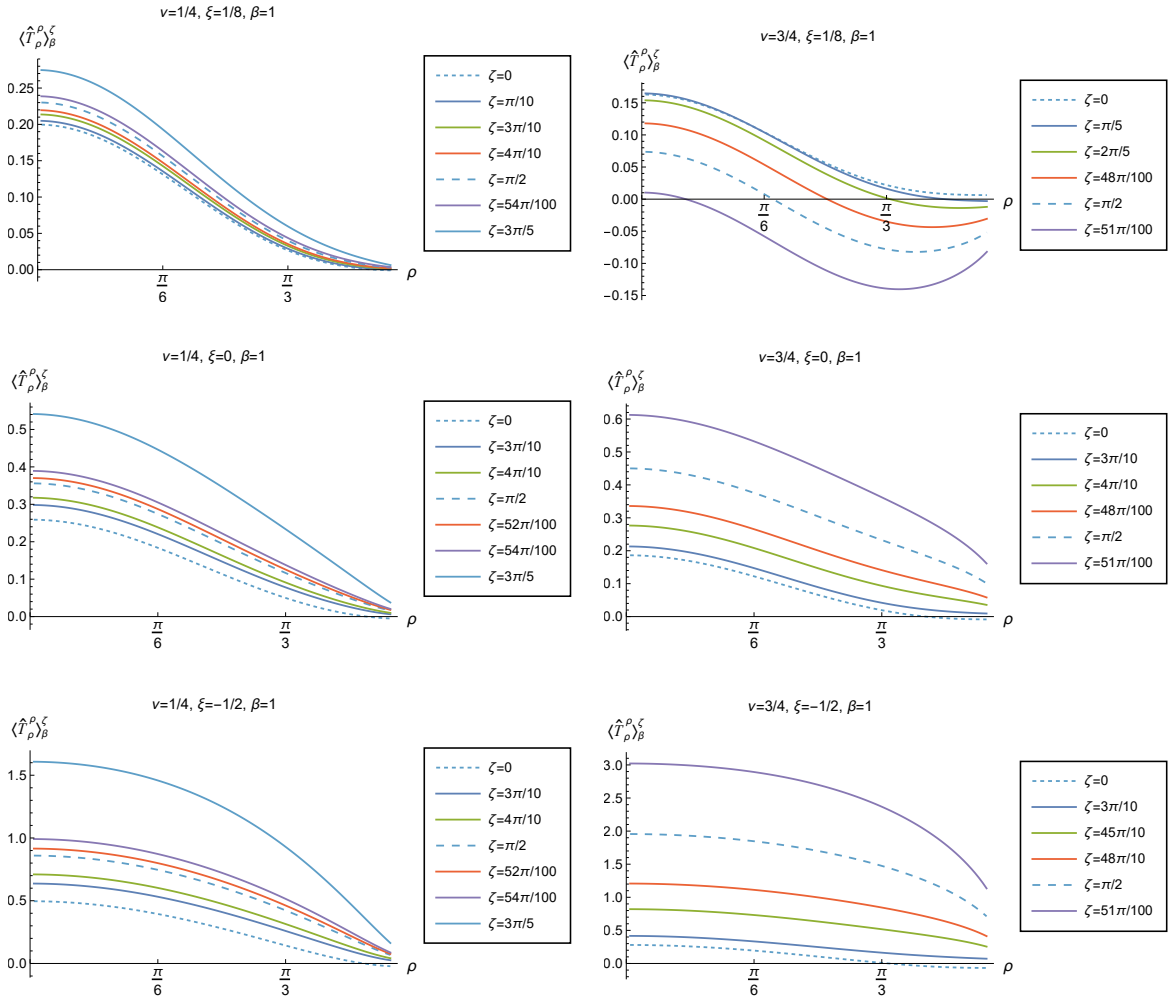

Figure 6.29: Renormalised t.e.v.s of the $\langle \hat{T}^{\rho}_{\rho} \rangle^{\zeta}_{\beta}$ component of the RSET with Robin boundary conditions and different coupling constants ξ. Plots show $\langle \hat{T}^{\rho}_{\rho} \rangle^{\zeta}_{\beta}$ as a function of the radial coordinate ρ for a selection of Robin parameters ζ. Top row $\xi = 1/8$, middle row $\xi = 0$ and bottom row $\xi = -1/2$. In the left column $\nu = 1/4$ and in the right column $\nu = 3/4$. For all plots, $\beta = 1$.

negative, and $\zeta = \pi/20$ where the profile dips just below the ρ-axis in a region around $\rho = \pi/6$. However, the most significant feature is the scale of the plots. For conformal coupling ($\xi = 1/8$), the pressure deviators are $\mathcal{O}(10^{-3})$ in magnitude for $\nu = 1/4$ and $\mathcal{O}(10^{-2})$ for $\nu = 3/4$. However, for $\nu = 1/4$, there is $\sim 10^2-$fold increase in the magnitudes of $-\Pi^{\zeta}_{\beta}$ with $\xi = -1/2$, compared to $\xi = 1/8$. The change is less dramatic with $\nu = 3/4$ where there is a $\sim 10-$fold increase in the magnitudes of $-\Pi^{\zeta}_{\beta}$ between $\xi = 1/8$ and $\xi = -1/2$. The changes in magnitudes seen with different coupling constants are greater than those seen when we vary the inverse temperature, β, Figure 6.25.

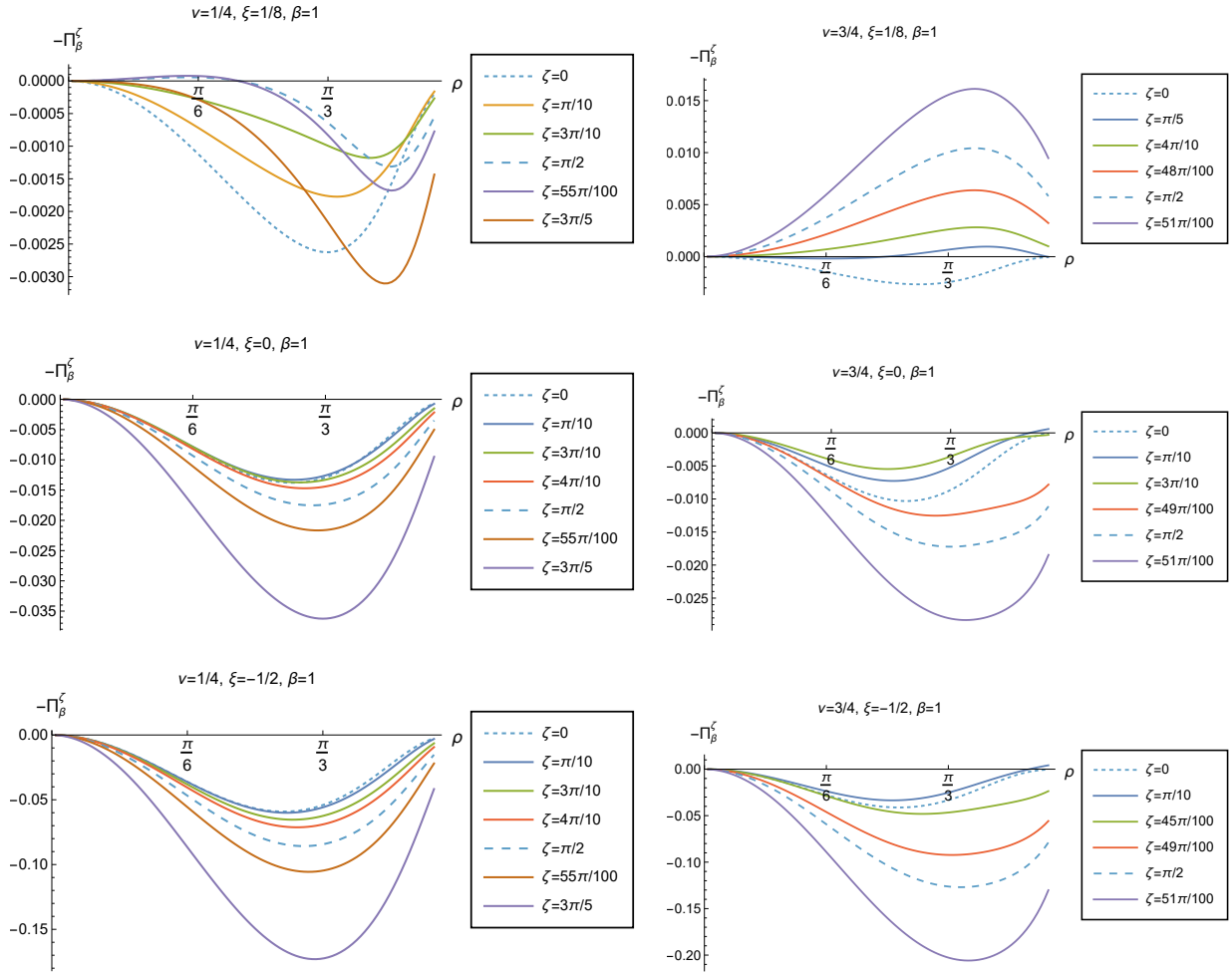

Figure 6.30: Negative thermal pressure deviators $-\Pi^{\zeta}_{\beta}$ with Robin boundary conditions and different coupling constants ξ. The plots show $-\Pi^{\zeta}_{\beta}$ as a function of the radial coordinate ρ, for a selection of Robin parameters ζ. In the left column $\nu = 1/4$ and in the right column $\nu = 3/4$. Top row $\xi = 1/8$, middle row $\xi = 0$ and bottom row $\xi = -1/2$. For all plots, $\beta = 1$.

One of the most intriguing findings relating to the coupling constant is that seen when we consider the additional effects of altering the temperature of the field, with fixed $\zeta = \pi/10$, as displayed in Figures 6.31, 6.32 and 6.33 for the energy density component of the RSET. The plots for different ν reveal similar findings. There is a cross-over point before which the energy density

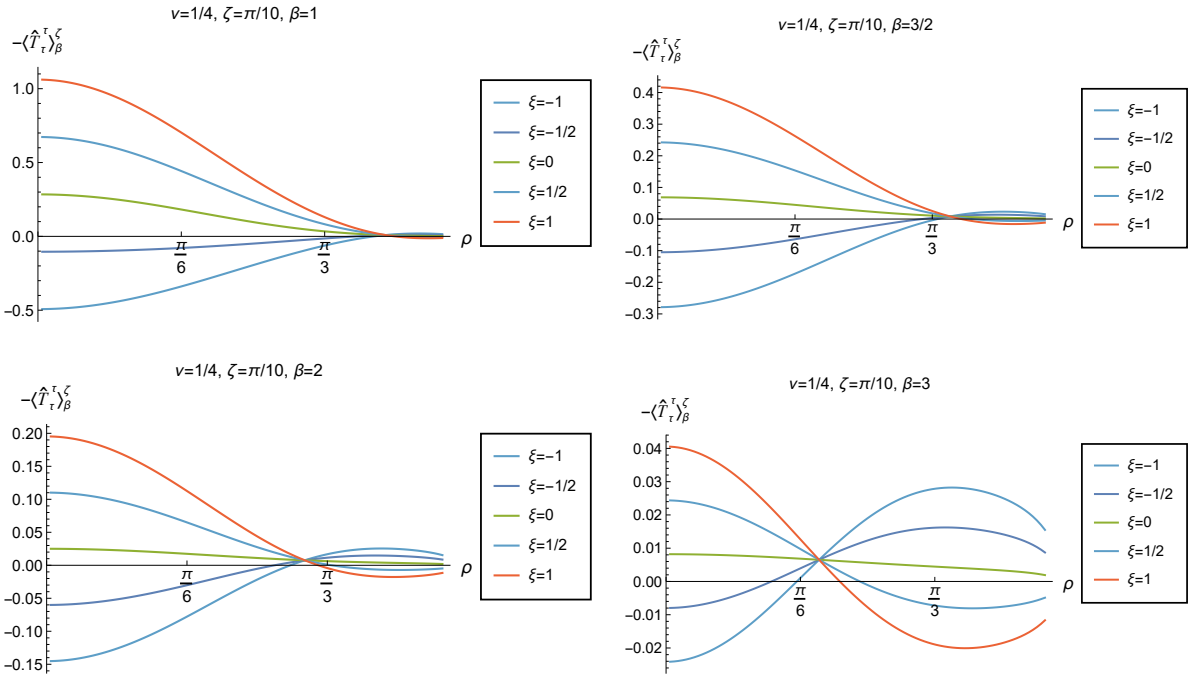

Figure 6.31: Renormalised t.e.v.s of the energy density component of the RSET $-\langle\hat{T}^{\tau}_{\tau}\rangle^{\zeta}_{\beta}$ as a function of the radial coordinate ρ with different coupling constants ξ and inverse temperatures β. Top row $\beta = 1$, second row $\beta = 3/2$, third row $\beta = 2$ and bottom row $\beta = 3$. For all plots, $\zeta = \pi/10$, $\nu = 1/4$.

decreases with decreasing ξ (and hence decreasing m^2) but beyond the cross-over, the opposite is seen with $-\langle\hat{T}^{\tau}_{\tau}\rangle^{\zeta}_{\beta}$ increasing with decreasing ξ. The cross-over point moves towards the space-time origin with increasing β (decreasing temperature) for a given value of ν. Furthermore, we see that for a given inverse temperature β, increasing ν pushes the cross-over point further towards the space-time origin such that for $\nu = 3/4$, $\beta = 2$, for example, the cross-over point is no longer evident.

Unlike the case seen with the energy density component of the v.e.v., Figure 6.15, the cross-over point for $-\langle\hat{T}^{\tau}_{\tau}\rangle^{\zeta}_{\beta}$ is no longer zero but adopts a positive value which is more evident with increasing β and ν. Beyond the common cross-over point, $-\langle\hat{T}^{\tau}_{\tau}\rangle^{\zeta}_{\beta}$ converges to its respective v.e.v. depending on the value of ν and ξ.

Figure 6.34 shows the (negative) thermal pressure deviators corresponding to Figures 6.31, 6.32 and 6.33 for $\nu = 1/4$, $\nu = 1/2$ and $\nu = 3/4$, with fixed $\zeta = \pi/10$ and two values of $\beta = 1$ and $\beta = 3$. For $\nu = 1/4$, $\zeta = \pi/10$, $\beta = 1$ we see a similar behaviour of $-\Pi^{\xi}_{\beta}$ as we did for the massless, conformally coupled case (Figure 6.22, middle) in that $-\Pi^{\xi}_{\beta}$ is zero at the space-time origin and boundary and attains its maximum magnitude in between. Increasing the value of ν, (left column in Figure 6.34) shows that $-\Pi^{\xi}_{\beta}$ becomes zero just before the space-time boundary is reached, beyond which the plots start to separate. This behaviour is more exaggerated when we consider the lower temperature of $\beta = 3$ (right column of Figure 6.34). With $\nu = 3/4$ we see that $-\Pi^{\xi}_{\beta}$ is

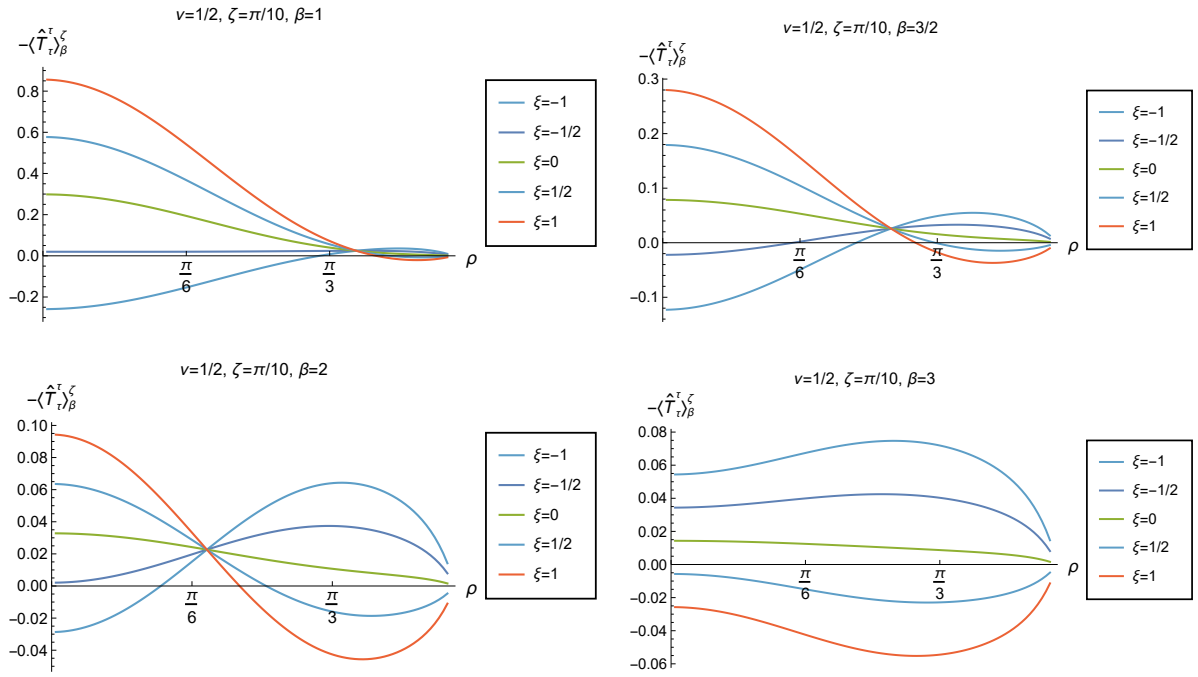

Figure 6.32: Renormalised t.e.v.s of the energy density component of the RSET $-\langle\hat{T}_\tau^{\ \tau}\rangle_\beta^\zeta$ as a function of the radial coordinate ρ with different coupling constants ξ and inverse temperatures β. Top row $\beta = 1$ (left), $\beta = 3/2$ (right), second row $\beta = 2$ (left) and $\beta = 3$ (right). For all plots, $\zeta = \pi/10$, $\nu = 1/2$.

zero at the space-time origin and there is a common cross-over point for the plots for some value of $\rho \in (0, \pi/2)$. Following this, the profiles increasingly spread out away from each other as the space-time boundary is approached. The spread of the $-\Pi_\beta^\xi$ plots at the space-time boundary with $\beta = 3$, (low temperature) is also evident in the vacuum case, Figures 6.16, 6.19. With $\beta = 3$ we see that increasing ν (and hence m^2 for fixed ξ) results in marked differences in the plots of $-\Pi_\beta^\xi$. Before the cross-over point is reached, the plots of $-\Pi_\beta^\xi$ for the different ξ are brought closer together when we increase the value of ν. The magnitude of the plots is notably reduced and appears increasingly 'compressed'. This is seen with the higher temperature of $\beta = 1$ but is less obvious.

§ 6.5 Conclusion

In this chapter we have determined the v.e.v.s and t.e.v.s of the nonzero components of the RSET for a quantum scalar field with general mass and curvature coupling. Dirichlet, Neumann or Robin boundary conditions were applied at the space-time boundary. The expectation values are computed numerically with MATHEMATICA. We see that changing the mass and coupling constant of the scalar field results in tangible effects on the v.e.v.s and t.e.v.s of the RSET. In Sections 6.1 and 6.2 we determined the v.e.v.s and t.e.v.s with Dirichlet and Neumann boundary conditions and note from (6.9) that the v.e.v.s with Dirichlet and Neumann boundary conditions are equal in magnitude but differ in sign. The v.e.v.s are only equal to zero when the field mass is zero, independent of the coupling constant ξ. This contrasts with the case of the massless, conformally coupled scalar

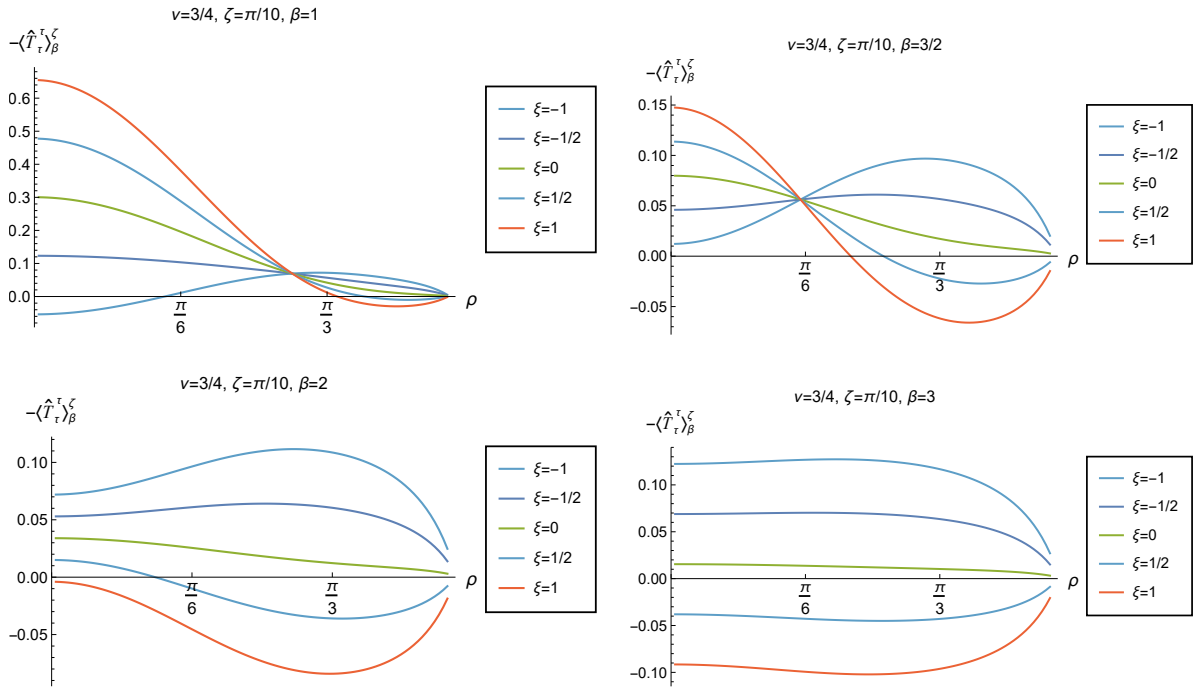

Figure 6.33: Renormalised t.e.v.s of the energy density component of the RSET $-\langle\hat{T}_\tau^{\ \tau}\rangle_\beta^\zeta$ as a function of the radial coordinate, ρ with different coupling constants, ξ and inverse temperatures, β. Top row $\beta = 1$ (left) and $\beta = 3/2$ (right), bottom row $\beta = 2$ (left) and $\beta = 3$ (right). For all plots, $\zeta = \pi/10$, $\nu = 3/4$.

field on adS4 where the v.e.v. with Dirichlet and Neumann boundary conditions is nonzero as it is determined entirely by the trace anomaly (3.20), whereas there is no trace anomaly in adS3 (for the massless, conformally coupled field). In Section 6.2, we find that the t.e.v.s of the energy density component of the RSET is sensitive to the inverse temperature β as well as the coupling constant ξ. The effect of temperature is mainly reflected in a change of scale, whereas the coupling constant has a significant effect in the profile of the plots for both Dirichlet and Neumann boundary conditions, Figure 6.3.

In Sections 6.3 and 6.4 we studied the effect of applying Robin boundary conditions to the RSET. The v.e.v.s of the nonzero components of the RSET (Section 6.3) are very sensitive to the different Robin boundary conditions applied (Figures 6.10–6.12). Interestingly, for $\nu = 1/4$ and $\nu = 3/4$ we see that the convergence of the plots towards the Neumann result occurs more slowly compared with the massless, conformally coupled field ($\nu = 1/2$, $\xi = 1/8$), where the convergence is more obvious. The different values of ν also have a dramatic effect on the behaviour of the RSET components with respect to the Robin parameter ζ, as demonstrated by the 3D surface plots in Figures 6.10–6.12. Furthermore, by allowing the coupling constant ξ to vary we can examine its effect on the RSET (Figures 6.14–6.19). All components of the RSET are very sensitive to the coupling constant ξ, independent of the Robin parameter ζ. We also see from Figures 6.16 and 6.19 that the pressure deviators increase noticeably in magnitude when the magnitude of ξ increases, especially towards the space-time boundary, suggesting that the quantum scalar field differs most from its classical counterpart for large $|\xi|$, more so as the space-time boundary is approached.

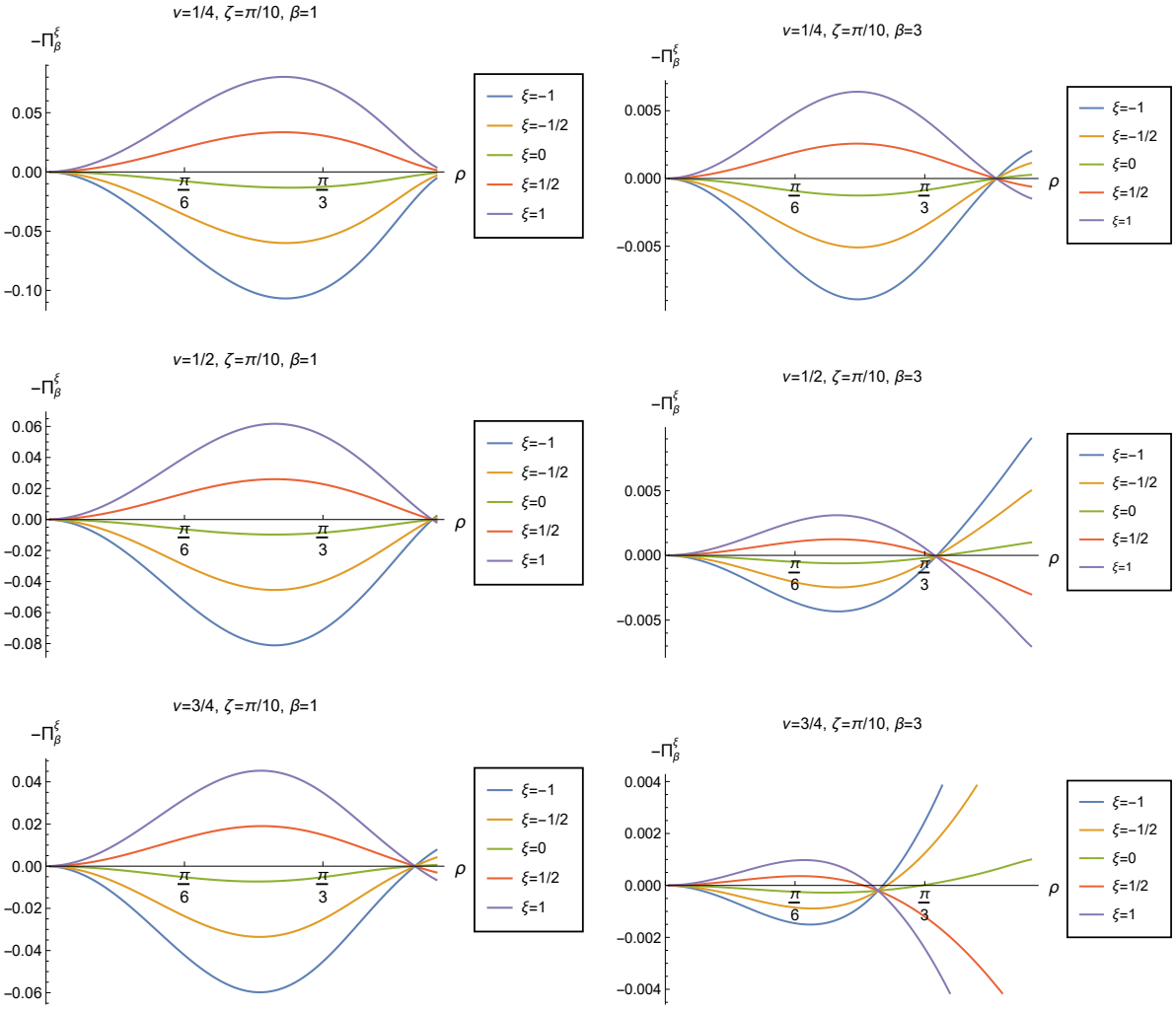

Figure 6.34: Negative thermal pressure deviators $-\Pi_\beta^\xi$ with different coupling constants ξ and values of ν. Top row $\nu = 1/4$, middle row $\nu = 1/2$ and bottom row $\nu = 3/4$. The left column has $\beta = 1$ and the right column has $\beta = 3$. For all plots, $\zeta = \pi/10$.

One of the most interesting findings in Section 6.3 is the discovery of negative energy densities for the v.e.v.s with $\nu = 1/4$ and $\nu = 3/4$. This is noticeable for some values of the Robin parameter ζ, for at least part of the space-time, Figure 6.10. This is not seen in the massless, conformally coupled case ($\nu = 1/2$, $\xi = 1/8$) where the energy densities are entirely positive throughout the space-time, similar to that seen in adS4 (Figure 3.4). However, with increasing temperatures (decreasing β), the energy densities become predominantly positive, even with $\nu = 1/4$ and $\nu = 3/4$ (Figures 6.20 and 6.23).

The question that was posed at the start of this chapter was whether the v.e.v.s and t.e.v.s of the RSET, with Robin boundary conditions, converge towards the Neumann result at the space-time boundary. For a massless, conformally coupled scalar field on adS4 (Chapter 3), we saw that the v.e.v.s and t.e.v.s of the RSET components converged towards the common Dirichlet/Neumann v.e.v. at the space-time boundary for all $\zeta < \zeta_{\text{crit}}$. When we consider a scalar field that is not massless and conformally coupled on adS3, we find that the v.e.v.s with Dirichlet and Neumann boundary conditions have different values (6.9), allowing us to be more specific about the convergence behaviour with Robin boundary conditions. In the massless, conformally coupled case ($\nu = 1/2$, $\xi = 1/8$), we have seen that the v.e.v.s and t.e.v.s of the RSET components appear to converge towards the common (zero) v.e.v. found with Dirichlet/Neumann boundary conditions (Figures 6.10–6.12, 6.20, 6.21). When we consider a scalar field that is not massless and conformally coupled (see for example Figure 6.28), we see that the convergence of the plots with different Robin boundary conditions is much slower at the space-time boundary. However it is plausible that the plots do converge towards the Neumann v.e.v., consistent with the findings for the vacuum polarisation in adS3 (Chapter 5) and adS4 [71].

Having computed the v.e.v.s and t.e.v.s of a number of RSETs for a scalar field with general mass and coupling, we can now use a selection of these RSETs as the source term in Einstein's equations (1.2) and determine the backreaction of the RSET on the underlying metric. This is the subject of the Chapter 7.

§ 6.6 Mathematical expressions of the RSET components

In this section we explicitly present the components of the RSET, with mixed indices, used in the numerical computations of the t.e.v.s with Neumann and Dirichlet boundary conditions as well as the v.e.v.s and t.e.v.s with Robin boundary conditions (6.16), reproduced here for convenience

$$\langle\psi|T_{\mu}^{\lambda}|\psi\rangle = \frac{1}{4\sqrt{2}\pi}\left[-w_{\mu}^{\lambda} + \frac{1}{2}(1-2\xi)w_{;\mu}^{;\lambda} + \frac{1}{2}\left(2\xi - \frac{1}{2}\right)\delta_{\mu}^{\lambda}\Box w - 2\xi w\delta_{\mu}^{\lambda}\right] \tag{6.21}$$

We start with the components for t.e.v.s with Dirichlet and Neumann boundary conditions.

6.6.1 Thermal expectation values with Neumann/Dirichlet boundary conditions

In the expressions below, we have defined the following quantities:

$$\begin{aligned}
X &= \nu\arccos\left[1 + 2\sec^2\rho\,\sinh^2\left(\frac{j\beta}{2}\right)\right], \\
Y &= \nu\arccos\left[\cosh(j\beta)\sec^2\rho - \tan^2\rho\right], \\
\Upsilon &= 2i\sec\rho\left[1 - 2\cos(2\rho) + \cosh(2j\beta) - 4\cosh(j\beta)\sin^2\rho\right]^{1/2},
\end{aligned} \tag{6.22}$$

and shall also require the following hypergeometric functions:

$$\begin{aligned}
\mathcal{F}_1 &= {}_2F_1\left(1-\nu, 1+\nu, \frac{3}{2}; -\sec^2\rho\,\sinh^2\left(\frac{j\beta}{2}\right)\right), \\
\mathcal{F}_2 &= {}_2F_1\left(2-\nu, 2+\nu, \frac{5}{2}; -\sec^2\rho\,\sinh^2\left(\frac{j\beta}{2}\right)\right), \\
\mathcal{F}_3 &= {}_2F_1\left(3-\nu, 3+\nu, \frac{7}{2}; -\sec^2\rho\sinh^2\left(\frac{j\beta}{2}\right)\right).
\end{aligned} \tag{6.23}$$

The following terms represent the difference between the t.e.v.s and respective v.e.v.s and are summed over $j > 0$, as discussed in Section 6.2. The $+/-$ signs represent Neumann and Dirichlet terms respectively.

$$w = \frac{1}{4\pi L}\left\{\pm\nu\mathcal{F}_1 + \frac{\sqrt{2}\cos^2\rho\,\cos X\,\mathrm{cosech}\left(\frac{j\beta}{2}\right)}{2\sqrt{\cos(2\rho)+\cosh(j\beta)}}\right\}, \tag{6.24}$$

$$\begin{aligned}
w_t^t = \frac{i\sin^2(2\rho)}{192\pi L^3}\Bigg\{ & \frac{3i\sqrt{2}\cos Y}{\{\cos(2\rho)+\cosh(j\beta)\}^{-3/2}}\mathrm{cosech}\left(\frac{j\beta}{2}\right)\left[\cos(2\rho)+2\cosh(j\beta)-1\right] \\
& - \frac{12\nu\,\sin Y}{[\cos(2\rho)+\cosh(j\beta)]} \pm 8i\mathcal{F}_2\nu\left(\nu^2-1\right)\sec^4\rho\sinh^2\left(\frac{j\beta}{2}\right)\Bigg\} \\
& + \frac{i\cos\rho\,\mathrm{cosech}\left(\frac{j\beta}{2}\right)}{768\pi L^3\{\cos(2\rho)+\cosh(j\beta)\}^4}\Big[16\cos^2\rho + 2\{2+3\cosh(j\beta)\}\cos(4\rho)
\end{aligned}$$

$$+ 13\cosh(j\beta) + 4\cosh(2j\beta) + 5\cosh(3j\beta) + 16\{\cosh(j\beta) + \cosh(2j\beta)\}\cos(2\rho)\Big]$$

$$\times \Bigg(\pm 4\Upsilon\mathcal{F}_2\nu(\nu^2-1)\{\cos(2\rho)+\cosh(j\beta)\}^{3/2} + 24\nu\cos^3\rho\,\mathrm{cosech}\left(\frac{j\beta}{2}\right)\sin Y\{\cos(2\rho)+\cosh(j\beta)\}$$

$$+ 3\sqrt{2}\Upsilon\cos Y\cos^4\rho\,\mathrm{cosech}^3\left(\frac{j\beta}{2}\right)[\sin^2\rho - \cosh(j\beta)]\Bigg)$$

$$- \frac{\cos^5\rho\,\sinh(j\beta)}{960\pi L^3\{\cos(2\rho)+\cosh(j\beta)\}^2\sinh^4\left(\frac{j\beta}{2}\right)}$$

$$\times \Bigg\{ 30\sqrt{2}\cos Y\sec\rho\,\cosh\left(\frac{j\beta}{2}\right)\{\cos(2\rho)+\cosh(j\beta)\}^{1/2}(\cosh(j\beta)-\sin^2\rho)$$

$$- \frac{15\Upsilon\,\nu\sin Y\cosh\left(\frac{j\beta}{2}\right)}{\sqrt{\cos(2\rho)+\cosh(j\beta)}}\Big[\cos(2\rho)+\cosh(j\beta)+2\sinh^2\left(\frac{j\beta}{2}\right)\Big]$$

$$+ \frac{60\sqrt{2}\cos Y\cosh\left(\frac{j\beta}{2}\right)}{\sqrt{\cos(2\rho)+\cosh(j\beta)}}(\cosh(j\beta)-\sin^2\rho)\sec\rho\sinh^2\left(\frac{j\beta}{2}\right)$$

$$\pm 80\mathcal{F}_2\nu(\nu^2-1)\sec^5(\rho)\sinh^3\left(\frac{j\beta}{2}\right)\cosh\left(\frac{j\beta}{2}\right)[\cosh(j\beta)+\cos(2\rho)][\sin^2\rho-\cosh(j\beta)]$$

$$- 15i\sqrt{2}\Upsilon\cos Y\sinh(j\beta) + 60i\nu\sec\rho\sin Y\sinh(j\beta)\Big[\cos(2\rho)+4\sinh^2\left(\frac{j\beta}{2}\right)\Big]$$

$$\pm 15i\Upsilon\mathcal{F}_2\nu(\nu^2-1)\{\cos(2\rho)+\cosh(j\beta)\}^{3/2}\sec^4\rho\sinh\left(\frac{j\beta}{2}\right)\sinh(j\beta)$$

$$\pm 30i\Upsilon\mathcal{F}_2\nu(\nu^2-1)\sqrt{\cos(2\rho)+\cosh(j\beta)}\sec^2\rho\sinh^3\left(\frac{j\beta}{2}\right)\sinh(j\beta)$$

$$\pm 4i\Upsilon\mathcal{F}_3\nu(\nu^2-4)(\nu^2-1)\{\cos(2\rho)+\cosh(j\beta)\}^{3/2}\sec^6\rho\,\sinh^3\left(\frac{j\beta}{2}\right)\sinh(j\beta)$$

$$- \frac{120i\nu^2\cos Y[\cos(2\rho)+\cosh(j\beta)]}{\sqrt{1-\{\tan^2\rho-\cosh(j\beta)\sec^2\rho\}^2}}\sec^3\rho\sinh^2\left(\frac{j\beta}{2}\right)\sinh j\beta\Bigg\}, \tag{6.25}$$

$$w_\rho^\rho = \frac{i\sin^2(2\rho)}{192\pi L^3}\Bigg\{ - \frac{3i\sqrt{2}\cos Y}{\{\cos(2\rho)+\cosh(j\beta)\}^{-3/2}}\mathrm{cosech}\left(\frac{j\beta}{2}\right)[\cos(2\rho)+2\cosh(j\beta)-1]$$

$$+ \frac{12\nu\sin Y}{\{\cos(2\rho)+\cosh(j\beta)\}} \pm 8i\mathcal{F}_2\nu(\nu^2-1)\sec^4\rho\sinh^2\left(\frac{j\beta}{2}\right)\Bigg\}$$

$$- \frac{i\,\mathrm{cosech}\left(\frac{j\beta}{2}\right)\cos^3\rho}{6144\pi L^3\{\cos(2\rho)+\cosh(j\beta)\}^4}\Bigg(- 16[2+2\cos(2\rho)+\cos(4\rho)]$$

$$+ 2\cosh(j\beta)\,[17 - 36\cos(2\rho) + 6\cos(4\rho) - \cos(6\rho)]$$

$$+ 8\cos(2j\beta)\left[2\cos(2\rho) - \cos(4\rho) - 3\right] + 2\cosh(3j\beta)\left[1 - 3\cos(2\rho)\right]\Bigg)$$

$$\times \Bigg(\pm 8\Upsilon\mathcal{F}_2\nu(\nu^2-1)\sec^4\rho\left\{\cos(2\rho)+\cosh(j\beta)\right\}^{3/2}$$

$$+ 3\sqrt{2}\Upsilon\cos Y \operatorname{cosech}^3\left(\frac{j\beta}{2}\right)\left[\cos 2\rho + 2\cosh j\beta - 1\right]$$

$$- 48\nu\sin Y\sec\rho\{\cos(2\rho)+\cosh(j\beta)\}\operatorname{cosech}\left(\frac{j\beta}{2}\right)\Bigg) - \frac{2i\sin^2\rho\,\cos^5\rho\,\operatorname{cosech}^2\left(\frac{j\beta}{2}\right)}{1920\pi L^3\{\cos(2\rho)+\cosh(j\beta)\}^2}$$

$$\times \Bigg\{ \pm 20\Upsilon\mathcal{F}_2\,\nu(\nu^2-1)\sec^6\rho\,\sinh^3\left(\frac{j\beta}{2}\right)\{\cos(2\rho)+\cosh(j\beta)\}^{1/2}\Big[5\cos(2\rho)+8\cosh(j\beta)-3\Big]$$

$$\pm 4\sqrt{2}\nu(\nu^2-1)\sec^8\rho\,\sinh^4\left(\frac{j\beta}{2}\right)\{\cos(2\rho)+\cosh(j\beta)\}\Big[-20i\sqrt{2}\mathcal{F}_2\cos^3\rho$$

$$+ 2\sqrt{2}\Upsilon\mathcal{F}_3(\nu^2-4)\sinh\left(\frac{j\beta}{2}\right)\{\cos(2\rho)+\cosh(j\beta)\}^{1/2}\Big]$$

$$+ 15\Bigg[2i\Big(2\sqrt{2}\cos Y\{\cos(2\rho)+\cosh(j\beta)\}^{1/2}\sec\rho + \Upsilon\nu\{\cos(2\rho)+\cosh(j\beta)\}^{1/2}\sec^2\rho\sin Y\Big)$$

$$+ 2\sec^2\rho\,\sinh^2\left(\frac{j\beta}{2}\right)(-3\sqrt{2}\Upsilon\cos Y + 8\nu\cos(2\rho)\sec\rho\sin Y)$$

$$+ \frac{4i\sinh^3\left(\frac{j\beta}{2}\right)}{\sqrt{\cos(2\rho)+\cosh(j\beta)}}\Big[2\sqrt{2}\cos Y\sec\rho\Big(1+2\nu^2\cos(2\rho)\sec^2\rho\Big) + \Upsilon\nu\sec^2\rho\sin Y\Big]$$

$$+ 32\nu\sec^3\rho\,\sin Y\sinh^4\left(\frac{j\beta}{2}\right) - 2\sqrt{2}\Upsilon\cos Y\sec^2\rho\,\sinh^2\left(\frac{j\beta}{2}\right) - 2\sqrt{2}\Upsilon\cos Y$$

$$+ 16\nu\sec^3\rho\,\sin Y\sinh^2\left(\frac{j\beta}{2}\right)\cosh(j\beta) + \frac{16\sqrt{2}i\cosh(j\beta)\sec^3\rho\,\nu^2\cos Y\sinh^3\left(\frac{j\beta}{2}\right)}{\sqrt{\cos(2\rho)+\cosh(j\beta)}}\Bigg]\Bigg\},$$

$$w_\theta^\theta = -\frac{i\cos^2\rho}{48\pi L^3}\Bigg\{ - \frac{6i\sqrt{2}\operatorname{cosech}\left(\frac{j\beta}{2}\right)\cos X\cos^2\rho}{\{\cos(2\rho)+\cosh(j\beta)\}^{3/2}}$$

$$\pm 8i\mathcal{F}_2\,\nu(\nu^2-1)\sinh^2\left(\frac{j\beta}{2}\right)\sec^4\rho + \frac{12\nu\sin X}{\{\cos(2\rho)+\cosh(j\beta)\}}\Bigg\} \pm \frac{\mathcal{F}_2\nu(\nu^2-1)}{12\pi L^3}$$

$$- \frac{i\sin^2(2\rho)\operatorname{cosech}^3\left(\frac{j\beta}{2}\right)}{128\pi L^3\{\cos(2\rho)+\cosh(j\beta)\}^{3/2}}\Bigg[\cos X[\cosh(j\beta)-\sin^2\rho]$$

$$+ \sqrt{2}i\nu\sin X\sinh\left(\frac{j\beta}{2}\right)\sqrt{\cos(2\rho)+\cosh(j\beta)}\Bigg], \tag{6.26}$$

$$w^{;t}_{;t} = \frac{\sin(2\rho)}{8\pi L^3}\Bigg\{ \frac{\sin(2\rho)}{4(\cos(2\rho)+\cosh(j\beta))^{3/2}}$$
$$\times \left[2\sqrt{2}\cos X\left(\cosh(j\beta)-\sin^2\rho\right)\operatorname{cosech}\left(\frac{j\beta}{2}\right) + 4i\nu\sqrt{\cos(2\rho)+\cosh(j\beta)}\,\sin X \right]$$
$$\pm \frac{4}{3}\nu(\nu^2-1)\mathcal{F}_2\sec^2\rho\,\tan\rho\,\sinh^2\left(\frac{j\beta}{2}\right)\Bigg\}, \tag{6.27}$$

$$w^{;\rho}_{;\rho} = \frac{\cos^2\rho}{960\pi L^3}\Bigg\{ -\frac{15\sqrt{2}\,\cos X\,\operatorname{cosech}\left(\frac{j\beta}{2}\right)}{(\cos(2\rho)+\cosh(j\beta))^{5/2}}$$
$$\times\Big(15\cos(2\rho)-10+2\cos(4\rho)+\cos(6\rho)$$
$$+8\{\cosh(2j\beta)-\cosh(j\beta)\}\cos(2\rho)+4\{5+\cos(4\rho)\}\cosh(j\beta)\Big)$$
$$-\frac{120i\nu\Big(7+4(2\cosh j\beta-1)\cos(2\rho)+\cos(4\rho)-4\cosh(j\beta)\Big)\sin X}{[\cos(2\rho)+\cosh(j\beta)]^2}$$
$$\pm 160\nu(\nu^2-1)\mathcal{F}_2\left(3\cos(2\rho)-5\right)\sec^4\rho\,\sinh^2\left(\frac{j\beta}{2}\right)$$
$$+\frac{960\sqrt{2}\,\nu^2\cos X\sin^2\rho\,\sinh\left(\frac{j\beta}{2}\right)}{[\cos(2\rho)+\cosh(j\beta)]^{3/2}}$$
$$+\frac{60\sin(2\rho)\tan\rho}{[\cos(2\rho)+\cosh(j\beta)]^{3/2}}\left[2\sqrt{2}\cos X[\cosh(j\beta)-\sin^2\rho]\operatorname{cosech}\left(\frac{j\beta}{2}\right)\right.$$
$$\left.+4i\nu\sqrt{\cos(2\rho)+\cosh(j\beta)}\sin X\right]$$
$$\pm 256\nu(\nu^2-4)(\nu^2-1)\mathcal{F}_2\,\sec^4\rho\,\tan^2\rho\,\sinh^4\left(\frac{j\beta}{2}\right)\Bigg\}, \tag{6.28}$$

$$w^{;\theta}_{;\theta} = \frac{\cot\rho}{4\pi L^3}\Bigg\{ -\frac{\sin(2\rho)}{4\{\cos(2\rho)+\cosh(j\beta)\}^{3/2}}\left[2\sqrt{2}\cos X\{\cosh(j\beta)-\sin^2\rho\}\operatorname{cosech}\left(\frac{j\beta}{2}\right)\right.$$
$$\left.+4i\nu\sqrt{\cos(2\rho)+\cosh(j\beta)}\,\sin X\right]\pm\frac{4}{3}\nu(\nu^2-1)\mathcal{F}_2\sec^2\rho\,\sinh^2\left(\frac{j\beta}{2}\right)\tan\rho\Bigg\}, \tag{6.29}$$

$$\Box w = -\frac{\cos^2\rho\,\cot\rho}{240\pi L^3}\Bigg\{\frac{15\cos X\sin(2\rho)}{\sqrt{2}\,\{\cos(2\rho)+\cosh(j\beta)\}^{5/2}}$$
$$\times\Big(-1+4\cos(2\rho)+\cos(4\rho)+4\cosh(2j\beta)+8\cosh(j\beta)\cos^2\rho\Big)$$

$$
\begin{aligned}
&\pm 40\nu(\nu^2-1)\mathcal{F}_2\sec^5\rho\,(\sin(3\rho)-7\sin\rho)\sinh^2\left(\frac{j\beta}{2}\right)\\
&+\frac{30i\nu\,[7+\cos(4\rho)+8\cosh(j\beta)\cos(2\rho)]\sin X\tan\rho}{\{\cos(2\rho)+\cosh(j\beta)\}^2}\\
&-\frac{240\sqrt{2}\nu^2\,\cos X\sin^2\rho\,\tan\rho}{\{\cos(2\rho)+\cosh(j\beta)\}^{3/2}}\sinh\left(\frac{j\beta}{2}\right)\\
&\pm 64\nu(\nu^2-4)(\nu^2-1)\mathcal{F}_3\,\sec^4\rho\,\tan^3\rho\sinh^4\left(\frac{j\beta}{2}\right)\Bigg\}. \qquad (6.30)
\end{aligned}
$$

6.6.2 VACUUM EXPECTATION VALUES WITH ROBIN BOUNDARY CONDITIONS

For the v.e.v.s with Robin boundary conditions, the following expressions are the difference between the Robin and Neumann terms and are labelled with the superscript ζ. We have defined the following quantities:

$$
\begin{aligned}
\mathcal{A}&=1+\ell^2+2\nu+\nu^2+2\ell(1+\nu)+\omega^2\\
\mathcal{J}&=-4\nu F_2\mathscr{N}^{\zeta}_{\omega\ell}\cos\zeta(\cos\rho)^{2\nu}-\frac{F_4\mathscr{N}^{\zeta}_{\omega\ell}}{(1+\nu)}|(1+\ell+\nu+i\omega)|^2\cos\zeta(\cos\rho)^{2+2\nu}\\
&\qquad-\frac{F_5}{(\nu-1)}|(1+\ell-\nu+i\omega)|^2\cos^2\rho(\mathscr{N}^{N}_{\omega\ell}-\mathscr{N}^{\zeta}_{\omega\ell}\sin\zeta)\\
\mathcal{C}&=\ell-1-\nu+(1+\ell+\nu)\cos2\rho\\
\mathcal{K}&=\mathscr{N}^{\zeta}_{\omega\ell}\cos\zeta\,\cos\rho^{2\nu}F_2+F_3\,(\mathscr{N}^{\zeta}_{\omega\ell}\,\sin\zeta-\mathscr{N}^{N}_{\omega\ell}), \qquad (6.31)
\end{aligned}
$$

where $\mathscr{N}^{\zeta}_{\omega\ell}$ and $\mathscr{N}^{N}_{\omega\ell}$ are the vacuum normalisation constants defined in (5.80, 5.81). We will also require the following hypergeometric functions:

$$
\begin{aligned}
F_1&={}_2F_1\Big(\frac{1}{2}(1+\ell+\nu+i\omega),\frac{1}{2}(1+\ell+\nu-i\omega),1+\ell;\sin^2\rho\Big),\\
F_2&={}_2F_1\Big(\frac{1}{2}(1+\ell+\nu+i\omega),\frac{1}{2}(1+\ell+\nu-i\omega),1+\nu;\cos^2\rho\Big),\\
F_3&={}_2F_1\Big(\frac{1}{2}(1+\ell-\nu+i\omega),\frac{1}{2}(1+\ell-\nu-i\omega),1-\nu;\cos^2\rho\Big),\\
F_4&={}_2F_1\Big(\frac{1}{2}(3+\ell+\nu+i\omega),\frac{1}{2}(3+\ell+\nu-i\omega),2+\nu;\cos^2\rho\Big),\\
F_5&={}_2F_1\Big(\frac{1}{2}(3+\ell-\nu+i\omega),\frac{1}{2}(3+\ell-\nu-i\omega),2-\nu;\cos^2\rho\Big),\\
F_6&={}_2F_1\Big(\frac{1}{2}(3+\ell+\nu+i\omega),\frac{1}{2}(3+\ell+\nu-i\omega),2+\ell;\sin^2\rho\Big),\\
F_7&={}_2F_1\Big(\frac{1}{2}(5+\ell+\nu+i\omega),\frac{1}{2}(5+\ell+\nu-i\omega),3+\ell;\sin^2\rho\Big),\\
F_8&={}_2F_1\Big(\frac{1}{2}(5+\ell-\nu+i\omega),\frac{1}{2}(5+\ell-\nu-i\omega),3-\nu;\cos^2\rho\Big),
\end{aligned}
$$

$$F_9 = {}_2F_1\Big(\frac{1}{2}(5+\ell+\nu+i\omega), \frac{1}{2}(5+\ell+\nu-i\omega), 3+\nu; \cos^2\rho\Big). \tag{6.32}$$

For the construction of the RSETs, the following terms are integrated over ω and summed over ℓ, as described in Section 6.3. As we are in Euclidean space we have used the index τ for the time coordinate.

$$w^{\zeta} = \frac{F_1\mathcal{K}}{4\pi^2}\cos^2\rho\,(\sin\rho)^{2\ell}, \tag{6.33}$$

$$w_{\tau}^{\ \tau\,\zeta} = -\frac{\cos^2\rho\,(\sin\rho)^{2\ell}\mathcal{K}}{64\pi^2L^2}\Bigg\{8F_1\mathcal{C} + \frac{2\mathcal{A}}{1+\ell}F_6\sin^2(2\rho) - 16F_1\omega^2\,\cos^2\rho\Bigg\}, \tag{6.34}$$

$$\begin{aligned} w_{\rho}^{\ \rho\,\zeta} = -\frac{\cos^2\rho\,(\sin\rho)^{2\ell}\mathcal{K}}{64\pi^2L^2(1+\ell)}\Bigg\{&8F_1(1+\ell)[1+3\ell+\nu+3(1+\ell+\nu)\cos(2\rho)] \\ &- 4F_6\mathcal{C}\cos^2\rho\,|(1+\ell+\nu+i\omega)|^2 - \frac{4F_7\,\mathcal{A}}{(2+\ell)}|(3+\ell+\nu+i\omega)|^2\cos^4\rho\sin^2\rho \\ &- 4F_6\mathcal{A}\cot\rho\sin(4\rho) + 2F_6\mathcal{A}\sin^2(2\rho)\Big(1+\nu+(1-\ell)\cot^2\rho\Big) \\ &+ 8F_1\mathcal{C}(1+\ell)\Big((1-\ell)\cot^2\rho+\nu\Big)\Bigg\}, \end{aligned} \tag{6.35}$$

$$w_{\theta}^{\ \theta\,\zeta} = \frac{\cos^2\rho\,(\sin\rho)^{2(\ell-1)}\mathcal{K}}{64\pi^2L^2}\Bigg\{8F_1\mathcal{C} + \frac{2\mathcal{A}}{(1+\ell)}F_6\sin^2(2\rho) - 16F_1\ell^2\,\cos^2\rho\Bigg\}, \tag{6.36}$$

$$\begin{aligned} w_{;\tau}^{\ ;\tau\,\zeta} = -\frac{\cos^2\rho\,(\sin\rho)^{2(1+\ell)}}{8\pi^2L^2}\Bigg\{&4F_1\ell\mathcal{K}\cot^2\rho + F_1(\mathcal{J}-4\mathcal{K}) \\ &+ \frac{F_6\mathcal{K}}{(1+\ell)}\,|(1+\ell+\nu+i\omega)|^2\cos^2\rho\Bigg\}, \end{aligned} \tag{6.37}$$

$$\begin{aligned} w_{;\rho}^{\ ;\rho\,\zeta} = \frac{\cos^2\rho\,(\sin\rho)^{2(1+\ell)}}{8\pi^2L^2}\Bigg\{&F_1\cos^2\rho\Big[\mathcal{J}(1+4\ell) - 4\mathcal{K}(1+5\ell)\Big] \\ &+ \frac{F_6}{(1+\ell)}|(1+\ell+\nu+i\omega)|^2\cos^2\rho\Big[\mathcal{K}\cos^2\rho(1+4\ell) + \sin^2\rho(\mathcal{J}-6\mathcal{K})\Big] \\ &+ 4F_1\Big[\mathcal{K}\ell\,(2\ell\cos^2\rho-1)\cot^2\rho - \sin^2\rho(\mathcal{J}-2\mathcal{K})\Big] \\ &+ \frac{F_7\mathcal{K}}{2(1+\ell)(2+\ell)}|(1+\ell+\nu+i\omega)|^2\,|(3+\ell+\nu)|^2\cos^4\rho\sin^2\rho \\ &+ \frac{F_1\sin^2\rho}{2}\Bigg(16F_2\mathcal{N}_r\nu^2\cos\zeta(\cos\rho)^{2\nu} + 4F_4\mathcal{N}_r|(1+\ell+\nu)|^2\cos\zeta(\cos\rho)^{2(1+\nu)} \\ &+ \frac{\mathscr{N}_{\omega\ell}^{\zeta}}{(1+\nu)(2+\nu)}|(1+\ell+\nu+i\omega)|^2\cos\zeta(\cos\rho)^{2(1+\nu)}\Big[4F_4\nu(2+\nu) \end{aligned}$$

$$+ F_9|(3+\ell+\nu+i\omega)|^2\cos^2\rho\Big]$$
$$+ \frac{\cos^2\rho}{(\nu-1)(\nu-2)}|(1+\ell-\nu+i\omega)|^2(\mathscr{N}^N_{\omega\ell}-\mathscr{N}^\zeta_{\omega\ell}\sin\zeta)\Big[4F_5(\nu-2)$$
$$- F_8|(3+\ell-\nu+i\omega)|^2\cos^2\rho\Big]\Bigg)\Bigg\}, \tag{6.38}$$

$$w^{;\theta\,\zeta}_{;\theta} = \frac{\cos^2\rho\,(\sin\rho)^{2\ell}}{8\pi^2L^2}\Bigg\{4F_1\ell\mathcal{K}\cot^2\rho + F_1(\mathcal{J}-4\mathcal{K}) + \frac{F_6\mathcal{K}}{1+\ell}\,|(1+\ell+\nu+i\omega)|^2\cos^2\rho\Bigg\}, \tag{6.39}$$

$$\Box w^\zeta = \frac{\cos^2\rho\,(\sin\rho)^{2\ell}}{16\pi^2L^2}\Bigg\{F_1(\mathcal{J}-4\mathcal{K})\Big(3+4\ell+(1+4\ell)\cos(2\rho)\Big)$$
$$+ \frac{2F_6}{(1+\ell)}|(1+\ell+\nu+i\omega)|^2\cos^2\rho\Big(\mathcal{K}\Big[1+\cos^2\rho(1+4\ell)\Big]+\mathcal{J}\sin^2\rho\Big)$$
$$+ 2F_1\Big[8\mathcal{K}\ell^2\cos^2\rho\cot^2\rho-(4\mathcal{K}-3\mathcal{J})\sin^2\rho\Big]$$
$$+ \frac{F_7\mathcal{K}}{(1+\ell)(2+\ell)}|(3+\ell+\nu+i\omega)|^2|(1+\ell+\nu+i\omega)|^2\cos^4\rho\sin^2\rho$$
$$- \frac{5F_6\mathcal{K}}{2(1+\ell)}|(1+\ell+\nu+i\omega)|^2\sin^2(2\rho)$$
$$+ F_1\sin^2\rho\Bigg(16F_2\mathscr{N}^\zeta_{\omega\ell}\nu^2\cos\zeta(\cos\rho)^{2\nu}+4F_4\mathscr{N}^\zeta_{\omega\ell}|(1+\ell+\nu)|^2\cos\zeta(\cos\rho)^{2(1+\nu)}$$
$$+ \frac{\mathscr{N}^\zeta_{\omega\ell}}{(1+\nu)(2+\nu)}|(1+\ell+\nu+i\omega)|^2\cos\zeta(\cos\rho)^{2(1+\nu)}\Big[4F_4\nu(2+\nu)$$
$$+ F_9|(3+\ell+\nu+i\omega)|^2\cos^2\rho\Big]$$
$$+ \frac{\cos^2\rho}{(\nu-1)(\nu-2)}|(1+\ell-\nu+i\omega)|^2(\mathscr{N}^N_{\omega\ell}-\mathscr{N}^\zeta_{\omega\ell}\sin\zeta)\Big[4F_5(\nu-2)$$
$$- F_8|(3+\ell-\nu+i\omega)|^2\cos^2\rho\Big]\Bigg)\Bigg\}. \tag{6.40}$$

6.6.3 Thermal expectation values with Robin boundary conditions

For the thermal expectation values, we will require the further definitions:

$$\mathcal{R} = -4\nu F_2\mathscr{N}^\zeta_{\omega\ell}\cos\zeta(\cos\rho)^{2\nu} - \frac{F_4\mathscr{N}^\zeta_{\omega\ell}|(1+\ell+\nu)\beta+2in\pi|^2\cos\zeta(\cos\rho)^{2(1+\nu)}}{(1+\nu)\beta^2}$$
$$- \frac{F_5|(1+\ell-\nu)\beta+2in\pi|^2\cos^2\rho(\mathscr{N}^N_{\omega\ell}-\mathscr{N}^\zeta_{\omega\ell}\sin\zeta)}{(\nu-1)\beta^2},$$
$$\mathcal{D} = (1+\ell+\nu)^2\beta^2+4\pi^2n^2. \tag{6.41}$$

We also use the hypergeometric functions given in (6.32) and the normalisation constants defined in (5.80, 5.81), with ω replaced by $2n\pi/\beta$.

As for the v.e.v.s, the following are the difference between the Robin and Neumann terms and are labelled with the subscript β. For the construction of the RSETs, the following terms are summed over ℓ and n as described in Section 6.4.

$$w^{\zeta}_{\beta} = \frac{F_1 \mathcal{K} \cos^2\rho\,(\sin\rho)^{2\ell}}{2\pi\beta}, \tag{6.42}$$

$$w^{\tau\,\zeta}_{\tau\,\beta} = -\frac{\cos^2\rho\,(\sin\rho)^{2\ell}\mathcal{K}}{32\pi L^2\beta^3}\Bigg\{ -64F_1\pi^2n^2\cos^2\rho + 8\beta^2\mathcal{C}F_1 + \frac{2\mathcal{D}F_6\sin^2(2\rho)}{(1+\ell)}\Bigg\}, \tag{6.43}$$

$$\begin{aligned} w^{\rho\,\zeta}_{\rho\,\beta} = -\frac{\cos^2\rho(\sin\rho)^{2\ell}\mathcal{K}}{32(1+\ell)\pi L^2\beta^3}\Bigg\{ & 32F_1(1+\ell)(1+\ell+\nu)\beta^2\cos^2\rho - 4F_6\mathcal{D}\cot\rho\sin(4\rho) \\ & + 8F_1\,\mathcal{C}(1+\ell)\beta^2 - 4F_6\,\mathcal{C}\beta^2\left|\left(1+\ell+\nu+\frac{2i\pi n}{\beta}\right)\right|^2\cos^2\rho \\ & - \frac{4F_7\cos^4\rho\sin^2\rho}{(2+\ell)\beta^2}\left|((3+\ell+\nu)\beta+2i\pi n)\right|^2\mathcal{D} + 2F_6\mathcal{D}\sin^2(2\rho) \\ & + \nu\left[8F_1(1+\ell)\beta^2\mathcal{C} + 2F_6\mathcal{D}\sin^2(2\rho)\right] + (1-\ell)\cot^2\rho\Big[8F_1(1+\ell)\beta^2\mathcal{C} + 2F_6\mathcal{D}\sin^2(2\rho)\Big]\Bigg\}, \end{aligned} \tag{6.44}$$

$$w^{\theta\,\zeta}_{\theta\,\beta} = -\frac{\cot^2\rho\,(\sin\rho)^{2\ell}\mathcal{K}}{32\pi L^2\beta^3}\Bigg\{16F_1\ell^2\beta^2\cos^2\rho\, - 8\beta^2\mathcal{C}F_1 - \frac{2\mathcal{D}F_6\sin^2(2\rho)}{(1+\ell)}\Bigg\}, \tag{6.45}$$

$$w^{;\tau\,\zeta}_{;\tau\,\beta} = -\frac{\cos^2\rho\,(\sin\rho)^{2(1+\ell)}}{4\pi L^2\beta}\Bigg\{4\ell F_1\mathcal{K}\cot^2\rho + F_1(\mathcal{R}-4\mathcal{K}) + \frac{F_6\,\mathcal{K}\,\cos^2\rho}{(1+\ell)\beta^2}|(1+\ell+\nu)\beta+2in\pi|^2\Bigg\}, \tag{6.46}$$

$$\begin{aligned} w^{;\rho\,\zeta}_{;\rho\,\beta} = \frac{\cos^2\rho\,(\sin\rho)^{2\ell}}{8\pi L^2\beta}\Bigg\{ & F_1\cos^2\rho\,[-8\mathcal{K}(1+5\ell)+2\mathcal{R}(1+4\ell)] \\ & + \frac{2\cos^4\rho}{(1+\ell)\beta^2}\left|((1+\ell+\nu)\beta+2in\pi)\right|^2F_6\mathcal{K}\,(1+4\ell) + 8\cot^2\rho F_1\mathcal{K}\ell(2\ell\cos^2\rho-1) \\ & + 8F_1(2\mathcal{K}-\mathcal{R})\sin^2\rho + \frac{F_6\sin^2(2\rho)}{2(1+\ell)\beta^2}\left|((1+\ell+\nu)\beta+2in\pi)\right|^2(\mathcal{R}-6\mathcal{K}) \\ & + \frac{F_7\,\mathcal{K}\,\cos^2\rho\sin^2(2\rho)}{4(1+\ell)(2+\ell)\beta^4}\left|((1+\ell+\nu)\beta+2in\pi)\right|^2\left|((3+\ell+\nu)\beta+2in\pi)\right|^2 \\ & + F_1\sin^2\rho\Bigg(16\nu^2F_2\mathscr{N}^{\zeta}_{\omega\ell}\cos\zeta(\cos\rho)^{2\nu} + \frac{4F_4\mathscr{N}^{\zeta}_{\omega\ell}\cos\zeta(\cos\rho)^{2(1+\nu)}}{(1+\nu)\beta^2}\left|(1+\ell+\nu)\beta+2in\pi\right|^2(1+2\nu) \\ & + \frac{F_9\mathscr{N}^{\zeta}_{\omega\ell}\cos\zeta(\cos\rho)^{2(2+\nu)}}{(1+\nu)(2+\nu)\beta^4}\left|((1+\ell+\nu)\beta+2in\pi)\right|^2\left|((3+\ell+\nu)\beta+2in\pi)\right|^2 \end{aligned}$$

$$+\frac{4F_5\,\cos^2\rho}{(\nu-1)\beta^2}\left|((1+\ell-\nu)\beta+2in\pi)\right|^2\left(\mathscr{N}^N_{\omega\ell}-\mathscr{N}^\zeta_{\omega\ell}\sin\zeta\right)$$
$$-\frac{F_8\,\cos^4\rho}{(\nu-2)(\nu-1)\beta^4}\left|((1+\ell-\nu)\beta+2in\pi)\right|^2\left|((3+\ell-\nu)\beta+2in\pi)\right|^2\left(\mathscr{N}^N_{\omega\ell}-\mathscr{N}^\zeta_{\omega\ell}\sin\zeta\right)\Bigg)\Bigg\}, \tag{6.47}$$

$$w^{;\theta\,\zeta}_{;\theta\,\beta}=\frac{\cos^2\rho\,(\sin\rho)^{2\ell}}{4\pi L^2\beta}\left\{4F_1\mathcal{K}\ell\cot^2\rho+F_1(\mathcal{R}-4\mathcal{K})+\frac{F_6\mathcal{K}\cos^2\rho}{(1+\ell)\beta^2}\left|(1+\ell+\nu)\beta+2in\pi\right|^2\right\}, \tag{6.48}$$

$$\Box w^\zeta_\beta=\frac{\cos^2\rho(\sin\rho)^{2\ell}}{8\pi L^2\beta}\Bigg\{2F_1(\mathcal{R}-4\mathcal{K})[1+\cos^2\rho(1+4\ell)]$$
$$+\frac{2F_6\mathcal{K}\cos^2\rho}{(1+\ell)\beta^2}\left|(1+\ell+\nu)\beta+2in\pi\right|^2\left[1+\cos^2\rho(1+4\ell)\right]$$
$$+2F_1\left[8\ell^2\mathcal{K}\cos^2\rho\cot^2\rho+(4\mathcal{K}-3\mathcal{R})\sin^2\rho\right]$$
$$+\frac{F_6\sin^2(2\rho)}{(1+\ell)\beta^2}\left|(1+\ell+\nu)\beta+2in\pi\right|^2(\mathcal{R}-10\mathcal{K})+\frac{F_6\mathcal{R}\sin^2(2\rho)}{(1+\ell)}\left|(1+\ell+\nu)\beta+2in\pi\right|^2$$
$$+\frac{F_7\mathcal{K}\cos^2\rho\,\sin^2(2\rho)}{(1+\ell)(2+\ell)\beta^4}\left|(1+\ell+\nu)\beta+2in\pi\right|^2\left|(3+\ell+\nu)\beta+2in\pi\right|^2$$
$$+F_1\sin^2\rho\Bigg(16\nu^2F_2\mathscr{N}^\zeta_{\omega\ell}\cos\zeta(\cos\rho)^{2\nu}+\frac{4F_4\mathscr{N}^\zeta_{\omega\ell}\,\cos\zeta(\cos\rho)^{2(1+\nu)}}{(1+\nu)\beta^2}\left|(1+\ell+\nu)\beta+2in\pi\right|^2(1+2\nu)$$
$$+\frac{F_9\mathscr{N}^\zeta_{\omega\ell}\cos\zeta(\cos\rho)^{2(2+\nu)}}{(1+\nu)(2+\nu)\beta^4}\left|(1+\ell+\nu)\beta+2in\pi\right|^2\left|(3+\ell+\nu)\beta+2in\pi\right|^2$$
$$+\frac{4F_5\,\cos^2\rho}{(\nu-1)\beta^2}\left|(1+\ell-\nu)\beta+2in\pi\right|^2\left(\mathscr{N}^N_{\omega\ell}-\mathscr{N}^\zeta_{\omega\ell}\sin\zeta\right)$$
$$-\frac{F_8\,\cos^4\rho}{(\nu-2)(\nu-1)\beta^4}\left|(1+\ell-\nu)\beta+2in\pi\right|^2\left|(3+\ell-\nu)\beta+2in\pi\right|^2\left(\mathscr{N}^N_{\omega\ell}-\mathscr{N}^\zeta_{\omega\ell}\sin\zeta\right)\Bigg)\Bigg\}. \tag{6.49}$$

Chapter 7

Quantum-corrected metric on adS3

In Chapter 6 we determined the vacuum and thermal expectation values of the RSET for a scalar field with general mass and coupling. In this chapter we use a selection of these RSETs to examine the backreaction on the underlying space-time geometry. There are a number of approaches that can be adopted to study the backreaction. A perturbative approach [46, 93] involves linearising the Einstein field equations (1.2) and considering first order corrections to the metric. An alternative method is to use an analytic approximation to a general RSET which is valid for a range of space-times so that the right hand side of (1.2) is expressed in terms of the unknown metric functions [5, 6]. In this chapter we follow the methodology in [24, 25, 26, 95]. We first compute the RSET using the adS3 metric which is a solution the vacuum Einstein equations

$$R_{\mu\nu} - \frac{1}{2}Rg_{\mu\nu} + \Lambda g_{\mu\nu} = 0. \tag{7.1}$$

The RSET is then used as the source term in (1.2) to find, nonperturbatively, the component functions of the quantum-corrected metric (QCM).

We use two different forms of the QCM ansatz and compute their component functions. The intention in this chapter is to give a flavour of the different types of QCM solutions that can be obtained. The emphasis will be on the energy density profiles of the RSETs and the coupling constants, rather than the boundary conditions. We do not intend to present a exhaustive account of all the different possible QCMs obtained with the RSETs obtained in Chapter 6, which we hope to leave for a future publication.

There is a paucity of literature when it comes to the study of the backreaction of quantum fields on pure adS space-time. Most of the work in this area has focused on the backreaction of quantum fields on black hole (BH) backgrounds, in particular the Schwarzschild [56, 57] or the BTZ BH [25, 26, 65, 67, 87]. The BTZ BH [10] is a (2+1)-dimensional black hole solution to GR which is asymptotically adS3. The study of the backreaction of quantum scalar fields on the BTZ background has produced some interesting findings. Using the stress energy tensor obtained from the BTZ metric as the source term, it was shown that quantum corrections to the BTZ metric produced a curvature singularity at the space-time origin [26, 67]. Also in [24, 26] it was found that the quantum backreaction forms an event horizon to mask naked singularities, thus acting as a form of cosmic censorship.

In a recent study [95], the backreaction of a massless, conformally coupled scalar field was studied on a background pure adS4. The RSETs for a number of thermal states were computed

subject to Dirichlet, Neumann and transparent boundary conditions. It was found that the mass functions of the QCM demonstrated solitonic behaviour with the 'mass' of the soliton dependent on the temperature of the scalar field. In this chapter we use similar metric ansatze for the QCM to [95] and study the backreaction from scalar fields with general mass and couplings. Allowing the field mass and coupling constant to vary can result in some exotic RSETs, some of which have negative energy densities and violate the classical energy conditions (see Section 1.8). The effect that these RSETs have on the backreaction is an area we explore in this chapter.

This chapter is set out as follows. In Section 7.1 we lay out some preliminary ground work needed before we can use the RSETs as source terms in Einstein's field equations. In Section 7.2 we use a metric ansatz for the quantum-corrected metric which has a similar form to the adS3 metric. This will allow direct comparisons to be made between the metric functions of the QCM and adS3. We then derive ordinary differential equations (ODEs) for the component functions of the QCM. In Section 7.3 we solve the differential equations derived in Section 7.2 for two of the QCM functions and use these to obtain an expression for the third. We use Taylor series expansions of the metric components and RSET terms which are then used for the initial conditions for the ODEs. In Section 7.4 we display the results for the QCM functions, comparing them to the corresponding terms on adS3. In Section 7.5 we use a general static, spherically symmetric metric in Schwarzschild-like coordinates as our alternative QCM ansatz. We present the results obtained for the mass functions and how they depend on the energy density profiles of the RSETs used as the source term in Einstein's equations. In Section 7.6, we examine further whether some of the mass functions plotted in Section 7.5 converge to a finite result. Finally in Section 7.7 we summarise our findings and make suggestions for future research in this area.

§ 7.1 Preliminaries

The adS3 metric which was used in the construction of the RSET in Chapter 6 is a solution of the vacuum Einstein field equations (7.1). In Chapter 6, the v.e.v.s and t.e.v.s of a number of RSETs for a scalar field with general mass and coupling were computed. To determine the quantum corrected metric, $\widetilde{g}_{\mu\nu}$, we use one of the RSETs obtained in chapter 6 as the source term in Einstein's equation (1.2) to give

$$\widetilde{R}_{\mu\nu} - \frac{1}{2}\widetilde{R}\,\widetilde{g}_{\mu\nu} + \Lambda\widetilde{g}_{\mu\nu} = 8\pi\,\langle T_{\mu\nu}\rangle. \tag{7.2}$$

In this chapter we set $G = 1$ and omit the $\hat{}$ on $T_{\mu\nu}$ for clarity. For a given state $|\psi\rangle$, we can express the expectation value of the stress energy tensor as

$$\langle\psi|T_{\mu\nu}|\psi\rangle = \langle\widetilde{T}_{\mu\nu}\rangle + \langle T_{\mu\nu}\rangle_0, \tag{7.3}$$

where $\langle T_{\mu\nu}\rangle_0$ represents the expectation value of the RSET in the vacuum state and $\langle\widetilde{T}_{\mu\nu}\rangle$ is the difference in the expectation values between $|\psi\rangle$ and the vacuum state. With Dirichlet and Neumann boundary conditions, the v.e.v. of the RSET, $\langle T_{\mu\nu}\rangle_0^{D/N}$, respects the underlying symmetry of adS3 and is thus a constant α multiplied by the space-time metric (6.7, 6.8). The constant α depends on ν and the coupling constant ξ. We can thus rearrange (7.2) as

$$\widetilde{R}_{\mu\nu} - \frac{1}{2}\widetilde{R}\,\widetilde{g}_{\mu\nu} + \{\Lambda - 8\pi\alpha\}\,\widetilde{g}_{\mu\nu} = 8\pi\,\langle\widetilde{T}_{\mu\nu}\rangle. \tag{7.4}$$

For the Dirichlet/Neumann vacuum states (6.7, 6.8), the constant α is given by

$$\alpha = \pm\frac{1}{12\pi L^3}\left\{\nu^3 + (6\xi - 1)\nu\right\}, \tag{7.5}$$

where ν is given in (4.16), ξ is the coupling constant and $+/-$ represent the Dirichlet and Neumann boundary conditions respectively. It is a simple matter to see that in the massless, conformally coupled case ($m = 0, \nu = 1/2, \xi = 1/8$), we have $\alpha = 0$. Equation (7.4) merely represents a renormalisation of the cosmological constant [95], so we can write (7.4) as

$$\widetilde{R}_{\mu\nu} - \frac{1}{2}\widetilde{R}\,\widetilde{g}_{\mu\nu} + \widetilde{\Lambda}\widetilde{g}_{\mu\nu} = 8\pi\,\langle\widetilde{T}_{\mu\nu}\rangle, \tag{7.6}$$

where $\widetilde{\Lambda} = \Lambda - 8\pi\alpha$ represents the renormalised cosmological constant. Finally we re-write (7.6) with mixed indices as this is the form of the RSETs derived in Chapter 6. This gives

$$\widetilde{R}_{\mu}^{\nu} - \left(\frac{1}{2}\widetilde{R} - \widetilde{\Lambda}\right)\delta_{\mu}^{\nu} = 8\pi\,\langle\widetilde{T}_{\mu}^{\nu}\rangle. \tag{7.7}$$

We use (7.7) as the form of Einstein's equations to calculate the quantum corrected metric $\widetilde{g}_{\mu\nu}$.

§ 7.2 Metric ansatz

We start with a general metric ansatz for a static, spherically symmetric three-dimensional spacetime of the form

$$ds^2 = -A(\rho)dt^2 + B(\rho)d\rho^2 + C(\rho)d\theta^2. \tag{7.8}$$

Inserting $\widetilde{g}_{\mu\nu}$ into (7.7) gives us three equations for the metric functions corresponding to the three nonzero components of $\langle\widetilde{T}_{\mu}^{\nu}\rangle$

$$0 = \widetilde{\Lambda} - 8\pi\langle\widetilde{T}_{t}^{t}\rangle - \frac{C(\rho)B'(\rho)C'(\rho) - 2B(\rho)C(\rho)C''(\rho) + B(\rho)C'(\rho)^2}{4B^2(\rho)C^2(\rho)}, \tag{7.9}$$

$$0 = \widetilde{\Lambda} - 8\pi\langle\widetilde{T}_{\rho}^{\rho}\rangle + \frac{A'(\rho)C'(\rho)}{4A(\rho)B(\rho)C(\rho)}, \tag{7.10}$$

$$0 = \widetilde{\Lambda} - 8\pi\langle\widetilde{T}_{\theta}^{\theta}\rangle + \frac{2A(\rho)B(\rho)A''(\rho) - A(\rho)A'(\rho)B'(\rho) - B(\rho)A'(\rho)^2}{4A^2(\rho)B^2(\rho)}, \tag{7.11}$$

where the prime denotes differentiation with respect to ρ. We also have the nonzero component of the conservation equations $\nabla_{\mu}\langle\widetilde{T}_{\rho}^{\mu}\rangle = 0$ where

$$\nabla_{\mu}\langle\widetilde{T}_{\rho}^{\mu}\rangle = \frac{1}{2}\left\{\frac{A'(\rho)}{A(\rho)}\left(\langle\widetilde{T}_{\rho}^{\rho}\rangle - \langle\widetilde{T}_{t}^{t}\rangle\right) + \frac{C'(\rho)}{C(\rho)}\left(\langle\widetilde{T}_{\rho}^{\rho}\rangle - \langle\widetilde{T}_{\theta}^{\theta}\rangle\right) + 2\langle\widetilde{T}_{\rho}^{\rho}\rangle'\right\}. \tag{7.12}$$

As a consistency check for equations (7.9– 7.12) we differentiate (7.10) and rearrange it to obtain an expression for $A''(\rho)$. This is then substituted into (7.11) to give

$$0 = \widetilde{\Lambda} - 8\pi\langle\widetilde{T}_{\theta}^{\theta}\rangle + \frac{A'(\rho)^2}{4A^2(\rho)B(\rho)} + 16\pi\langle\widetilde{T}_{\rho}^{\rho}\rangle'\frac{C(\rho)}{C'(\rho)} + \frac{A'(\rho)}{2A(\rho)B(\rho)}\left\{\frac{C'(\rho)}{C(\rho)} + \frac{B'(\rho)}{2B(\rho)} - \frac{C''(\rho)}{C'(\rho)}\right\}. \tag{7.13}$$

Rearranging (7.9) gives an expression for $C''(\rho)$ which, after substituting into (7.13) (and after some algebra) gives

$$0 = 8\pi \left\{ \langle \widetilde{T}^{\rho}_{\rho} \rangle - \langle \widetilde{T}^{\theta}_{\theta} \rangle + \frac{C(\rho)}{C'(\rho)} \left[\frac{A'(\rho)}{A(\rho)} (\langle \widetilde{T}^{\rho}_{\rho} \rangle - \langle \widetilde{T}^{t}_{t} \rangle) + 2 \langle \widetilde{T}^{\rho}_{\rho} \rangle' \right] \right\}. \tag{7.14}$$

It can now be seen that the conservation equation (7.12) is simply $C'(\rho)/16\pi C(\rho)$ times (7.14), showing that Einstein's equations (7.9–7.11) lead to the conservation of the RSET.

We now rearrange equations (7.9–7.12) to obtain differential equations for $C(\rho)$ and $A(\rho)$ in terms of the components of the RSET and their derivatives. For $C(\rho)$ we have

$$\begin{aligned}
0 = \widetilde{\Lambda} - 8\pi \langle \widetilde{T}^{t}_{t} \rangle &- \frac{8\pi C \langle \widetilde{T}^{\rho}_{\rho} \rangle' \left(\langle \widetilde{T}^{t}_{t} \rangle - \langle \widetilde{T}^{\rho}_{\rho} \rangle \right)}{\left(\langle \widetilde{T}^{\theta}_{\theta} \rangle - \langle \widetilde{T}^{\rho}_{\rho} \rangle \right) C' - 2C \langle \widetilde{T}^{\rho}_{\rho} \rangle'} \\
&- \frac{C \left(\widetilde{\Lambda} - 8\pi \langle \widetilde{T}^{\rho}_{\rho} \rangle \right) \left(\langle \widetilde{T}^{t}_{t} \rangle' - \langle \widetilde{T}^{\rho}_{\rho} \rangle' \right)}{C' \left(\langle \widetilde{T}^{\rho}_{\rho} \rangle - \langle \widetilde{T}^{\theta}_{\theta} \rangle \right) + 2C \langle \widetilde{T}^{\rho}_{\rho} \rangle'} + \frac{CC'' \left(\widetilde{\Lambda} - 8\pi \langle \widetilde{T}^{\rho}_{\rho} \rangle \right) \left(\langle \widetilde{T}^{t}_{t} \rangle - \langle \widetilde{T}^{\rho}_{\rho} \rangle \right)}{C' \left[C' \left(\langle \widetilde{T}^{\theta}_{\theta} \rangle - \langle \widetilde{T}^{\rho}_{\rho} \rangle \right) - 2C \langle \widetilde{T}^{\rho}_{\rho} \rangle' \right]} \\
&+ \frac{\left(\langle \widetilde{T}^{t}_{t} \rangle - \langle \widetilde{T}^{\rho}_{\rho} \rangle \right) \left(\widetilde{\Lambda} - 8\pi \langle \widetilde{T}^{\rho}_{\rho} \rangle \right)}{\left[C' \left(\langle \widetilde{T}^{\theta}_{\theta} \rangle - \langle \widetilde{T}^{\rho}_{\rho} \rangle \right) - 2C \langle \widetilde{T}^{\rho}_{\rho} \rangle' \right]^2} \Bigg\{ C'^2 \left(\langle \widetilde{T}^{\theta}_{\theta} \rangle - \langle \widetilde{T}^{\rho}_{\rho} \rangle \right) \\
&- CC' \left(\langle \widetilde{T}^{\theta}_{\theta} \rangle' - \langle \widetilde{T}^{\rho}_{\rho} \rangle' \right) - CC'' \left(\langle \widetilde{T}^{\theta}_{\theta} \rangle - \langle \widetilde{T}^{\rho}_{\rho} \rangle \right) + 2C^2 \langle \widetilde{T}^{\rho}_{\rho} \rangle'' \Bigg\},
\end{aligned} \tag{7.15}$$

where we have omitted the arguments of the $C(\rho)$ function for clarity. Likewise for $A(\rho)$ we have

$$\begin{aligned}
0 = -8\pi \langle \widetilde{T}^{\theta}_{\theta} \rangle &+ \frac{4 \left(\langle \widetilde{T}^{\rho}_{\rho} \rangle - \langle \widetilde{T}^{\theta}_{\theta} \rangle \right)^2 (8\pi \langle \widetilde{T}^{\rho}_{\rho} \rangle - \widetilde{\Lambda})}{A'^2 \left[2 \langle \widetilde{T}^{\rho}_{\rho} \rangle' + \frac{A'}{A} \left(\langle \widetilde{T}^{\rho}_{\rho} \rangle - \langle \widetilde{T}^{\theta}_{\theta} \rangle \right) \right]^2} \Bigg\{ - \frac{\widetilde{\Lambda} A'^2 \left[A' \left(\langle \widetilde{T}^{\rho}_{\rho} \rangle - \langle \widetilde{T}^{t}_{t} \rangle \right) + 2A \langle \widetilde{T}^{\rho}_{\rho} \rangle' \right]^2}{4A^2 \left(\langle \widetilde{T}^{\rho}_{\rho} \rangle - \langle \widetilde{T}^{\theta}_{\theta} \rangle \right)^2 \left(8\pi \langle \widetilde{T}^{\rho}_{\rho} \rangle - \widetilde{\Lambda} \right)^2} \\
&+ \frac{\left[A' \left(\langle \widetilde{T}^{t}_{t} \rangle - \langle \widetilde{T}^{\rho}_{\rho} \rangle \right) - 2A \langle \widetilde{T}^{\rho}_{\rho} \rangle' \right] \left(A'^3 - 2AA'A'' \right)}{4A^2 \left(\langle \widetilde{T}^{\theta}_{\theta} \rangle - \langle \widetilde{T}^{\rho}_{\rho} \rangle \right) \left(8\pi \langle \widetilde{T}^{\rho}_{\rho} \rangle - \widetilde{\Lambda} \right)} \\
&+ \frac{A'^3 \left[A' \left(\langle \widetilde{T}^{\rho}_{\rho} \rangle - \langle \widetilde{T}^{t}_{t} \rangle \right) + 2A \langle \widetilde{T}^{\rho}_{\rho} \rangle' \right]}{4A \left(\langle \widetilde{T}^{\rho}_{\rho} \rangle - \langle \widetilde{T}^{\theta}_{\theta} \rangle \right) \left(8\pi \langle \widetilde{T}^{\rho}_{\rho} \rangle - \widetilde{\Lambda} \right)} + \frac{2\pi A'^2 \left[A' \left(\langle \widetilde{T}^{\rho}_{\rho} \rangle - \langle \widetilde{T}^{t}_{t} \rangle \right) + 2A \langle \widetilde{T}^{\rho}_{\rho} \rangle' \right] \langle \widetilde{T}^{\rho}_{\rho} \rangle'}{A \left(\langle \widetilde{T}^{\rho}_{\rho} \rangle - \langle \widetilde{T}^{\theta}_{\theta} \rangle \right) \left(8\pi \langle \widetilde{T}^{\rho}_{\rho} \rangle - \widetilde{\Lambda} \right)^2} \\
&+ \frac{A'^2 \left[A' \left(\langle \widetilde{T}^{\rho}_{\rho} \rangle - \langle \widetilde{T}^{t}_{t} \rangle \right) + 2A \langle \widetilde{T}^{\rho}_{\rho} \rangle' \right] \left(\langle \widetilde{T}^{\rho}_{\rho} \rangle' - \langle \widetilde{T}^{\theta}_{\theta} \rangle' \right)}{4A \left(\langle \widetilde{T}^{\rho}_{\rho} \rangle - \langle \widetilde{T}^{\theta}_{\theta} \rangle \right)^2 \left(8\pi \langle \widetilde{T}^{\rho}_{\rho} \rangle - \widetilde{\Lambda} \right)} - \frac{A'A'' \left[A' \left(\langle \widetilde{T}^{\rho}_{\rho} \rangle - \langle \widetilde{T}^{t}_{t} \rangle \right) + 2A \langle \widetilde{T}^{\rho}_{\rho} \rangle' \right]}{4A \left(\langle \widetilde{T}^{\rho}_{\rho} \rangle - \langle \widetilde{T}^{\theta}_{\theta} \rangle \right) \left(8\pi \langle \widetilde{T}^{\rho}_{\rho} \rangle - \widetilde{\Lambda} \right)} \\
&+ \frac{A'^2 \left[A'^2 \left(\langle \widetilde{T}^{\rho}_{\rho} \rangle - \langle \widetilde{T}^{t}_{t} \rangle \right) - A\, A' \left(\langle \widetilde{T}^{\rho}_{\rho} \rangle - \langle \widetilde{T}^{t}_{t} \rangle \right) - AA'' \left(\langle \widetilde{T}^{\rho}_{\rho} \rangle - \langle \widetilde{T}^{t}_{t} \rangle \right) - 2A^2 \langle \widetilde{T}^{\rho}_{\rho} \rangle'' \right]}{4A^2 \left(\langle \widetilde{T}^{\rho}_{\rho} \rangle - \langle \widetilde{T}^{\theta}_{\theta} \rangle \right) \left(8\pi \langle \widetilde{T}^{\rho}_{\rho} \rangle - \widetilde{\Lambda} \right)} \Bigg\}
\end{aligned} \tag{7.16}$$

The differential equations (7.15, 7.16) are solved using MATHEMATICA to obtain $C(\rho)$ and $A(\rho)$ expressed as interpolating functions. We then use (7.10) to obtain an expression for $B(\rho)$ as

$$B(\rho) = \frac{A'C'}{4AC\left(8\pi\langle\widetilde{T}^{\rho}_{\rho}\rangle - \widetilde{\Lambda}\right)}. \tag{7.17}$$

§ 7.3 Solving the ODEs

Before we can use the differential equations for $C(\rho)$ and $A(\rho)$ given in (7.15, 7.16), it should be borne in mind that the components of the RSETs used in these equations have been computed numerically (see Sections 6.2–6.4). To convert the numerical data into functions that can be differentiated and used in (7.15, 7.16), we use the Interpolation function in MATHEMATICA to order nine to improve accuracy (Figure 7.1).

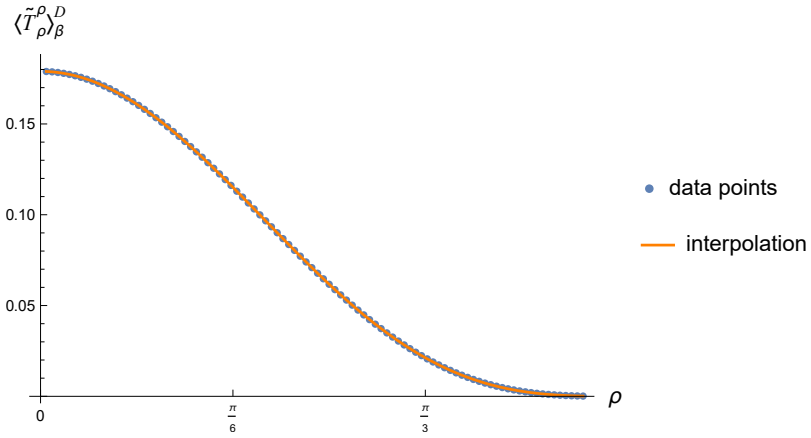

Figure 7.1: Comparison of the numerically obtained data points for the $\langle\widetilde{T}^{\rho}_{\rho}\rangle$ component of the RSET (blue dots) with the corresponding interpolation function obtained from MATHEMATICA with interpolation order nine. This is for the massless, conformally coupled field with Dirichlet boundary condition and inverse temperature $\beta = 1$.

We solve the differential equations (7.15, 7.16) for $C(\rho)$ and $A(\rho)$ using the NDSolveValue command in MATHEMATICA. The assumptions we make about the series expansions of $A(\rho), C(\rho)$ (see (7.19) below) means that the ODEs (7.15, 7.16) are singular at the space-time origin. We therefore start the numerical integration at $\rho = \epsilon$ for $\epsilon \ll 1$. To do this we require Taylor series expansions of the metric functions and the RSET components near the space-time origin ($\rho \to 0$). For the RSET components, we use the series expansion of the interpolating functions obtained in MATHEMATICA. This reveals that the coefficients of the odd powers of ρ increasingly vanish with higher interpolation order. For example with for the massless, conformally coupled field ($\nu = 1/2$, $\xi = 1/8$), the coefficient of the ρ^3 term is $\sim 10^{-2}$ with Interpolation order three whilst it is $\sim 10^{-9}$ with Interpolation order 9. Thus, consistent with the findings in [95], we find that the series expansions of the RSET components near the space-time origin contain only even powers of ρ, giving

$$\begin{aligned}
\langle \widetilde{T}^t_t \rangle &= T_{00} + T_{02}\,\rho^2 + T_{04}\,\rho^4 + T_{06}\,\rho^6 + \mathcal{O}(\rho^8),\\
\langle \widetilde{T}^\rho_\rho \rangle &= T_{10} + T_{12}\,\rho^2 + T_{14}\,\rho^4 + T_{16}\,\rho^6 + \mathcal{O}(\rho^8),\\
\langle \widetilde{T}^\theta_\theta \rangle &= T_{20} + T_{22}\,\rho^2 + T_{24}\,\rho^4 + T_{26}\,\rho^6 + \mathcal{O}(\rho^8).
\end{aligned} \tag{7.18}$$

This is in keeping with the expressions obtained for the RSET components for Dirichlet and Neumann boundary conditions in (6.24–6.26) which can be seen to consist of even powers of ρ. As a result of the form of the series expansion of the RSET components (7.18), it is natural to assume that the expansions of the metric functions also contain only even powers of ρ, namely

$$\begin{aligned}
A(\rho) &= A_0 + A_2\,\rho^2 + A_4\,\rho^4 + A_6\,\rho^6 + \mathcal{O}(\rho^8),\\
B(\rho) &= B_0 + B_2\,\rho^2 + B_4\,\rho^4 + B_6\,\rho^6 + \mathcal{O}(\rho^8),\\
C(\rho) &= C_2\,\rho^2 + C_4\,\rho^4 + C_6\rho^6 + C_8\rho^8 + \mathcal{O}(\rho^{10}).
\end{aligned} \tag{7.19}$$

where the coefficients A_i, B_i, C_i are to be determined. For the $C(\rho)$ expansion we start with the $\mathcal{O}(\rho^2)$ term, which matches the behaviour of the original adS metric (2.9), and include terms for up to $\mathcal{O}(\rho^8)$ to give four terms for each of the expansions in (7.18, 7.19).

To find expressions for the metric coefficients A_i, B_i, C_i in terms of the RSET coefficients T_{ij}, we insert (7.18, 7.19) into the Einstein equations (7.9, 7.10, 7.11) and the conservation equation (7.12). We then obtain a series expansion of the resulting equations and equate powers of ρ. Attempts to use the regularity of the invariant curvature scalar obtained by contracting the Ricci tensor with itself ($R_{\mu\nu}R^{\mu\nu}$), proved fruitless as this was already found to be regular near the space-time origin. However, as we are in a static space-time, there is freedom to rescale the time coordinate and thus we can choose $A_0 = 1$. We are then able to obtain values for the remaining A_i, B_i coefficients in terms of the T_{ij} ones.

In order to avoid a conical singularity in the metric, we need to constrain the value of C_2. To see why this is needed, consider the metric of a flat two-dimensional space in polar coordinates, given by

$$ds^2 = dr^2 + r^2 d\theta^2. \tag{7.20}$$

If we compare the leading order terms of the spatial part of the QCM ansatz we have

$$\begin{aligned}
ds^2 &= B_0\,d\rho^2 + C_2\,\rho^2 d\theta^2,\\
&= B_0\left(d\rho^2 + \frac{C_2}{B_0}\rho^2 d\theta^2\right).
\end{aligned} \tag{7.21}$$

Therefore, we need to set $C_2 = B_0$ as a different value of C_2 will result in an angular defect/excess and a conical singularity.

The metric coefficients for the lowest order terms are

$$\begin{aligned}
A_0 &= 1,\\
A_2 &= \frac{3T_{12} - T_{22}}{T_{00} - T_{10}},
\end{aligned}$$

$$C_2 = B_0 = \frac{3T_{12} - T_{22}}{(T_{00} - T_{10})(8\pi T_{10} - \widetilde{\Lambda})}. \tag{7.22}$$

Higher order terms become very large and unwieldy and are therefore not shown. It can be demonstrated that the denominators in all of the metric coefficients are nonvanishing.

Having obtained the values of the coefficients of the $C(\rho)$ and $A(\rho)$ expansions we need to choose a starting point (initial condition) for the integration in the NDSolveValue command. Using the series (7.19), we find (7.15, 7.16) are singular at the origin. Therefore we start the integration at a point ϵ close to the origin. We consider starting points of $\epsilon = 10^{-3}$, $\epsilon = 10^{-5}$ and $\epsilon = 10^{-6}$ and examine the resulting solutions obtained from the NDSolveValue command. We find that the Interpolating functions for $C(\rho)$, produced by the different values of ϵ, had matching profiles. Thus we use $\rho = 10^{-6}$ as the starting point of the integration. As the metric functions are divergent at the space-time boundary (as is the case for the adS3 metric components), the end-point for the integration was chosen to be at $\rho = \pi/2 - 10^{-6}$. As (7.15, 7.16) are second order differential equations we also need to stipulate the initial conditions for $C'(\rho)$ and $A'(\rho)$ but this found trivially by differentiating the relevant power series in (7.19). The metric functions $A(\rho)$ and $C(\rho)$ obtained by solving the ODEs (7.15, 7.16) are returned in MATHEMATICA as Interpolation functions which are suitable for differentiating and using in subsequent analysis.

§ 7.4 QCM components

In presenting our results, we select four different RSETs obtained in Chapter 6 to give a flavour of the different types of QCM solutions obtained. Figure 7.2 shows the QCM components obtained using the RSET for a minimally coupled ($\xi = 0$) scalar field in a thermal state with Dirichlet boundary conditions and a selection of inverse temperatures β, with $\nu = 1/4$. The QCM functions are displayed as ratios with the corresponding terms in the adS3 metric where we have set the adS3 length scale $L = 1$. The energy density component of the RSET is the difference between the thermal and vacuum states and is positive for all inverse temperature β. Figure 7.2 shows that $A(\rho)$ closely matches its adS3 counterpart ($\sec^2\rho$) until $\rho \sim \pi/6$ following which it increases monotonically, reaching its maximum at the space-time boundary. For $\beta > 1$ it appears that $A(\rho)$ begins to plateau as $\rho \to \pi/2$. The magnitude of the increase in $A(\rho)$ is temperature-dependent. Increasing temperature (decreasing β) results in greater deviation from the corresponding adS3 metric function. For $\beta = 3$ we see only a minimal increase throughout the space-time.

We see a different picture for the $B(\rho)$ function, where the maximum separation between the different values of β is seen at the space-time origin. As with $A(\rho)$, the greatest deviation from the adS3 metric term is with the highest temperature ($\beta = 1$). As the space-time boundary is approached, the $B(\rho)$ functions converge and approach the same value. For the $C(\rho)$ function we see a different qualitative behaviour to that seen with $A(\rho)$ and $B(\rho)$. The profiles for the different inverse temperatures β stay separated throughout the space-time. With increasing temperature we see increasing deviation of $C(\rho)$ from its adS3 counterpart, with the $\beta = 3$ profile differing the least.

The profiles of the metric functions for the massless, conformally coupled field (Figure 7.3) are very similar qualitatively to those seen for the minimally coupled field and $\nu = 1/4$ (Figure 7.2). Changes in the mass/coupling appear to have little effect. Comparing the the profiles in Figure 7.3

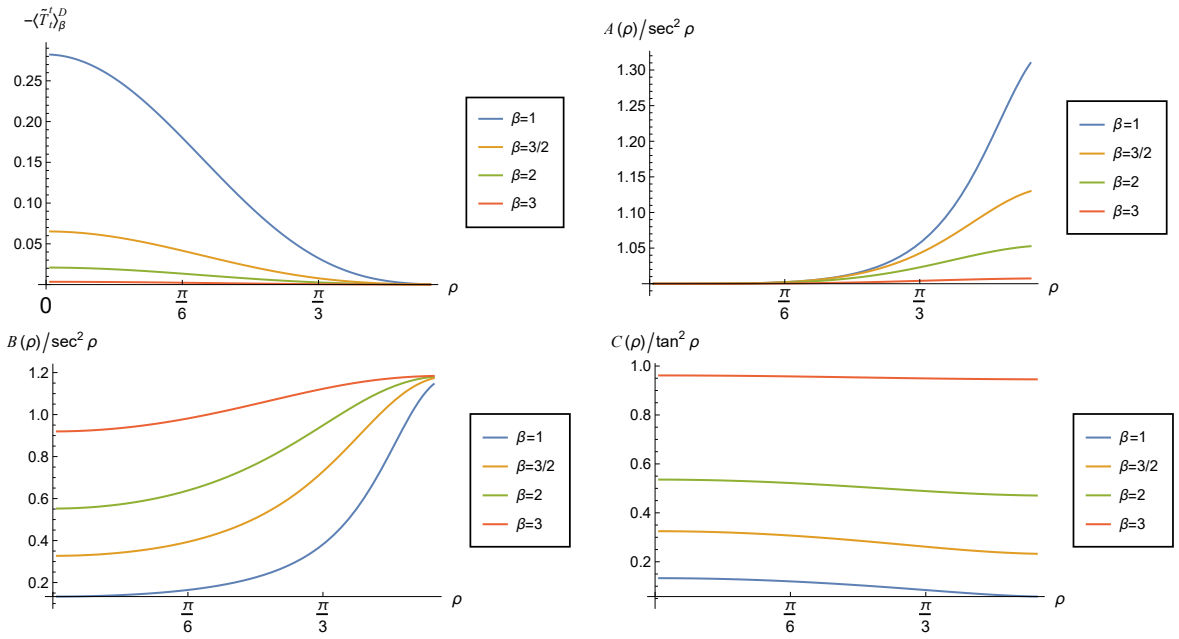

Figure 7.2: The components of the quantum corrected metric (7.8) (as ratios with the corresponding ads3 functions), obtained for a scalar field with $\nu = 1/4$, $\xi = 0$ (minimal coupling) and the Dirichlet boundary condition applied at the space-time boundary. Profiles are shown for a selection of inverse temperatures β. Top left shows the energy density component of the RSET (difference between the thermal and vacuum states). For all plots the adS3 length scale $\tilde{L} = 1$.

to those seen with the massless, conformally coupled field in adS4 [95], we find that the $B(\rho)$ and $C(\rho)$ profiles are also qualitatively similar in both cases. With the $A(\rho)$ function, we see the maximum departure from the adS4 term at the space-time boundary (as in Figure 7.3) but with increasing temperature, we see a decrease in $A(\rho)$ in adS4.

In Figure 7.4 we use a RSET with very different energy density profiles, compared to Figure 7.2, obtained by using a scalar field with a negative coupling $\xi = -1/2$. Not surprisingly, this produces qualitatively different results for the QCM functions. The $A(\rho)$ profile is similar to that seen in the minimally coupled case, with $A(\rho)$ resembling pure adS3 at the space-time origin. At $\rho \sim \pi/6$, the $A(\rho)$ profiles begin to deviate away from pure adS3 but only in the high temperature ($\beta = 1$) case is $A(\rho)$ greater than its pure adS3 counterpart. The other $A(\rho)$ profiles decrease with increasing ρ, attaining a minimum as the space-time boundary is approached. The $B(\rho)$ functions behave similar qualitatively to the minimally coupled case, with the maximum separation between the profiles found at the space-time origin. All profiles appear to converge together towards the space-time boundary where the $B(\rho)$ functions are ~ 2.5 times greater than in pure adS3. The $C(\rho)$ functions have a near constant value throughout space-time, decreasing with increasing temperature. However, the low temperature $\beta = 3$ profile is ~ 1.2 times that in pure adS3, even at the space-time origin and increases slowly as we approach the space-time boundary.

In Figure 7.5 we use RSETs obtained using Robin boundary conditions in the vacuum state with $\nu = 3/4$, $\xi = 1/8$. As with the thermal states studied in Figures 7.2 – 7.4, when Robin boundary conditions are applied, the maximal symmetry of adS space-time is broken. For the RSETs we use the difference between the Robin and Neumann v.e.v.s of the RSETs and renormalise the

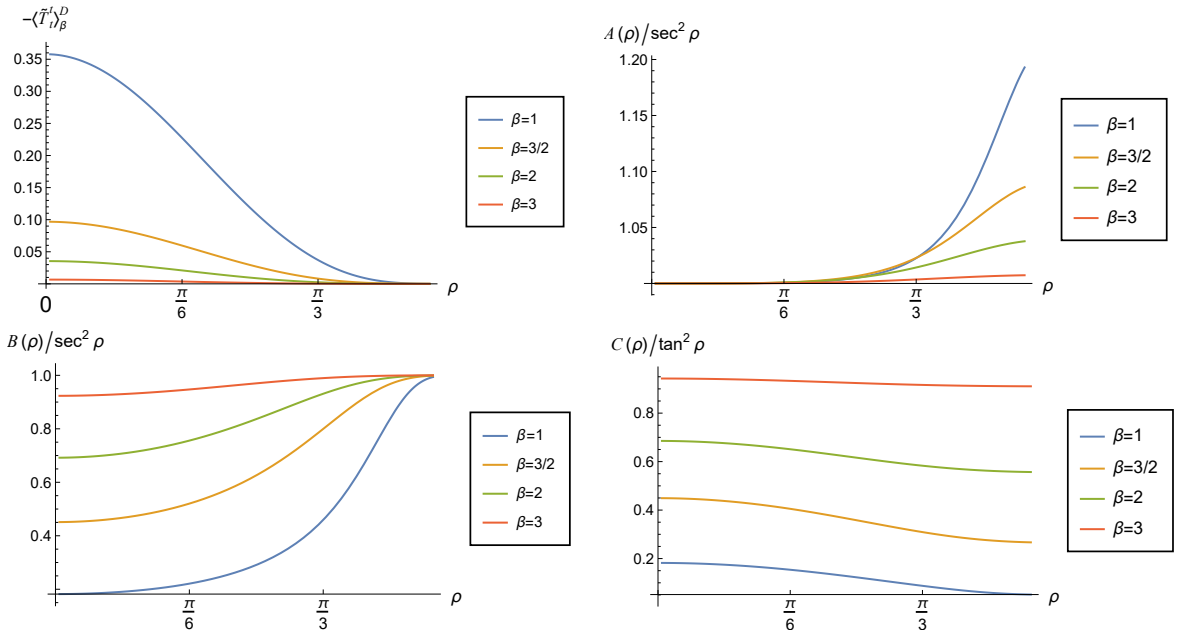

Figure 7.3: The components of the quantum corrected metric (7.8) (as ratios with the corresponding ads3 functions), obtained for a scalar field with $\nu = 1/2$, $\xi = 1/8$ (massless, conformally coupled) and the Dirichlet boundary condition applied at the space-time boundary. Profiles are shown for a selection of inverse temperatures β. Top left shows the energy density component of the RSET (difference between the thermal and vacuum states). For all plots the adS3 length scale $\tilde{L} = 1$.

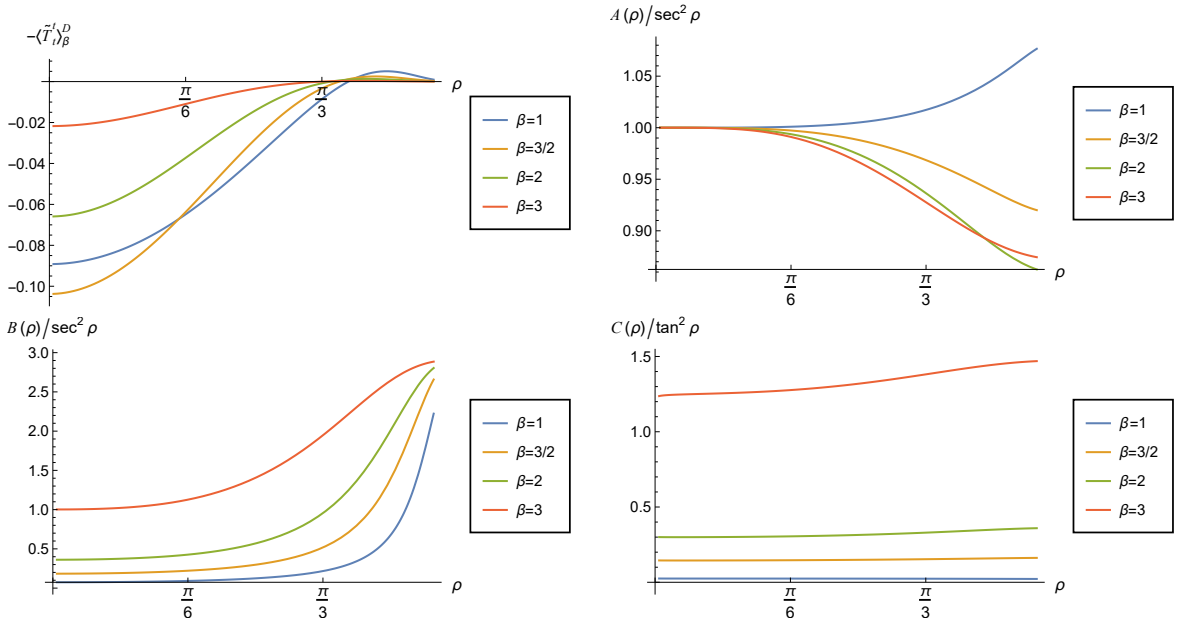

Figure 7.4: The components of the quantum corrected metric (7.8) (as ratios with the corresponding ads3 functions). The RSET is obtained for a scalar field with $\nu = 1/4$, $\xi = -1/2$ and applying the Dirichlet boundary condition at the space-time boundary. The profiles show a selection of inverse temperatures β. Top left shows the energy density component of the RSET (difference between the thermal and vacuum states). For all plots, then adS3 length scale $\tilde{L} = 1$.

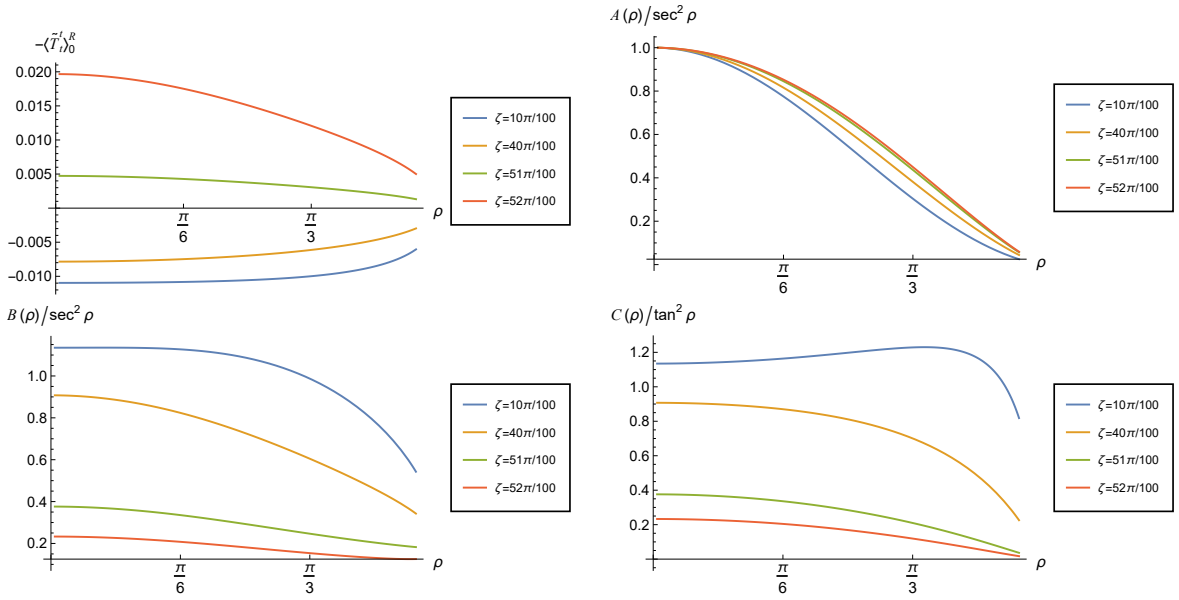

Figure 7.5: The components of the quantum corrected metric (7.8) (as ratios with the corresponding ads3 functions), obtained for a scalar field with $\nu = 3/4$, $\xi = 1/8$ in the vacuum state. A selection of Robin boundary conditions have been applied to the scalar field at the space-time boundary. Top left shows the energy density component of the RSET (difference between the vacuum Robin and vacuum Neumann states).

cosmological constant using the Neumann v.e.v. (7.5). A selection of Robin parameters ζ was chosen to give varied energy density profiles, with two profiles being entirely negative and two entirely positive. We see that the plots of the QCM functions are markedly different from those seen in Figures 7.2 – 7.4. The $A(\rho)$ profiles are similar for the different Robin parameters chosen. At the space-time origin, the $A(\rho)$ profiles equate to the adS3 counterpart but then decrease monotonically reaching a value approaching to zero at the space-time boundary. The profiles for the $B(\rho)$ and $C(\rho)$ functions are qualitatively similar. Both profiles show the maximum separation between the different Robin parameters at the origin before decreasing and moving towards each other as the space-time boundary is approached. The difference in the profiles of the QCM metric functions in Figure 7.5 compared to Figures 7.2 – 7.4 is likely to be because the energy density of the RSET $-\langle \widetilde{T}^t_t \rangle$, with Robin boundary conditions, converges to zero very slowly as $\rho \to \pi/2$.

§ 7.5 Alternative QCM ansatz

We now consider another static, spherically symmetric metric ansatz for the QCM but using Schwarzschild-like coordinates

$$ds^2 = -f(r)e^{\psi(r)}dt^2 + \frac{1}{f(r)}dr^2 + r^2 d\theta^2, \tag{7.23}$$

where $-\infty < t < \infty$, $0 \leq \theta \leq 2\pi$ and $r \in [0, \infty)$ represents the radial coordinate. The functions $f(r)$ and $\psi(r)$ are to be determined. The function $f(r)$ is given by

$$f(r) = \frac{r^2}{\widetilde{L}^2} - M(r), \tag{7.24}$$

where $\widetilde{L}$ is the renormalised adS3 radius of curvature related to the renormalised cosmological constant by $\widetilde{\Lambda} = -1/\widetilde{L}^2$ and $M(r)$ is a mass function. For $r^2 > 0$ with $\psi(r) = 0$ and $M > 0$, the metric shown in (7.23) represents the static BTZ metric [10] where the constant M is the mass of the BTZ black hole. Using (7.23) as our ansatz, we can consider the limit of $M(r)$ as $r \to \infty$ (if there is such a limit) as the mass of the metric or coordinate mass [27].

Comparing (7.23) to (7.8) we note that the metric has undergone a coordinate transformation $\rho \to r$ where

$$r^2 = C(\rho). \tag{7.25}$$

Furthermore, the functions $f(r)$, $\psi(r)$ and $M(r)$ can be expressed in terms of the metric functions in (7.8) as

$$f(r) = \frac{C'(\rho)^2}{4C(\rho)B(\rho)}, \tag{7.26}$$

$$\psi(r) = \frac{4A(\rho)B(\rho)C(\rho)}{C'(\rho)^2}, \tag{7.27}$$

$$M(r) = \frac{r^2}{\widetilde{L}} - \frac{C'(\rho)^2}{4C(\rho)B(\rho)}. \tag{7.28}$$

Using (7.19), the behaviour of $f(r)$ near the space time origin ($\rho \to 0$) is given by

$$f(r) = \frac{C_2}{B_0} + \mathcal{O}(\rho^2). \tag{7.29}$$

As we have set $C_2 = B_0$ to avoid a conical singularity, we have $f(r) \to 1$, as $\rho \to 0$, $r \to 0$. Using (7.24), we also have

$$M(r) \to -1 \qquad \text{as} \qquad r \to 0, \qquad \rho \to 0. \tag{7.30}$$

In pure adS3 $M = -1$ and is a constant. This can be seen by using (7.28) and the corresponding components of the adS3 metric (2.9) in place of $B(\rho), C(\rho)$.

We now seek to find an equation for $M(r)$. To do this we insert the metric ansatz (7.23) into (7.7), to obtain a differential equation for $M(r)$,

$$\frac{dM}{dr} = -16\pi\sqrt{C(\rho)}\,\langle \widetilde{T}^t_t \rangle(\rho). \tag{7.31}$$

It will be noted that the left hand side of (7.31) is the derivative of M with respect to the radial coordinate r, whilst the right hand side of (7.31) contain terms dependent on ρ. However, using (7.25) we have

$$\frac{dM}{d\rho} = -8\pi C'(\rho)\,\langle \widetilde{T}^t_t \rangle(\rho). \tag{7.32}$$

We now numerically integrate (7.32) with respect to ρ, using the NIntegrate function in MATHEMATICA, with the constant of integration is given by $M(0) = -1$. The integration is performed for $\rho \in [\pi/200, 94\pi/200]$ as this matches the range of the $\langle \widetilde{T}_t^t \rangle$ term. We thus obtain $M(\rho)$ numerically. Using (7.25) and the previously determined metric function $C(\rho)$, we can obtain $M(r)$ which we use to produce plots of $M(r)$. It will be seen that the ranges of the r coordinate in the $M(r)$ plots are not all the same. This is a reflection of using the $C(\rho)$ functions only up to $\rho = 94\pi/200$ to reflect the range of the RSETs components, with the different $C(\rho)$ functions resulting in different ranges for the radial coordinate r.

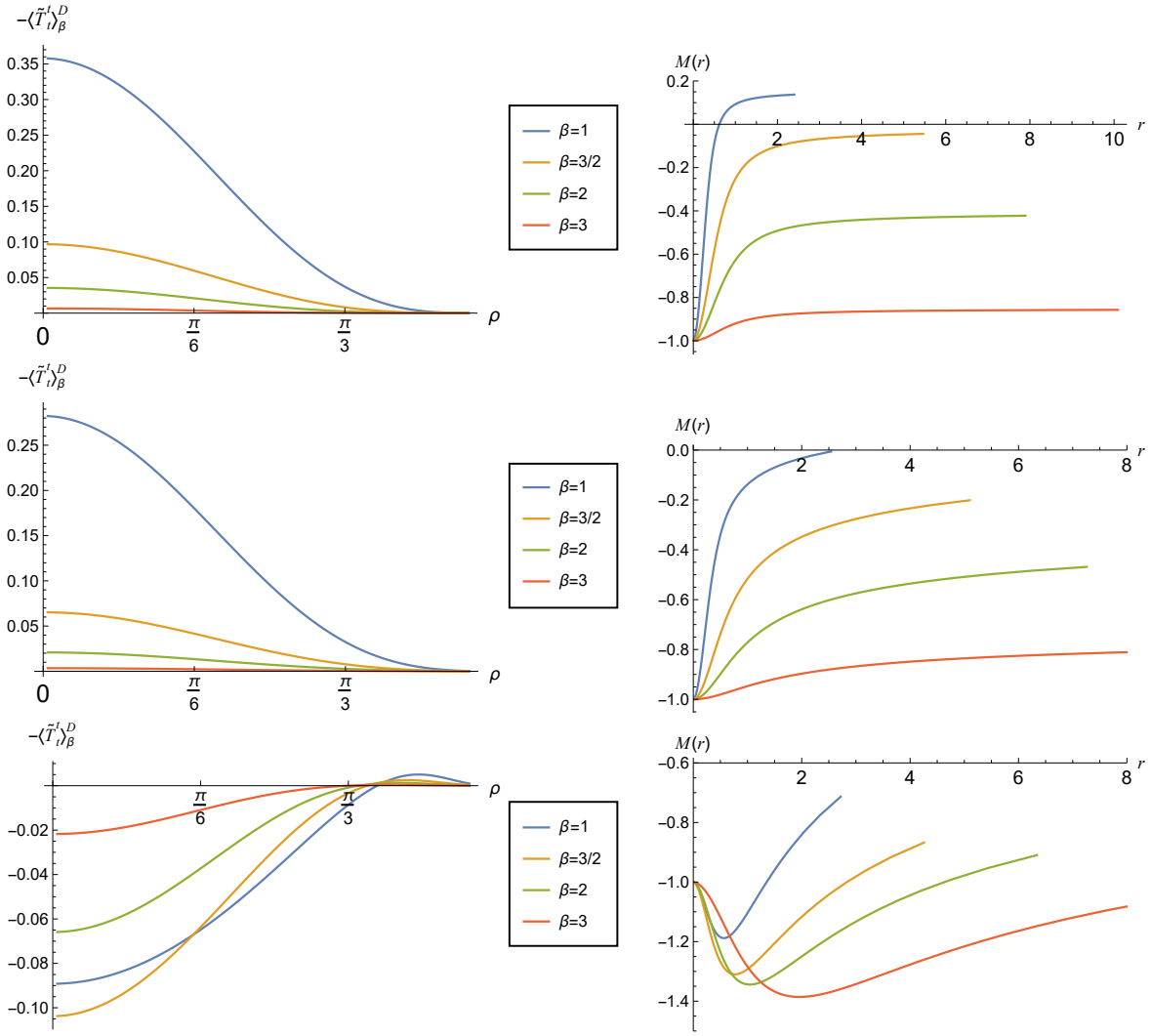

Figure 7.6: Mass functions $M(r)$ (right) with the corresponding energy density profiles (left) for a selection of thermal states with a range of inverse temperatures β. Top row, $\nu = 1/2$, $\xi = 1/8$ (massless, conformally coupled). Second row, $\nu = 1/4$, $\xi = 0$ (minimally coupled) and third row, $\nu = 1/4$, $\xi = -1/2$. For all plots, Dirichlet boundary conditions were applied.

In analysing our results on adS3, we compare them to those obtained on adS4 with a massless, conformally coupled scalar field [95], where it was noted that the mass functions started at $M(0) = 0$, fixed by the integration constant, and then increased steeply before reaching a plateau. The $M(r)$

profiles in [95] tended to a finite limit as $r \to \infty$. This was described as demonstrating a solitonic behaviour, with the mass of the soliton given by the limit of $M(r)$ as $r \to \infty$.

To present the results of the $M(r)$ plots we use the RSETs from Figures 7.2–7.5. In addition we also use the RSET obtained from a scalar field with $\nu = 1/2$ in a thermal state with $\beta = 1$ and a selection of coupling constants ξ, with the Neumann boundary condition applied at the space-time boundary. Figure 7.6 shows the mass functions (right) obtained with a selection of thermal RSETs (left) with a range of inverse temperatures β. For all plots in Figure 7.6, Dirichlet boundary conditions were applied. The top row shows the thermal RSETs for a massless, conformally coupled scalar field with $\nu = 1/2$, $\xi = 1/8$. The energy density profiles (left) remain positive throughout space-time. The corresponding $M(r)$ plots (right) start at $M(r) = -1$ (fixed by the constant of integration) but as we move away from the space-time origin, the $M(r)$ profiles each increase monotonically with increasing r. The value of $M(r)$ is greater with rising temperature (decreasing β) and the separation between the different profiles increases with increasing r. All profiles appear to plateau at some value of r giving a solitonic appearance but only for the highest temperature $\beta = 1$ does $M(r)$ rise above zero (see Section 7.6 for further analysis on this matter). For the lowest temperature case studied ($\beta = 3$), we see that $M(r)$ remains close to -1 resembling the case of pure adS3 where $M = -1$. The $M(r)$ plots for the massless, conformally coupled field with Dirichlet boundary conditions (Figure 7.6, top) are qualitatively similar to those seen with the equivalent scalar field in adS4 [95].

In Figure 7.6 middle row, the energy densities and $M(r)$ plots are shown for thermal states with $\nu = 1/4$, $\xi = 0$. These RSETs also possess energy density profiles (left) that are positive throughout space-time. The corresponding $M(r)$ plots are shown on the right and qualitatively resemble those seen for the massless, conformally coupled case. We see that the $M(r)$ profiles start at -1 at the space-time origin for all inverse temperatures β, consistent with pure adS3. As we move away from the origin, the $M(r)$ profiles each increase monotonically with increasing r but all profiles remain negative throughout space-time (although the profile for $\beta = 1$ may becomes positive if the range of the r coordinate were extended). By examining the profiles alone it is difficult to say whether the mass functions plateau and become solitonic in appearance. More will be said about this point in Section 7.6. For the lowest temperature case studied ($\beta = 3$), we see that $M(r)$ remains close to -1 consistent with pure adS3.

In Figure 7.6, bottom row, we examine RSETs with predominantly negative energy densities (left). We use a scalar field with $\xi = -1/2$, $\nu = 1/4$. The $M(r)$ profiles (right) are qualitatively very different from those seen with either the minimally or conformally coupled field. At the space-time origin the $M(r)$ profiles all start at $M(r) = -1$ as in the case of pure adS3, but moving away from the origin, the profiles initially decrease with $M'(r) < 0$, attaining a minimum at some value of r where $M'(r) = 0$. The values of the minima decrease with decreasing temperature. All profiles then increase monotonically towards the space-time boundary, but only the profiles with $\beta < 2$ rise above -1. None of the profiles show any evidence of reaching a plateau. The behaviour of the $M(r)$ profiles in Figure 7.6, bottom row, may be understood by examining the corresponding energy density profiles. From (7.31), and noting that $r = \sqrt{C(\rho)}$ (7.25), it can be seen that $M'(r)$ depends on the energy density of the RSET. As the energy densities of the RSETs are initially negative, we see an initial decrease $M(r)$, attaining a minimum when the energy density profiles

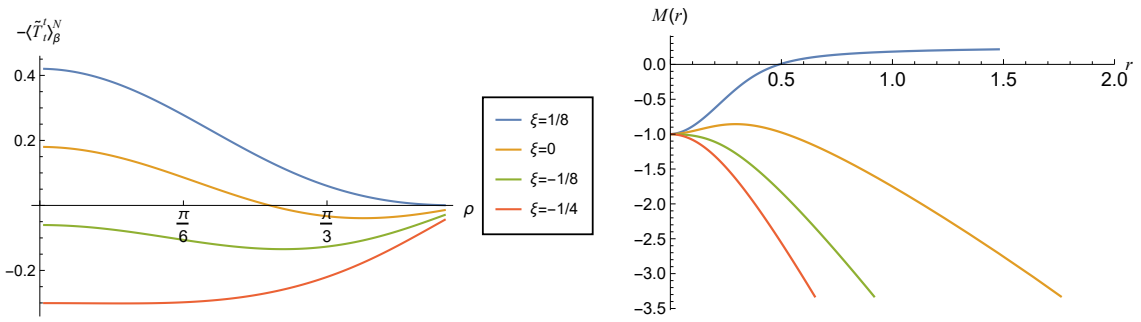

Figure 7.7: Mass functions $M(r)$ (right) with the corresponding energy density profiles (left) for a scalar field with $\nu = 1/2$ in a thermal state with $\beta = 1$ and a selection of coupling constants ξ. The Neumann boundary condition has been applied to the scalar field at the space-time boundary.

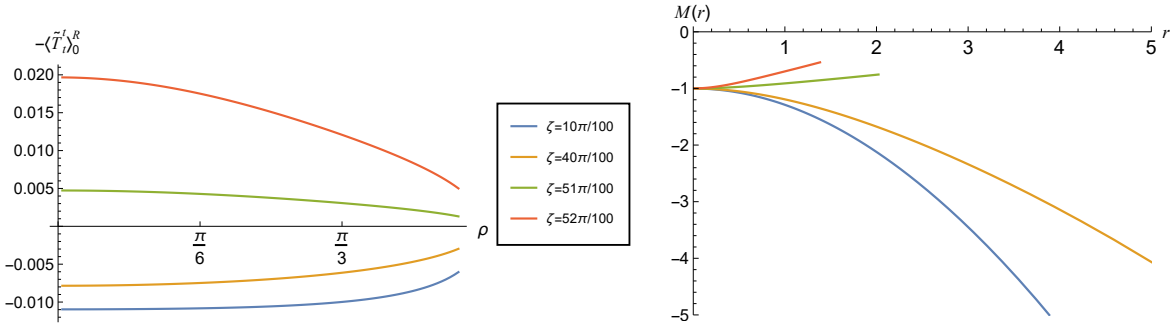

Figure 7.8: Mass functions $M(r)$ (right) with the corresponding energy density profiles (left) for a scalar field in the vacuum state with $\nu = 3/4$, $\xi = 1/8$ and Robin boundary conditions applied using a selection of Robin parameters ζ.

become zero (which occurs at different values of r for each temperature profile). When the RSETs become positive, we see $M(r)$ begin to rise.

Figure 7.6 shows the dramatic effect that varying the coupling constant ξ has on both the energy density profiles and the consequent $M(r)$ plots, especially when we have a negative ξ. We can examine this further by examining a scalar field in a thermal state with fixed inverse temperature β, and a variety of coupling constants. This is shown in Figure 7.7 with the Neumann boundary condition applied to the scalar field.

In Figure 7.7, we examine a selection of RSETs with $\nu = 1/2$, $\beta = 1$ and a range of coupling constants ξ. The Neumann boundary condition was applied to the scalar field at the space-time boundary. The coupling constants are chosen to produce a range of energy density profiles (left), some of which are negative for part or all of the space-time. The corresponding $M(r)$ plots are shown on the right. For $\xi = 1/8$ (conformal coupling), we have a standard energy density profile which is positive throughout space-time. The $M(r)$ profile increases monotonically from -1 at the origin, and plateaus at a small positive value. The profile is that of a soliton and resembles that seen in the massless, conformally coupled case with Dirichlet boundary conditions and $\beta = 1$ (Figure 7.6 top row). The $M(r)$ profile with minimal coupling ($\xi = 0$) increases initially away from the origin before decreasing monotonically with increasing r. The $M(r)$ profiles seen with the

negative coupling constants ($\xi = -1/8$, $\xi = -1/4$) decrease monotonically moving away from the origin. Only the $M(r)$ profile with $\xi = 1/8$ exhibits a solitonic shape.

In Figure 7.8, we have a selection of vacuum RSETs (left) obtained using Robin boundary conditions with a range of Robin parameters ζ, with $\nu = 3/4$. The corresponding plots for the $A(\rho), B(\rho), C(\rho)$ functions are shown in Figure 7.5. The values of ζ were chosen to give two energy density profiles which are entirely positive energy ($\zeta = 51\pi/100$ and $\zeta = 52\pi/10$) and two entirely negative ($\zeta = 10\pi/100$ and $\zeta = 40\pi/100$). As can be seen, the profiles of the $M(r)$ plots (right) are very different to those seen in thermal states with Dirichlet boundary conditions, Figure 7.6. All profiles start at $M(r) = -1$ as before but the $M(r)$ profiles for the RSETs with negative energy densities ($\zeta = 10\pi/100$, $40\pi/100$) decrease monotonically (become progressively more negative) with increasing r, as we move away from the space-time origin. The $M(r)$ profiles with positive energy densities ($\zeta = 51\pi/100$, $52\pi/100$) increase monotonically as we move away from the boundary but the ranges of the r coordinates are restricted compared to their negative energy counterparts. None of the $M(r)$ profiles show any evidence of plateau and do not seem to converge to a finite limit as $r \to \infty$ and, therefore, do not exhibit a solitonic behaviour.

§ 7.6 Mass function at the boundary

In Figure 7.6 (top), it appeared that the mass function profiles for the massless, conformally coupled scalar field converged to a finite limit as $r \to \infty$. This is consistent with the finding in [95] and depicts a solitonic behaviour of $M(r)$. We now give additional evidence to support this conclusion. It can be seen in Figure 7.3 that the ratios of $C(\rho)/\tan^2(\rho)$ converge to a temperature-dependent finite limit C_∞^β as $\rho \to \pi/2$. Thus, using the Taylor series expansion of $\tan^2(\rho)$ near $\rho \to \pi/2$, we have

$$r^2 = C(\rho) \sim C_\infty^\beta \left(\frac{\pi}{2} - \rho\right)^{-2} + \mathcal{O}\left(\frac{\pi}{2} - \rho\right)^0 . \tag{7.33}$$

In keeping with [95], we make the assumption that near the space-time boundary as $\rho \to \pi/2$, the expansion of the $\langle \widetilde{T}_t^t \rangle$ component of the RSET takes the form

$$\langle \widetilde{T}_t^t \rangle = \mathcal{T}_\infty \left(\frac{\pi}{2} - \rho\right)^a + \mathcal{O}\left(\frac{\pi}{2} - \rho\right)^{a+1} , \tag{7.34}$$

for constants $\mathcal{T}_\infty$ and a. Using (7.31), we can express the derivative of the mass function near the boundary as $r \to \infty$, $\rho \to \pi/2$ to leading order as

$$\begin{aligned} \frac{dM}{dr} &\sim -16\pi \sqrt{C_\infty^\beta}\, \mathcal{T}_\infty \left(\frac{\pi}{2} - \rho\right)^{a-1} \\ &\sim \mathcal{O}(r^{(1-a)}). \end{aligned} \tag{7.35}$$

For $M(r)$ to converge to a finite limit as $\rho \to \pi/2$ and to avoid a logarithmic behaviour as $r \to \infty$ we require that $a > 2$. To determine an approximation for a we perform a log-log plot of $\langle \widetilde{T}_t^t \rangle$ in (7.34) with the leading order term in the right hand side of (7.34), displayed in Figure 7.9. We then use the LinearModelFit function in MATHEMATICA to compute an approximation to the constant a. To improve the accuracy of the linear model fit we have chosen the range of ρ in

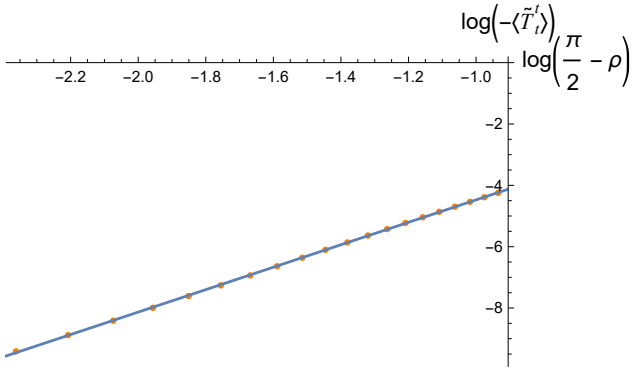

Figure 7.9: Loglog plot of the first term of the RHS of (7.34) (orange dotted) for a massless, conformally coupled field ($\nu = 1/2$, $\xi = 1/8$) with $\beta = 1$. We determine the coefficient a using a LinearModelFit (blue line). See text for further details.

Figure 7.9 to be $\rho \in [74\pi/200, 94\pi/200]$ as we are really interested in the behaviour of $\langle \widetilde{T}^t_t \rangle$ as we approach the space-time boundary. We find a good approximation between the log-log plot (orange dots) and the linear model fit (blue line) giving $a \sim 3.6$. This supports the conclusion that $M(r)$ converges to a finite limit as $r \to \infty$ for the massless,conformally coupled scalar field. Performing the same analysis for higher values of β (lower temperatures) gives similar values of $\alpha > 3$.

In the case of the minimally coupled scalar field ($\nu = 1/4$, $\xi = 0$) shown in Figure 7.6 (middle), the convergence of the $M(r)$ plots to a finite value as $r \to \infty$ is less obvious to the naked eye. Repeating the analysis as for the massless, conformally coupled case, we find that for $\beta = 1$ we have $a \sim 2.7$, suggesting that the $M(r)$ plot does indeed converge. When we increase β (decrease the temperature) we find that a decreases with increasing β. Thus for $\beta = 3$, we have $a \sim 2.2$. This is still above the limit for a logarithmic behaviour suggesting again that for all values of β, the $M(r)$ plots in Figure 7.6 (middle) converge to some finite limit, demonstrating a solitonic behaviour.

§ 7.7 Conclusions

This chapter contains the concluding work in this thesis. We have computed the backreaction of a selection of RSETs on the underlying adS3 space-time geometry. In some respects it aims to close the loop regarding the different themes of research presented in the other chapters. We have used a selection of RSETs from Chapter 6 as the source term in Einstein's field equations to compute the QCM, with the emphasis being on the profiles of the RSETs rather than specifically focusing on boundary conditions. We have chosen, as the source term, RSETs with different energy density profiles, including some that are mostly or wholly negative throughout space-time. We have used two different metric ansatze for our QCMs. The first (7.8) has a similar form to the adS3 metric, so we can compare the component functions to the corresponding terms in the adS3 metric. The second metric ansatz (7.23) is that of a static, spherically symmetric metric in Schwarzschild-like coordinates, whereby we compute the 'mass' function. We compare our work with [95], where the QCM on adS4 was computed using a massless, conformally coupled scalar field with Dirichlet, Neumann and transparent boundary conditions.

Inserting the QCM ansatz (7.8) into the Einstein equations, we obtain three expressions for the

metric ansatz functions $A(\rho), B(\rho), C(\rho)$ in terms of the three nonzero components of the RSET. We use these equations (7.9, 7.10, 7.11), together with the conservation equation (7.12), to obtain ODEs for the different components of the QCM. As the RSET components used in the ODEs have been obtained numerically we first use the Interpolation function in MATHEMATICA to convert the data sets into a form that can be differentiated. The ODEs are solved numerically with MATHEMATICA and the individual QCM functions are displayed as ratios with the corresponding terms in ads3. For the three thermal states with Dirichlet boundary conditions, shown in Figures 7.2 – 7.4, we see that the metric functions have temperature-dependent profiles with the lowest temperature (highest β) ones most closely resembling their adS3 counterparts.

The behaviour of the QCM metric functions when Robin boundary conditions are used to derive the vacuum RSETs (Figure 7.8) are quite different to those seen in the thermal states. The $B(\rho)$ and $C(\rho)$ terms are dependent on the Robin parameter, with the $\zeta = 10\pi/100$ profile most closely resembling the adS3 Dirichlet case except towards the boundary. The $A(\rho)$ profiles have little dependence on the Robin parameter. All plots match their adS3 counterparts at the space-time origin and all decrease monotonically as they approach the space-time boundary, except for the $C(\rho)$ profile with $\zeta = 10\pi/100$, which appears to first increase towards the space-time boundary before decreasing.

We also use a general ansatz for a static, spherically symmetric metric (7.23) in Schwarzschild-like coordinates and determine the 'mass' functions, with the same RSETs used in Figures 7.3–7.5. Additionally, we use the RSETs obtained from the scalar field in a thermal state with Neumann boundary conditions and $\nu = 1/2$, $\beta = 1$ with a selection of coupling constants. The $M(r)$ plots are shown in Figures 7.6 – 7.8. In [95], where a massless, conformally coupled scalar field was studied in adS4, it was found that the mass functions exhibited solitonic behaviour for all inverse temperatures β. This observation was supplemented by an additional argument.

For the RSETs examined in this chapter, on a background adS3, we only see a solitonic type of behaviour for the mass functions with the massless, conformally coupled scalar field and possibly the minimally coupled field with $\nu = 1/4$, both with Dirichlet boundary conditions (Figure 7.6). Solitonic behaviour was also noted with the massless, conformally coupled field with Neumann boundary conditions and $\beta = 1$ (Figure 7.7). The $M(r)$ profiles seemed to converge to a finite limit that was very much temperature-dependent. This was supported by an additional argument. From (7.31) it can be seen that, in order for the $M(r)$ plots to converge, we require that $\langle \widetilde{T}_t^t \rangle$ rapidly converges to zero as we approach the space-time boundary. It may be that the lack of convergence seen with some of the $M(r)$ plots is because the RSETs computed in Chapter 6 were obtained for $\rho \in [\pi/200, 94\pi/200]$. Numerical error in the computation of the RSETs prevented us from easily going closer to the space-time boundary. In keeping with [27, 95], if $M(r)$ converges to a finite limit, we refer to this limit as the mass of the metric or soliton. When the $M(r)$ profile does not converge it is not possible to clearly define a notion of coordinate or metric mass and in these cases the significance of the mass functions remain an open question.

The selection of RSETs chosen in this chapter, as the source terms for the study of the QCMs, was limited primarily due to time constraints. The intention was to give a flavour of the different types of QCM solutions possible with the RSETs obtained in Chapter 6. It would be interesting to give a more comprehensive account of the role played by the coupling constant and boundary conditions and to what extent we can obtain solitonic type of solutions for the mass functions.

Furthermore, in the choice of expansion for the $C(\rho)$ function in (7.19), we set $C_2 = B_0$ so as to avoid a conical singularity. It would be interesting to examine the results if we relaxed this restriction and considered an expansion where $C_0 \neq 0$. Preliminary results in this area suggest the possibility of black hole solutions to the QCM. We intend to expand on this in a forthcoming publication.

Chapter 8

Conclusions and outlook

In this thesis we have used the framework of quantum field theory in curved space-time to study a free quantum scalar field $\hat{\Phi}$ propagating on a background classical, curved anti-de Sitter space-time (adS). We have focused on the numerical computation of expectation values of the scalar field, using MATHEMATICA, in both three (adS3) and four (adS4) dimensions. The main aims of the thesis are

- To compute the v.e.v.s and t.e.v.s of the renormalised stress energy tensor (RSET) for a massless, conformally coupled scalar field in adS4 with a range of Robin boundary conditions.
- To compute the v.e.v.s and t.e.v.s of the renormalised vacuum polarisation $\langle\hat{\Phi}^2\rangle$ for a scalar field with general mass and coupling to the background adS3. We have used Dirichlet, Neumann and Robin boundary conditions applied to the scalar field at the space-time boundary.
- To compute the v.e.v.s and t.e.v.s of the RSET for a scalar field with general mass and coupling in adS3 with a range of Robin boundary conditions.
- To determine the backreaction of a selection of RSETs on the underlying adS3 space-time geometry and calculate the components of the quantum-corrected metric (QCM).

Anti-de Sitter space-time is a maximally symmetric solution to Einstein's field equations (1.1) with a constant negative curvature. The lack of global hyperbolicity necessitates the use of boundary conditions. Using Hadamard renormalisation, in the covering space of adS3 (CadS3), we have numerically computed the renormalised vacuum polarisation (VP) of a scalar field with general mass and coupling for a range of Robin boundary conditions. We have shown that there is an upper limit for the value of the Robin parameter ζ_{crit}, beyond which our scalar field becomes classically unstable. We work in Euclidean space where the Green's functions are unique without the need for an '$i\epsilon$' prescription.

Our motivation in computing the VP was centered on [71] where the VP was calculated for a massless, conformally coupled scalar field on adS4 using a range of Robin boundary conditions. In [71], it was found that for all Robin boundary conditions, the VP converged to the Neumann result at the space-time boundary except Dirichlet which had its own limit. We wanted to see whether the findings in [71] applied to a scalar field with general mass and curvature coupling. Our results are displayed in Figures 5.7–5.9 and show that both the v.e.v.s and t.e.v.s of the VP with Robin boundary conditions do indeed converge towards the Neumann result at the space-time boundary, except for Dirichlet which has its own limit. This supports the conclusion in [71] that the

Neumann boundary condition represents the generic behaviour of the field even though Dirichlet boundary conditions are most commonly studied in the literature.

For the determination of the RSET of a massless, conformally coupled scalar field in adS4, we use the representation of the Euclidean Green's functions with Robin boundary conditions from [71] and given in (3.37). This conveniently allows us to formulate the RSET, with Robin boundary conditions, as a combination of the RSET with Dirichlet and Neumann boundary conditions (3.46) together with a regular (or Robin) contribution. The RSET with Dirichlet and Neumann boundary conditions is obtained from [2]. The Robin contribution to the RSET was computed by applying a second order differential operator $\mathcal{T}_{\mu\nu}$ [35] to the regular contribution G_R^E in (3.37).

Our results for the v.e.v.s and t.e.v.s of the RSET with Robin boundary conditions in adS4 are displayed in Figure 3.4 and Figures 3.8–3.10. It can be seen that both the v.e.v.s and t.e.v.s of the RSET with Robin boundary conditions converge to the common v.e.v. seen with Dirichlet and Neumann boundary conditions (3.19). This is in agreement with the findings in [71] and Chapter 5 for the VP on adS3.

In Chapter 6 we extend the work in Chapter 3 and compute the v.e.v.s and t.e.v.s of the RSET for a scalar field with general mass and coupling. We work in adS3 as this simplifies the angular component of the Green's functions and avoids the use of conical (Mehler) functions. When we move away from the massless, conformally coupled field, we find that the v.e.v.s with Dirichlet and Neumann boundary conditions are no longer the same (6.9). This allows us to see whether the RSETs with Robin boundary conditions converge to the Neumann result.

The v.e.v.s and t.e.v.s of the RSET are computed using the Green's functions given in (5.83–5.85) for the vacuum state. Thermal Green's functions are computed from the vacuum ones by making the substitution $\omega \to n\kappa$ where $n \in \mathbb{N}$ and κ is related to the temperature of the field by (3.23). We follow the approach of [35] and determine the regular state-dependent component of the Hadamard parametrix (1.77) which we use in (6.16).

The results for the v.e.v.s and t.e.v.s with Robin boundary conditions are displayed in Figures 6.10–6.12 and Figures 6.23, 6.24. These figures support the finding that the v.e.v.s and t.e.v.s with Robin boundary conditions converge towards the Neumann result as the space-time boundary is approached. This is in keeping with the results seen with the VP in [71] and Chapter 5 and also for the RSET for the massless, conformally coupled scalar field in Chapter 3. However the convergence of the RSETs with Robin boundary conditions as the space-time boundary is approached is quite slow, particularly for the thermal states, which needs to be taking into account when making our conclusions.

Using a scalar field with general mass and coupling, in vacuum and thermal states, with different boundary conditions, presents us with an opportunity to change a number of different variables. As a result we are able to generate many plots to show the behaviour of the RSET when we vary such parameters as the temperature of the field, the coupling constant ξ and Robin parameter ζ. This has produced RSETs with some interesting properties, such as negative energy densities throughout some or all of the space-time. This is seen most clearly when we move away from the massless, conformally coupled scalar field. We find negative energy densities for both the vacuum (see for example Figure 6.10) and thermal states (see for example Figure 6.26), using different Robin boundary conditions and coupling constants.

Quantum states possessing negative energy densities violate the classical weak energy condition

(WEC) and may not even satisfy some quantum energy inequalities (Section 1.8). How such fields affect the properties of the quantum-corrected metric when we consider the backreaction of the RSET was in part the motivation for the research in Chapter 7. This contains the concluding work in this thesis, and in some respects some of the most significant aspects, as it details the interaction of the quantum field with the underlying space-time geometry. In studying the backreaction, we use a selection of the RSETs computed numerically in Chapter 6 as the source term in Einstein's field equations (1.2) and compute the components of the quantum-corrected metric (QCM). Our intention was to give a flavour of the possible types of solutions produced when we vary the field temperature, boundary conditions and coupling constants. We followed the methodology in [95] which looked at the backreaction for the massless, conformally coupled scalar field with Dirichlet, Neumann and transparent boundary conditions on adS4. In [95], the RSETs all possessed positive energy density profiles throughout space-time. Our focus in Chapter 7 was to chose RSETs with a mixture of positive and negative energy densities. We chose two metric ansatze for the QCM. The first (7.8) takes the form of the adS3 metric (2.9) which allows us to directly compare the component functions of the QCM with those of adS3 (Figures 7.2–7.5). The second metric ansatz chosen was also that of a general static, spherically symmetric metric but in Schwarzschild-like coordinates (7.23). Using this metric our attention was focused on the behaviour of the mass function $M(r)$ (7.28). It was seen in [95] that the mass functions demonstrated a solitonic profile for all thermal states studied regardless of whether Dirichlet, Neumann or transparent boundary conditions were used. This is likely to be a result of all the RSETs studied possessing a positive energy density throughout space-time and converging rapidly to zero as the space-time boundary is approached.

In Chapter 7, we found a solitonic behaviour of the mass functions for the massless conformally coupled field with Dirichlet (Figure 7.6 top) and Neumann (Figure 7.7) as well as for the minimally coupled scalar field with $\nu = 1/4$. These RSETs enjoy positive energy densities throughout space-time. When the mass function converges to a finite value, we can consider the limit of $M(r)$ as $r \to \infty$ as the mass of the soliton or coordinate mass. None of the RSETs containing negative energy densities demonstrated a solitonic profile for the mass function plots and the interpretation of the mass functions in these cases is an open question.

Throughout his thesis, except for Chapter 3, we have used the parameter ν (4.16), to encode information about the mass and coupling constant of the scalar field. We have computed the VP (Chapter 5) and RSET (Chapter 6) using three different values of ν, namely $\nu = 1/4, 1/2, 3/4$, where $\nu = 1/2$ represents the massless, conformally coupled scalar field. However, each value of ν can represent a range of values of the mass of the scalar field (m^2) and coupling constant ξ as shown in Figure 4.1. Indeed, when we looked at variations in the coupling constants with fixed ν for the RSETs in Chapter 6 (see Figure 6.14, for example), the mass of the field also changes in accordance with (4.16). An attempt to separate the effects of changing the mass and coupling constants was made to a limited degree in Figures 6.7 and 6.8 for thermal states with Dirichlet and Neumann boundary conditions. For fixed ξ/m^2 we can derive three values of m^2/ξ respectively corresponding to the three values of ν. In future research it would be worthwhile to compute the VP and RSETs where the mass and coupling constant are treated as independent variables and see to what extent they individually contribute to some of the exotic RSETs seen in Chapter 6.

It would also be worthwhile computing the QCM with a much wider range of RSETs from

Chapter 6 as the source term. This would allow us to determine the contributions made by varying the boundary conditions, temperature and coupling constants in a more comprehensive way. Also a different choice of metric ansatz can be used where the Taylor expansion of the $C(\rho)$ function is not constrained by setting $C_2 = B_0$. Preliminary work in this area has produced QCMs consistent with black hole solutions. We plan on presenting a more exhaustive account of the backreaction on adS3 in a future publication.

Finally, it would be instructive to compute the VP and RSET of a scalar field with general mass and coupling, with Robin boundary conditions on the BTZ background. The BTZ is a (2+1)-dimensional black hole solution to Einstein's field equations (1.2) and is asymptotically of adS3 geometry [9, 10]. We may expect that far from the black hole, renormalised expectation values would approach those of pure adS. Thus we have focused on the behaviour of the VP and RSET close to the boundary (Sections 3.8, 5.3). The BTZ metric can be derived by identifying points in adS3 [9, 10] and the Green's function for a massless, conformally coupled scalar field on a BTZ background has be found using the method of images [65, 89]. The renormalised VP and SET have been computed for a massless, conformally coupled scalar field with transparent [89], Dirichlet [63, 65] and Neumann [65] boundary conditions. Also, the Green's functions for the ground state of a massive scalar field has been constructed for Robin boundary conditions on a rotating BTZ background [21], but the VP and SET remain to be computed. Once the RSETs for a scalar field with general mass and coupling on a BTZ background have been computed, these could be used as source terms in Einstein's equations to compute the QCM, thus extending the work in [25, 26, 65, 67, 87]. The effects of RSETs with negative energy densities on the singularities of the BTZ black hole would be an exciting avenue to explore in future work.

Bibliography

[1] O. Aharony, S. S. Gubser, J. Maldacena, H. Ooguri, and Y. Oz. Large n field theories, string theory and gravity. *Phys. Rept.*, 323:183, 2000.

[2] B. Allen, A. Folacci, and G. W. Gibbons. Anti-de Sitter space at finite temperature. *Phys. Lett. B*, 189:304, 1987.

[3] B. Allen and T. Jacobson. Vector two-point functions in maximally symmetric spaces. *Commun. Math. Phys.*, 103:669, 1986.

[4] V. E. Ambrus, C. Kent, and E. Winstanley. Analysis of scalar and fermion quantum field theory on anti-de Sitter spacetime. *Int. J. Mod. Phys. D*, 27:1843014, 2018.

[5] J. Arrechea, C. Barceló, R. Carballo-Rubio, and L. J. Garay. Schwarzschild geometry counterpart in semiclassical gravity. *Phys. Rev. D*, 101:064059, 2020.

[6] J. Arrechea, C. Barceló, R. Carballo-Rubio, and L. J. Garay. Reissner–Nordström geometry counterpart in semiclassical gravity. *Class. Quant. Grav.*, 38:115014, 2021.

[7] A. Ashtekar and E. Bianchi. A short review of loop quantum gravity. *Rept. Prog. Phys.*, 84:042001, 2021.

[8] S. J. Avis, C. J. Isham, and D. Storey. Quantum field theory in anti-de Sitter space-time. *Phys. Rev. D*, 18:3565, 1978.

[9] M. Banados, M. Henneaux, C. Teitelboim, and J. Zanelli. Geometry of the (2+1) black hole. *Phys. Rev. D*, 48:1506, 1993.

[10] M. Banados, C. Teitelboim, and J. Zanelli. The black hole in three-dimensional space-time. *Phys. Rev. Lett.*, 69:1849, 1992.

[11] C. Barceló and M. Visser. Traversable wormholes from massless conformally coupled scalar fields. *Physics Letters B*, 466:127, 1999.

[12] V. S. Barroso and J. P. M. Pitelli. Boundary conditions and vacuum fluctuations in AdS_4. *Gen. Rel. Grav.*, 52:29, 2020.

[13] C. A. Bayona and N. R. F. Braga. Anti-de Sitter boundary in Poincare coordinates. *Gen. Rel. Grav.*, 39:1367, 2007.

[14] I. Bengtsson. Anti de-Sitter space. *http: // www. physto. se/ ingemar/ Kurs. ps*, 2009.

[15] M. Benini, C. Dappiaggi, and A. Schenkel. Algebraic quantum field theory on spacetimes with timelike boundary. *Ann. H. Poincaré*, 19:2401, 2018.

[16] D. Bernard and A. Folacci. Hadamard function, stress tensor and de Sitter space. *Phys. Rev. D*, 34:2286, 1986.

[17] N. D. Birrell and P. C. W. Davies. *Quantum Fields in Curved Space*. Cambridge Monographs on Mathematical Physics. Cambridge Univ. Press, Cambridge, UK, 1984.

[18] C. G. Bollini and J. J. Giambiagi. Dimensional renormalization: The number of dimensions as a regularizing Parameter. *Nuovo Cim. B*, 12:20, 1972.

[19] P. Breitenlohner and D. Z. Freedman. Stability in gauged extended supergravity. *Annals Phys.*, 144:249, 1982.

[20] M. R. Brown and A. C. Ottewill. Photon propagators and the definition and approximation of renormalized stress tensors in curved space-time. *Phys. Rev. D*, 34:1776, 1986.

[21] F. Bussola, C. Dappiaggi, H. R. C. Ferreira, and I. Khavkine. Ground state for a massive scalar field in the BTZ spacetime with Robin boundary conditions. *Phys. Rev. D*, 96:105016, 2017.

[22] L. de Souza Campos, C. Dappiaggi, and L. Sinibaldi. Hidden freedom in the mode expansion on static spacetimes. *Gen. Rel. Grav.*, 55:50, 2023.

[23] S. M. Carroll. *Spacetime and geometry: an introduction to general relativity*. Addison Wesley, San Francisco; London, 2004.

[24] M. Casals, A. Fabbri, C. Martínez, and J. Zanelli. Quantum dress for a naked singularity. *Phys. Lett. B*, 760:244, 2016.

[25] M. Casals, A. Fabbri, C. Martínez, and J. Zanelli. Quantum backreaction on three-dimensional black holes and naked singularities. *Phys. Rev. Lett.*, 118:131102, 2017.

[26] M. Casals, A. Fabbri, C. Martínez, and J. Zanelli. Quantum-corrected rotating black holes and naked singularities in (2+1) dimensions. *Phys. Rev. D*, 99:104023, 2019.

[27] P. T. Chruściel and R. Wutte. Gluing-at-infinity of two-dimensional asymptotically locally hyperbolic manifolds. *arXiv*: 2401.04048, 2024.

[28] E. Curiel. A primer on energy conditions. *Einstein Stud.*, 13:43, 2017.

[29] C. Dappiaggi, H. Ferreira, and A. Marta. Ground states of a Klein-Gordon field with Robin boundary conditions in global anti-de Sitter spacetime. *Phys. Rev. D*, 98:025005, 2018.

[30] C. Dappiaggi and H. R. C. Ferreira. Hadamard states for a scalar field in anti–de Sitter spacetime with arbitrary boundary conditions. *Phys. Rev. D*, 94:125016, 2016.

[31] C. Dappiaggi and H. R. C. Ferreira. On the algebraic quantization of a massive scalar field in anti-de-Sitter spacetime. *Rev. Math. Phys.*, 30:1850004, 2017.

[32] C. Dappiaggi, H. R. C. Ferreira, and B. A. Juárez-Aubry. Mode solutions for a Klein-Gordon field in anti-de Sitter spacetime with dynamical boundary conditions of Wentzell type. *Phys. Rev. D*, 97:085022, 2018.

[33] C. Dappiaggi, B. A. Juárez-Aubry, and A. Marta. Ground state for the Klein-Gordon field in anti–de Sitter spacetime with dynamical Wentzell boundary conditions. *Phys. Rev. D*, 105:105017, 2022.

[34] C. Dappiaggi and A. Marta. Fundamental solutions and Hadamard states for a scalar field with arbitrary boundary conditions on an asymptotically AdS spacetimes. *Math. Phys. Anal. Geom.*, 24:28, 2021.

[35] Y. Decanini and A. Folacci. Hadamard renormalization of the stress-energy tensor for a quantized scalar field in a general spacetime of arbitrary dimension. *Phys. Rev. D*, 78:044025, 2008.

[36] D. Deutsch and P. Candelas. Boundary effects in quantum field theory. *Phys. Rev. D*, 20:3063, 1979.

[37] B. S. DeWitt. Dynamical theory of groups and fields. *Conf. Proc. C*, 630701:585, 1964.

[38] B. S. DeWitt. Quantum field theory in curved space-time. *Phys. Rept.*, 19:295, 1975.

[39] NIST Digital Library of Mathematical Functions. Release 1.1.12 of 2023-12-15. F. W. J. Olver, A. B. Olde Daalhuis, D. W. Lozier, B. I. Schneider, R. F. Boisvert, C. W. Clark, B. R. Miller, B. V. Saunders, H. S. Cohl, and M. A. McClain, eds.

[40] J. Earman and C. Glymour. Relativity and eclipses: The british eclipse expeditions of 1919 and their predecessors. *Historical studies in the physical sciences*, 11:49, 1980.

[41] A. Einstein. The field equations of gravitation. *Sitzungsber. Preuss. Akad. Wiss. Berlin (Math. Phys.)*, 1915:844, 1915.

[42] E. Elizalde, S. D. Odintsov, A. Romeo, A. A. Bytsenko, and S. Zerbini. *Zeta regularization techniques with applications*. World Scientific Publishing, Singapore, 1994.

[43] H. Epstein, V. Glaser, and A. Jaffe. Nonpositivity of energy density in quantized field theories. *Nuovo Cim.*, 36:1016, 1965.

[44] C. J. Fewster. Lectures on quantum energy inequalities. *arXiv*: 1208.5399, 2012.

[45] C. J. Fewster. *Quantum Energy Inequalities*. In: Wormholes, warp drives and energy conditions. Ed. F.S.N. Lobo, Springer International Publishing, Cham, 2017.

[46] E. E. Flanagan and R. M. Wald. Does back reaction enforce the averaged null energy condition in semiclassical gravity? *Phys. Rev. D*, 54:6233, 1996.

[47] L. H. Ford. Quantum coherence effects and the second law of thermodynamics. *Proc. Roy. Soc. Lond. A*, 364:227, 1978.

[48] S. A Fulling. *Aspects of quantum field theory in curved space-time.* London Mathematical Society student texts. Cambridge University Press, 1989.

[49] S. A. Fulling, M. Sweeny, and R. M. Wald. Singularity structure of the two point function in quantum field theory in curved space-time. *Commun. Math. Phys.*, 63:257, 1978.

[50] O. Gannot and M. Wrochna. Propagation of singularities on AdS spacetimes for general boundary conditions and the holographic Hadamard condition. *J. Inst. Math. Jussieu*, 21:67, 2022.

[51] J. Hadamard. *Lectures on Cauchy's problem in linear partial differential equations.* Yale University Press; O.U.P., New Haven: London, 1923.

[52] S. W. Hawking. The occurrence of singularities in cosmology. *Proc. Roy. Soc. Lond. A*, 294:511, 1966.

[53] S. W. Hawking. Particle creation by black holes. *Commun. Math. Phys.*, 43:199, 1975. [Erratum: *Commun. Math. Phys.,* 46, 206 (1976)].

[54] S. W. Hawking. Zeta function regularization of path integrals in curved space-time. *Commun. Math. Phys.*, 55:133, 1977.

[55] S. W. Hawking and G. F. R. Ellis. *Large scale structure of space-time.* Cambridge Monographs on Mathematical Physics. Cambridge University Press, Cambridge, UK, 1973.

[56] D. Hochberg, T. W. Kephart, and J. W. York. Positivity of entropy in the semiclassical theory of black holes and radiation. *Phys. Rev. D*, 48:479, 1993.

[57] D. Hochberg, T. W. Kephart, and J. W. York. Effective potential of a black hole in thermal equilibrium with quantum fields. *Physical Review D*, 49:5257, 1994.

[58] A. Ishibashi and R. M. Wald. Dynamics in nonglobally hyperbolic static space-times. 2. General analysis of prescriptions for dynamics. *Class. Quant. Grav.*, 20:3815, 2003.

[59] A. Ishibashi and R. M. Wald. Dynamics in nonglobally hyperbolic static space-times. 3. Anti-de Sitter space-time. *Class. Quant. Grav.*, 21:2981, 2004.

[60] C. Kent. Quantum scalar field theory on anti-de sitter space. PhD thesis. University of Sheffield, *https://etheses.whiterose.ac.uk/4911*, 2013.

[61] C. Kent and E. Winstanley. Hadamard renormalized scalar field theory on anti-de Sitter spacetime. *Phys. Rev. D*, 91:044044, 2015.

[62] E.-A. Kontou and K. Sanders. Energy conditions in general relativity and quantum field theory. *Class. Quant. Grav.*, 37:193001, 2020.

[63] D. A. Kothawala, S. Shankaranarayanan, and L. Sriramkumar. Quantum gravitational corrections to the stress-energy tensor around the BTZ black hole. *JHEP*, 09:095, 2008.

[64] T. Lancaster and S. Blundell. *Quantum field theory for the gifted amateur.* Oxford University Press, Oxford, 2015.

[65] G. Lifschytz and M. Ortiz. Scalar field quantization on the (2+1)-dimensional black hole background. *Phys. Rev. D*, 49:1929, 1994.

[66] E. M. Lifshits and L. D. Landau. *Fluid mechanics*. Course of theoretical physics; 6. Pergamon, Oxford, 1959.

[67] C. Martinez and J. Zanelli. Back reaction of a conformal field on a three-dimensional black hole. *Phys. Rev. D*, 55:3642, 1997.

[68] C. W Misner, J. A. Wheeler, and K. S. Thorne. *Gravitation*. W. H. Freeman, San Francisco, 1973.

[69] T. Morley. Vacuum polarisation on asymptotically anti-de sitter space-times. PhD thesis. University of Sheffield, *https://etheses.whiterose.ac.uk/28483*, 2020.

[70] T. Morley, S. Namasivayam, and E. Winstanley. Renormalized stress-energy tensor on global anti-de Sitter space-time with Robin boundary conditions. *Gen. Rel. Grav.*, 56:38, 2024.

[71] T. Morley, P. Taylor, and E. Winstanley. Quantum field theory on global anti-de Sitter space-time with Robin boundary conditions. *Class. Quant. Grav.*, 38:035009, 2021.

[72] V. F Mukhanov and S. Winitzki. *Introduction to quantum effects in gravity*. Cambridge University Press, Cambridge, 2007.

[73] S. Namasivayam and E. Winstanley. Vacuum polarization on three-dimensional anti-de Sitter space-time with Robin boundary conditions. *Gen. Rel. Grav.*, 55:13, 2023.

[74] S. Namasivayam and E. Winstanley. Quantum-corrected metric on three dimensional anti-de Sitter space-time. *In preparation*, 2024.

[75] S. Namasivayam and E. Winstanley. Renormalised stress energy tensor on three dimensional anti-de Sitter space-time with Robin boundary conditions for a scalar field with generalised mass and coupling. *In preparation*, 2024.

[76] K. Oldham, J. Myland, and J. Spanier. *An atlas of functions. With Equator, the atlas function calculator*. Springer Science+Business Media, Heidelberg, Germany, 2009.

[77] L. Parker and S. A. Fulling. Adiabatic regularization of the energy momentum tensor of a quantized field in homogeneous spaces. *Phys. Rev. D*, 9:341, 1974.

[78] L. E. Parker and D. J. Toms. *Quantum field theory in curved spacetime: quantised fields and gravity*. Cambridge Monographs on Mathematical Physics. Cambridge University Press, Cambridge, 2009.

[79] W. Pauli and F. Villars. On the invariant regularization in relativistic quantum theory. *Rev. Mod. Phys.*, 21:434, 1949.

[80] R. Penrose. Gravitational collapse and space-time singularities. *Phys. Rev. Lett.*, 14:57, 1965.

[81] S. Perlmutter et al. Measurements of Ω and Λ from 42 High Redshift Supernovae. *Astrophys. J.*, 517:565, 1999.

[82] M. E. Peskin and D. V. Schroeder. *An introduction to quantum field theory*. Addison-Wesley, Reading, USA, 1995.

[83] J. P. M. Pitelli, V. S. Barroso, and R. A. Mosna. Boundary conditions and renormalized stress-energy tensor on a Poincaré patch of AdS_2. *Phys. Rev.*, D99:125008, 2019.

[84] E. Poisson, A. Pound, and I. Vega. The motion of point particles in curved spacetime. *Living reviews in relativity*, 14:7, 2011.

[85] R. V. Pound and G. A. Rebka, Jr. Apparent weight of photons. *Phys. Rev. Lett.*, 4:337, 1960.

[86] J. S. Schwinger. On gauge invariance and vacuum polarization. *Phys. Rev.*, 82:664, 1951.

[87] K. Shiraishi and T. Maki. Quantum fluctuation of stress tensor and black holes in three dimensions. *Phys. Rev. D*, 49:5286, 1994.

[88] L. M. Sokołowski. The bizarre anti-de Sitter spacetime. *Int. J. Geom. Meth. Mod. Phys.*, 13:1630016, 2016.

[89] A. R. Steif. The quantum stress tensor in the three-dimensional black hole. *Phys. Rev. D*, 49:585, 1994.

[90] H. Stephani. *Relativity: an introduction to special and general relativity*. Cambridge University Press, Cambridge, third edition, 2004.

[91] J. L. Synge. *Relativity: the general theory*. Series in physics. North-Holland, Amsterdam, 1960.

[92] G. 't Hooft and M. J. G. Veltman. Regularization and renormalization of gauge fields. *Nucl. Phys. B*, 44:189, 1972.

[93] P. Taylor and C. Breen. Semiclassical backreaction on asymptotically anti–de Sitter black holes. *Phys. Rev. D*, 103:025006, 2021.

[94] P. Taylor, C. Breen, and A. Ottewill. Mode-sum prescription for the renormalized stress energy tensor on black hole spacetimes. *Phys. Rev. D*, 106:065023, 2022.

[95] J. C. Thompson and E. Winstanley. Quantum-corrected anti-de Sitter space-time. *arXiv*: 2405.20422, 2024.

[96] J. H. Van Vleck. The correspondence principle in the statistical interpretation of quantum mechanics. *Proc. Nat. Acad. Sci.*, 14:178, 1928.

[97] M. Visser. van Vleck determinants: Geodesic focusing and defocusing in Lorentzian space-times. *Phys. Rev. D*, 47:2395, 1993.

[98] R. M. Wald. The back reaction effect in particle creation in curved space-time. *Commun. Math. Phys.*, 54:1, 1977.

[99] R. M. Wald. Trace anomaly of a conformally invariant quantum field in curved space-Time. *Phys. Rev. D*, 17:1477, 1978.

[100] R. M. Wald. On the Euclidean approach to quantum field theory in curved space-time. *Commun. Math. Phys.*, 70:221, 1979.

[101] R. M. Wald. Dynamics in nonglobally hyperbolic, static space-times. *J. Math. Phys.*, 21:2802, 1980.

[102] R. M. Wald. *Quantum field theory in curved space-time and black hole thermodynamics*. Chicago Lectures in Physics. University of Chicago Press, Chicago, IL, 1995.

[103] B. Zwiebach. *A first course in string theory*. Cambridge University Press, Cambridge, second edition, 2009.